Cavity-enhanced hyperspectral Raman and Absorption Microscopy

Thomas Hümmer

München 2019

Cavity-enhanced hyperspectral Raman and Absorption Microscopy

Dissertation
an der Fakultät für Physik
der Ludwig–Maximilians–Universität
München

vorgelegt von
Thomas Hümmer
aus München

München, den 16.5.2019

Erstgutachter: Prof. Dr. Theodor W. Hänsch
Zweitgutachter: Prof. Dr. David Hunger
Tag der mündlichen Prüfung: 26.7.2019

Zusammenfassung

Diese Arbeit stellt ortsaufgelöste Raman- und Absorptionsspektroskopie, verstärkt durch einen durchstimmbaren optischen Mikroresonator, vor. Allein aufgrund ihrer Größe interagiert nanoskalige Materie nur schwach mit Licht und entzieht sich daher oft der direkten Beobachtung. Optische Resonatoren können schwache Signale durch konstruktive Interferenz von Licht verstärken. Mittels Mikroresonatoren mit kleiner Strahltaille und eines rastermikroskopischen Ansatzes können damit ortsaufgelöste Messungen durchgeführt werden. In dieser Arbeit werden Techniken für empfindliche Mikroskopie und Spektroskopie entwickelt, ihre Leistung analysiert und Messungen an Nanoteilchen durchgeführt.

Als Grundlage für schnelle und kontrollierte spektroskopische Messungen wird ein hochstabiler, zugleich aber weit durchstimmbarer und transversal scannbarer Resonator-Aufbau entwickelt. Eine Längenstabilität von etwa $200\,\mathrm{fm}$ wird gezeigt, deutlich unterhalb der Linienbreite des Resonators. Um Spektroskopie zu ermöglichen werden mehrere Ansätze zur Stabilisierung und Durchstimmung der Resonanzwellenlänge entwickelt.

Mit Hilfe des Resonators mit kleinem Modenvolumen wird Raman-Streuung durch den Purcell-Effekts verstärkt. Durch den direkten Vergleich der Raman-Emissionsstärke ein und desselben einzelnen Kohlenstoff-Nanoröhrchens im Resonator zu einer konfokalen Messung kann der Purcell-Faktor bestimmt und die erwartete Skalierung mit dem Modenvolumen gezeigt werden. Mit resonatorverstärkter Raman-Mikroskopie können dann Informationen über den Durchmesser und die elektronischen Eigenschaften einzelner Kohlenstoff-Nanoröhrchen extrahiert werden.

Um die Empfindlichkeit weiter zu steigern, wird die Ramanspektroskopie auf ein Schema ausgedehnt, bei dem der Anregungslaser und die Raman-Streuung gleichzeitig mit verschiedenen longitudinalen Moden resonant sind. Hierzu wird eine maßgeschneiderte Spiegelbeschichtung entwickelt. Sie erlaubt Zugriff auf einen weiten Bereich des Raman-Spektrums ($900\,\mathrm{cm}^{-1}$bis $1800\,\mathrm{cm}^{-1}$) durch kontinuierliche Änderung der Resonatorlänge.

Resonator-verstärkte Absorptionsmessungen werden durch eine optimierte Datenerfassungselektronik und die hohe mechanische Stabilität im Vergleich zu bisherigen Experimenten um mehr als drei Größenordnungen beschleunigt. Dies erlaubt hochempfindliche Absorptionsmikroskopie in Echtzeit und die Aufnahme hyperspektraler Absorptionsbilder mittels eines durchstimmbaren Lasers.

Absorptionsspektroskopie und -mikroskopie wird an Kohlenstoff-Nanoröhrchen und 2D-Materialien durchgeführt. Dabei werden absolute Absorptionsquerschnitte, Polarisationsabhängigkeit, räumliche Substrukturen und Resonanzen auf ppm-Niveau sichtbar.

In einem Exkurs wird Absorptionsspektroskopie mit breitbandigen Lichtquellen in Kombination mit integrierenden Photodetektoren untersucht. Erste Messungen zeigen, dass Absorption kleiner als 10^{-6} mit Picowatt-Intensitäten gemessen werden kann, nur begrenzt durch Schrotrauschen. Dies liegt weit unter der Leistung die bei konventioneller Absorptionsspektroskopie benötigt werden würde.

In einer Analyse der derzeitigen Grenzen der Empfindlichkeit und Geschwindigkeit wird Potential für weitere Verbesserungen aufgezeigt. Die vorgestellte Mikroresonator-Plattform, ihre spektroskopische Empfindlichkeit und die mikroskopisch aufgelösten Messungen könnten eine Basistechnologie für die Grundlagenforschung werden.

Abstract

This thesis introduces spatially resolved Raman scattering and absorption spectroscopy of individual nanoscale matter, enhanced using a tunable optical micro-cavity. By the virtue of their small size, individual nanoscale solid state systems provide weak interaction with light and therefore often escape direct observation. Optical resonators, can be used to enhance weak signals by constructive interference of light. By means of micro-cavities with a small mode waist and a scanning microscopy approach, sensitive spatially resolved measurements can be performed. In this work, techniques for sensitive microscopy and spectroscopy are developed, their performance analysed and measurements performed on nanoscale systems.

As the basis for fast and controlled spectroscopic measurements, a highly stable yet widely tunable and transversally scannable cavity setup is developed. Cavity length stability of $200\,\mathrm{fm}$ is reported, well below the typical linewidth of a high finesse cavity. To perform spectroscopy, several schemes for stabilizing and precise sweeping of the cavity resonance wavelength are implemented.

By means of the Purcell effect, Raman scattering is enhanced. Directly comparing the Raman emission strength of one and the same individual carbon nanotube inside the cavity to a confocal measurement, we determine the Purcell factor and show the expected scaling inversely with the cavity's mode volume. Furthermore, cavity enhanced Raman imaging is shown to reveal information on the diameter and electronic properties of individual nanotubes.

To further boost sensitivity, Raman spectroscopy is extended to a scheme where the excitation laser and Raman scattering are simultaneously resonant with different longitudinal modes of the cavity. To this end, a tailored dielectric mirror coating is developed. It provides a broad accessible region of the Raman spectrum ($900\,\mathrm{cm}^{-1}$ to $1800\,\mathrm{cm}^{-1}$) by continuously changing the cavity length. Detrimental effects on the coating's actual performance due to the strong curvature of the micro-sized mirrors are discovered and explained.

Cavity enhanced absorption imaging is sped up by more than three orders of magnitude compared to our previous scanning cavity experiments, enabled through optimized data acquisition electronics and the high mechanical stability. This opens the way for real-time absorption imaging at the sub parts-per-million sensitivity level and recording hyperspectral absorption images using a tunable laser.

Absorption spectroscopy and microscopy is performed on carbon nanotubes and 2D materials. This reveals absolute absorption cross sections, polarization dependent absorption, spatial substructures and absorption resonances on the parts-per-million scale.

In a small excursion, first steps to perform absorption spectroscopy using broadband light sources in combination with integrating photodetectors are explored. Sub-parts-per-million absorption, only limited by shot noise, can be detected using picowatt intensities, well below the powers needed in conventional absorption spectroscopy.

Analysing the current limitations for sensitivity and speed, plenty of potential for further improvements is identified. The micro-cavity platform, its spectroscopic sensitivity and its microscopic resolved measurements are envisioned to be an enabling technology for fundamental science.

Contents

1. Introduction

Since the first systematic spectroscopy measurements in the 19th century by Fraunhofer[1], Kirchhoff and Bunsen[2], optical spectroscopy is not only used to analyse remote giant objects like stars in outer space but also reveals information about the tiniest amounts of matter. It is a powerful tool to explore inner workings of materials, elements and molecules, their composition, for fundamental research as well as in applied sciences[3]. It is not only possible to map important electronic properties, but also mechanical vibrations by using Raman and infrared spectroscopy[4]. High precision Doppler-free spectroscopy of simple atoms and molecules has lead to the discovery and validation of foundations of quantum mechanics[5].

Advent of Cavity enhancement for spectroscopy. To enhance the strength and resolution of spectroscopic signals, optical resonators where used for more than 100 years. Beginning with the pioneering work by Fabry and Pérot in 1899[6], the optical resonator bearing their names, made of two plane, reflective surfaces, was used as a wavelength filter to achieve higher resolved spectroscopy. With the invention of the stable spherical mirror resonator in the late 1950s[7] the true optical 'cavity resonator', confining light in all three dimension, was born[8]. This offered even stronger resolving power with simplified alignment and higher transmission. Furthermore, optical resonators were at the heart of lasers, with their frequency control and intense monochromatic radiation leading to the rise of high precision laser absorption spectroscopy in the 1960s and 1970s[9]. Starting from the 1980s, cavity enhanced absorption spectroscopy got a boost in sensitivity from time-based measurements of transient signals by quickly switching or modulating lasers or cavity geometry, known as *cavity ring-down spectroscopy*[3, 10].

In cavity based spectroscopy, the cavity resonator determines the frequencies at which the measurement takes place, offering higher resolution spectroscopy as compared to dispersing spectrometers.

Besides this increased spectral resolution, cavities can also enhance absorption signals by a sample, if the medium to be analysed can be brought inside the resonator. There, several effects of enhancement might play a role. For absorption spectroscopy of gases and liquids, an increase of the effective path length by light traversing the cavity multiple times, enhances absorption signals and improves sensitivity, especially in small sample volumes. Furthermore, for spectroscopy of fluorescence and (Raman) scattering, resonant enhancement inside the resonator increase the intensity of the excitation light and therefore the optical processes.

Later on, another effect of enhancement could be harnessed, when microscopic high finesse cavities emerged: the Purcell effect, where the change of the (dielectric) environment modifies the optical density of states and increases the strength of vacuum fluctuations at a sample. This can increase various optical processes involving spontaneous emission[11]. After being demonstrated in microwave cavities by Haroche et al in 1983, cavity enhanced spontaneous

emission in the near infrared and optical regions of the spectrum became accessible at the end of the 1980s[12].

State of the art and limitations of cavity enhanced spectroscopy. To date, cavity enhancement techniques for spectroscopy are mostly limited to a subset of materials, large ensembles, to absorption measurements and are not spatially resolved. All of these issues will be addressed to some extent in this work.

Apart from a few exceptions, cavity enhanced absorption spectroscopy is so far limited to gaseous and liquid samples. First work to measure solid samples were conducted in 1999 when absorption of a film of C-60 molecules was analysed in a cavity ring-down measurement[10]. In the following years first measurements were performed on polymer thin films and epitaxial grown reflectors. There, it was possible to detect losses in the tens of parts-per-million(ppm) region in SiO_2 and Ta_2O_5 films[10].

Currently, '*cavity enhanced spectroscopy*' generally refers solely to cavity enhanced *absorption* spectroscopy[3, 10] [1]. Other interesting spectroscopy experiments like Raman scattering have only been conducted in a few proof-of principle experiments and not yet found any wide adoption in research or any application. The reason for this is that cavity Raman enhancement requires not only a high finesse cavity, but also a cavity enclosing only a microscopic volume, making experiments more involved by explicitly needing microcavities[13]. This is because the Purcell effect, enhancing processes involving spontaneous emission of radiation, scales inversely with the volume occupied by the cavity mode. To date, cavity-enhanced Raman scattering was observed in liquid organic molecules inside a planar microcavity[14], semiconductor material inside a monolithic cavity[15, 16], and recently for gas inside a fibre-based cavity[17, 18]. In the high-Q modes of whispering-gallery resonators formed in micro-droplets[19], no vacuum-enhanced spontaneous emission enhancement but low threshold Raman lasing can be observed. The first single nanoscale solid-state system showing cavity enhanced emission were carbon nanotubes that were randomly distributed on photonic crystal slab cavities[20].

To date, cavity enhanced Raman and absorption spectroscopy is so far limited to a single (often spread out across hundreds of micrometer) point in space, and inhomogeneities in samples (common in solid states systems) could not be imaged with current experiments.

Fibre-based scanning-cavity microscopy and spectroscopy. To extend cavity based spectroscopy to microscopic imaging, a cavity with a tightly confined mode is needed. Additionally, to enhance fluorescence and Raman scattering in solids, where broad spectral lines prevail (due to short lifetime of phonons in the solid environment), a small mode volume is needed to increase the Purcell effect. Furthermore, lot of 'photon round-trips', quantified by a high finesse, are desired to enhance both absorption signals and the Purcell effect. A cavity meeting these requirements is the high finesse *fibre based Fabry-Pérot cavity* developed in the mid-2000s[21, 22]. Here, the usage of a mirror made by a microscopic concave depression on the end-facet of an optical fibre provides small radii of curvature and therefore enables small mode volume and mode waist cavities. The breakthrough machining technique for these

[1] Apparent, for example, from the book titled 'Cavity-Enhanced Spectroscopy and Sensing' only covering absorption spectroscopy

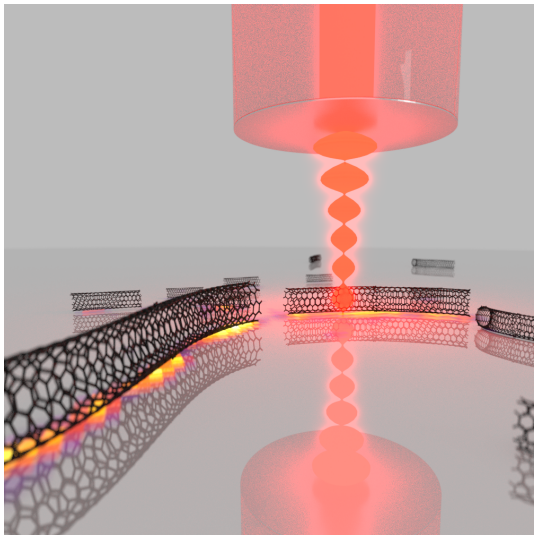

Figure 1.0.1.: Artistic vision (pretty unphysical and not to scale, yet beautiful and instructive) of the scanning cavity microscope during a measurement on carbon nanotubes. Light (red) is coupled in through the optical fibre (cylinder on top, on bottom its reflection in the large planar mirror can be seen) and forms a standing wave between the mirror on the fibre-end-facet and the large planar mirror, which hosts carbon nanotubes (black tubes). On the mirror, a real measurement of cavity enhanced Raman scattering in carbon nanotubes overlayed, acquired by raster scanning the fibre-mirror across the planar mirror.

depressions employs CO_2 laser pulses and yields smooth dielectric mirror surfaces, crucial for low scattering dielectric mirrors and consequently high finesse cavities.

When building a cavity out of one fibre-based mirror and one large planer mirror that hosts a solid sample, a scanning microscope can be constructed[23, 24], see Fig. 1.0.1 for an artistic vision of the setup. With this technique, highly sensitive cavity enhanced absorption microscopy was demonstrated by Mader et al[25] with a a cavity Finesse of 6×10^4. At the same time scanning cavity microscopy measuring dispersion of nanoparticles using a mirror on a cantilever tip was demonstrated, featuring a rather low finesse (60) but ultra-small mode volume cavity ($< \lambda^3$)[26].

Using this scanning cavity setups results in spatially resolved measurements of dispersive shifts (polarizability tensor)[27], absorption[25], strong light-matter interaction in 2D semiconductors[28], fluorescence in NV- and SiV-centres in diamond and excited state lifetime changes therein[29, 30] .

Scope and outline of this work. This work extends the scanning cavity-based microscopy to perform absorption and Raman *spectroscopy*. For the first time, hyper-spectral images of nanoscale objects, both in absorption and Raman scattering, can be acquired profiting from speed and sensitivity gains of cavity enhancement. This puts cavity sensing into a new role, where this enhancement might be used to gain new insight into spatial inhomogeneous nanoscale solid state systems. Exemplary absorption and Raman measurements are performed on solid state low dimensional nano-systems, like carbon nanotubes and 2D semiconductors materials.

To this end, several measurement techniques and technological advances were developed

and will be discussed to great detail in this work. Furthermore, speed of absorption measurement are increased by orders of magnitude in comparison to earlier measurements. The current limitations of absorption and Raman spectroscopy sensitivity are explored systematically.

This work is outlined as follows:

- In Chapter 2, the concept and theoretical foundations of scanning cavity microscopy and enhancement is introduced, both for absorption and Raman scattering measurements. Furthermore, a very concise introduction to fibre-based cavities is given, highlighting the differences of this platform in contrast to other cavity realizations.
- Chapter 3 proceeds to the actual implementation of the scanning cavity microscope. This chapter elaborates in great detail about the design considerations, implementation and actual performance of optical, mechanical and electronic components of the microscope.
  - For fast and stable operation, a setup with high cavity length stability ($\sim 100\,\mathrm{fm}$) yet transversally widely scannable ($\sim 100\,\mu\mathrm{m}$) mechanical setup was developed.
  - Optical components developed include a scheme to passively lock the frequency of a diode laser to the cavity resonance. Furthermore, a tailored dielectric high reflectivity coating is presented, that promises to both enhance excitation intensities and detection of Raman scattering, while providing a wide spectroscopically accessible region.
  - Broadband light sources and detectors for extinction spectroscopy with accompanying measurement schemes are tested and compared.
  - Electronics include a fast field-programmable gate array (FPGA) based detection scheme and various schemes to lock and continuously sweep the cavity length and resonance frequency for spectroscopy.
- The overall performance and limits of sensitivity of cavity measurements and their reasons are explored in Chapter 4.
- In Chapter 5, measurements on different nanoscale example systems like carbon nanotubes and 2D-materials are presented.
- Chapter 6 recapitulates the results and outlines improvements and application of this technology for the near and more distant future.

Finally, the detailed Appendix is another substantial part of this work. It is a collection of theoretical and applied knowledge that is needed or beneficial for operating fibre-based cavities. It should transfer to great detail experience and lessons learned in the early days of fibre based cavity setups and be a helpful reference for future researchers in this field.

2. Foundations of Scanning cavity microscopy and spectroscopy

This chapter introduces how fibre-based optical cavities can be used to build a raster-scanning microscope. It focuses on the theoretical concepts and calculations, while the details of the practical optical and mechanical implementation and its performance are deferred to the next chapters.

First, fibre-based micro cavities are introduced, including their special properties. Then, the fundamental principle of the scanning cavity microscope is explained.

Finally, the enhancement principles behind cavity-based extinction measurements and cavity-enhanced Raman-scattering are introduced. For both measurements, the expected sensitivity gain is calculated and different measurement techniques are explored.

2.1. Fibre-based micro-cavities

This is a very concise introduction to the basic concepts of fibre-based micro-resonators as developed and used in our group. It will not go into great detail about technical details, manufacturing, realizations, applications and history of such cavities as the reader is referred to preceding works from our group by Hunger[21], Mader[25] and Kaupp[31]. Instead, it will be mainly focused on the conceptional and practical difference to other common cavities and aspects not yet discussed in these works.

2.1.1. Optical cavities

Optical cavities are basically resonators for light waves. Common to all resonators is using reflective elements to confine a wave to a certain region in space. This constraint on the spatial extent of the wave, and therefore its wavelength, is also accompanied with a strongly frequency dependent response via the dispersion relation. This leads to both enhancement of power inside a cavity and enhanced frequency selective sensitivity when measuring signals by means of a cavity.

Among many other applications, optical cavities are used for lasers[32], enhanced absorption spectroscopy[3], high harmonic generation and strongly enhanced light matter interaction in cavity quantum electrodynamics[13]. There are many realizations of optical cavities, using photonic crystals, plane mirrors, fibre rings, microdisks or microspheres to confine light[13, 33].

2.1.2. Fibre-based high reflectivity mirrors

The cavities used in this work are based on optical fibres. The fibre is cleaved and an concave depression is formed by shooting a short pulse of a CO_2-laser on the end-facet. The crucial discovery to create high reflectivity, low loss mirrors (and therefore high finesse cavities) was the usage of this CO_2 laser for machining[21]. The proper selection of pulse power, duration and focussing leads to quick evaporation and removal of material, while the remaining molten glass leads to a smooth surface through surface tension. Roughness on the order of an Ångström [31], is crucial to apply many dielectric layers for a highly reflectivity Bragg mirror coating, without increased scattering losses. The result is a tiny ($0.1 - 5\,\mu m$ deep and $5 - 20\,\mu m$ wide) and strongly curved (radius of curvature $5 - 200\,\mu m$), highly reflective concave mirror on the end of the fibre tip, see Fig. 2.1.1a.

Combining two of these fibre-based mirrors, a low mode volume cavity can be formed, see Fig. 2.1.1b. Here, both incoming and out-coming light is conveniently coupled to a single mode fibre. Furthermore, such a fibre-mirror can be used in conjunction with a planar mirror on a multi-mode fibre (Fig. 2.1.1c) or even with a much larger macroscopic planar mirror reflector (Fig. 2.1.1d).

The breakthrough nature of this mirror machining technique can be understood when looking at how the term 'high finesse' was used over time. While fibre-based optical cavities with a finesse of 100 where called 'high finesse' in 2005[34], only five year later more than three orders of magnitude higher levels were designated with this term[21]. Today the finesse can exceed 2×10^5[35, 36].

The CO_2-laser can also be used as a post-treatment tool to smooth precisely formed, but rough mirror profiles created by other techniques[37, 38], e.g. by focused ion beam milling[39, 40]. Furthermore, it can be applied to different mirror substrates, e.g. fused silica plates[40].

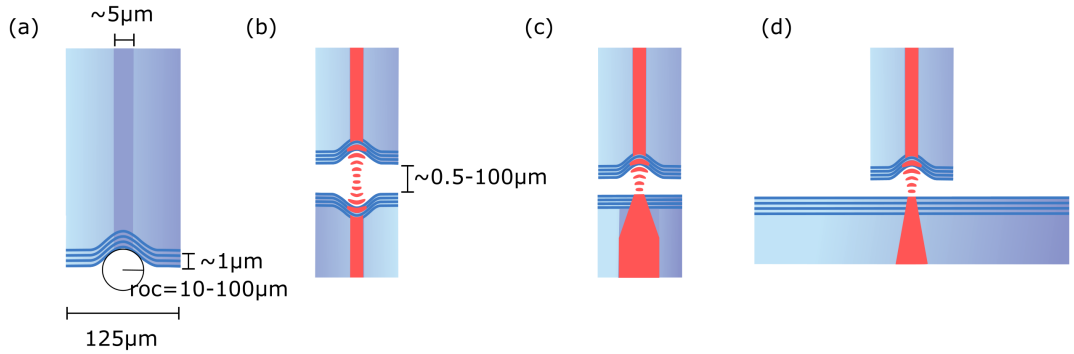

Figure 2.1.1.: (a) Schematic of a high reflectively coated single-mode fibre-based concave mirror. The fibre end-facet features a concave depression (with radius of curvature["roc"] $5 - 200\,\mu m$), coated with a high reflectivity coating (depicted by alternating bright and dark blue layers). The dark blue shaded area is the fibre core, which is around 5µm in diameter for common single mode fibres (not to scale in the drawing). (b-d) Different combinations of mirrors to realize fibre-based cavities: two concave single mode fibre mirrors (b), a concave single mode fibre mirror combined with a flat large-core multi-mode fibre mirror (c), or a planar macroscopic mirror (d).

2.1.3. Particularities

The cavities used in this work have their differences, advantages and disadvantages compared to the zoo of other optical cavities available. Compared to cavities formed with macroscopic mirrors ($\gg 100\,\mu\mathrm{m}$ in diameter) they feature:

- Fibre-based mirrors can have much smaller radii of curvature and extent, down to a few micrometre.
- The manufacturing of the mirrors does not depend on super-polishing of the surface, as the smoothness of the mirror is intrinsically given by the laser-based machining process. Using a CO_2-laser to melt a depression into the fibre end-facet reduces roughness below $0.2\,\mathrm{nm}$ by surface tension[21, 31]. Therefore, together with their small size, hundreds of fibre-micro mirrors might be manufactured automatized for the cost of single macroscopic mirror.
- The small size and shallow depth of the mirror profile allows for cavities as short as the theoretical minimum resonance length, half of the wavelength used ($\lambda/2$)[30]. Together with a small radius of curvature, ultra-low-mode volume cavities, below λ^3, can be achieved.
- The low roughness and almost perfectly spherical profile reduce scattering losses to a few parts per million (ppm), a point where even with the best dielectric coatings available, losses in the visible region are dominated by absorption in the dielectric stack of the mirrors. Therefore, the achievable finesse approaches the records set by carefully machined and polished macroscopic mirrors[41, 42, 36].
- Inherent fibre coupling simplifies coupling in light, however, accompanied by a limited coupling efficiency, because the mode of the single mode fibre and the cavity mode do not necessary match, see Appendix A.3.1.
- Due to the short length of the cavities, the cavity quality factor, proportional to the photon lifetime inside the cavity, is reduced. Furthermore, the free spectral range (FSR) between adjacent modes is significantly larger, leading to completely different behaviour compared to macroscopic cavities. E.g. at the shortest cavity lengths only a single mode can be resonant across the whole stop-band of the coating.
- The short cavity length furthermore translates fluctuations of the cavity length much stronger to resonance frequency changes but also allows for faster mechanical tuning of the optical resonance frequency, see Appendix A.2.

Differences to other microscopic cavities[13, 31], such as photonic crystal cavities, VCSEL (vertical cavity surface emitting laser) cavities and plasmonic resonators include:

- Open-access for simplified and versatile placing and coupling of matter inside the cavity.
- Easy and fast length adjustment through mechanical motion of one of the mirrors, e.g. by a piezo element, allow fast tuning and modulation in the MHz range (but slower than for smaller optical micromechanical (MEMS) resonators). This is in stark contrast to common tuning mechanisms such as length change through temperature or refractive index change through gas condensation, used to tune photonic crystal or monolithic

cavities. This is, however, accompanied by elevated instability of the cavity length and therefore fluctuations of the resonance frequency

- Limited to larger mode volumes compared to cavities based on plasmonic effects, where sub-wavelength confinement can be achieved.

These unique features make fibre-based cavities a widely used tool to increase light matter interaction in quantum optics experiments[21, 22].

As will be shown in the next chapter, especially the open-access, tiny size and ease of tuning lay the ground for using fibre-based cavities to enhance light matter interaction and build a microscope with high sensitivity.

2.2. Scanning cavity microscope

The scanning cavity microscope is, as the name suggests, based on a scanning microscopy principle. Similar to an electron microscope or a confocal microscope, a beam is used to raster scan a sample and at each point a signal is measured. Finally, and image is reconstructed by combining all the individual measurements. Here, the field that probes the sample is the standing-wave light field between a macroscopic planar mirror and a microscopic concave mirror at the end-facet of a fibre. The schematic setup and an actual implementation is shown in Fig. 2.2.1. A sample is prepared on the large planar mirror. When the fibre is brought close enough to the large mirror, an optical cavity is formed. By moving the fibre transversally across the mirror, different parts of the sample can be brought inside the cavity mode. By measuring, for example, transmitted, reflected or scattered light leaving the cavity for each point, an image of the sample can be recorded by raster scanning.

When varying the cavity length, different wavelengths become resonant with the cavity and spectroscopic measurements can be performed. If this is done for each point, so-called hyper-spectral images can be acquired.

Therefore, the cavity setup includes intrinsically a highly frequency selective element, and precise spectroscopic measurements are possible. However, in contrast to a narrow band filter, it does not only remove radiation but also enhances parts of it.

As mentioned in the introduction, the cavity can enhance a wide variety of light-matter interactions, be it absorption, Rayleigh-scattering, spontaneous emission or Raman scattering. This unique feature is used to perform highly sensitive measurements. In the next sections, the theory behind the enhancement and cavity-enhanced measurement techniques are explained for extinction and Raman spectroscopy.

What will be not discussed in this work, but should be mentioned here briefly, are the numerous other possibilities of cavity enhanced scanning microscopy measurements that have already been performed (of which many in our group). To mention just a few: fluorescence [29, 30, 23, 24], emitter lifetime[31], super-resolution via higher order modes[25, 43], dispersion/ polarizability[27], and strong light-matter coupling mode splitting[28].

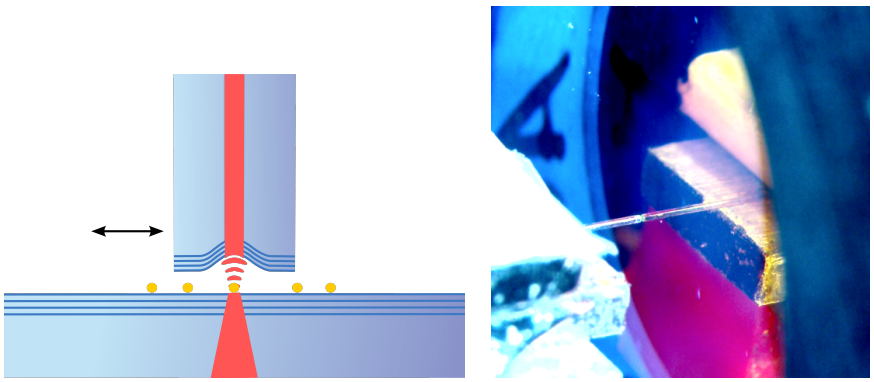

(a) (b)

Figure 2.2.1.: (a) Schematic side view of a scanning cavity setup. A fibre end-facet and a larger planar mirror, both coated with a high reflectivity coating (illustrated by the layered dark blue lines) face each other and form the cavity. By moving the fibre transversal to the planar mirror, the cavity can be established at different points on its surface (illustrated by the black arrow). Nanoscale objects brought onto the planar mirror (golden spheres) can be imaged by raster-scanning the transversal position of the fibre. Here, light (red) is coupled in via the fibre core, establishes a standing wave inside the cavity and transmitted past the plane mirror. (b) Photograph of a fibre and its reflection in the macroscopic planar mirror.

2.3. Extinction spectroscopy

Extinction is the reduction of light passing by a sample. It is a combination of absorption and scattering. Scattering can be measured with high sensitivity by established dark-field microscopy, due to the deflection of photons and simple detection by spatial filtering. However, this is not possible for absorption. Absorption measurements are commonly a relative measurement, they study the intensity of a beam before and after having impinged on a sample. The typical absorption cross-section for a single dye molecule is on the order of $0.01 - 0.1\,\mathrm{nm}^2$. Focussing of light is limited in the best case by the diffraction limit, yielding areas on the order of $5 \times 10^4\,\mathrm{nm}^2$ for visible radiation. Therefore, a single molecule may absorb below $1\,\mathrm{ppm}$ (part per million) of the photons incident onto it[44]. As a consequence, a sensitive transmission measurement needs to measure a small change on a large background. This is further complicated by the fact that shot noise in the detection of N photons scales as $\sqrt{N}$. Therefore, measuring a change in transmission to $1\,\mathrm{ppm}$ requires reliable detection of 10^{12} photons[45].

In contrast to that, fluorescence or scattering can be implemented as 'zero background' measurement, due to the spectral or spatial separation, respectively, of incoming and outgoing radiation. There, single photons can be measured against an otherwise dark background.

2.3.1. Potential of absorption measurements

Due to this conceptual simplicity of sensitive photoluminescence (PL) measurements, many experiments on single nanoparticles and even single molecules were performed[46]. However, a lot of molecules are not fluorescing, due to nonradiative relaxation to the ground state or to intermediate dark states[45]. Especially solid-state nano-systems often exhibit a low quantum

yield due to "quenching" by nonradiative transfer of energy to the environment or at impurities. With the help of sensitive absorption measurements the cause of quenching, blinking and bleaching could be explored[47, 48]. In photovoltaic research, 'dark' states that couple extremely weakly to light yet play a crucial role in limiting the performance of photovoltaic devices based on organic materials. With enhanced absorption sensitivity such dark states may be detected directly in absorption spectroscopy to provide feedback to material design and device optimization.

Furthermore, complementary information from absorption and fluorescence, like their relative intensity and frequency shift, may be used to deduce phonon populations and vibrational states[49].

2.3.2. Sample extinction and cavity lineshape

In this section, the extinction of light by an object inside the cavity is inferred from measuring the transmitted light through the cavity. The cavity enhancement of the extinction signal can be understood intuitively: one can think of the cavity as two reflective mirrors where a photon bounces back and forth. If an object is placed between the mirrors, the photons passes the object many times. The probability that the photon gets absorbed or scatters simply scales with the average number of round-trips a photon takes, which is quantified by a number called the *finesse* of the cavity.

In detail, things are a bit more complicated as coupling light into the cavity through the highly reflective mirror is only possible after a certain build-up time in the steady state, when many photons interfere constructively[33, 32]. We will assume that this build-up is instantaneous, since the cavity decay rate is in the pico-second range for these short cavities used ($\approx$ GHz linewidth), and order of magnitudes faster than the used detectors ($\approx$ MHz) and mechanical frequencies ($\approx$ kHz). In this case, the extinction of a sample inside the cavity manifests in a modification of the cavity transmission amplitude and linewidth, as derived in Appendix A.1.4. This is illustrated in Fig. 2.3.1, where we see that additional losses by the sample, given by its the single-pass extinction A, decreases the amplitude and broadens the transmission resonance.

Several different measurement schemes can be used to derive the extinction from this change of lineshape.

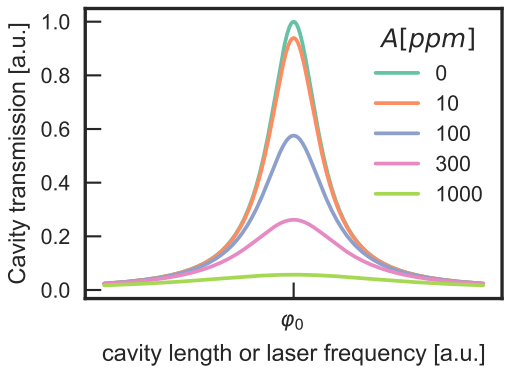

Figure 2.3.1.: Transmission of a cavity with finesse $\mathcal{F} = 10000$ ($R \approx 300$ ppm) around a resonance 'φ_0' with various values for the extinction by the samples, A.

2.3.3. Via peak transmission (of narrow laser)

For this measurement a laser with a linewidth much smaller than the cavity linewidth is used, usually an external cavity diode laser (ECDL) with $< \mathrm{MHz}$ short term linewidth. The cavity length is modulated and its resonance sweeps over the laser frequency[1]. The transmitted power is measured time-resolved with a photodiode. The laser therefore samples the cavity resonance and its lineshape, including amplitude and linewidth.

The transmission through a high finesse cavity on resonance can be expressed as (see Appendix A.1.4 for detailed derivation),

$$T_{\mathrm{c,res}} \approx \frac{4T_1T_2}{(T_1+T_2+L_1+L_2+2A)^2} = \frac{4T_1T_2}{L_\Sigma^2}\,. \tag{2.3.1}$$

For this derivation we have assumed that the sum of all losses from the cavity, L_Σ, consisting of mirror transmission ($T_{1|2}$), mirror losses (absorption and scattering) ($L_{1|2}$) and losses at the specimen inside the cavity (A) is small,

$$L_\Sigma = T_1+T_2+L_1+L_2+2A = L_\mathrm{c}+2A \ll 1\,. \tag{2.3.2}$$

L_c are the cavity intrinsic losses without the sample and the factor of 2 at the sample losses stem from the fact that "light passes the object twice" per round-trip.

The absolute value of the transmitted power does not only depend on the power of the light source (I_L) and the mode matching of the coupling into the cavity fibre (η_m), but also on imperfect mode matching of the mode guided inside the fibre to the cavity mode (η_m), reflections at the back face of the out-coupling mirror (η_o) and other to a certain degree unknown or uncontrollable parameters[21]. The total transmitted power therefore is

$$I_\mathrm{T} = I_\mathrm{L}\eta_f\eta_m T_\mathrm{c}\eta_o \tag{2.3.3}$$

To extract the absolute value of the extinction from the sample in an experiment, it is the simplest to get rid of these unknown factors by normalizing to empty cavity transmission ,$T_{\mathrm{c},0}$, yielding

$$T_\mathrm{n} = \frac{T_\mathrm{c}}{T_{\mathrm{c},0}} = \frac{L_\mathrm{c}^2}{(L_\mathrm{c}+2A)^2}\,. \tag{2.3.4}$$

$T_{\mathrm{c},0}$ can be observed at points where nothing is between the mirrors.

Solving for the extinction, A, and rewriting the empty cavity losses in terms of the empty cavity finesse, $\mathcal{F} \approx 2\pi/L_\mathrm{cav}$, yields

$$A = \frac{\pi}{\mathcal{F}}\left(T_\mathrm{n}^{-1/2}-1\right)\,. \tag{2.3.5}$$

The normalized maximum transmission amplitude of the cavity relates directly to the extinction by the specimen inside the cavity. The only factor needed to do absolute extinction measurements is the cavity finesse. As the finesse can be reliably measured to sub 1% precision (see Appendix B.1 for methods), absolute extinction can be determined. With the known cavity

[1] Theoretically, also the laser wavelength could be swept. However this would need a continuous tunable single mode operating laser over wide wavelength. For the sake of practicality, the cavity length is swept

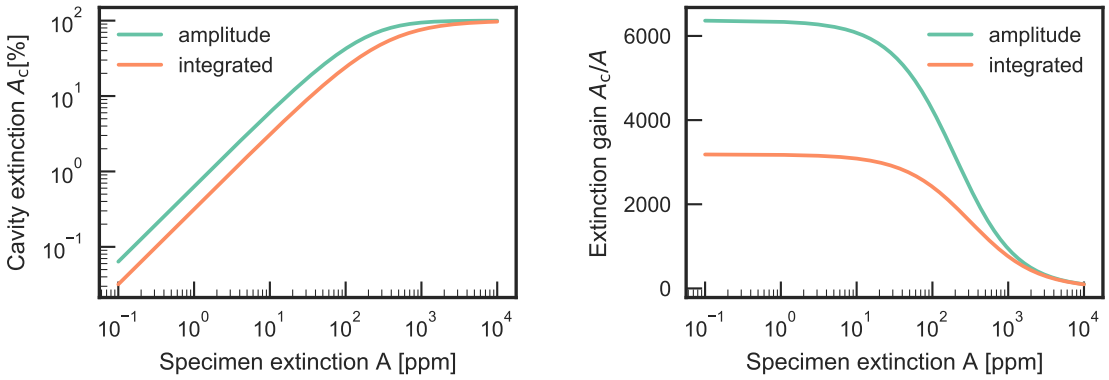

(a) **(b)**

Figure 2.3.2.: (a) Extinction of the normalized cavity transmission as a function of the extinction of the specimen between the mirrors (b) Cavity extinction sensitivity ("gain") for different extinction levels inside the cavity. Calculations for a cavity with finesse $\mathcal{F} = 10000$. Comparison of transmission-amplitude measurement and integrated transmission measurement methods.

mode size even absolute extinction cross sections of nanoscale objects can be extracted (see Appendix A.4) .

Let's define the relative extinction through the cavity by

$$A_c = 1 - T_n \,. \tag{2.3.6}$$

As can be seen in Fig. 2.3.2a, already small sample extinction leads to strong extinction of the cavity transmission. This raises the sensitivity of a extinction measurement, when assuming transmission measurements are usually limited by detector and light source noise, or small parasitic interferences in the detection path. In Fig. 2.3.2b, the "gain" of the cavity extinction measurement compared to a single-pass extinction measurement is shown. For faintly absorbing samples ($A \ll L_\Sigma$) the gain is approximately

$$\frac{A_c}{A} \approx \frac{2}{\pi}\mathcal{F} \,. \tag{2.3.7}$$

For stronger extinction the "sensitivity gain" by the cavity is reduced. This can be understood when considering that the finesse of the cavity is reduced by the absorbing specimen itself, leading to less pronounced cavity effects.

The measurement is independent of the sweeping speed across the resonance (if the measured lineshape is not washed out by the limited bandwidth of the photodetector). Hence, if a sufficiently fast detector and appropriate sweeping speed is used, this makes a robust measurement without needing calibration of the sweeping speed. As it also does not require precise stabilization of the cavity length, it was the first to be implemented[43, 25].

To extend this measurement to spectroscopy, a tunable laser has to be used and measurements have to be repeated for several wavelengths.

2.3.4. Via integrated transmission (of narrow laser)

Another method to infer the extinction is to sweep over the transmission resonance and measure the time integrated signal of the transmitted power. This corresponds to an integration over the transmission lineshape instead of probing just its amplitude.

Integrating the Lorentzian transmission lineshape around a resonance (see Eq. (A.1.21)) yields

$$\int_{-\infty}^{\infty} d\varphi \frac{1}{1+\left(\frac{2}{\delta\varphi}\right)^2 \varphi^2} = \pi \frac{\delta\varphi}{2} \tag{2.3.8}$$

where $\delta\varphi = L$ is the linewidth. As with the amplitude measurement, we normalize the transmission to the empty cavity. Rewriting using the finesse yields the normalized integrated transmission

$$T_{\mathrm{n,int}} = \frac{T_{\mathrm{c,\,int}}}{T_{\mathrm{c,0,int}}} \frac{\pi}{\mathcal{F}} \sqrt{1-A} \frac{1}{1-(1-A)\left(1-\pi/\mathcal{F}\right)} \,. \tag{2.3.9}$$

Solving for the sample extinction and approximating $A \ll 1$, yields

$$A = \frac{2\pi}{\mathcal{F}} \left(T_{\mathrm{n,int}}^{-1} - 1\right) \,. \tag{2.3.10}$$

This formula is similar to the previous result extracting the extinction from peak transmission, Eq. (2.3.5), except the missing square root dependence on the transmission and a factor of two. Both methods amplify the detection proportional to the inverse of the finesse, for weak sample extinction. However, this integrated measurement is a factor two less sensitive there, compared to the amplitude measurement, as can be seen in Fig. 2.3.2. This can be understood as follows: extinction inside the cavity affects the lineshape of the transmission in two ways: it decreases the amplitude but also increases the linewidth. Both effects counteract to a certain degree, when integrating the whole line and lead to a smaller dependency of the transmission on the specimen extinction than just looking at the amplitude.

Integration across the line makes the signal linear dependent on the sweep speed of the cavity resonance. This constraint adds noise and taking this into account adds complexity compared with the amplitude measurement technique. On the other side, integrating the signal decreases measurements noise and low-noise detectors such as CCD or CMOS arrays can be used.

2.3.5. Via white-light transmission

Another way to measure the integrated intensity is to illuminate the cavity with a broadband light source (see Section 3.7.3 for details on light sources) and measuring transmission. If the illumination is spectrally broader than the linewidth of the cavity (order of $100\,\mathrm{pm}$) and narrower than the spacing of adjacent modes (order of $100\,\mathrm{nm}$), a single fundamental cavity mode is illuminated. The transmission at the cavity resonance can be measured continuously without modulating the cavity length. As with the time-averaging of transmission, Eq. (2.3.10) can be used to extract the extinction from the normalized transmission.

Advantages of these techniques are that spectra can be acquired by simply tuning the cavity

length, and using it as a filter. Furthermore, measurement rates are not limited by mechanical modulation speed of the cavity resonance. However, the length of the cavity has to be measured and stabilized for a stable signal, as the measurement wavelength is not defined by the light source as in the measurement schemes involving a narrow band laser.

2.3.6. SNR at constant damage

Assuming a shot noise limited measurement of transmission, the noise is proportional to the intensity transmitted through the cavity, P_t. As we have seen, the extinction signal scales with intensity and is amplified proportional to the finesse, cf. Eq. (2.3.5). Together, the the signal-to-noise ratio of the extinction measurement using the cavity scales as follows,

$$\mathrm{SNR} \propto \frac{\mathcal{F} P_\mathrm{t}}{\sqrt{P_\mathrm{t}}} \propto \sqrt{P_\mathrm{t}}\mathcal{F} \tag{2.3.11}$$

However, the standing wave inside the cavity also enhances the power inside the cavity (see Appendix A.1.7 for derivation) by the factor

$$C_e \approx 4\frac{\mathcal{F}}{\pi}\,. \tag{2.3.12}$$

Consequently, also the power absorbed by the sample, $P_\mathrm{abs} \propto AC_e$, increases. Absorption can lead to sample damage, especially in biological samples, e.g. through heating or directly by breaking up chemical bonds. This limits the maximal power practical for a measurement. To yield the same damage with the cavity as in a measurement without the cavity, the in-coupled, and therefore transmitted power as well, has to be decreased by $1/C_e \propto 1/\mathcal{F}$. However, as the SNR scales weaker, the "signal-to-noise ratio at constant damage"[50, 51], scales with the square root of the finesse,

$$\mathrm{SNR}_d \propto \mathcal{F}\sqrt{\frac{1}{C_e}} \propto \sqrt{\mathcal{F}}\,. \tag{2.3.13}$$

This means that weaker samples can be detected, that would be destroyed in simple single-pass measurements.

2.3.7. Other methods

Here, additional methods to cavity enhanced extinction measurements are discussed briefly.

Via cavity linewidth (using narrow laser). As with the amplitude method, the cavity transmission lineshape is sampled using a narrow laser. However, this time not the amplitude but the width of the resonance is extracted.

This makes the measurement insensitive to laser intensity fluctuations, if they are on timescales longer than a sweep over the cavity line. However, high frequency fluctuations on the timescale of the traversal of the resonance can still pose a problem. Furthermore, the nonlinearity of expansion of the piezo element used for cavity length sweeping or high frequency mechanical vibrations of the cavity length lead directly to measurement errors. Furthermore, a detector and electronics with good time resolution are required.

Via reflection (using narrow laser). Extinction measurements using the narrow laser can also be performed in reflection. Here, a dip in the cavity reflection on resonance can be observed. The minimum value on resonance given by, as derived in Appendix A.1.5,

$$R_{\mathrm{c,min}} \approx \frac{1 - R_1 - R_2\,(1-A)^2 + R_1 R_2\,(1-A)^2}{\left(1 - \sqrt{R_1 R_2}\right)^2}\,. \tag{2.3.14}$$

If no losses are present in the system or the cavity is impedance matched (see Appendix A.1.5), the reflection on resonance even drops to zero.

Using reflected light simplifies the measurement setup as only one optical access is needed and all optics are inherently fibre coupled. This is especially intriguing when operating the setup in an inaccessible environment like a cryostat.

However, this method has also a few downsides: Reflection measurements show enhanced fluctuations of the signal due to parasitic interferometers in front of the cavity. Furthermore, due to non-unity mode matching of the mode of the cavity and the mode guided in the fibre and spatial mode filtering by the fibre core, the reflection lineshape deviates from the symmetric Lorentzian lineshape[21, 52, 53]. Also, in contrast to transmission measurements, relating the reflection signal to sample extinction does not only depend on the finesse, that can be determined accurately, but on losses of the mirrors individually. Depending on this, sample extinction can cause a decrease or increase the reflection. With an impedance matched cavity, the reflection is even insensitive to small sample extinction. This complicates the extraction of information from the reflected signal. However, a more detailed analysis might show potential for more sensitive measurements in reflection than in transmission.

Via ring-down (using pulsed laser). Ring-down measurements probe the exponential decay of energy stored inside the cavity, which is proportional to the losses of the cavity. This way, highly sensitive measurements robust against laser fluctuations are possible. However, the short length in micro-cavities leads to sub-nanosecond lifetimes and thus renders the technique challenging. Furthermore, the need of pulsed lasers and fast detectors complicates the setup. The high sensitivity roots in the extraction of time constants from numerical fitting exponential functions to the ring-down signal, and therefore costly data processing decreases measurement rates. This impedes the potential for scanning microscopy, where ideally thousands of points should be scanned per second.

2.4. Raman spectroscopy

The Raman effect[4] describes inelastic scattering of photons at molecules and solids where phonons are created (or annihilated). Due to energy conservation, the phonon's energy is transferred to (or taken from) the scattered photon. In this way, the analysis of Raman scattered light – Raman spectroscopy – can reveal a wealth of information on the structure and composition of matter through its vibrational and rotational states. However, due to the involvement of two photons and a phonon in the process, the scattering cross-section is very weak, more than six orders of magnitude weaker than elastic Rayleigh scattering.

Therefore, for the enhancement of the weak Raman signal , many different techniques have

been developed. Here, the focus is on cavity enhancement of Raman scattering, that has been explored only rudimentary and not found any application so far. By deriving the formula for the enhancement, we will explore the reason behind the difficulty of Raman enhancement with a cavity in this section.

2.4.1. Theory of cavity enhancement for Raman scattering

Raman scattering is, in its most general form, a non-linear optical phenomenon where a photon of angular frequency ω_1 is absorbed and one photon with ω_2 is emitted, while the matter involved makes a transition from an initial state $|i\rangle$ to a final state $|f\rangle$[54, ch. 10]. Most commonly, the Raman process describes the creation (*stokes shifted* photons to longer wavelength) or destruction of phonon modes (*anti-stokes shifted* to shorter wavelengths), while the electronic initial and final state are the same.

The Raman process can be derived using second order (or higher order) perturbation theory [55, 54, 56], starting from an initial state, scattering to an intermediate states $|s_i\rangle$ and then into the final state. This yields the transition probability per unit time, unit volume and unit energy ($d(\hbar\omega_2)$)

$$\frac{dW}{d(\hbar\omega_2)} = \frac{8\pi\omega_1\omega_2}{\epsilon(\omega_1)\,\epsilon(\omega_2)} |\langle f|M|i\rangle|^2 \left|\langle\alpha_f|a_2^+ a_1|\alpha_i\rangle\right|^2 g(\omega_1,\omega_2) \ . \tag{2.4.1}$$

Here, $\epsilon(\omega)$ is the dielectric constant at ω, $|\alpha_{i,f}\rangle$ denote the initial and final state of the radiation field and $\langle f|M|i\rangle$ is the transition matrix element of light matter coupling. $g(\omega_1,\omega_2)$ is the joint density of states (DOS) [55]. It is used to describe transitions that are not only between discrete energy levels of a quantum system, but involve continua of states[55]. In solids, the final photonic and intermediate phononic states include continua, and therefore the joint DOS is composed of the photonic DOS, $\rho(\omega_2)$, as well as the phononic/electronic DOS, $L(\omega_1,\omega_2)$ [2],

$$g(\omega_2,\omega_1-\omega_2) = \rho(\omega_2)\,L(\omega_1,\omega_2) \ . \tag{2.4.2}$$

$L(\omega_1,\omega_2)$ holds the lineshapes of the phonon transitions. For a single phonon it is usually Lorentzian-shaped and its width is given by the lifetime of the phonon.

When assuming the simple case of $\langle\alpha_i| = \langle n_1, n_2|$ and $\langle\alpha_f| = \langle n_1-1, n_2+1|$, i.e. meaning the removal of a phonon at excitation energy and addition of a photon at the scattered energy, the field matrix element simplifies to[3]

$$\left|\langle\alpha_f|a_2^+ a_1|\alpha_i\rangle\right|^2 = n_1(n_2+1) \ . \tag{2.4.3}$$

Therefore, the emission depends on the photon number in the mode it is emitting to, n_2. The case of $n_2 = 0$ corresponds to spontaneous emission (or "vacuum stimulated emission") while $n_2 > 1$ corresponds to stimulated emission. We also see from this formula that the Raman signal is, as expected, also proportional to the input intensity, n_1, which can be enhanced by

[2] Sometimes the DOS is also normalized to mode volume and may include the angular dependence of matter-field coupling [11, chapter 2]

[3] Note that this also a good approximation for strongly populated coherent state [11, chapter 2]

the cavity, as we saw in the section on extinction spectroscopy, cf Eq. (2.3.12). However, we are interested in another effect that is not yet fully visible.

The total transition probability is yielded by integrating

$$W \propto |M_{fi}|^2 \int_0^\infty d\omega_2 \, \rho(\omega_2) \, L(\omega_1, \omega_2) \ , \tag{2.4.4}$$

where the matrix element is now written as M_{fi} and moved in front of the integral as it is assumed to only depend weakly on ω_2.

The photonic DOS, $\rho(\omega_2)$, depends on the surrounding of the matter, and therefore the environment can alter Raman scattering rate. Especially a cavity can modify this factor by modifying this *distribution of states in frequency.*

But the surrounding enters in another place as well, since it modifies the *spatial distribution* of the field of a photon. This enters through the transition matrix element, which includes the electric field at the position of the matter, $|M|^2 \propto \left|\vec{E}(\vec{r}_{\mathrm{ma}})\right|^2$.

The magnitude of the electric field *per photon* at the point of the material is given by

$$E(\vec{r}_{\mathrm{ma}}) = \left(\frac{\hbar\omega}{2\epsilon(\vec{r})\, V_m}\right)^{\frac{1}{2}} \tag{2.4.5}$$

This formula directly originates from energy normalization of a single photon ,

$$\hbar\omega = 2\int d^3r \epsilon(\vec{r}) \left|\vec{E}(\vec{r})\right|^2 . \tag{2.4.6}$$

The quantity V_m is the mode volume, defined by the field at the position of interest and the integration of the energy over all space

$$V_m \equiv \frac{\int d^3r \, \epsilon(\vec{r}) \left|\vec{E}(\vec{r})\right|^2}{\epsilon(\vec{r}_0) \left|\vec{E}(\vec{r}_0)\right|^2} . \tag{2.4.7}$$

For the free space case this is just the unit volume.

The DOS of photons in three dimensions[4],

$$\rho_{\mathrm{fs}}(\omega) = \frac{\omega^2 n^3 V_{fs}}{\pi^2 c^3} , \tag{2.4.8}$$

emerges from the dispersion relation, $\omega = ck'/n$ (states numbered by wavenumber k' in a material with refractive index n), and counting the number of modes in a defined volume V_{fs}.

2.4.2. Purcell factor

The Purcell factor(PF) compares the emission rate of a two level system inside a cavity to the emission rate in free space. Analogous, we here generalise it to quantify enhancement of Raman scattering rates,

[4] Note that with this DOS, the scattering rate is $W(\omega_1 \approx \omega, \omega_2 \approx \omega) \propto \omega^4$[57], recovering the well-known forth-order dependency Raman scattering cross sections.

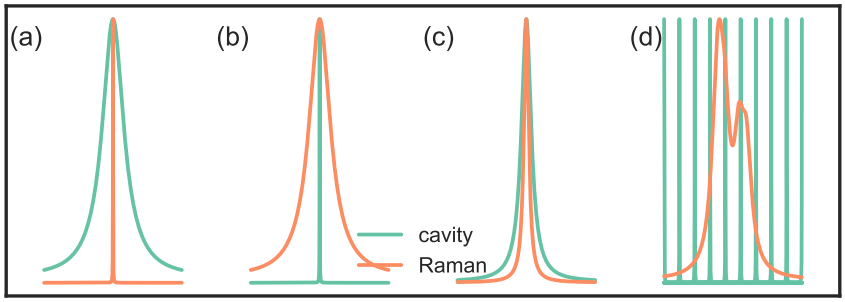

Figure 2.4.1.: Spectral shape of Cavity line and Raman line. (a) Raman line much narrower than cavity line. (b) Cavity line much narrower than Raman line. (c) Comparable linewidths. (d) Narrow cavity line swept (here shown as multiple lines), sampling a complex Raman lineshapes. In principle, also multiple cavity resonances could be matching a complex Raman spectrum, and (d) could hold true for a sufficiently long fixed cavity length.

$$F_p = \frac{W_{\mathrm{cav}}}{W_{free}} = \frac{\int_0^\infty d\omega\, L\left(\omega_1-\omega_2\right)\rho_{\mathrm{cav}}\left(\omega_2\right)/V_m}{\frac{1}{3}\int_0^\infty d\omega\, L\left(\omega_1-\omega_2\right)\rho_{\mathrm{fs}}\left(\omega_2\right)/V_{fs}}. \tag{2.4.9}$$

The additional factor of $1/3$ in the free space rate compared to the cavity rate emerges from the fact that we assume that averaging over random dipole orientations, relative to vacuum electric field leads to reduced coupling. Contrary, for the cavity we assume that the dipole is aligned parallel with the electric field of the single mode of the cavity. To perform the integration, some knowledge about the cavity resonance and Raman transition lineshape is needed. Depending on their shape relative to each other, what can be called spectral matching, we will differentiate several cases, sketched in Fig. 2.4.1.

Raman line narrower than cavity line. In this case, the cavity's DOS is assumed to be a Lorentzian shaped peak

$$\rho_{\mathrm{cav}}(\omega) = \frac{1}{\pi}\frac{\delta\omega/2}{(\omega-\omega_{\mathrm{c}})^2+(\delta\omega/2)^2}, \tag{2.4.10}$$

centred around ω_c, with $\delta\omega$ being the full width at half maximum (FWHM). As it describes a single ("quasi"[11]) mode, it is normalized, $\int_0^\infty d\omega\rho_{\mathrm{cav}}(\omega)=1$. Other modes are assumed to be far off-resonant and ignored. The Raman lineshape, $L\left(\omega\right)$, is assumed to be peaked and much narrower then both the cavity linewidth or the free space DOS, see Fig. 2.4.1a. Therefore, we can approximate it with a delta-function, $L\left(\omega\right)=\delta\left(\omega_2-\omega_1+\Delta\omega\right)$, where $\Delta\omega$ is the energy of the excitation (e.g a phonon) involved, and perform the integrations

$$F_p = \frac{\rho_{\mathrm{cav}}\left(\omega_1-\Delta\omega\right)/V_m}{\frac{1}{3}\rho_{\mathrm{fs}}\left(\omega_1-\Delta\omega\right)/V_{fs}} \tag{2.4.11}$$

Assuming that the cavity and the phonon transition are resonant, $\omega_c=\omega_1-\Delta\omega$, and inserting the free DOS leads to

$$F_p = \frac{\frac{2}{\pi\delta\omega}/V_m}{\frac{1}{3}\frac{\omega^2 n^3 V_{fs}}{\pi^2 c^3}/V_{fs}} = \frac{c^3}{\omega^3}\frac{\omega}{\delta\omega}\frac{6\pi}{n^3}\frac{1}{V_m} \tag{2.4.12}$$

Note that the arbitrary volume used for the integration over the free space DOS in vacuum drops out. Writing in terms of the wavelength in vacuum using $\omega = ck/n = 2\pi c/\lambda$ and introducing the quality factor of the cavity, $Q_c = \frac{\omega}{\delta\omega}$, the Purcell factor assumes the well-known form,

$$F_p = \frac{3}{4\pi^2}\left(\frac{\lambda}{n}\right)^3 \frac{Q_c}{V_m}\,. \tag{2.4.13}$$

Interestingly, Raman scattering scales with ω^4 in free space, while it scales only with ω^2 inside the cavity, due to reduced dimensionality. This makes Raman scattering for longer wavelengths more accessible inside a cavity, if longer wavelengths are used.

We will call this the *ideal Purcell factor*, as it depends solely on the properties of the cavity and as it coincides with the classical derivation by Purcell with a narrow two-level system emitting into a broad cavity.

Note that if not resonant with a Raman line, the emission into a cavity mode is inhibited instead of enhanced.

Raman line broader than cavity line. In the opposite case, we assume the cavity to be so narrow that it can be modelled by a Delta-function. The Raman line can most of the time be modelled as a Lorentzian, see Fig. 2.4.1b. In a derivation analogue to the previous one, almost the same Formula emerges:

$$F_{p,\text{eff}} = \frac{3}{4\pi^2}\left(\frac{\lambda}{n}\right)^3 \frac{Q_r}{V_m}\,. \tag{2.4.14}$$

However, the quality factor of the cavity has been replaced with the quality factor of the Raman transition, defined analogous as $Q_r = \frac{\delta\omega_r}{\omega}$ where $\delta\omega_r$ is the FWHM of the Raman transition. This width is set by the lifetime of phonons involved.

Comparable linewidths. If the cavity and the Raman DOS have comparable linewidths and are both modelled by Lorentzians (see Fig. 2.4.1c), the following more general *effective Purcell factor* emerges (after some approximation and contour integration) [58]

$$F_{p,\text{eff}} = \frac{3}{8\pi^2}\left(\frac{\lambda}{n}\right)^3 \frac{Q_{\text{eff}}}{V_m}\,. \tag{2.4.15}$$

The introduced effective quality factor is composed of the cavity and Raman line quality factors

$$Q_{\text{eff}} \approx \left(\frac{1}{Q_\text{c}} + \frac{1}{Q_\text{r}}\right)^{-1} \tag{2.4.16}$$

and leads to the cases explored above for $Q_c \gg Q_r$ and $Q_c \ll Q_r$, respectively.

Broadband enhancement. The last case we consider is a for a broadband Raman measurement, where we want to use the cavity to measure multiple Raman lines or the exact shape of Raman features. For this one can modulate the cavity resonance (by changing the length) linearly from $\bar{\omega} - \Delta\omega/2$ to $\bar{\omega} + \Delta\omega/2$ and this way time-average the enhancement at different frequencies. The Raman features are given by an arbitrary phenomenological DOS function

that is normalized, $\int_0^\infty L(\omega) = 1$, , see Fig. 2.4.1d. Let us assume that the cavity line is narrower than any feature (e.g. a high finesse cavity coupled to broad phonons in solid state systems), since this is the maximum enhancement that can be achieved.

The time averaged broadband Purcell enhancement is given by comparing the integrated emission rate in the same time collected with and without a cavity,

$$\begin{aligned} F_{p,\mathrm{bb}}(\bar{\omega}) &= \frac{\int_{\bar{\omega}-\Delta\omega/2}^{\bar{\omega}+\Delta\omega/2} d\omega_c \int_0^\infty d\omega\, L(\omega_1-\omega_2)\,\delta(\omega-\omega_c)/V_m}{\int_{\bar{\omega}-\Delta\omega}^{\bar{\omega}+\Delta\omega} d\omega_c \frac{1}{3}\int_0^\infty d\omega\, L(\omega_1-\omega_2)\,\rho_{\mathrm{fs}}(\omega)/V_{fs}} \\ &\approx \frac{1/V_m}{\Delta\omega\frac{1}{3}\frac{\bar{\omega}^2 n^3}{\pi^2 c^3}} \\ &\approx \frac{3}{4\pi^2}\left(\frac{\lambda}{n}\right)^3 \frac{\pi\bar{\omega}}{2\Delta\omega}\frac{1}{V_m} \\ &= \frac{3}{4\pi^2}\left(\frac{\lambda}{n}\right)^3 \frac{Q_{bb}}{V_m} \end{aligned} \tag{2.4.17}$$

We used the approximation that the free space spectral density changes slowly in the region of the features, and moved it into the front of the integral, evaluated at the centre frequency. In the last line, the formula was brought into the same form as the other Purcell factors, by introducing the broadband effective quality factor

$$Q_{bb} = \frac{\pi}{2}\frac{\bar{\omega}}{\Delta\omega} \tag{2.4.18}$$

which is given by the centre wavelength and the bandwidth of the sweep.

In the next section, we will discuss the expected Purcell enhancement for realistic fibre-based cavities.

2.4.3. Single-resonant enhancement

To put the Purcell effect to use, the sample inside the cavity is excited by a laser, and the cavity is tuned to resonance with a Raman line of interest, sketched in Fig. 2.4.2. In order to perform spectroscopy, different Raman shifts should be recorded and the cavity therefore needs to be tuned resonant with different wavelengths. To couple the excitation light into the cavity independent of the cavity length, an excitation wavelength beyond the stop-band of the mirror coating is used, where the cavity is transparent and the intensity at the sample almost independent of the cavity length. Since only the collection wavelength is resonantly enhanced by the cavity we call this measurement scheme “single resonant cavity enhanced Raman scattering”.

As we have seen, the Purcell effect can enhance scattering into the cavity mode compared to free space. It scales with the inverse mode volume, and depends on the linewidth of the feature on the different quality factors.

In Fig. 2.4.3, the ideal, effective and broadband Purcell factors are calculated as expected for two exemplary cavities. All Purcell factors increase strongly towards shorter cavity lengths, where the mode volume shrinks. It becomes evident that to get some enhancement on broad

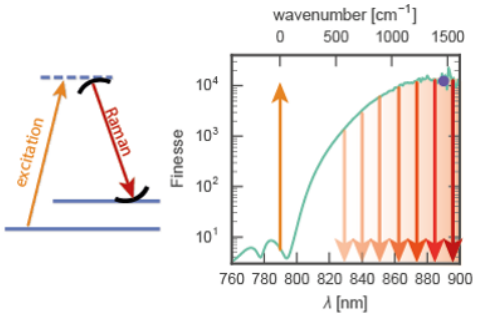

Figure 2.4.2.: Principle of cavity enhanced Raman spectroscopy illustrated with a level diagram (a) and with the wavelength dependence of the cavity finesse (b). The up-facing arrows mark the excitation light in a transparent region of the mirrors. Depending on the cavity's resonance condition (schematically depicted by black curved "mirrors" in the level scheme), Raman scattering is enhanced at a certain wavelength. This is depicted by multiple down-facing arrows, each for one cavity length.

Raman lines, a micro-cavity is needed: As the effective Purcell factor is limited by the linewidth of the Raman feature, where a common width in s solid is on the order of $\delta\tilde{\nu} = 10\,\mathrm{cm}^{-1}$ (corresponding to $Q_r \approx 1100$, $\delta\lambda \approx 0.8\,\mathrm{nm}$), the effective Purcell factor drops below unity for cavity length of $d \gtrsim 10\,\mu\mathrm{m}$ with mirror radius of curvature $R = 100\,\mu\mathrm{m}$. There, one actually funnels less photons into the cavity mode as are scattered into free space. This need for extreme microscopic cavities to enhance Raman scattering is the reason that is has been only demonstrated in a few experiments and that cavity enhanced Raman spectroscopy has not found an application yet.

In gases, narrower Raman linewidths than in solids are common. Therefore, higher effective Purcell factors are expected. However, as the effective Purcell factor scales with $\propto V_m^{-1}$ but the number of molecules inside the cavity scales with $\propto V_m$, smaller cavities do not necessary yield stronger Raman signals. A gain in signal strength through the cavity is here mainly attributed to the effective collection of cavity enhanced Raman scattering and enhancement of the excitation light by multiple passes. Both of these effects will be discussed in the following.

Efficient collection. Apart from the Purcell factor, another effect enhances the detected signal in cavity enhanced Raman spectroscopy: the cavity enhanced scattering is completely directed into the single cavity mode mode and can therefore be collected and detected efficiently.

In contrast to free-space emission into 4π, the Purcell enhanced emission is coupled in a single mode, and therefore its spectral and spatial coherence is ideal. Using asymmetric cavity mirrors or detectors at both ends of the cavity, close to $100\,\%$ of scattered light can be collected without needing high-NA objectives. Only losses in the mirrors or at the sample reduces this efficiency. On the fibre side the light is even readily coupled into the single mode fibre.

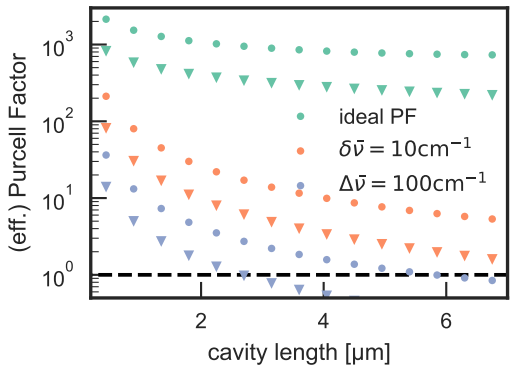

Figure 2.4.3.: Theoretical Purcell factors for cavities with $\mathcal{F} = 10^4$ and radius of curvature $100\mu\text{m}$ (triangles) and $15\mu\text{m}$ (dots), respectively, at Raman wavelength $900\,\text{nm}$. The ideal Purcell factor, the effective Purcell factor for a Raman feature with FWHM linewidth $\delta\bar{\nu} = 10\,\text{cm}^{-1}$($Q_r \approx 1100$, $\delta\lambda \approx 0.8\,\text{nm}$), and the broadband Purcell factor when sweeping the cavity resonance over $\Delta\bar{\nu} = 100\,\text{cm}^{-1}$($Q_{\text{bb}} \approx 170$, $\Delta\lambda \approx 5\,\text{nm}$) are shown. Each data point is evaluated at a cavity resonance.

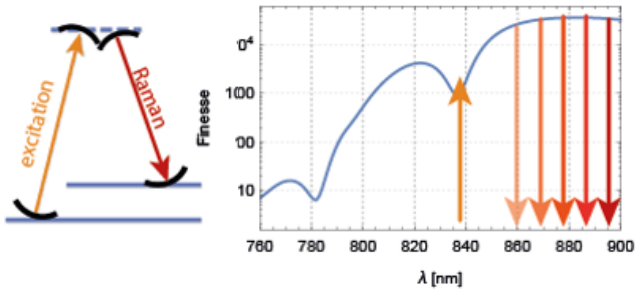

(a) **(b)**

Figure 2.4.4.: Principle of double-resonant cavity enhanced Raman spectroscopy explained at level diagrams (a) and inside finesse vs wavelength plots (b). The cavity enhances both the excitation via power build-up and scattering via the Purcell effect.

Spectroscopy. To perform spectroscopy, the length of the cavity and with it the resonance condition is tuned. Measurements at several cavity lengths have to be combined to yield the overall measurement. The performance gain of the cavity therefore depends on the width of the spectral region of interest. It is maximal when only a single, sharp Raman feature is of interest.

If the cavity length is known and the spacing of the modes large enough, no additional dispersing element behind the cavity (like a spectrometer) is needed to resolve high resolution spectra.

2.4.4. Double-resonant enhancement

In addition to the scattered light, the cavity could be used to simultaneously enhance the exciting laser intensity, as sketched in Fig. 2.4.4a. This is beneficial in several ways:

The cavity boosts the light intensity at the sample by the factor $C_e \approx 4\frac{\mathcal{F}}{\pi}$ relative to the incoming power (see Eq. (A.1.36)). Therefore, even illuminating with a low-power laser could yield detectable Raman scattering. Furthermore, this decreases fluorescence and Raman scattering inside the in-coupling fibre, which usually contributes to a broad background when higher powers are used ($\approx \mathrm{mW}$). Furthermore, since also the intensity of transmitted excitation light would be lower, this would facilitate separating this light from the Raman scattering signal.

However, things also get more complicated as the excitation light has to be resonant with the cavity at the same time as the scattered light. To have to different wavelengths resonant one can use adjacent longitudinal modes. However, this is only possible for a few wavelengths and when doing spectroscopy it is desirable to collect wide band Raman spectra. Petrak et al.[17] used the changes of the reflection phase of the mirror to find suitable cavity lengths. They showed micro-cavity enhanced spectroscopy of atmospheric gases but were only able to measure Raman shifts continuously over a bandwidth of $50\,\mathrm{cm}^{-1}$.

In Section 3.2 an optimized mirror coating and laser excitation technique will be presented to overcome this limitation and enable double-resonant Raman scattering continuously across $1000\mathrm{cm}^{-1}$.

3. Building blocks

So far, the introduction of scanning cavity microscopy and its measurement principles have been discussed in the last chapter in theory. In this chapter, we will move on to the actual implementation of a scanning cavity microscope.

First, a brief overview of the optical setup is given.

Several novel parts and techniques have been developed during this work, to perform both Raman and absorption spectroscopy, and to improve sensitivity and speed. These building blocks of the scanning cavity microscope are introduced in this chapter.

For Raman spectroscopy. First, an optimized optical coating for double-resonant Raman spectroscopy is presented, where both the pump beam and the Raman shifted probe wavelength are simultaneously resonant with the cavity.

As the introduced coating needs a tunable laser, a scheme for passively locking a widely tunable laser diode to the cavity resonance by optical feedback is presented.

For stability. Then a mechanical setup that offers a high passive cavity length stability while at the same time offering a long transversal and cavity length scan range is introduced.

Furthermore, several techniques to measure and stabilize the cavity length where developed and used, a key requirement for spectroscopy since the resonance wavelengths depend on the cavity length.

For extinction spectroscopy. For fast extinction measurements, a digital readout technique is introduced to measure the amplitude of up to a million transmission resonances per second.

Finally, components for a measurement scheme based on broadband light sources and detection with singe-photon sensitive detectors are discussed.

3.1. Setup overview

The basic optical setup is shown in Fig. 3.1.1. A laser (or another light source, see Section 3.7.3) is coupled into the single mode fibre of a fibre-based beam splitter. One output port is connected to the cavity fibre. Transmitted or Raman scattered light behind the planar mirror is collimated by a simple achromatic lens and detected on (avalanche) photodiodes, cameras, photon counters or a grating spectrometer. Other ports of the beam splitter are used to verify the power coupled into the fibre (PD_{in}) and to measure the reflected signal (PD_{refl}). If needed, additional lasers can be coupled in via the fibre beam splitter.

Both the fibre and the mirror can be positioned. The fibre can be scanned precisely, repeatable and continuous by piezo elements in all three directions. The mirror is moved by DC-motors to be able to scan different areas of the planar mirror.

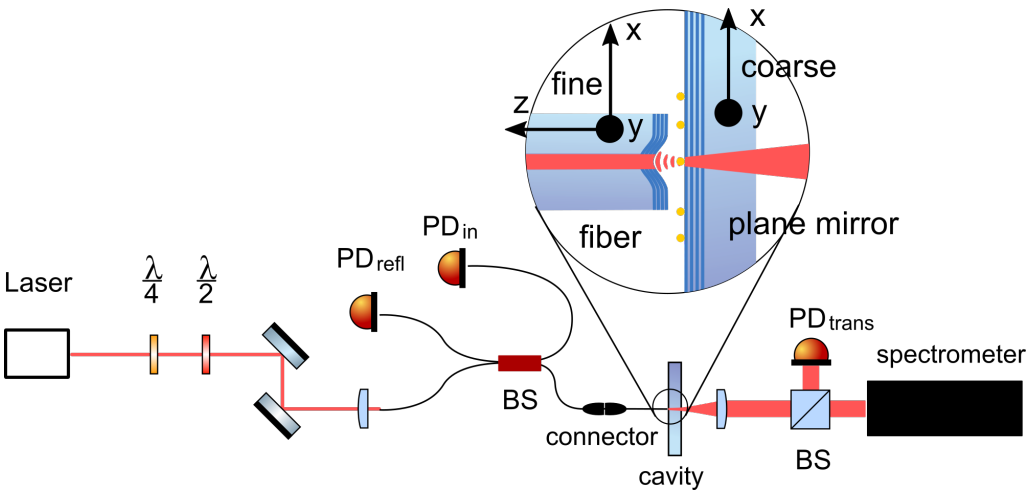

Figure 3.1.1.: Schematic of the scanning cavity setup. BS: fibre based and normal non-polarizing beam splitters. PD: photodiodes. The fibre and the planar mirror (magnified in the zoomed-in circle) can both be positioned with devices not shown in this sketch. The fibre can be scanned continuously and precisely in x,y ('transversal'), z (cavity length, 'longitudinal') direction. The mirror can be positioned coarsely in x,y direction to have access to different areas of the planar mirror.

3.2. Mirror coating for double-resonant Raman

In this section, an optimized dielectric mirror coating for performing flexible broadband cavity enhanced double resonant Raman spectroscopy is developed. Apart from validating the expected performance, measurements on this coating show unexpected effects that are explained by the strong curvature of the miniature concave mirror.

3.2.1. Problem

In the double-resonant Raman scheme, as introduced and motivated in Section 2.4.4, both excitation and collection of the Raman process should be resonantly enhanced by the cavity. For this, both wavelengths lie inside the high reflective band of the mirror coating and therefore have to be simultaneously resonant with the cavity. To be resonant at the same time, multiple longitudinal modes can be used. However, due to the need for short cavity length for strong Purcell enhancement, they are distributed sparsely, see Fig. 3.2.1a.

The Raman shift to be measured is the distance between the excitation and collection energies. For powerful spectroscopy, being able to measure a wide range of energy (usually given in wavenumbers, $\tilde{\nu} = \omega/(2\pi c) = \lambda^{-1}$, and cm^{-1} in the community) is desired. The problem is that by changing the cavity length, both the excitation and collection resonances shift almost the same amount in frequency, as can be seen in Fig. 3.2.1a. Therefore, their relative distance changes only slightly and only a small range of energies is accessible. In this section, specific optimized mirrors to increase the accessible energy range for double resonant Raman spectroscopy will be introduced.

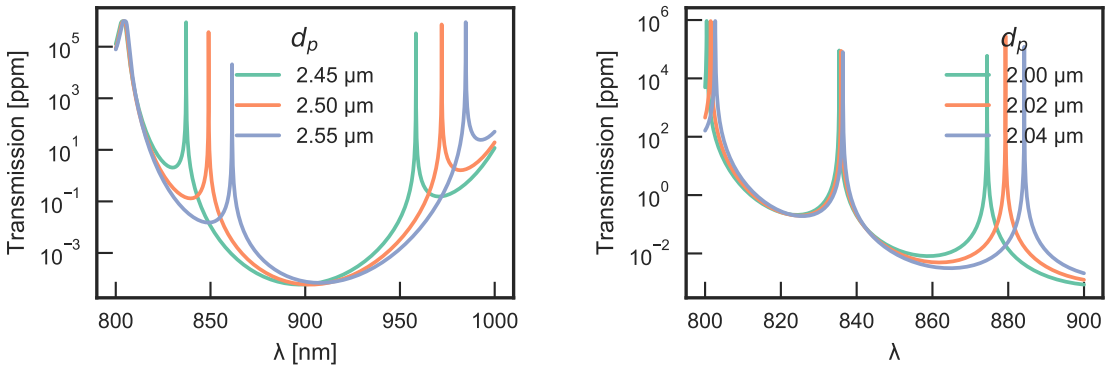

Figure 3.2.1.: Theoretical cavity transmission spectra for different cavity mirror separations, d_p. (a) For a simple $\lambda/4$ Bragg reflector centred around $900\,\mathrm{nm}$, made of 18 layers pairs of SiO_2 and Ta_2O_5. (b) For an optimised reflector where the reflection phase as a function of wavelength is optimised.

Resonance spacing. The resonance wavelength of a cavity mode of order q depends on the distance between the mirror d_p (physical cavity length), as derived in Appendix A.2,

$$2\pi q = 2d_p(\frac{2\pi}{\lambda}) + \varphi_m(\lambda) + \zeta(d, R)\ . \tag{3.2.1}$$

Here φ_m is the phase shift at the mirror on reflection and is in general wavelength-depend for dielectric mirrors, and ζ is the Gouy phase shift.

The position of the resonances can be tuned by changing the cavity length, as can be seen in Fig. 3.2.1a, where the transmission spectrum of a short cavity is shown for different lengths. The Raman shift that can be measured is given by the difference of the excitation, $\tilde{\nu}_e$, and collection, $\tilde{\nu}_c$, wavenumbers. And since one can see that the modes move almost the same amount when changing the cavity length, this difference does not change strongly. Therefore, only a limited spectral range can be measured. For doing broadband Raman spectroscopy, however, a wide range of wavenumbers should be accessible continuously.

In Fig. 3.2.1b a more favourable behaviour of the longitudinal modes is shown. There, the modes shift at different 'speeds' and therefore their relative distance changes stronger when changing the cavity length. In this section we will explore how to achieve to this behaviour.

Let's analyse what sets the spectral distance between two resonances in more detail. As can be seen in Eq. (3.2.1), the spectral position of a resonance depends on the cavity length, d_p, and the the reflection phase φ_m at the mirror. As the Gouy phase is the same for both resonances, it does not play a role for the difference. The reflection phase changes across the stop-band of a Bragg reflector, and is plotted in Fig. 3.2.2a for a standard $\lambda/4$ coating centred around $900\,\mathrm{nm}$. Furthermore, the finesse when used in a cavity is shown. In Fig. 3.2.2b, we see how the resonance wavelength for two adjacent longitudinal mode orders and their relative distance changes as a function of cavity length. Although this provides already limited tuning, some problems become apparent:

1. Although each modes' wavelengths changes by more than hundred nm, the distance

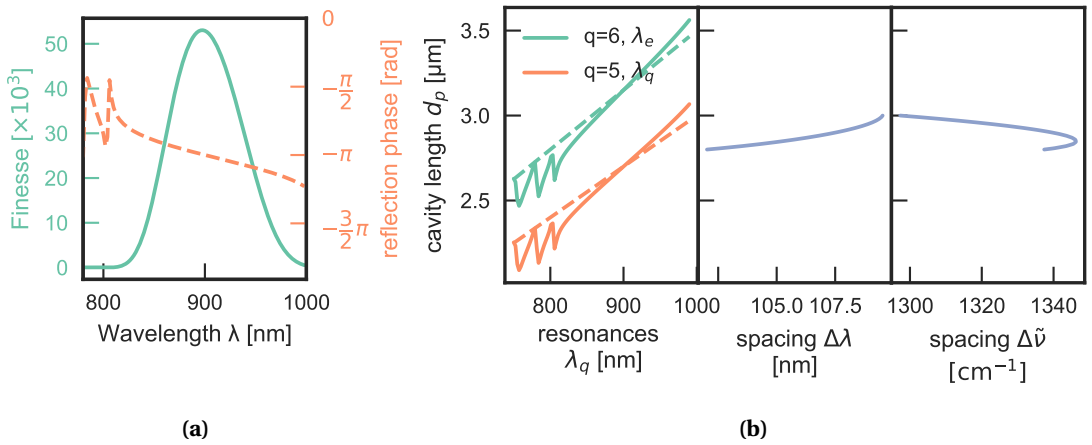

Figure 3.2.2.: (a) Finesse (green) and reflection phase (orange) at the simple $\lambda/4$ Bragg reflector. (b) Position of two adjacent resonances of longitudinal mode order q as a function of cavity length. The dashed line would be the case when assuming a constant reflection phase. Their spacing in wavelength and wavenumbers is plotted below.

between the modes is almost constant because the resonances move almost in 'parallel'. Only approximately a range of $50\,\mathrm{cm}^{-1}$ is accessible.

2. The spacing is larger than the high finesse bandwidth of the coating, see Fig. 3.2.2b. This could be reduced with longer cavity lengths where, however, the mode volume is larger and the collection enhancement significantly weaker (see Section 2.4.3).
3. Also due to the large spacing, smaller wavenumbers are not accessible.
4. The excitation spans a large wavelength range, needing a wide tunable laser for excitation.

3.2.2. Optimized coating

To overcome the aforementioned problems, the reflection phase of the mirror coatings can be tailored. The mirrors, used to build high finesse cavities, are distributed Bragg reflectors that work by constructively interfering reflections from multiple interfaces of stacked dielectric layers with alternating high and low refractive indices. Using materials with low absorption (different glasses) and processes that generate smooth layers of these materials (here: ion beam sputtering (IBS)), so-called super-mirrors with reflectance of more than 99.9995%[59] can be made.

Like, in *chirped mirrors* used for pulse compression, the thickness of the stacks can be varied to let different wavelengths penetrate more or less into the stack. In this way, different wavelengths experience different effective cavity lengths. Various designs where evaluated: chirped mirrors with continuously varying thickness, resonators formed inside the stack , and different centre wavelength $\lambda/4$ stacks assembled on top of each other. The latter provided the best properties for minimizing for losses, maximizing penetration depth variation and additional constraints detailed later on in this section. The coating formed by a $950\,\mathrm{nm}$ $\lambda/4$ stack (10 layer pairs with an additional last high reflective layer) and a $830\,\mathrm{nm}$ stack (10 layer

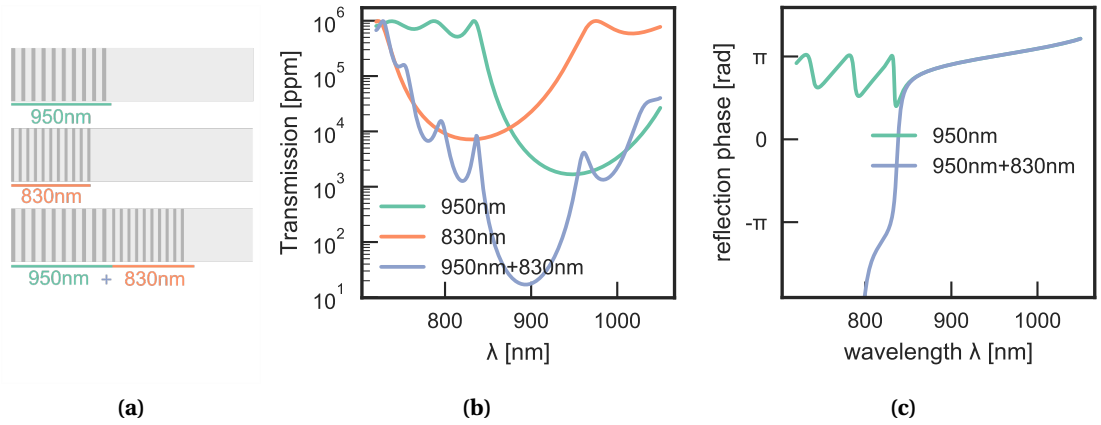

Figure 3.2.3.: (a) Schematic of coatings: $950\,\mathrm{nm}\lambda/4$ stack(top), $830\,\mathrm{nm}\lambda/4$ stack (middle), and both combined (bottom). On the right is the substrate, the left side faces to the inside of the cavity. The light shaded layers are SiO_2 with low reflective index while the dark shaded layers are $Ta_2O_5$with high refractive index. (b) Transmission of the coatings. (c) Reflection phase of the coatings.

pairs) on top of each other is shown in Fig. 3.2.3a. In (b) the transmission of these stacks is plotted. At the edge of the stop band of the top $950\,\mathrm{nm}$ stack, at around $830\,\mathrm{nm}$, the reflection phase changes rapidly, as can be seen in Fig. 3.2.3c. However, unlike when using the single stack, the transmission does not increase because the bottom $830\,\mathrm{nm}$ stack contains the wave, see Fig. 3.2.3b. Therefore, even at this point a high finesse cavity can be formed.

Forming a cavity with one of these mirrors and a second normal $\lambda/4$ mirror, the tuning of the cavity length leads to a differential shift between the resonances, depending on their spectral position, as envisioned in Fig. 3.2.1b.

Comparison of theory and experiment. This optimized coating design was applied to laser-machined concave fibre mirrors using ion beam sputtering (IBS) by the commercial optical coating manufacturer manufacturer Laseroptik GmbH. The optical properties were tested in a cavity, formed with a common $\lambda/4$ stack as the second mirror. The sudden change of effective cavity length can be measured and imaged by recording white light transmission spectra for different cavity lengths. This is shown in Fig. 3.2.4b. Overlaid are the fundamental cavity mode resonances calculated according to Eq. (3.2.1), using only the the simulated reflection phase of the coating stack.

We see a qualitatively good agreement to the theory calculated in Fig. 3.2.4a. However, to reproduce the coating exactly, the central wavelength had to be shifted by $12\,\mathrm{nm}$ to longer wavelengths. A shift of $11 \pm 1\,\mathrm{nm}$ with respect to theory was observed in all (10) fibres that were measured. The otherwise good theoretical agreement hints at a problem during the coating process. The evaporation rate during the IBS coating process depends on the precise positioning of the sample to be coated. According to the coating manufacturer the evaporation rate changes by 1% if the sample is misplaced by $1\mathrm{mm}$, as a rule of thumb. The observed shift of $12\,\mathrm{nm}$ of the coating at $940\,\mathrm{nm}$ would therefore correspond to misalignment of $1.3\,\mathrm{mm}$. This shift has been observed in wavelength resolved measurements of the cavity finesse as well.

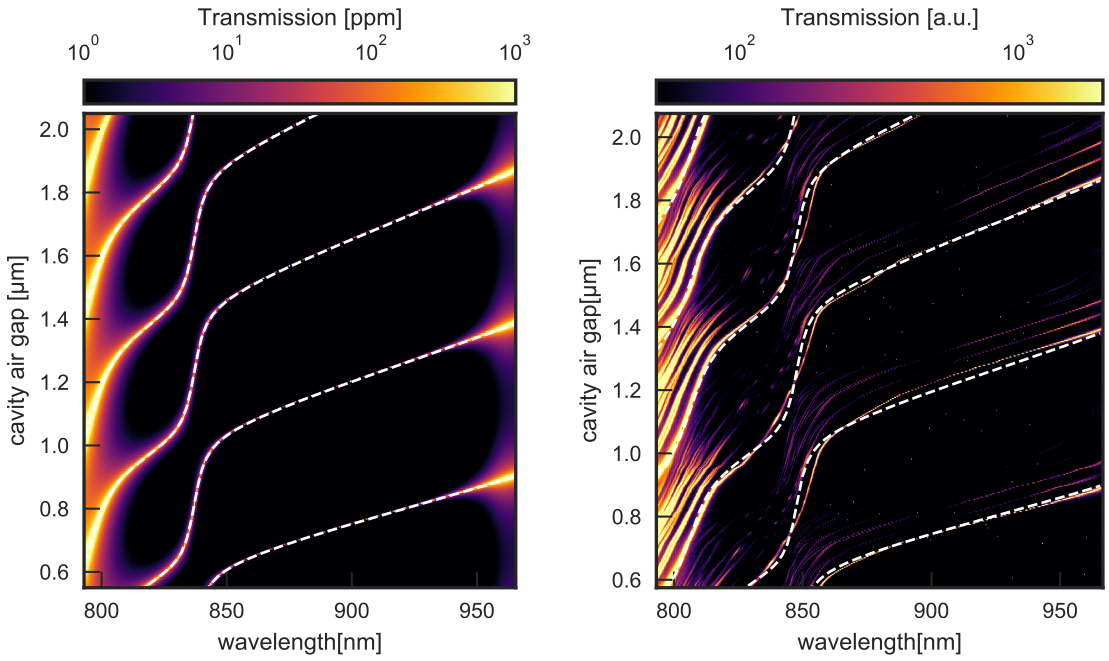

(a) **(b)**

Figure 3.2.4.: False-colour map comparing experimentally obtained and theoretically predicted cavity transmission spectra as a function of cavity length. (a) Simulated transmission of the fundamental cavity mode. The dashed line is the centre position of the fundamental cavity resonance. (b) Experimental transmission spectrum taken for several cavity lengths. Cavity air gap axis is only correct to a few percent due to piezo non-linearity and positioning errors. Above the fundamental mode, which has the highest intensity, several higher order modes can be seen, shifted to longer cavity lengths or shorter wavelengths. The dashed line is the theoretical position of the resonance. It had to be shifted by $12\,\mathrm{nm}$ to longer wavelengths to fit the data.

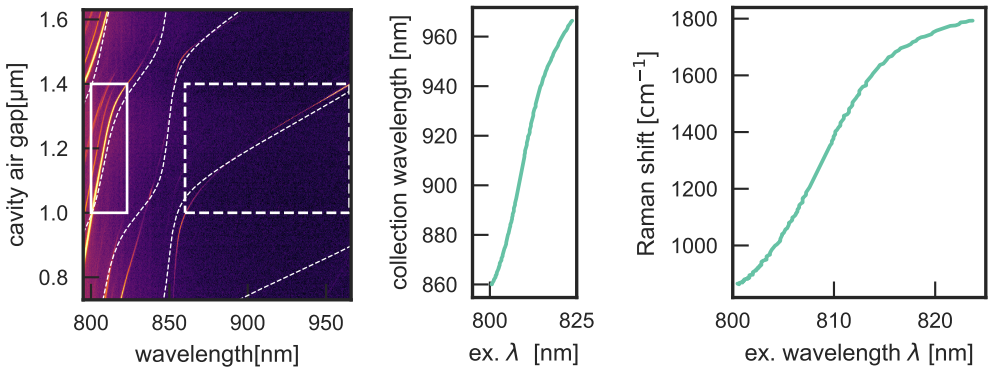

(a) **(b)** **(c)**

Figure 3.2.5.: (a) False-colour map of measured transmission spectra (arbitrary units). The dashed lines just guides the eye to the fundamental mode. (b) Collection wavelength (extracted from the experimental transmission data in the right dashed box in (a)) as a function of excitation wavelength (collected from the left solid box) from a cavity length sweep from 1.0 to 1.4µm. (b) Same data converted to Raman shift between these two wavelengths.

3.2.3. Tuning range

To measure the Raman shift accessible, the resonance wavelengths were extracted from the transmission spectra shown in Fig. 3.2.5a. The 'excitation wavelength' was the mode from $800\,\mathrm{nm}$ to $825\,\mathrm{nm}$ (solid rectangle). The 'collection wavelength' was in the high finesse region between $860\,\mathrm{nm}$ and $965\,\mathrm{nm}$ (dashed rectangle) . In Fig. 3.2.5b we see these simultaneous resonances plotted as a function of each other. In Fig. 3.2.5c the Raman shift calculated from this is shown, spanning $900\,\mathrm{cm}^{-1}$ to $1800\,\mathrm{cm}^{-1}$ continuously accessible by simply tuning the cavity by $0.4\,\mu\mathrm{m}$. For this the excitation laser has to be tuned $25\,\mathrm{nm}$.

Note that this region is available even in the the lowest accessible longitudinal mode. The depth of the concave fibre profile is already $0.41\mu\mathrm{m}$ and the fibre started touching the planar mirror at about $0.95\,\mu\mathrm{m}$ cavity air gap, due to residual misalignment and imperfect cleaving of the fibre. This makes Raman measurements over a large range possible with minimal mode volume, boosting the Purcell factor. With a conventional coating one has to increase the cavity length by more than a factor of two.

At longer cavity lengths, shorter Raman shifts become accessible. Furthermore by using the directly adjacent resonances (using the resonance between the boxes in Fig. 3.2.5a), wavenumbers down to $300\,\mathrm{cm}^{-1}$ come into reach.

3.2.4. Additional coating constraints and simulation

For being suited for a scanning cavity microscope, two different coatings for the planar mirror and the fibre are used. The constraints to be met by these coatings are are explained and simulated in this section. Technical details of simulating these coatings are summarized in Appendix C.1.1.

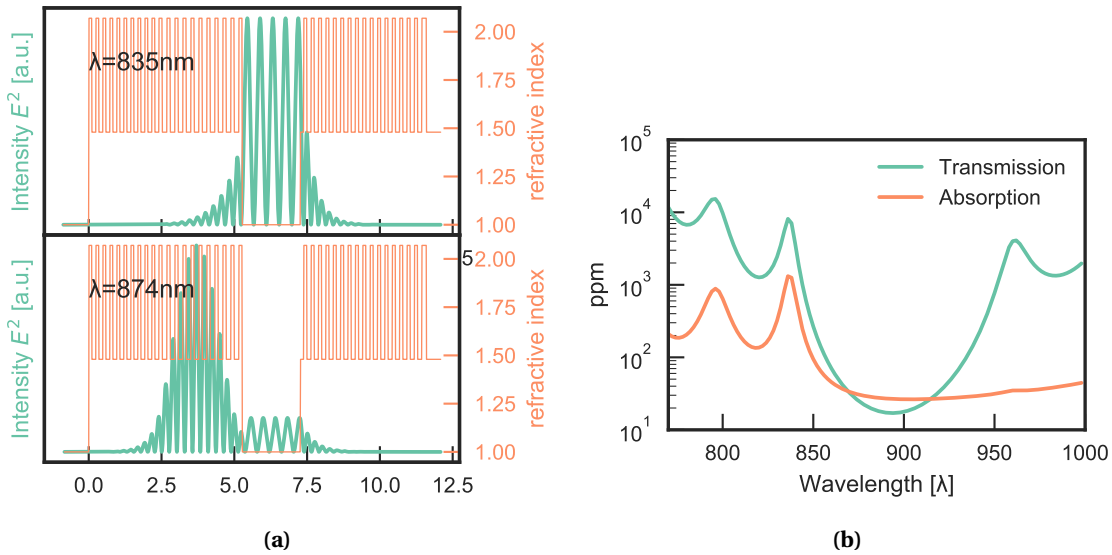

(a) **(b)**

Figure 3.2.6.: (a) Simulation of the cut along the cavity axis showing energy distribution inside the a cavity where one mirror (left) is made from this stack. In orange, the refractive index profile is plotted. For two different wavelengths. (b) Absorption and transmission of the cavity mirrors.

High finesse and low mirror losses. In Fig. 3.2.6a, we see the energy distribution inside the cavity for two different wavelengths. For wavelengths where the top stack is reflective, the major part of the energy is stored between the mirrors when on resonance. However, at shorter wavelengths where the wave penetrates the top layers and "gets stopped" by the bottom layers, the most energy is stored inside the coating. Therefore, scattering at the layer interfaces and especially absorption inside the stack lead to elevated losses. The coating was optimized to both yield a strong change in penetration depth and low losses by simulating many different stacks. In Fig. 3.2.6b the strong losses around $840\,\mathrm{nm}$ hints at high intensities inside the coating stack.

However, at the wavelength region where excitation $(800 - 830\,\mathrm{nm})$ and detection $(870 - 930\,\mathrm{nm})$ are planned the finesse is well above 10^3 and 10^4, respectively, as can be seen in Fig. 3.2.7.

Field enhancement. The original goal of the double-resonant measurement scheme is to also enhance the excitation power. It should be sufficiently high so low powered laser diodes can be used. As derived in Appendix A.1.7, the power enhancement relative to the power coming from behind mirror i with transmission T_i is given by

$$C_e = 4T_i \frac{\mathcal{F}^2}{\pi^2}\,. \tag{3.2.2}$$

Here, losses due to suboptimal mode matching were neglected. In Fig. 3.2.7d the enhancement when coupling in from the fibre side is plotted. In the region where the excitation is envisioned $(800\,\mathrm{nm}$ - $830\,\mathrm{nm})$ this is above 500.

Field maximum position. In the scanning cavity microscopy scheme the objects to be measured are placed on the planar macroscopic mirror. For the objects to interact with the light field, the optical coating of the planar mirror has to be designed that the standing wave has sufficient intensity at its surface. Ideally an anti-node of the electric field is found there.

As an example, the formula for the mode volume (Eq. (A.3.12)) to calculate the Purcell effect, is only valid when the emitter is placed in an anti-node of the field. Contrary, in an node of the electric field, the emission would be inhibited.

The field at the surface of the mirror depends on the mirror reflectivity, R, and the reflection phase ϕ. The intensity from the interference of incoming and reflected field at the surface normalized to the incoming intensity ($|u_0|^2$) is

$$I_{\text{surf}} = \left|\frac{u}{u_0}\right|^2 = \left|1+\sqrt{R}e^{i\phi}\right|^2 = 1+R+2\sqrt{R}\cos\phi\,. \tag{3.2.3}$$

For almost perfect reflectivity in a high finesse cavity this simplifies to

$$I_{\text{surf}} \approx 2+2\cos\phi\,, \tag{3.2.4}$$

meaning the intensity can be up to four times larger than the incoming field for reflection phase $\phi = 0$ or down to zero for $\phi = \pi$. The field at the surface of the mirror is plotted in Fig. 3.2.7c. It is not fully optimized as is decays considerable from its maximum at longer wavelengths. The reason for this is that existing mirrors were used. Even after the commercial coating process the field maximum can be adjusted, by adding an additional low-reflective layer, like fused silica (by sputtering) or PMMA (by spin coating). This will however also slightly modify the reflectivity of this mirror.

Shallow penetration depth. As detailed in Appendix A.5.4, the electric field can penetrate up to several µm into dielectric coatings, which can increase the mode volume significantly. This effect is particular large when moving away from the central design wavelength of a $\lambda/4$ coating, or when chirped coatings are used. Therefore, $\lambda/4$ reflectors are used at least for the top layers of the coating. Furthermore, the penetration is significantly more pronounced when the last layer of a coating has low refractive index. On the fibre mirror side, the last layer is therefore designed to have high refractive index. However, this is of course not possible for the planar mirror since this comes along with a field node where the sample is placed.

The calculated penetration depth is shown in Fig. 3.2.7e. It is low in the region where Raman signals should be measured ($860\,\text{nm} - 940\,\text{nm}$) and therefore a low mode volume and high Purcell factor is provided there. The penetration is larger for the planar mirror because of the low refractive index last layer. It increases significantly for the fibre mirror, where the $950\,\text{nm}$-centred top layers get transmissive at $840\,\text{nm}$, and a resonance forms, as shown in Fig. 3.2.6a. [1]

[1] At $840\,\text{nm}$, where a resonance inside the coating forms, the penetration depth gets particular large, even exceeding the physical height of the coating stack. To understand this, it has to be remembered that the (energy) penetration depth is defined by comparing the energy stored inside the mirror and in front of the mirror, as explained in Appendix A.5.4. Through energy normalization, this reduces the field "per photon" at the point of the sample, see Section 2.4.1. This is how the mode volume is defined, via integrating over the energy.

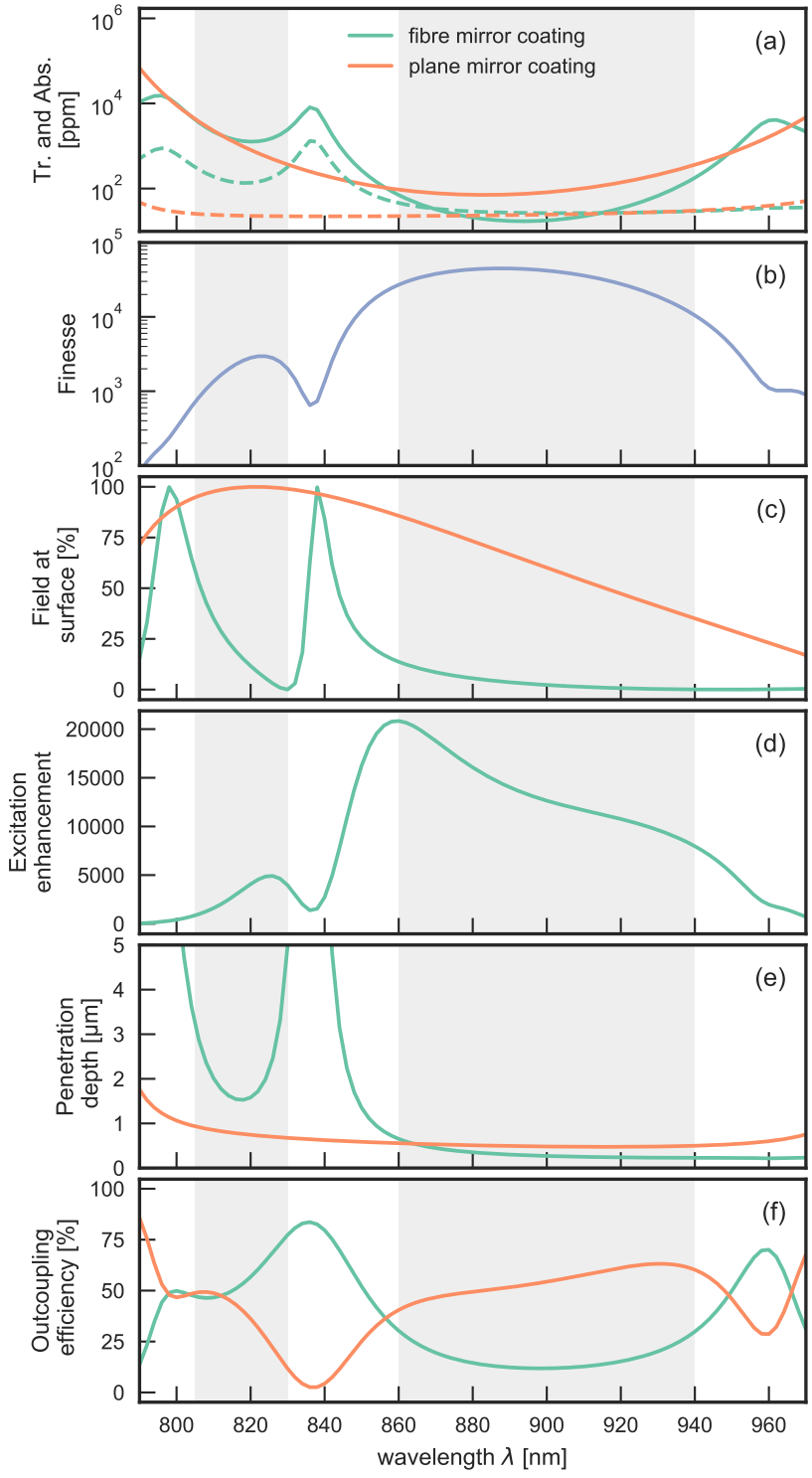

Figure 3.2.7.: Properties of the fibre coating (green), the planar mirror coating (orange) and of the cavity (blue) as a function of wavelength. The left grey shaded region is where excitation is envisioned ($805\,\mathrm{nm} - 830\,\mathrm{nm}$), while the right is for Raman collection ($860\,\mathrm{nm} - 940\,\mathrm{nm}$). (a) Solid lines are mirror transmission. Dashed lines are absorption in the mirror.

The penetration depth can be further reduced by using a large contrast of refractive index materials to make up the layers, because there the reflection from each interface is stronger.

Out-coupling efficiency. The Raman photons created inside the cavity should be out-coupled predominantly through the mirror where the detector is located, instead through the other mirror or getting absorbed inside the coating. In this setup the detector is placed behind the planar mirror. In the high finesse limit, the out-coupling efficiency through mirror i is given by the respective mirror transmission divided by all other loss channels (see Appendix A.1.6)

$$\eta_c = \frac{T_i}{T_1 + T_2 + L_1 + L_2 + 2A}\,. \tag{3.2.5}$$

Here, $T_{1,2}$ are the mirror transmission, $L_{1,2}$ the mirror scattering and absorption losses and A extinction at the sample. For the proposed coatings the out-coupling efficiency is plotted in Fig. 3.2.7f . In the wavelength region where Raman signals should be measured ($860\,\mathrm{nm}$-$940\,\mathrm{nm}$) this is primarily through the planar mirror due to its higher transmission.

3.2.5. Triple resonance: Angle tuning

Sometimes not only the shift between the excitation and collection wavelength might be interesting, but also their absolute position. For example, it could be desirable to have the excitation wavelength resonant with an intrinsic electronic transition of the sample[2]. This greatly enhances the signal through 'resonant' Raman scattering[60]. As a third resonance condition has to be met, we call this 'triple resonance' cavity enhanced Raman measurement. This adds some difficulty as the absolute position and the difference between the cavity resonances are both set by the cavity length.

The absolute position of the wavelengths, at the same relative shift, can be changed by going to different longitudinal mode orders. Another degree of freedom, that can be used is the angle between the cavity fibre mirror and the planar mirror. Adjusting this slightly changes the effective coating thickness and this way the penetration depth and double resonance condition. When small enough, this angular adjustment does not decrease the cavity finesse (e.g. by enhanced mode clipping losses). Both these tuning possibilities are analysed in in Fig. 3.2.8 where the double resonance condition for different mode orders and different angular alignments is shown. The angle was tuned by 2° between the green and orange data points, and by another 1° between the orange to blue points. For the same shift (e.g. $1600\,\mathrm{cm}^{-1}$), this 3° angular tuning allows to move the excitation wavelength by $9\,\mathrm{nm}$ (from $823\,\mathrm{nm}$ to $832\,\mathrm{nm}$). Even more flexibility is given by going to different mode orders.

3.2.6. Effects from inhomogeneous coating

In the spectral region where the reflection phase changes quickly, some interesting effects become visible. This can be attributed to general properties of strongly curved Bragg reflectors. However, in the central region of a $\lambda/4$ Bragg reflector, this effect is less pronounced and may only lead to a finesse that is lower than predicted. The effect stems from the predominantly

[2] Given by the transition matrix element of the matter in Eq. (2.4.1)

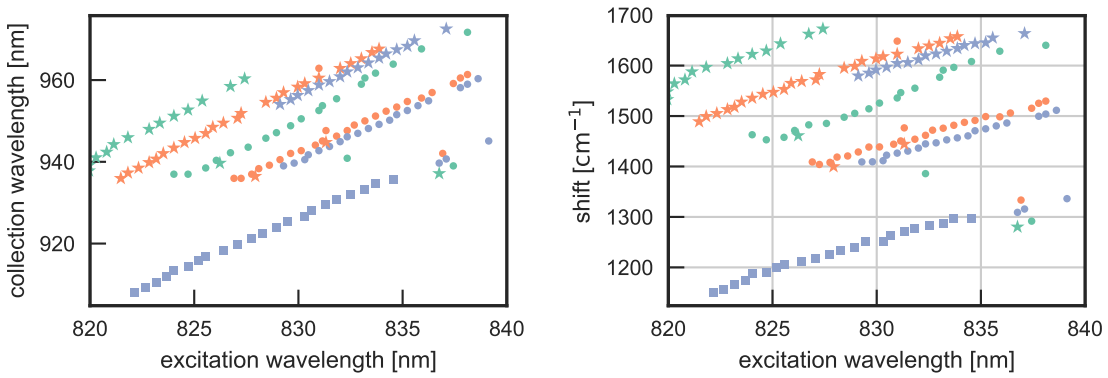

(a) **(b)**

Figure 3.2.8.: (a) Double resonance condition for different angular alignments (shown with different colours: green to orange 2° change, orange to blue 1° change) and the second (⋆) , third (·), forth (■) resonance counted from first contact with the mirror. (b) Same data as in (a) but given in wavenumber shift between excitation and collection wavelength.

directed deposition of the coating in the sputtering process[61], leading to effective thickness variation of the layers across the curved mirror profile.

This variation of the effective thickness can explain the exact resonance positions in the region where the mode starts to penetrate the coating.

Explanation of slope of fundamental mode. In Fig. 3.2.9a we see that the slope in the penetrating region is not as steep as would be expected (see for example a dashed line). This can be explained by the fact that the cavity mode senses, due to its spacial extent, different coating thicknesses. At the sides of the concave mirror profile, see Fig. 3.2.9b, the coating layers are effectively thinner for the mode, as its wavefronts always arrives perpendicular to the mirror surface. This thickness variation stems from the fact that the coating was deposited in a directed sputtering process. If the surface normal has an angle α to the deposition axis at a point of the mirror, the coating is effectively thinner by the factor $\cos\alpha$. In a first simple approximation we can assume that 'one half of the mode' senses the intended coating layer thickness (at the centre) while the other half senses a coating shifted to smaller wavelengths. The two halves of the modes are shifted in wavelength as can be seen by the left and right dashed lines in Fig. 3.2.9a. The total resonance condition for the mode is then given by the average of both, the solid line in Fig. 3.2.9b. Choosing appropriate values, this simple model can already reproduce the observed more shallow slope of the resonance positions.

Higher order transverse modes. The same effect is even more pronounced for higher order transverse modes, as they have a larger extent, associated by the number of nodes in x and y direction, depicted with the tuple (n, m), see Appendix A.3.2.

In Fig. 3.2.10a, we see that higher order transverse modes of the same order lift their degeneracy and are split in the penetrating region. This is because modes of same mode order, $\mathrm{ord} = 1 + m + n$, may have different extent, given in x and y direction by $d_x \propto \sqrt{n}$, $d_x \propto \sqrt{m}$, respectively. For example the mode $(2, 2)$ has same order, and Gouy phase shift, as $(4, 0)$.

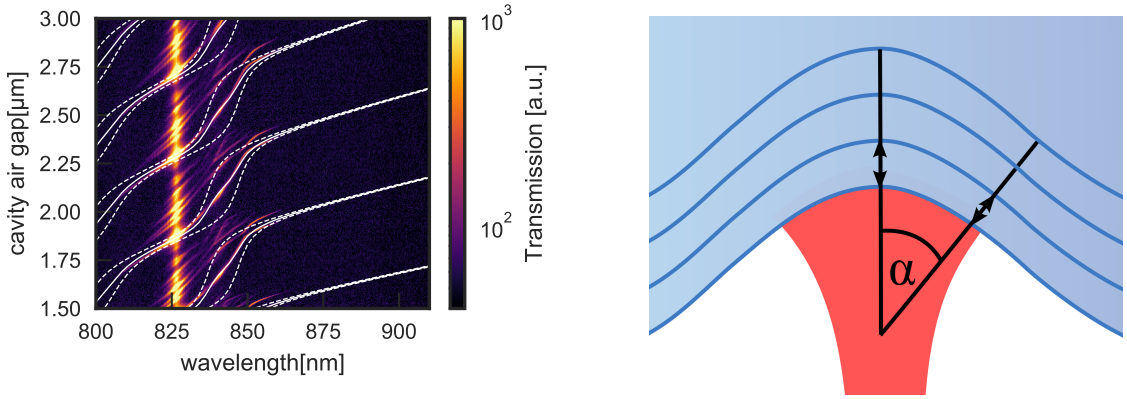

(a) **(b)**

Figure 3.2.9.: (a) Reproducing the fundamental cavity mode resonance position. The dashed lines are simulations for two different effective coating thicknesses (with 1.2% difference). The solid line is the average of the two lines. (b) The concave profile on the fibre with schematic coating layers. Across the curved mirror profile, the effective thickness of the coating layers varies when seen from the surface normal (lines) . The cavity mode (red area) has a finite extend. The arrows highlight the different coating thicknesses under different angles.

Therefore, both modes are usually degenerate. However, the mode $(2,2)$ is more compact in one direction and therefore senses an effectively different coating. This different coating shifts the onset of the phase variation to a different wavelength, and therefore the modes split up in this region.

In general, as can be seen in Fig. 3.2.10b, higher order transverse modes have a slope shifted to shorter wavelengths as they sense an effective thinner layered coating. Also the 'drops' are not as sharp as they average over a larger range of coating thicknesses (due to their larger extent), smearing it out.

To explain this behaviour, we use a white-light-interferometric measurement of the mirror profile (see Fig. 3.2.11aa) to extract the angle at each position, shown in Fig. 3.2.11b. With the known cavity length and assuming the mode is centred at the minimum of the mirror profile, the transversal field distribution of the cavity modes can be calculated. An example is shown in Fig. 3.2.11c. We see that the shown mode has significant intensity in regions with a mirror profile angle between 0° and 8°. From this, the histogram of power impinging under a certain angle is calculated and shown in Fig. 3.2.13 for various modes. We see that higher order transverse modes have indeed a broader distribution shifted to larger angles.

Mode mixing. In Fig. 3.2.10b we see that higher order transverse modes cross each other and are coupled, showing avoided crossings. The strength of this avoided crossing hints towards strong scattering between these modes. Reproducing this this is out of scope of this work but it could be done when calculating the exact eigen-modes of the cavity based on the actual mirror profile[62].

Finesse reduction. As a result of the admixture of different coating thicknesses a mode sees, the finesse that can be reached may be limited. This may explain discrepancies of expected and measured finesse, especially at the edges of the stop band, as discussed in Appendix C.1.2.

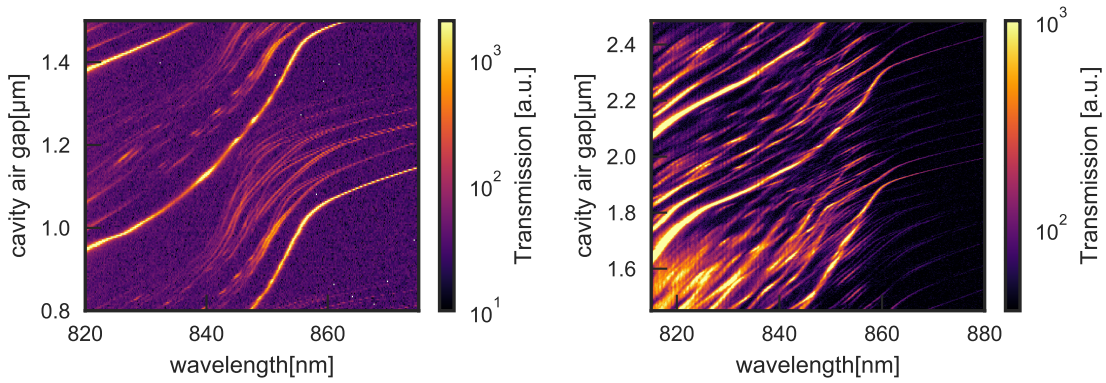

(a) **(b)**

Figure 3.2.10.: (a) Different slopes and lifting of degeneracy for higher order transverse modes hinting at influence from layer thickness variation for larger modes. (b) Avoided crossings of higher order transverse modes.

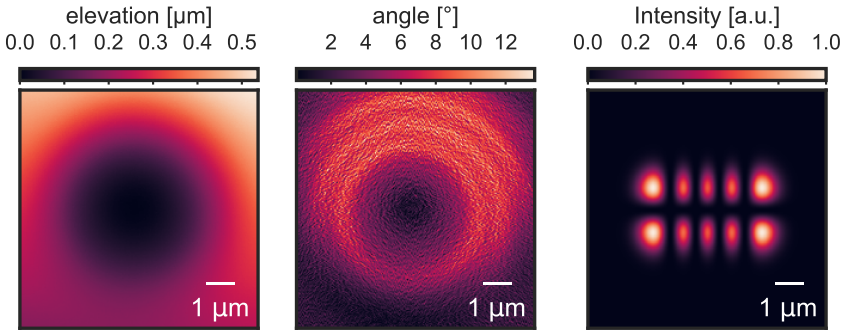

(a) **(b)** **(c)**

Figure 3.2.11.: (a) Profile of the fibre mirror surface, measured using the the white light interferometer. (b) Local angles extracted from (a). (b) Simulated intensity distribution of the cavity mode of order $(4, 1)$ for a cavity length of $1\,\mu m$ in the same area as (c) for comparison.

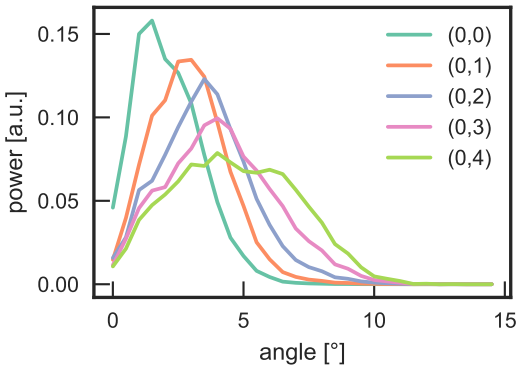

Figure 3.2.12.

Figure 3.2.13.: Fraction of power impinging on the fibre mirror under different angles for various higher order transverse modes, given by the tuple (n, m).

3.2.7. Discussion

The optimized optical coating presented provides a large continuous double resonant tuning range from $900 - 1800\,\mathrm{cm}^{-1}$ accessible through a only small change of cavity length ($0.4\,\mu\mathrm{m}$), as can be seen in Fig. 3.2.5b. This requires an a excitation wavelength change of only $20\,\mathrm{nm}$. The excitation power is enhanced by a factor of $500 - 3000$ in this region. These wavenumber shifts are accessible at the shortest cavity length. Together with the shallow penetration depth into the coating stack at the collection wavelength this offers small cavity mode volumes and therefore promises strong Purcell enhancement.

However, the extended size of the modes on the strongly curved mirrors leads to previously unexpected effects of the effective phase variation across the wavelengths. This has to be considered when designing coatings for double-resonant micro-cavities. Mirrors with larger radii of curvature also could reduce the effect of 'smearing out' the slope of the reflection phase change and could, along with more optimizations to the coatings, increase the accessible region of Raman shifts further.

3.3. Optical feedback laser

Here, a laser for Raman excitation that is passively locked to a resonance of the micro-cavity via optical feedback is presented.

3.3.1. Problem

For double resonant Raman, in combination with the aforementioned optimized mirror coatings, a widely tunable ($\gtrapprox 10\,\mathrm{nm}$) laser is needed to continuously measure a broad region of Raman shifts. Although such lasers are available as motorized external cavity diode lasers or Ti:sapphire-lasers, they are expensive, complicated to operate and offer slow tuning speeds. Furthermore, the cavity resonance and the laser wavelength have to be synchronized, needing elaborate locking schemes. In order to have a narrow-linewidth laser always resonant with the cavity, an passive locking scheme using optical feedback from the cavity was developed.

3.3.2. Working principle

In this optical feedback scheme, light that entered the cavity is injected back into the laser diode and forces the laser to run on the wavelength selected by the cavity resonance. Independent of this work, similar principles were first used for macroscopic cavities in atomic physics[63] in 1990 and in the cavity-based absorption spectroscopy community starting around the year 2000[10, 3, 64, ch.5].

Here, the cavity acts both as the device to do microscopy and the external cavity to provide laser feedback. This reduces the parts needed and the laser automatically is resonant with the cavity without having to synchronise laser frequency and cavity length by electronic feedback. Furthermore, in contrast to common external cavity diode lasers (ECDL), the external cavity used here is very short and has high finesse (µm instead of cm and up to $\mathcal{F} = 200000$ instead of around 10) . This allows for fast mechanical tuning of the laser frequency while guaranteeing single mode operation because of the large spectral mode spacing of the short cavity. This has

the potential to greatly simplify broadband operation and cut costs due to unneeded laser diode stabilization and control (cavity length and temperature).

In order to force the laser to the frequency set by the cavity, only light that entered the cavity has to be fed back to the laser. There are different methods for this, e.g. using light transmitted by the cavity or spatially filtering the shape of the cavity mode[3]. We developed a simplified system that separates resonant light reflected inside the cavity and off-resonant light (reflected at the first cavity mirror) using its differing polarization state, similar to a polarization-based isolator[65, 66].

The working principle is sketched in Fig. 3.3.1. Light leaving the laser diode is highly linear polarized ($\gtrsim 99\%$) and passes an polarizing beamsplitter. Using a $\lambda/4$ waveplate it is converted to circular polarized light. If the light is not resonant with the cavity, it does not enter the cavity, and gets reflected at the first cavity mirror. Upon this reflection the circular polarized light changes it handedness. Therefore, after passing the waveplate on the way back to the laser diode, it is linear polarized perpendicular to the initial light. Therefore on the way back it gets filtered out by the polarizing beam splitter . This is different for wavelengths that are resonant and therefore enter the cavity. Even small imperfections inside the cavity mirrors lead to (unspecified) change of polarization. The cavity therefore acts as another effective waveplate. Light reflected from inside the cavity therefore gets a different polarization, and a part of if can passes the polarizing beamsplitter on the way back and seeds the laser diode[3].

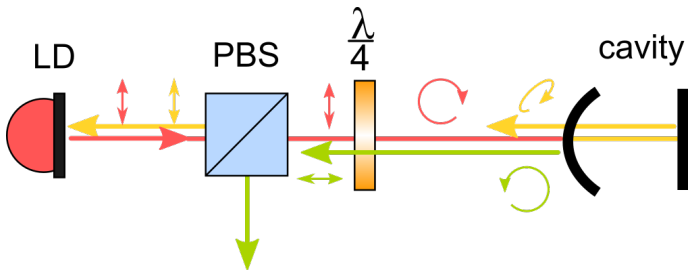

Figure 3.3.1.: Scheme of cavity feedback into the laser diode (LD): Broadband linear polarized light leaves the laser diode (red). The direct reflection (green) from the first cavity mirror gets filtered out by the combination of waveplate ($\lambda/4$) and polarizing beam splitter (PBS). Only light entering the cavity (yellow) exhibits unspecified polarization changes and part of this light gets passed into the laser diode for feedback.

3.3.3. Experimental results

This this scheme was realized using a anti-reflection coated broadband laser gain chip manufactured by *Eagleyard photonics* with tuning range from 780 to 850nm[4].

In the spectrum in Fig. 3.3.2a, we see indeed that it runs single mode and changing the cavity length proves that the wavelength is indeed set by the cavity length. However, this is only given as long as a fundamental cavity resonance is in the wavelength range of the gain profile. In other cases it either does not lase, lases on a wavelength set by a higher order transverse cavity

[3] The polarizing beamsplitter is not even needed, as the light from the laser diode is highly linear polarized ($\gtrsim 99\%$). The orthogonal direct reflected light leads to a polarization mismatch and it can not contribute to stimulated emission inside the laser diode.

[4] named *EYP-RWE-0840-06010-1500-SOT02-0000*

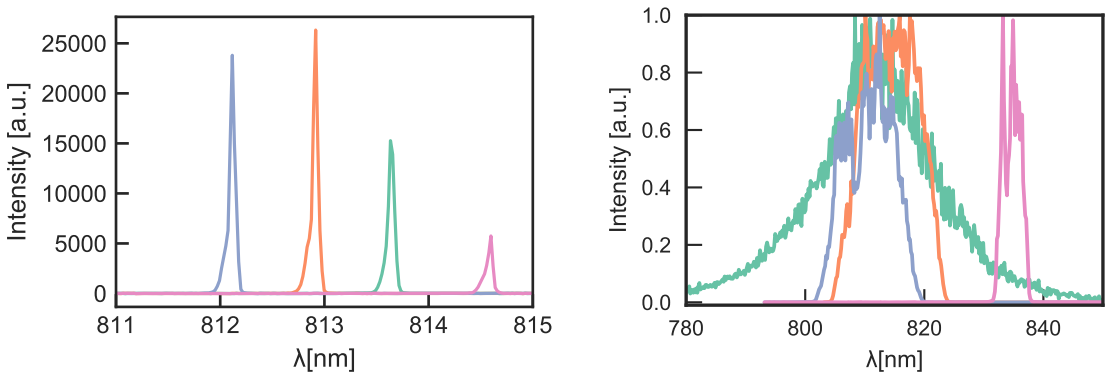

(a) **(b)**

Figure 3.3.2.: (a) Spectrum of the laser at different cavity lengths. Measured in front of the cavity by using a beamsplitter. The linewidth is limited by the spectrometer resolution. (b) Laser diode spectrum when operated without feedback (green). Tuning range when operated with feedback from the cavity (other lines). This was recorded by sweeping the cavity length and integrating the cavity transmission.

mode or on wavelength defined by a parasitic reflection. As the wavelength is only set by the cavity, no temperature controller for the laser diode is needed.

In Fig. 3.3.2b the integrated tuning range that is accessible can be seen. For this measurement, the cavity length was swept and all wavelengths were integrated on a spectrometer. Its width is mostly limited by chromaticity of the fibre coupling. Different tuning ranges can be accessed by changing the fibre coupling and are shown in different colours. The laser can be tuned continuously for $20\,\mathrm{nm}$. The feedback is very sensitive to the polarization state sent to the cavity, in order to filter out the direct reflection. As the cavity is fibre coupled with a non-polarization maintaining fibre, bends of the fibre lead to small polarization changes. In order to compensate this, an additional $\lambda/2$ waveplate is introduced and both waveplates need to be aligned precisely for broadband feedback and lasing to occur.

In Fig. 3.3.3a, the cavity transmission on a photodiode recorded with an oscilloscope is shown. The cavity length is tuned linearly and changing the lasing wavelength. The horizontal time axis has been converted to show the resonance wavelength, calibrated using spectrometer measurements. Fast modulations of the transmission amplitude by more than 50% can be seen. They originate from interference in parasitic resonators, that modulate the laser feedback under wavelength change. The period of these modulations, $\Delta\lambda_{\mathrm{par}}$, is related to the parasitic resonator length via $\Delta\lambda_{\mathrm{par}} = \lambda^2/(2d_{\mathrm{par}})$, see Appendix B.4.11. In Fig. 3.3.3b, the Fourier transform of the modulations is shown, converted to the corresponding parasitic resonator lengths. The main contribution stems from resonators of about $6\,\mathrm{mm}$ length. Most likely, this are reflections inside the laser diode (1500μm physical length and refractive index of about 3.6).

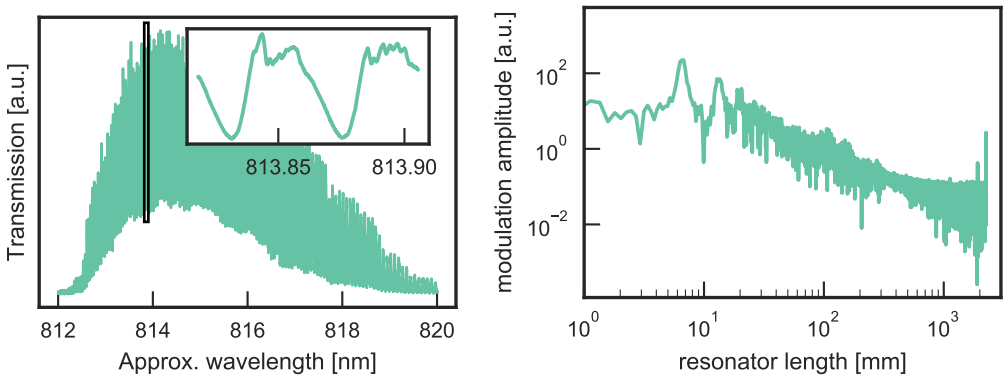

Figure 3.3.3.: (a) Cavity transmission using the optical feedback laser under length change. Recorded with a photodiode on an oscilloscope. The time axis has been converted to the laser resonance wavelength. The inset is a zoomed in view to the part marked by the black box. (b) Fourier transform of the central region in (a) and converted to parasitic resonators lengths contributing to the observed modulations.

3.3.4. Discussion

It was shown that the (unknown) change of polarization of the light inside the cavity can be used to separate it from the light directly reflected at the entry mirror of the cavity using the proposed polarization-based isolation scheme. Using an AR-coated laser diode, a $20\,\mathrm{nm}$ wide tunable laser was synchronized with to the cavity resonance with simple optical feedback. The laser indeed runs single mode when the cavity resonance is inside the gain bandwidth of the laser. The line-width of the laser was determined to be less than $2\,\mathrm{pm}$, limited by the detection resolution.

A downside was the appearance of strong modulation when tuning the wavelength. This is most likely a result of multiple competing resonators which show constructive and destructive interference with each other for different wavelengths. One resonator is the micro-cavity itself, that sets the lasing wavelength. The dominant parasitic resonator seems to be given by the laser diode, although its end facet is anti-reflection coated.

Another downside of this scheme is that achieving high powers and maximum tuning range needed careful optimization of the polarization state. This also points to a general downside of the isolation scheme: polarization of the laser can not be chosen arbitrary.

However, the strongly enhanced excitation using the double resonant scheme can be used to measure weak Raman transitions, as will be presented in Section 4.2.

3.4. Stable mechanical scanning setup

In this section a stable mechanical platform for the microscope is presented, suited for fast absorption measurements, Raman spectroscopy and quantum optics experiments.

3.4.1. Problem

The first incarnations of scanning cavity microscopes were based on off-the-shelf nano-positioning stages to control cavity length and transversal position[43, 25, 30, 29]. With this already interesting experiments could be conducted[30, 29, 31, 62, 24, 25]. However, for several reasons a more mechanically optimized, custom designed setup might be interesting to advancement the technique. First, it turned out that the stability of the cavity length needed to be improved for a high finesse cavity to stay resonant with a narrow linewidth quantum emitter for longer periods of time. Second, for embedding the setup into a closed-cycle cryostat, a small-scale, low temperature compatible and stable setup was needed. Third, potential adoption of the technique as a general (maybe commercial) tool beyond proof of principle demonstrations would significantly benefit from more stable and faster scannable cavities, for faster data acquisition rates, ease of use and lower priced components. To fulfil these needs, a more integrated approach is developed here, where all components are specially adapted to the task and to each.

A first prototype of a stiff mechanical setup, that did not yet provide transversal scanning (as needed for microscopy), was characterised and improved during the bachelor thesis of Frederik Bopp. It demonstrated that passive sub-picometre stability for a fibre plus-planar-mirror-setup is possible and first insights to the influence of electronic noise, environment, and acoustic isolation were gained. The next step was to extend this to a full scannable microscopy setup and to determine if under this circumstances a stability on this length scale is still possible.

3.4.2. Mechanical requirements

Ultra-stable, cryogenic compatible scanning probe setups have been developed for atomic force microscopy (AFM)[67] and scanning tunnelling microscopy (STM)[68]. This can be used as a source of inspiration, however, this setup differs significantly in its mechanical requirements.

The challenge, in contrast to other scanning probe setups, is mainly because of two reasons:

1. The length stability requirements (on the axis of the cavity length, perpendicular to the scan axes) are more stringent. If one would like to be able to stay in the maximum of an resonance of the cavity (FWHM linewidth under length change is $9\,\mathrm{pm}$ with finesse $\mathcal{F} = 5 \times 10^4$ at $900\,\mathrm{nm}$), a sub picometre distance stability between fibre tip and sample mirror is needed. This is orders of magnitude smaller than needed for AFM and still slightly smaller than for STM.
2. A longer transversal scanning range across the sample is required. In AFM or STM the resolution is on the order of nanometres, making scans across a micrometer sufficient to resolve structures of interest. The scanning cavity setup's resolution however is on the order of a micrometer (see Appendix A.3), around the diffraction limit of light[25]. Therefore, a scan area the order of 100µm would be desired, in order to image structures and record meaningful pictures comparable to conventional confocal or wide-field microscopy. A repeatable position below the 1µm resolution of the microscope is desired in the transversal axis to address specific point.

These design goals somehow contradict each other: longer scan ranges usually come with lower mechanical resonance frequencies and therefore higher instability. This can be seen in a review article, comparing dozens of different piezo-based scanners, together with their scanning range and first resonance frequency[67]. However, the requirements are needed on different axis on the system and therefore a properly adopted integrated approach can meet these requirements.

Further requirements on the wish-list for a powerful cavity-based microscopy setup and a quantum optics platform are:

- For certain measurement modes a long cavity length range should be accessible in a continuous scan. For example, to access different longitudinal mode orders to make different laser wavelengths simultaneously resonant with the cavity. To access a few mode orders, each separated by $\lambda/2$, several micrometre continuous longitudinal scanning range are needed.
- As the setup should be compatible with mounting into a cryostat, where the scan range of piezo elements is greatly reduced by up to a factor of approximately 5-10 at 4 Kelvin[69], a mechanism to mechanically amplify the piezo motion is needed. The need for mechanical amplification of piezo elements can be calculated with a coarse approximation: In their maximum rated operating voltage range common commercial stacked piezo elements can extend about 1.5µm per mm of their length. To achieve a 100µm scanning range, 67mm long piezo stacks would be needed at room temperature. At $4\,\mathrm{K}$, the length of the needed piezo element would exceed the dimension of our cryostat chamber (sized approximately 60x60x100mm) .
- The movement along all axes should be reproducible, in cavity length axis to a few nanometres, and in the transversal scan axes to micrometer.
- Low drifts, e.g. due to temperature changes, are desired in order to stay in a cavity length regime that is accessible with continuous piezo tuning.
- To record fast scans with a hundreds of lines per second, the resonance of the parts controlling the transversal movement should be well above a kHz.

3.4.3. Performance of previous setup

The first cavity setup used commercial *ECS3030* nano-positioners by *attocube*. Three of these piezo slip-stick positioners were combined to have two-axis lateral movement and cavity length control. With this, long range positioning across $20\,\mathrm{mm}$ on all axes is possible. The positioners offer fast optical encoder based readout with an integrated FPGA based controller and a fast 'closed loop' mode where the readout feedback is used to move to a absolutely specified positions. The controller offers excellent speed of readout and control from the computer (not seen in other positioning products) with 1000's of commands fed and read out from the controller per second. Fast positioning was possible in earlier charges of the product, as the used positioners, with settling times of about 0.1s [5]

[5] However later models only have a 10 times slower settling time as experienced with other research groups.

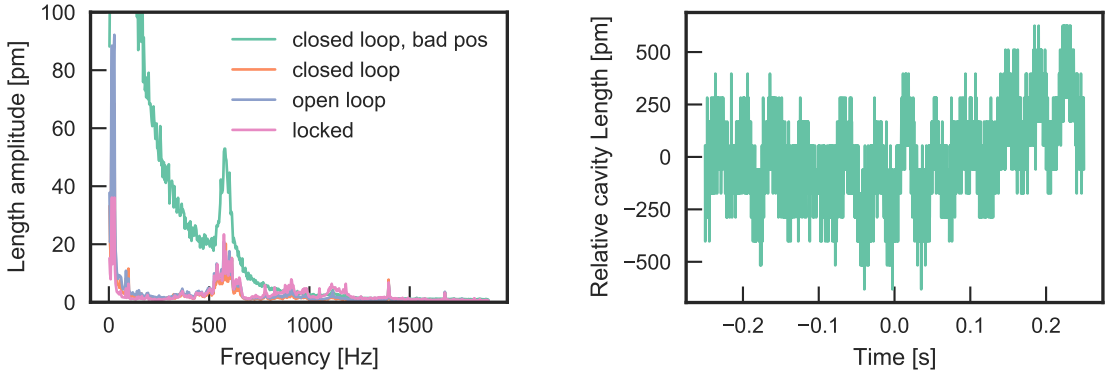

(a) **(b)**

Figure 3.4.1.: Stability measurement on the old cavity setup. (a) Spectral analysis of the cavity length fluctuations. Plotted are the spectra for attocube positioner in closed loop mode at a bad position, where electronic oscillations appear. The open loop (positioning deactivated) and closed loop at a working position mode show the same result. Another line shows the performance with a fast side-of-fringe lock. (b) Time resolved relative length fluctuations in open loop mode.

Cavity length fluctuations. To find out how good these positioners are suited for length-critical cavity operation we measured the fluctuations of the cavity length. For this we used the fringes of the transmission of a laser in a fairly transmissive part of the spectrum ($\mathcal{F} \ll 10$). The transmission was recorded on a photodiode and the slope of the side of a fringe converted to a length change to convert voltage levels to position readout, see Fig. 3.4.1b. By recording the Fourier transform (FFT) of the transmission on an oscilloscope, resonances and stability of the setup were be measured.

In the beginning, control loop oscillations of a few nm at certain positions were discovered, if the positioner was in closed loop mode. When the length was commanded to multiple of 10nm these oscillations disappeared and stability improved to $210\,\mathrm{pm}$ RMS. Therefore it is assumed that these oscillations are caused by the digital electronics of the control loop. This was either an error in the software or a method to dither the cavity length beyond the digital resolution of some of the components. The problem was not yet known to the manufacturer. Seemingly nobody measured that exact before or needed that stability. Next, closed loop operation was turned off and then the piezo elements inside the positioners were grounded,which, however, did not improve the performance. Therefore, the remaining noise can be attributed to mechanically caused vibrations. In the FFT spectra shown in Fig. 3.4.1a low frequency noise and drifts and a clear resonance at 500Hz can be identified.

With the help of a $42\,\mathrm{kHz}$bandwidth digital lock[6] (see.Section 3.5.2) the cavity length was stabilized. In a quiet surrounding the best stability achieved was $120\,\mathrm{pm}$ RMS.

Repeatability and drifts. Next, coarse long term stability and position reproducibility is analysed. To measure large length fluctuations, a different method to measure the cavity length is needed. A spectrally broader light source is coupled into the cavity and the cavity length is derived from the wavelength of the transmission peaks determined by a spectrometer.

[6] modified *nPoint LC.400* 20bit, $42\,\mathrm{kHz}$ bandwidth digital piezo controller and amplifier, -30 to $150\,\mathrm{V}$

A superluminiscent diode (SLED) with 20nm FWHM broad Gaussian shaped emission is used. The highest resolving grating (1200 lines per mm) achieves a spectral resolution of about 0.02nm. As the cavity length drifts, this translates to a shift of the resonances reduced by the longitudinal mode order, cf. Eq. (A.2.16). At the used cavity length of about 20µm a transmission wavelength shift of 0.02nm at 780nm corresponds to a length change of about 1nm.

The positioner was set to closed loop mode where it actively regulates the position using its internal optical readout.

Measuring the length change of the setup for several minutes, average thermal drifts of about 100pm/s with extreme parts up to 300pm/s can be observed, see Fig. 3.4.2a. Furthermore, the cross coupling between lateral movement and cavity length axis is measured, i.e. how steps in the lateral direction change the cavity length. To this end, 4µm long steps forth and back were repeated while the cavity length was monitored. As can be seen in Fig. 3.4.2b, each step induces short time length oscillation spikes of about 40nm and permanent length changes between 5 and 15nm. Finally, the position reliability under external shock is tested by knocking on the table. Most of the time the cavity settles in the same position (<5nm), but in certain cases can deviate as much as 30nm after impact, c.f. Fig. 3.4.2c. In conclusion, the position readout of the positioner and the actual cavity length only agree below 50nm for short time scales (minutes) and few position changes (below ≈ 5).

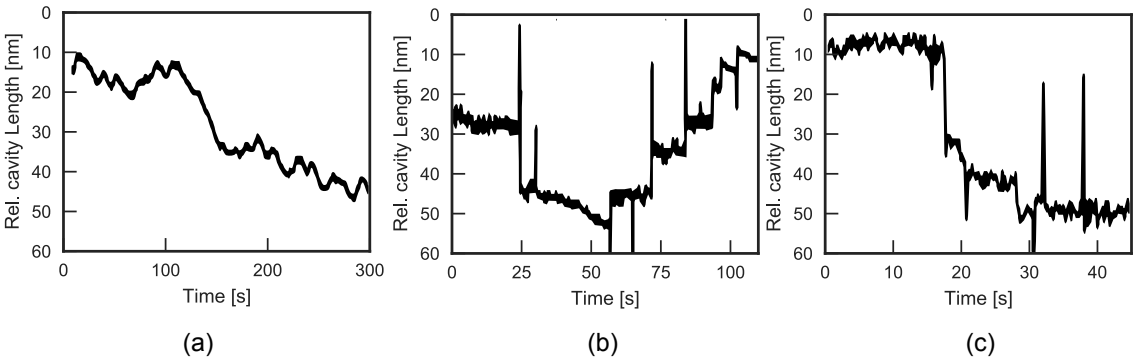

Figure 3.4.2.: Old setup cavity length stability: (a) drifts over several minutes. (b) cross coupling between axes: length change when making 4µm long transversal steps forth and back. (c) length change when knocking onto the optical table repeatedly. The cavity length is given relative to an arbitrary point.

3.4.4. Design choices to increase cavity stability

To reduce length fluctuations below the picometre level, for an orders of magnitude more stable scanning cavity setup, a lot of significant improvements are needed. Instead of focussing on the actual implementation of the setup, the design principles that lead to the mechanical design are discussed here.

Overview. For positioning, piezo elements will be used for all axes, as combined with flexures, they provide precise, continuous and repeatable positioning. Additionally, coarse positioning

of the cavity length and the mirror is enabled with motors. All elements are assembled around a solid metal base block.

High first resonance frequency. In Fig. 3.4.3a, the spectrum of the acoustic background noise in the laboratory is shown, recorded using the integrated microphone of a laptop computer. It may not be representative at very low frequencies below 50Hz due to limitations of microphone but the general picture gets evident: the acoustic noise power decreases significantly to higher frequency. This means that a system with higher resonance frequencies will pick up considerably less acoustic noise, as low frequency vibrations do not resonate with the system. As can be seen later on, the mechanical noise of the cavity length fluctuations is dominated by acoustic noise together with electronic noise coupled into the positioning piezo elements.

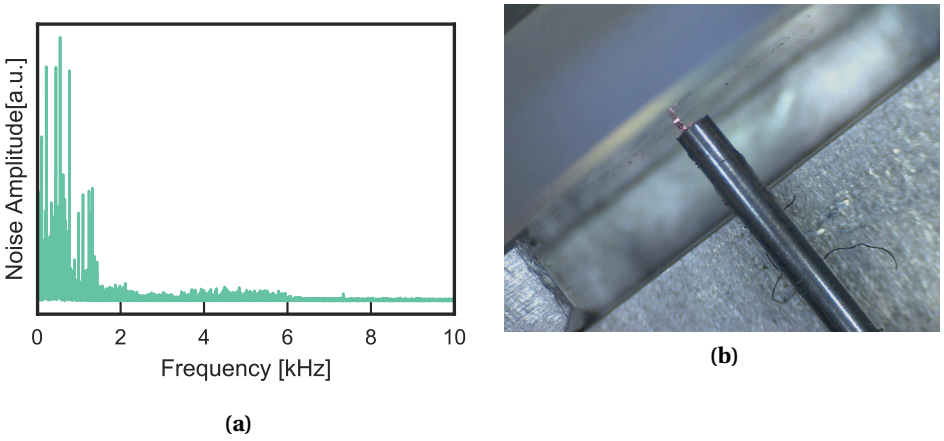

Figure 3.4.3.: (a) Ambient acoustic noise spectrum in the laboratory. (b) Fibre, glued into a needle, facing the planar mirror. In-coupled light glowing red.

The fundamental resonance frequency is also presumable an upper limit for the bandwidth of an active stabilization of the cavity length, using a feedback loop. A resonator driven above the resonance exhibits a phase delay of up to π and therefore length fluctuations may be enhanced instead of suppressed if a too high feedback bandwidth is used.

Choice of material. Choice of a stiff but light material increases resonance frequencies[7]. When simulating the system with a mechanical finite element solver (FEM) approximately the same resonance frequencies for Aluminium, Titanium and stainless steel were obtained because of their similar density to elastic module ratio, see table Table 3.4.1. Aluminium was chosen for ease of machining and low price. However, a setup made of stainless steel or Titanium is less sensitive to external acoustic and arbitrary forces due to higher stiffness. These materials also reduce thermal drifts due to their smaller thermal expansion coefficients, and especially since they are better matched to the used piezo elements' expansion coefficients.

[7] As the resonance frequency of a mass m on a spring with a spring constant k scales as $\propto \sqrt{\frac{k}{m}}$
[8] from *PI Ceramic*
[9] *PI P-882* from *PI Ceramic*

	Density [g/cm^2]	elastic module [GPa]	coefficient of thermal expansion [ppm/K]
Aluminium	2.8	70	23
Titanium (Ti-6Al-4V alloy)	4.43	110	9.0
Stainless steel (common)	7.85	210	12...17
Piezo PZT (common)[8]	7.8		-4...-6
Piezo stack[9][70]			+7

Table 3.4.1.: Potential materials for the setup and their properties. Coefficient of thermal expansion given around room temperature.[65, 71, 72]

Miniaturization. As detailed in Appendix Appendix A.6, making the setup smaller (characterized by length L) can significantly increase resonance frequencies ($\propto L^{-1}$) decrease acoustic vibration in-coupling ($\propto L$) and displacement under acceleration ($\propto L^2$) and thermal drifts ($\propto L$).

Additional design principles. Furthermore, the following principles where followed to maximize stability:

- Stiffen to raise resonant frequency and remove displacement per applied force.
- Minimize mass for higher resonance frequency.
- Use of passive vibration isolation to reduce in-coupling of vibrations. If a light setup is built, decoupling from the environment can be achieved by simple means, e.g. with an elastomer or foam support. PTFE (Teflon) can be used to damp high frequencies at low temperatures.
- Gluing the cavity fibre into a needle to increase stiffness and reduce vibrations there, shown in Fig. 3.4.3b.
- Simulation using finite element analysis (FEM) allows reliable rapid optimization of structures with regard to mechanical resonance frequencies and vibration mode shape.
- An optimized structure to reduce the *amplitude* of the cavity length fluctuations, especially at the lowest frequency mechanical modes.
- Use flexures as they allow fast, continuous, and repeatable tuning in length and transversally without stiction and friction. Together with piezo elements this enables continuous control on the picometre level.
- Use parallel kinematics, instead of serial kinematics (e.g. no stacking of positioners on top of each other), to reduce amplitudes and maximize resonance frequencies.

3.4.5. Implementation

In Fig. 3.4.4 a schematic of the mechanical setup is shown. The cavity fibre mirror is glued into a syringe needle, which is attached to a lever. This part is used for fine positioning the fibre and continuous scanning of the cavity length and transversal position. The lever can be flexed to change the cavity length ("z"-direction) and move in one direction parallel to the mirror ("y") by piezo elements. The third axis ("x") is positioned using a piezo element flexing the needle with the fibre. A screw serially attached to this piezo element can change the angle

of the fibre coarsely, in order to bring the cavity mirrors into parallel alignment. The cavity length can be set coarsely by a screw serially attached to the piezo changing the cavity length. Extreme precise and faster regulation of the cavity length on a sub pm length scale can be achieved using an additional shorter stroke piezo.

The plane cavity mirror can be positioned coarsely in x and y direction to scan different regions on the sample.

First rough prototypes were self-made using the milling machine while later improved design iterations were produced by the university's machine shop staff.

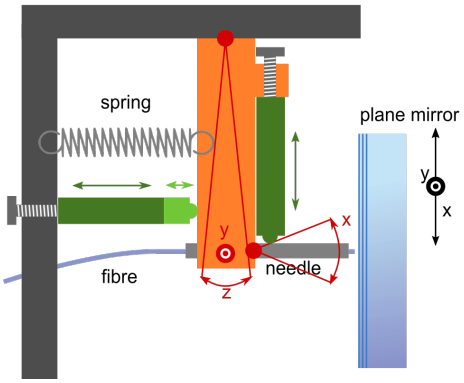

Figure 3.4.4.: Schematic of the mechanical setup. Stack piezos (dark green) position a lever (orange) and the cavity fibre (blue) inside the syringe needle (light grey) to move the cavity fibre in x,y,z direction. The plane mirror can be positioned coarsely in x and y direction. Screws can be used to change the cavity length and the cavity fibre angle coarsely. Red dots depict the pivot point of the rotational motion for positioning in x and z direction. The piezo for positioning the lever in y direction is not shown but pushes the lever upwards (out of the plane in the drawing, shown by the arrow next to the red "y"). The spring pushed the lever back against the length changing piezos. The additional shorter stroke piezo (light green) is used for extreme precise positioning of the cavity length.

3.4.6. Continuous modifications and analysis

To create an actively and passively stable setup, many design iterations were undertaken. The resulting final setup itself was then again optimized with changes to electronics, lock feedback parameters, mechanical decoupling, cabling, springs, laser power, environment (air-condition, noise), and acoustic isolation.

After each modification, to determine its impact, the passive stability of the setup and a vibration frequency spectrum was measured. As this was of crucial importance and repeated many times, a computer program to continuously measure and calculate the fully calibrated length fluctuations was developed. To check reproducibility, measurements were repeated and averaged, and several steps were reverted.

Length fluctuation measurement

For a high bandwidth measurement of cavity length fluctuations down to the femtometre level, the transmission of the cavity on the slope of a narrow transmission resonance, T_{cav}, can be used[35]. Assuming a Lorentzian transmission resonance, see. **??** and shown in Fig. 3.4.5a, the

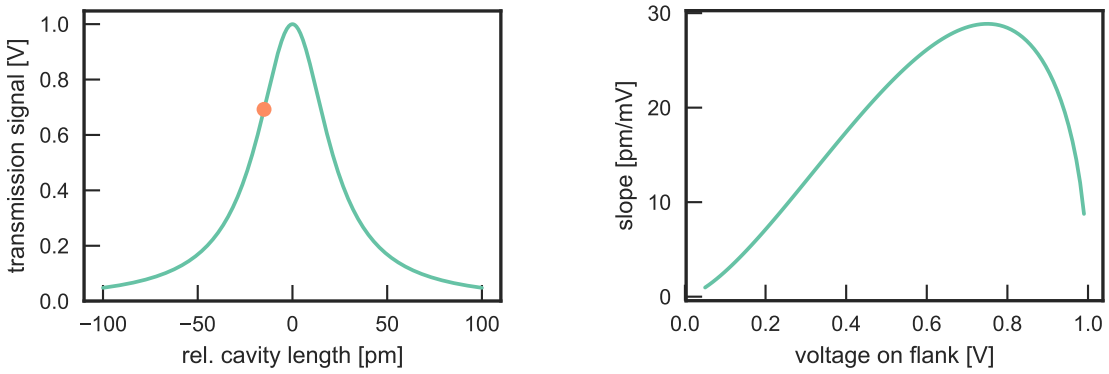

(a) **(b)**

Figure 3.4.5.: (a) Calculated cavity transmission under length change for $\mathcal{F} = 10000$, $\lambda = 900\,\mathrm{nm}$ and maximum transmission photodiode signal $1\,\mathrm{V}$. (b) Conversion factor at different voltage levels.

transmission signal can be converted to a position. Inverting the Lorentzian line shape on one of its sides, the slope can be extracted

$$\frac{dx}{dT_\mathrm{c}}(T_\mathrm{c}) = \delta d \left(\frac{T_\mathrm{c,res}}{T_\mathrm{c}} - 1\right)^{-1/2} \frac{T_\mathrm{c,res}}{T_\mathrm{c}^2}\,, \tag{3.4.1}$$

to convert transmission fluctuations to cavity length fluctuations. Here, δd is the FWHM linewidth under length change (see Appendix A.2) measured via the finesse, $\mathcal{F} = \frac{\lambda/2}{\delta d}$. Also, the (maximum) cavity transmission on resonance, $T_\mathrm{c,res}$, must be measured once.

In Fig. 3.4.5a a theoretical transmission signal under cavity length change is shown. In Fig. 3.4.5b the extracted factor for converting the measured voltage changes to position changes is calculated. For small length fluctuations this conversion can be approximated to be linear. It works best at about 75% of the peak height where the curvature of the Lorentzian is zero.

Note that for length fluctuations larger than the peak width, the position fluctuation spectrum is not linear to the voltage fluctuations and unphysical higher order frequencies may appear with this simple conversion.

To keep the system at the slope of the resonance during measurements, a slow digital feedback loop to a piezo is used to compensate length drifts. This is only possible if the system is already from the beginning stable enough, otherwise fast feedback loops or lasers at lower finesse wavelengths have to be used[35]. However, since the passive stability of the setup is of interest, to further diagnose and optimize the internal mechanical resonances, the lock should not distort the measurement. Therefore, the feedback output is low pass filtered above $10\,\mathrm{Hz}$, see Section 3.5.2 for details.

Impact of modifications

Here, the modifications of the setup and their impact on the stability are discussed. A more practical and detailed guide to measure, and improve cavity stability can be found in Appendix B.4.12.

First, ground loops were eliminated by separating grounds of the piezo elements from other grounds, twisting cables leading to the piezos, disconnecting unneeded piezos and low-pass filtering if possible, as well as using isolated and low-noise electronics to set the cavity length (*SRS DS345* function generator). Furthermore, the setup is isolated from the table using an $2\,\mathrm{mm}$ elastomer sheet. With these preparations, excursions were lower than the cavity linewidth and noise spectra could be measured. The integrated position noise was $\sigma_d = 2.5\,\mathrm{pm}$ RMS (root mean square).For increased sensitivity, the measurements were performed at a finesse of 2×10^4. However, even here the detection noise still contributes significantly, as will be detailed later on.

In Fig. 3.4.6a the strength of length fluctuations are shown while different parameters of the setup are changed. The following modifications increased the stability significantly:

- First, the function generator was disconnected from a long piezo stack, used to sweep over long cavity lengths, that extends $0.15\,\mu m/V$. This reduced vibrations stemming from electronic noise significantly, and total vibrations were below$2\,\mathrm{pm}$ (modification labelled as "no long piezo" in Fig. 3.4.6a).
- Multiple modifications of the spring that pushes the lever against the piezo elements lead to strong decreases. The spring was tightened and later on changed to a even stiffer Teflon spring ("new spring", "tighter spring" and "teflon spring").
- A lot of effort was put into modifying and fixing cables, that lead to the piezo elements ("fix cables") . As the cables are attaching to the movable part of the cavity via the piezos, their vibrations strongly affect the cavity length. When fixing them onto the setup's base block, especially noise below $100\,\mathrm{Hz}$ improves, because their low eigen-frequency vibrations are inhibited.
- That cavity length fluctuations are then dominated by acoustic in-coupling via air can be seen a by adding a housing for acoustic isolation ("acoustic isol.") that improves noise levels by almost a factor of two. Furthermore, the low frequency sound of the air-conditioning affects the stability slightly ("a/c off").
- A factor of three in stability can be gained by increasing laser power and profiting from photothermal self locking of the cavity[35] ("inc. laser"). Before this, at lower power levels, the laser did not strongly contribute to stabilization of the cavity, as can be seen when the length fluctuations where measured on the opposite slopes, where effects by the laser would destabilize the cavity instead of stabilizing it ("other flank").

Remarkable insight can be gained, by plotting the vibration spectra of each measurement as a *spectrogram* shown in Fig. 3.4.7. There, trends become visible, hard to spot when comparing individual spectra. We see that, by reattaching cables and piezos behind the length-changing lever, resonance frequencies change drastically and a split resonance becomes degenerate, reducing length fluctuations significantly. This is surprisingly an almost continuous trend across each improvement to the cabling or piezos. The changes to the setup shown in Fig. 3.4.7 were carried out during three days.

Final vibration spectrum. In Fig. 3.4.8a the final vibration spectrum is shown. Most of the vibrations are low frequency $< 100\,\mathrm{Hz}$, with more peaks around $6\,\mathrm{kHz}$. Above this frequencies

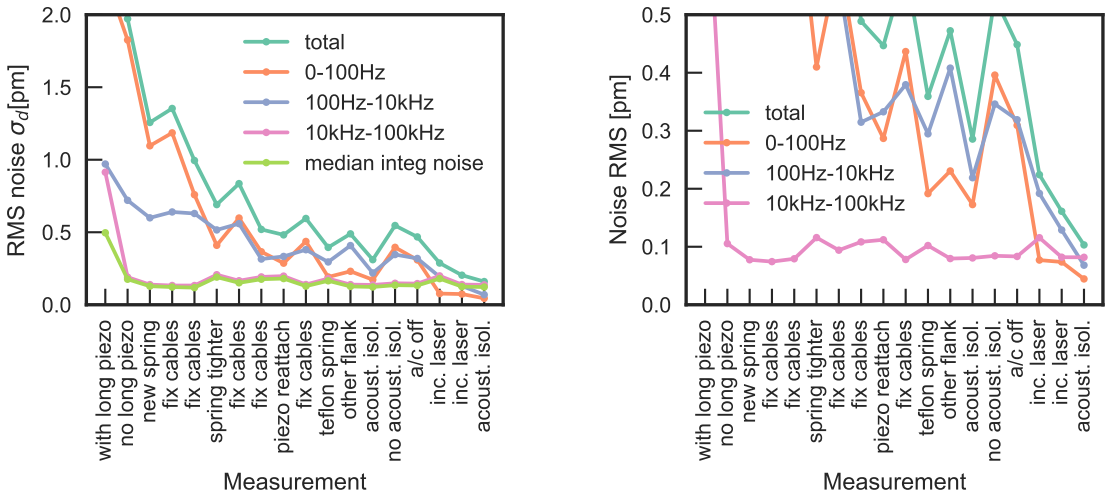

Figure 3.4.6.: (a) RMS (root means square) vibration noise level, σ_d in different frequency regions and the total noise up to 100 kHz, across different iterations of the setup. A short title of each modification is shown on the horizontal axis. (b) The same but with background (detection) noise subtracted.

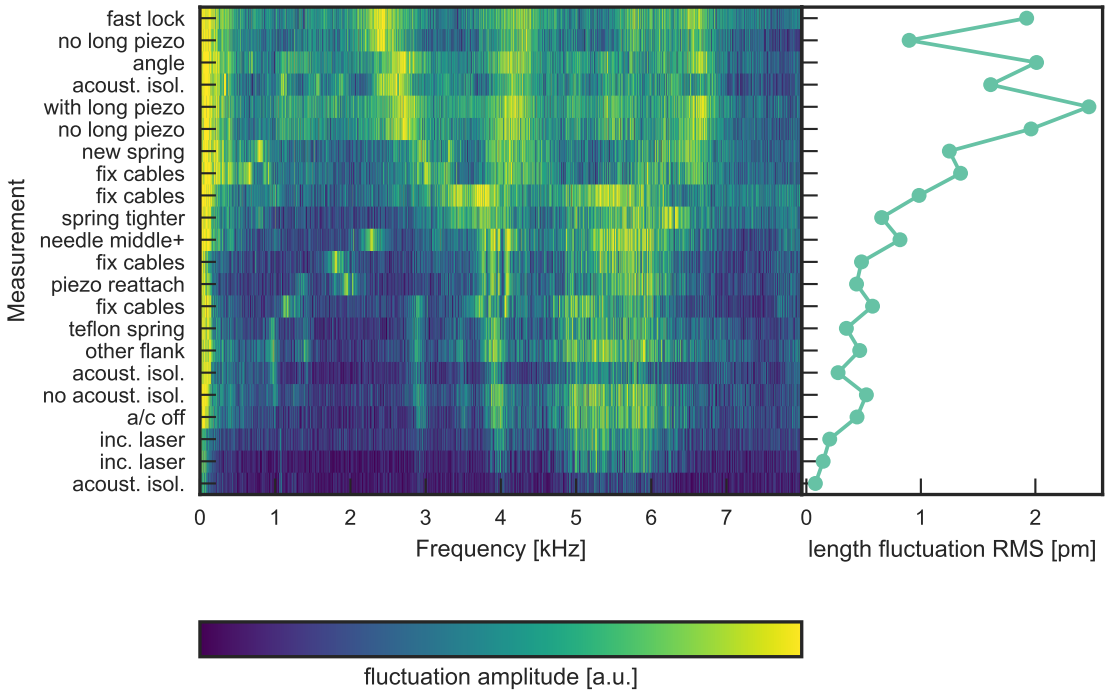

Figure 3.4.7.: Vibration spectrum visualized across modifications of the setup (a 'spectrogram'). On the right side the corresponding total length fluctuations are shown.

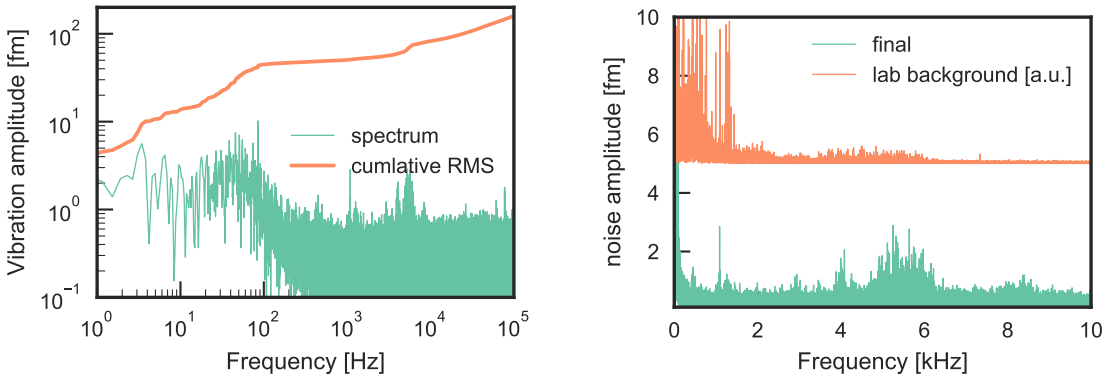

(a) **(b)**

Figure 3.4.8.: (a) Final vibration spectrum and cumulative RMS noise (integrated until this frequency). (b) Final spectrum, along with lab noise background (amplitude in arbitrary units and shifted upwards for better visibility), as measured for Fig. 3.4.3a.

no important frequencies contribute and mostly broad background contributes to increased fluctuations, as can be seen in the smooth increase of the cumulative RMS noise. Therefore, it is assumed that this is mostly background originating from white noise of the photo diode length detection. Taking the median of the spectrum as a coarse approximation of the background level and integrating this over the spectrum yields a background noise of $122\,\mathrm{fm}$. This method is used to subtract the background noise in the measurements in Fig. 3.4.6b.

In Fig. 3.4.8b, the final spectrum is shown, along with the measurement of the lab background sound is shown. Low frequency vibrations are present but suppressed compared to the lab noise background. The broad background noise between $4\,\mathrm{kHz}$ and $6\,\mathrm{kHz}$ can be identified in the setup vibrations, with a resonant enhancement at $4\,\mathrm{kHz}$. However, the first strong resonance seems to be at around $8\,\mathrm{kHz}$, visible in the vibration spectrum although no background noise is visible.

Simulation. The mechanical setup was designed using CAD (computer aided design) software[10]. The built-in FEM (finite element method) mechanical solver was used to simulate the mechanical vibration normal modes with their frequencies and relative amplitude distribution. This allows for rapid optimization without production of a physical prototype in the machine shop. The design was carefully improved in multiple iterations to yield higher resonance frequencies. Furthermore, a focus was to reduce oscillation amplitudes of these normal modes at the location of the cavity fibre and in the direction of the optical axis of the cavity.

The simulation tool was also used to appropriately design the flexures that position the fibres. The flexures have to be strong enough to not break under repetitive load, have high resonance frequencies to offer fast positioning and be stiff enough to not get excited by acoustic noise. On the other hand they need be weak enough to be moved by piezo elements, where the blocking force is limited to approx. $300\,\mathrm{N}$. The flexures also need to be a lever, in order to amplify the small motion of the piezos by about a factor of 5-10 to be able to position the fibre over about

[10] Autodesk Inventor

100 µm, especially when considering reduced piezo displacement at cryogenic temperatures.

3.4.7. Stability and scan range

Stability

With slow drift compensation (< 10 Hz bandwidth), the setup yielded a passive stability of 300 fm. With additional weak photothermal stabilization through the laser this reduces to 160 fm. Omitting lower frequency components < 150 Hz), that can be easily locked away with low effort this reduces further to below 150 fm without and 60 fm with photothermal stabilization.

Comparison to other setups. How does the stability compare to other fibre cavity setups? The old stock attocube positioner based setup achieved a passive stability of 210 pm RMS and 120 pm when using a fast lock with a bandwidth $>$ kHz. Matthias Mader from our group reported passive stability of 150 pm for a large scale setup, where the mirrors of the cavity are held by arms spanning more than 200 mm and a 200 Hz bandwidth lock.

Other experiments report numbers for setups that are not transversally scannable but only in the direction of the cavity length:

Gallego et al. showed a short-term stability of 0.24 pm for a simple piezo-acutuated, 93.3 µm long fibre-fibre cavity stabilized with a Pound-Drever-Hall (PDH) -lock with 3 kHz bandwidth[52]. In addition, they presented a cavity glued into a single block that can only be temperature-tuned with the same stability level, however, without using an electronic feedback loop[52].

Brachmann et al. reached a stability of 110 fm for a fibre on a shear piezo and a planar mirror held by a commercial gimbal mirror mount, using a thoroughly optimized PDH lock with 1.1 kHz bandwidth together with photothermal stabilization with a bandwith of 500 kHz [35].

Using active and passive isolation platforms, an acoustic enclosure and inside the quiet environment of a bath cryostat Warburton et al. showed a passive stability of 0.5 pm[73, 74].

The key finding is that the presented setup shows similar or better stability than setups with less degrees of freedom and reduced cavity length tuning range. The addition degrees of freedom seem not to reduce the achievable stability if proper mechanical and electronic components are optimized with care. Passive stability and mechanical decoupling seems to play a major role here.

Continuous cavity length tuning. For a variety of measurements it is interesting to span multiple free spectral ranges in a continuous way. The long stack piezo was used to enable a long travel range even without using a high voltage amplifier and to have sufficient reserves when operated at low temperatures. In Fig. 3.4.9a, the cavity transmission of a single mode laser at 900 nm, using the full output range of the function generator (Stanford Research DS345). At a peak-to-peak amplitude of 20V about 4µm can be reached, corresponding to nine visible transmission peaks. The known distance of these peaks was used to calibrate the piezo voltage to a length scale, see Fig. 3.4.9b. The piezo non-linearity and hysteresis contribute to a non-linear voltage to cavity length ratio, which however can be well-approximated and

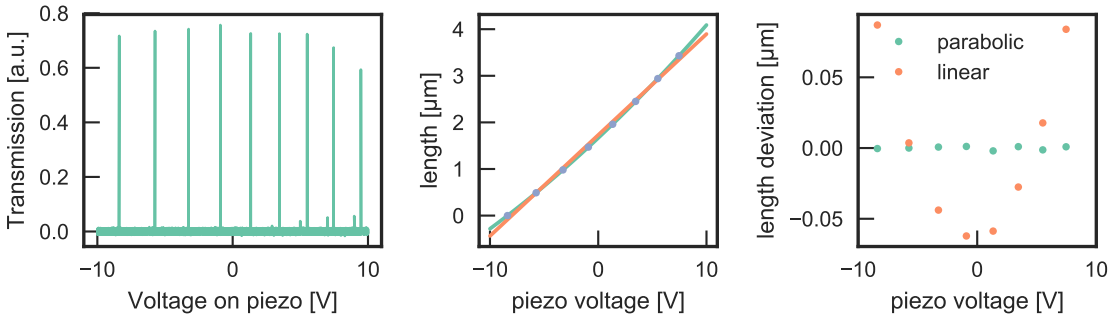

(a) **(b)** **(c)**

Figure 3.4.9.: Analysis of continuous tuning of cavity length using piezo element. (a) $900\,\mathrm{m}$-Laser transmission when a voltage ramp is applied. (b) Known transmission peak distance used to calibrate voltage to cavity length. The orange line is a linear fit while the green line is a quadratic polynomial fit. (c) Residuals of the linear and parabolic fit.

compensated with a quadratic order polynomial to a residual error below $5\,\mathrm{nm}$ across the whole scan range, see Fig. 3.4.9c.

Scannable area and speed

The downside of a custom built setup is that the positioning needs to be calibrated. One way to achieve this is by recording a cavity transmission microscopy scan and deduce the scanned area from the features recorded. The cavity mode radius is known from the mirror radius of curvature and cavity length with approximately 10% accuracy, $1.63 \pm 0.15\,\mu\mathrm{m}$. With a Gaussian fit to the features in Fig. 3.4.10 the scan range was calibrated. In the present example the scan range is $62 \times 60\,\mu\mathrm{m}^2$. This was achieved with applying a range of $70\,\mathrm{V}$ in the horizontal and $60\,\mathrm{V}$ in vertical direction to the piezos, which corresponds to piezo displacements of roughly $10\,\mu\mathrm{m}$. The maximum voltage rating for the piezos, $-20\,\mathrm{V}$ to $150\,\mathrm{V}$, could increase the scan range to more than $150 \times 160\,\mu\mathrm{m}^2$. At cryogenic temperatures, the piezos are rated for $-150\,\mathrm{V}$ to $150\,\mathrm{V}$ and a rough estimate, with assumed 5-fold reduced piezo displacement per Volt would still yield a scannable area of $50 \times 50\,\mu\mathrm{m}^2$.

A more accurate calibration can be performed either using a pattern on the mirror (written with the CO_2 laser for fibre machining) or imaging the cavity fibre position with a camera (see Fig. 5.2.1), but has not yet been performed.

Feed-forward length compensation

As the cavity position is scanned transversally across the sample, cross-coupled changes to the axis of the cavity length are inevitable. In any positioner, residual imperfections in the mechanics will translate the long transversal positional changes of up to $100\,\mu\mathrm{m}$ to the cavity length axis where under some circumstances already nm-scale length changes can be unwanted. Furthermore, the particular realization of the setup with it's parallel kinematic lever cross-couples movements between all axis. This length change can be compensated actively by measuring the cavity length at each point during a scan. However, if the length

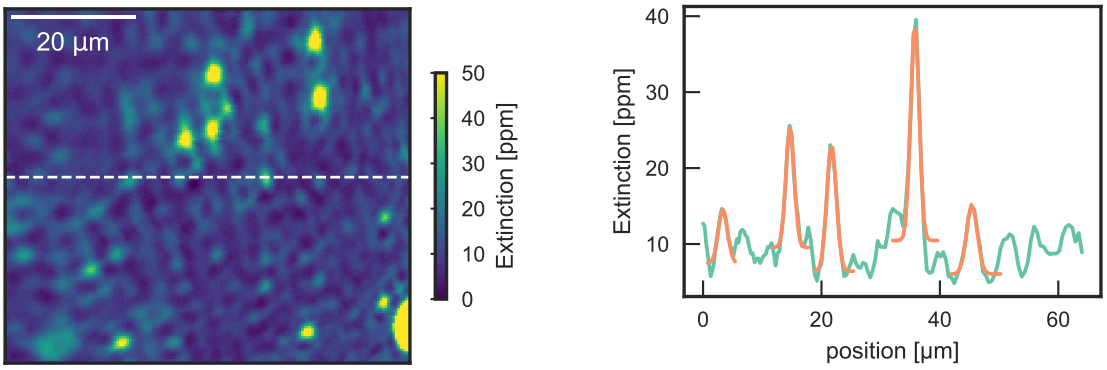

(a) **(b)**

Figure 3.4.10.: (a) Cavity extinction scan of an arbitrary sample to calibrate the scan range. (b) Cut at the dashed line in (a) with Gaussian fits to prominent features.

deviation is reproducible and can be compensated up front, one does not have to measure the cavity length precisely all the time (at a sub-nm level), which may also not be available in all measurement modes. In this so-called *feed-forward* scheme, the length change is measured and recorded only once and on subsequent scans the electronics compensate the length deviation, by expanding the length-changing piezo accordingly. In Fig. 3.4.11a the determined feed forward length correction is mapped for a large-area scan. In Fig. 3.4.11b the residual cavity length change after applying this feed-forward compensation is shown. The length change can be reduced about three orders of magnitude from more than $1.6\mu\mathrm{m}$ peak-to-peak without to $2\,\mathrm{nm}$ with compensation. The standard deviation of the residual length change is $360\,\mathrm{pm}$. The length was measured by modulating the cavity length and using a single-mode laser as a length reference. The time difference between the trigger of the sweep and when transmission was observed yields the length at each point. Iteratively, the information about the residual length differences at each point was applied to the compensation piezo until the residual length changes could not be improved any more. The scheme is so far limited by electronics, leading to ground-loops, modulating the cavity length on this length scale, and time invested in software and optimizing the measurement. As this was just a quick proof-of principle development and the residual length changes showed a reproducible pattern, single digit pm level should be in reach. With further improvement, the $16\,\mathrm{bit}$ of the digital-to-analogue converter starts to limit the compensation, corresponding to a minimal step size of $20\,\mathrm{V}/2^{16} \times 155\,\mathrm{nm/V} = 47\,\mathrm{pm}$. Combined with an active stabilization, continuously measuring the cavity length, the femtometre level might come into reach.

Drift stability

To measure cavity length drifts, the same measurement principle was applied without lateral scanning. In Fig. 3.4.12b an average drift of $10\,\mathrm{pm/s}$ with extremes up to $20\,\mathrm{pm/s}$ can be observed. These drifts are about one order of magnitude slower than in the old setup. To reduce this further, changing electronic components only had a minor impact. Hence, the main source is attributed to temperature changes leading to relative thermal expansion of the

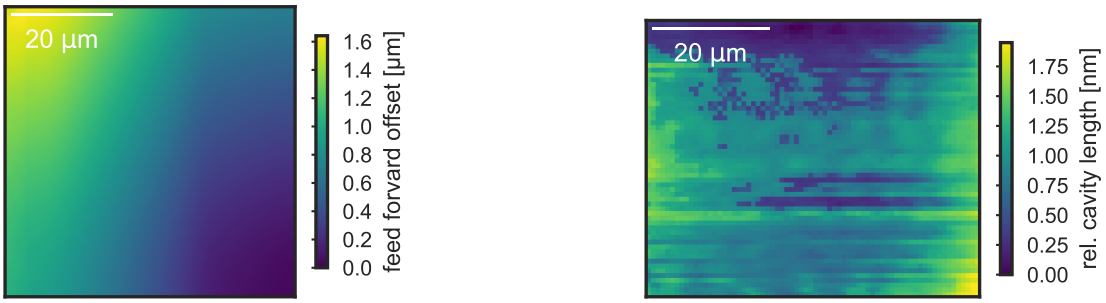

(a) **(b)**

Figure 3.4.11.: (a) Length correction applied by the cavity length offset piezo in the feed-forward scheme. (b) Residual cavity length changes. The scan is roughly $50\,\mu\mathrm{m} \times 50\,\mu\mathrm{m}$ with $500\,\mathrm{points/s}$.

components constituting the setup. [11]

Using a housing, low thermal expansion materials (see Table Table 3.4.1) or temperature stabilization could further reduce drifts.

Modulation speed

For a high transmission measurement rate in the narrow-laser measurement scheme, the cavity length has to be modulated at high frequency. Although it is well above the fundamental mechanical resonance frequencies of the setup ($\approx 5\,\mathrm{kHz}$), this can still be done with sufficient amplitude at up to$1\,\mathrm{MHz}$ when a resonance is used. In Fig. 3.4.12a, a fast modulation is shown. No glitches hinting at other excited resonances can be seen. As length drifts are about $5\,\mathrm{pm/s}$, an active length compensation feedback is necessary to keep the resonance in the centre of the modulation.

Potential improvements

The stability of the setup could be further improved with a few straightforward improvements. First, acoustic isolation and cabling could be definitely improved further, as the current make-shift solutions were just assembled in a few minutes from pieces available in the laboratory. As this were the two biggest improvements together with stronger laser power, which could also be increased, this has potential to increase passive stability. Furthermore, a faster digital or analogue cavity lock (faster then the current $< 10\,\mathrm{Hz}$ bandwidth) could severely improve active stabilisation. When operating the setup in a low vacuum, acoustic noise coupling over the air could be minimized. With all this at hand, in all three dimensions scannable cavities with stability below the fm might be in reach.

A downside of the piezo based positioning is the hysteresis of piezo elements. Although scanning a piezo in the same manner is repeatable below the nanometre level, as has been shown for example in Fig. 3.4.11a, if scan parameters change or a fixed position should be driven to, hysteresis (position depends on 'history' of previous positions) and creep (length

[11] Assuming a $20\,\mathrm{mm}$ long arm holding the opposing mirrors of the cavity and a mismatch of the materials (mostly between piezos and aluminium) of $10\,\mathrm{ppm/K}$ this corresponds to a temperature change of roughly $0.1\,\mathrm{mK/s}$, which might be a realistic figure in the lab

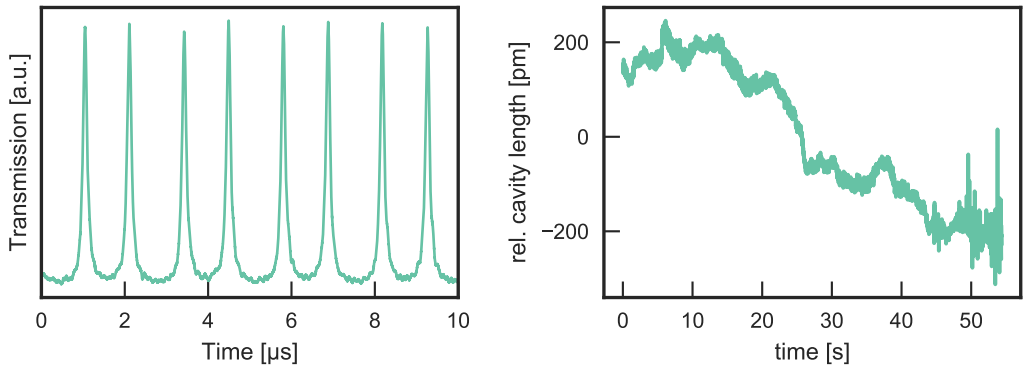

(a) **(b)**

Figure 3.4.12.: (a) Cavity length modulation with a sinusoidal voltage signal of $420\,\mathrm{kHz}$ around a cavity resonance. The cavity length change spans about $80\,\mathrm{pm}$. The linewidth of the transmission peak is about $20\,\mathrm{pm}$ (b) Exemplary cavity length drifts. The fast oscillation at the end are test with intentional induced noise: clapping, drumming on a lab-desk and knocking on the floated optical table, in this order.

changes even after a certain voltage has been applied) of the piezo play a role. Here, an active readout, a clever feed-forward algorithm or a savvy users are needed.

3.4.8. Discussion

The optimized setup yielded excellent passive stability by combining careful mechanical design to increase resonance frequency, simple passive isolation and great care taken with cabling and electronics. With slow drift compensation ($< 10\,\mathrm{Hz}$ bandwidth), the setup yielded a passive stability of $300\,\mathrm{fm}$, with additional photothermal stabilization this reduces to $160\,\mathrm{fm}$ and when looking at $> 150\,\mathrm{Hz}$ the position noise is just $60\,\mathrm{fm}$. This is over three magnitudes better then the old setup $(200\,\mathrm{pm})$. Prospected optimizations like better acoustic isolation, high bandwidth active and stronger optical self-locking, more improved cabling, improved mechanical decoupling, and stiffer materials could reduce vibrations even further, maybe even to the attometre level.

Drifts are on average smaller than $10\,\mathrm{pm/s}$ and presumable a result from thermal fluctuations, that can be further reduced by housing, active thermal stabilization or choice of better matched and low expansion materials.

The level of stability is not at the expense of flexibility or microscopy scan area and on par with monolithic setups with reduced degrees of freedom. Transversally, about 100×100µmcan be scanned, with a first proof-of-concept feed-forward length correction stabilizing the length during a scan to $360\,\mathrm{pm}$. This greatly simplifies operation as a spectroscopy tool.

3.5. Active cavity length stabilization

3.5.1. Problem

In many experiments the cavity length has to be kept constant or tuned in a controlled way. This is because the cavity length defines the resonances of the cavity and in in this way all spectral parameters like the transmission spectrum or lifetime of emitters inside. For the different spectroscopic measurements in this work, several different length stabilization schemes, or 'cavity locking' methods, have been developed.

3.5.2. Locking schemes

All feedback schemes described here use optical signals from the cavity, feed them into a digital computer based locking logic and use a piezo element to correct the cavity length.

Side of fringe Lock. To measure the cavity length stability a simple side of fringe lock at the cavity transmission of a narrow linewidth laser was developed. As the passive stability of the cavity was already good enough to keep the cavity resonance in the vicinity of the laser line on short time scales and the interest was to measure the intrinsic frequency response of the mechanical system, a slow lock ($10\,\mathrm{Hz}$ bandwidth), mainly compensating thermal drifts, was enough. A simple lock via analogue-to-digital conversion of the cavity transmission and digital-to-analogue conversion of the voltage output to a piezo was implemented using a $16\,\mathrm{bit}$ computer interface[12]. A computer program written in the python programming language was used, that could be used to quickly debug and alter locking parameters and implement complicated re-locking logic if the transmission signal was lost due to large length excursions. The lock was limited to the integrating part of a PID(proportional-integral-derivative)-controller and an analogue low-pass filter removes high frequency components from steps in the digitalization. Stability down to the femtometre scale where possible, see Section 3.4 although the $16\,\mathrm{bit}$ ($2^{16} = 65536$ steps) digitalization only provided a resolution of about $1\,\mathrm{pm}$in combination with the piezo. This was possible due to 'oversampling' the output by running the digital lock loop with $1000\,\mathrm{Hz}$, above the cut-off frequency of the filter.

Two-laser lock. This locking scheme was usedfor Raman spectroscopy and microscopy using the old setup based on commercial positioners. For spectroscopy, the cavity length has to be set and kept at a wide range of lengths, with positioning down to nm precision. Due to the bad reproducability of the old setup, exhibiting length glitches across several hundred nanometres, the cavity length had to be measured absolutely across several free spectral ranges (FSR). To determine the cavity length unambiguously, the transmission amplitude of two lasers is used. The first laser, at $790\,\mathrm{nm}$, is simultaneously used for Raman excitation, while the second auxiliary laser was at $690\,\mathrm{nm}$. As both are in the transparent region of the coating, they exhibit only broad interferometer-like modulations when the cavity length is swept, see Fig. 3.5.1. First, the transmission as a function of cavity length is measured by ramping a piezo. Subsequently, for locking, the transmission of both lasers is continuously measured. From

[12] *National Instuments PCIe-6353*

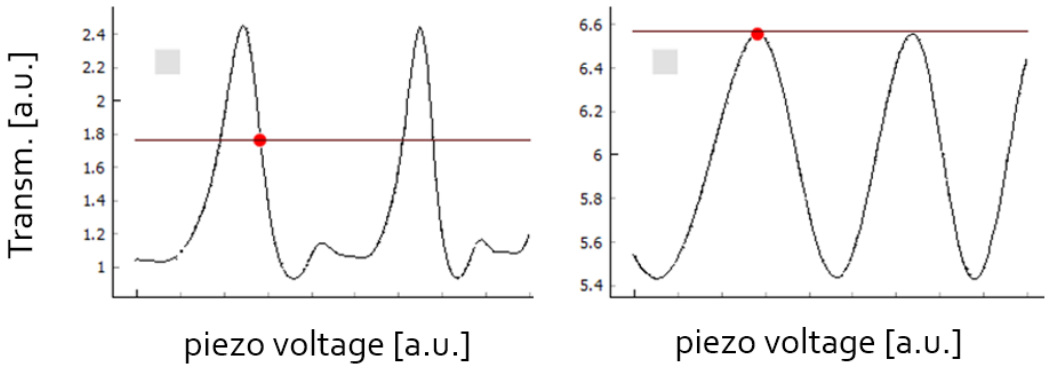

Figure 3.5.1.: Two-laser lock using the transmission of a 780 nm (left panel) and 690 nm laser (right right). The straight lines marks the respective currently measured laser level. The red dot is at the cavity length (here given in arbitrary piezo voltages here) extracted from he two parallel measurements.

this, the computer extracts the cavity length based on the recorded transmission sweep data, see Fig. 3.5.1. Together with a software based PID regulator and a feedback onto the piezo, a lock with a few hundred Hertz bandwidth is built.

Feedback laser wavelength lock. This locking scheme is used for double-resonant Raman spectroscopy, using the optical feedback laser, as introduced in Section 3.3. Again, it allows to tune the cavity length in steps and record Raman spectra this way. As the laser is seeded by and automatically optically locked to the cavity resonance, the wavelength of the laser holds information on the cavity length.

To detect the laser wavelength at sufficient high rate, a homebuilt rudimentary spectrometer was quickly assembled. To this end, the light at one of the ports of the fibre beam splitter in the excitation path of the cavity is used. It is weakly focused after leaving the fibre, reflected by an optical dispersion grating (1200 lines per mm) and imaged by a fast but inexpensive USB camera. By only reading out a part of the camera chip (region of interest=ROI) as much as 500 measurements per second could be taken. The wavelength was extracted from the spatial peak position of the beam on the detector. As the spectrometer does not have to resolve multiple closely spaced wavelengths at the same time, the beam had not be tightly focused and no additional optics where needed. The calibration was done once using a pre-calibrated wave-meter as a reference at two points. With a feedback loop onto a piezo, the cavity could be tuned to any length where lasing was observed with resolution better than 0.2 nm and a bandwidth of about 100 Hz, limited by the readout delay of the camera.

Transmission wavelength lock. Resolving white-light cavity transmission on a spectrometer, the distance or the position of the transmission peaks can be used to construct a lock over long cavity length range.

scheme	≈ cavity length range	≈ bandwidth	≈ resolution (stability)	used for
side of fringe	20 pm	100 kHz	1 fm (100 fm)	stability measurement
two-laser	2 µm	200 Hz	1000 pm (1000 pm)	single frequency Raman scans
feedback laser wavelength	50 nm	5 Hz	$<$ 200 pm	double resonant Raman spectroscopy
transmission wavelength	20 µm	10 Hz	200 pm	length determination
PDH transmision	20 pm (50 pm)	100 kHz		tight locking at resonance (not used here)
top of fringe locking	none (25 pm)	100 kHz		locking at resonance (not used here)[75]

Table 3.5.1.: Different locking and length measurement schemes employed in this work, their performance and use cases. The 'cavity length range' is the range of lengths that can be set using these methods. With locking schemes that centre to a resonance, the number in brackets describes the region where the lock catches. Theses ranges are approximated for a cavity finesse of 10000.

3.5.3. Discussion

The methods for locking the cavity length had to be adapted for the specific use case. They are summarized with their application, the range where the cavity can be locked and their bandwidth in Table 3.5.1.

Implementing these schemes digitally is helpful where tuning is desired or ambiguity of length detection in different longitudinal mode orders should be avoided. Furthermore, it provides a flexible way to program sophisticated relocking schemes, offers short implementation times and easy integration into measurement procedures. In future, fast locking using an FPGA may increase locking bandwidth considerably, while retaining the flexibility of a digital scheme.

For reasons of simplicity and due to higher costs (no high frequency electronics and electronic optical modulators (EOMs) are needed) no Pound-Drever-Hall (PDH) cavity locking has been used, as e.g. used by Brachmann et al.[35].

Using a inexpensive (100€ evaluation board) and simple programmable micro-controller, Huang et al. devise a simple scheme to lock to the top of a transmission resonance[75]. This top-of-fringe lock could be realized straightforward without needing additional components and the same simplicity as the side-of-fringe locking.

3.6. Fast data acquisition and reduction

Performing fast measurements is crucial for scanning cavity microscopy for various reasons: First, faster imaging is convenient for the user. Second, repeated fast measurements can increase sensitive by either simply averaging multiple measurements, or by compensating drifts and fluctuations by rapid referencing. Furthermore, time dependent processes might be observable with sufficient high measurement rates.

Fast measurements needs fast data acquisition. Here, electronic components are presented

to speed up absorption measurements based on the narrow-laser transmission amplitude technique, as introduced in Section 2.3.3.

Problem. The measurement of cavity transmission by sweeping the cavity resonance across a narrow linewidth laser was the first and simplest method to implement cavity based absorption microscopy. It does not need any active stabilization and is robust against cavity length fluctuations because of short interrogation time of the resonance ($< \mu s$).

However, to sample the sharp cavity resonance, sampling rates exceeding several million samples per seconds are needed. In the beginning a fast digital oscilloscope[13] was used to acquire transmission data and transfer the maximum transmission to the computer. This required expensive equipment and the transfer and analysis of data limited scanning rates to about $50\,\mathrm{points/s}$. Although the oscilloscope offers fast sampling, data reduction and transfer are the real bottleneck.

Integrated circuits using an FPGA. To overcome this limitation, a field programmable gate array (FPGA) was used for fast data recording and reduction. An FPGA is an integrated circuit that can be 'rewired' using software. This allows reliable and precisely timed data acquisition and analysis exceeding billions of calculations per seconds. The hardware used is a 250€ 'Red Pitaya' board offering a FPGA core clocked at $125\,\mathrm{MHz}$ combined with two $14\,\mathrm{bit}$, $50\,\mathrm{MHz}$ analog in- and outputs with $125\,\mathrm{MSamples/s}$ and an embedded Linux operating system.

The FPGA is programmed using the software *Xilinx Vivado*, and the *verilog* programming language closely following an online tutorial[14] for the basic in- and output-processing. The FPGA reduces the data by reading out the maximum of the cavity transmission as well as the linewidth and location of the peak.

As a quick-and-dirty solution, reducing time and skill for programming, the FPGA was first used as a black box to 'downsample' the analogue cavity transmission signal. For this, the FPGA takes the maximum voltage that occurred during a fixed time bin at its analogue input port and outputs this maximum value to its analogue output port in the adjacent time bin. Exemplary input and output signals during a cavity length scan can be seen in Fig. 3.6.1. This simple design allows to put the FPGA in between the cavity transmission signal and the computer-based digital-to-analog converter, which can only sample with $1\,\mathrm{MSample/s}$ without needing to change data acquisition on the computer.

Discussion. The FPGA offers an inexpensive, fast and flexible method to record and process cavity transmission data in high resolution. The linewidth, position and amplitude of the cavity resonance can be measured at high speed. In conjunction with the stiff mechanical setup scans with up to 10^4 transmission measurements per second were performed using a narrow linewidth laser. This allows to operate the cavity in a completely new 'real time'-like mode: more than a full frame per second can be captured. This allowsr allows to look at the sample like in a wide-field microscope, e.g. transversally moving the mirror, simplifying orientation on the sample. Therefore, no absolute positioning sensor may be needed to locate parts of a sample.

[13] LeCroy HRO 6 Zi, 12-Bit, 1GHz bandwidth
[14] http://antonpotocnik.com/?p=519284

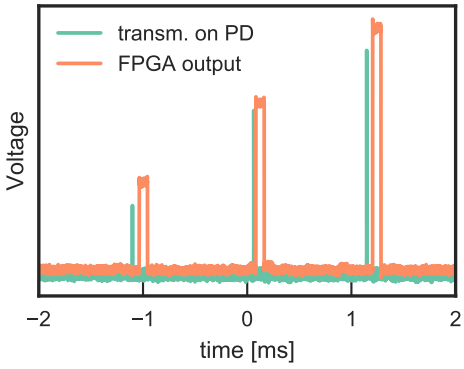

Figure 3.6.1.: Cavity transmission signal and FPGA measured maximum in time bin of approximately 100 µs.

The measurement frequency is only limited by mechanical modulation speed of the cavity and the speed of the detector (10 MHz) to resolve the lineshape under long cavity sweeps.

Apart from data acquisition, the FPGA may also provide the possibility to continuously regulate the cavity length via an active feedback loop to centre the cavity length modulation around the laser. Consequently, the modulation amplitude could be reduced boosting stability, speed and simplicity of operation. Driving the setup with a low amplitude tightly around a resonance at a high resonance frequencies of the mechanical system may allow to capture millions of samples per second.

3.7. Broadband spectroscopy

This section explores broadband light sources and integrating imaging detectors for sensitive broadband cavity enhance extinction spectroscopy. This reduces setup complexity, as the cavity can be used as an enhancing and frequency selective element at the same time.

3.7.1. Problem

Ideally, cavity enhanced spectroscopy could be performed with an inexpensive, broadband light source, without the need for a stabilized, tunable laser source. Detectors with sensitivity at the single photon level, such as CMOS, CCD or silicon count APDs, together with the amplification of the absorption signal by the high finesse cavity may allow to use a variety of broadband low power light sources, and still get decent absorption sensitivity and detection speed.

The problem when coupling light into the fibre and further on into the cavity is that only a single mode is supported (or two modes, if both independent linear polarization modes are considered). How much light can be launched into a single mode is fundamentally constrained in thermal and spatial incoherent sources, as we will see below. Therefore, lasers and in general stimulated emission are used to achieve higher occupation of a single mode. Several light sources were used in the experiments and the performance of some more are discussed theoretically in this section.

3.7.2. Transmitted power

For a given spectral power density P_λ of a light source, the transmitted power through the cavity is given by the spectral integral over the cavity mode,

$$P_t = P_\lambda T_{\mathrm{c,res}} \int d\lambda \frac{1}{1 + (2/\delta\lambda)\,\lambda} = P_\lambda T_{\mathrm{c,res}} \frac{\pi}{2} \delta\lambda\,. \tag{3.7.1}$$

Here, a Lorentzian cavity mode with FWHM $\delta\lambda$ is assumed. For $P_\lambda = 1\,\mathrm{nW/nm}$, a symmetric and ideal, lossless cavity, $T_{\mathrm{c,res}} = 1$, finesse $\mathcal{F} = 10^4$ and longitudinal mode order 5, at $\lambda = 900\,\mathrm{nm}$ (using $\delta\lambda = \lambda/q\mathcal{F} = \lambda/Q$), this yields a transmission of $0.03\,\mathrm{nW}$, or a rate of $1.3 \times 10^8\,\mathrm{photons/s}$. However, this rate decreases linear with higher finesse, longer cavities (with narrower cavity linewidth), or when asymmetric mirrors and mirrors with losses are used, where the transmission on resonance decreases, $T_{c,\mathrm{res}} < 1$. In contrast to long macroscopic cavities, the wide free spectral range at low mode orders may yield only a single mode inside the high finesse spectral region of the cavity. However, as we have seen, the transmission of this single mode is considerably higher.

With this, even low powered broadband sources can be used, if shot noise limited detection can be assumed. Assuming 100 measurements per second and a 30% quantum efficiency detector, this are $N = 4 \times 10^5$ detected photons per measurements and would ideally allow to theoretically measure cavity transmission down to a precision of 0.16% (as shot noise scales with $\sqrt{N}$) and therefore extinction to $0.25\,\mathrm{ppm}$ with $10\,\mathrm{ms}$ integration time.

3.7.3. Broadband light source

In this part, several light sources for broadband cavity-enhanced absorption spectroscopy are investigated. The theoretical issues liming the amount of energy coupled into the cavity and measurements of their performance is discussed.

Super-continuum laser. A super-continuum source provides a single spatial mode across all wavelengths. The *Fianium WhiteLase SC450* with 2W of power spanning $400\,\mathrm{nm}$ to $2.4\,\mu\mathrm{m}$ was investigated. This source can launch about $1.5\,\mathrm{mW/nm}$ light into the SM800 single mode fibre at $900\,\mathrm{nm}$. The source was used for various measurements: The pulsed operation principle with its $\approx 50\,\mathrm{pm}$ long pulses was used to determine the cavity finesse by measuring the cavity ring down time. Absorption measurements were performed with a heavily attenuated beam and a single-photon counter avalanche photodiode. Transmission measurements using continuous photodiodes would need low-pass filtering to flatten of spikes by pulsed operation.

As these sources are bulky, expensive, and have have limited lifetime - especially when compared to diode based devices - simpler alternatives as broadband light sources were investigated.

Superluminiscent LEDs. A superluminiscent diode (SLED) can be understood as a laser diode where feedback is suppressed, therefore operated below its lasing threshold. It uses amplified spontaneous emission (ASE) in a waveguide, which is usually contributing to the pedestal observed in the spectral background of a laser diode, to offer spatial coherent light and therefore be able to launch more power into a spatial mode than possible with a pure

thermal light source or a common light emitting diode. These devices can have up to $70\,\mathrm{nm}$ broad emission profiles (flat-top or Gaussian) around $900\,\mathrm{nm}$, can launch several mW of power into a single mode fibre, and usually start at $1500€$. A bit lower powered but already fibre-pigtailed products from *exalos* stand out here due to their low price staring from $400€$, supplying $50\,\mathrm{nW/nm}$ in its central region[15]. This SLED turned out to not need an optical isolator although the strong back-reflection from the fibre cavity can exceed 10%. It offers low spectral ripple as can be seen in Fig. 3.7.1a.

Laser diode ASE. However, simple laser diodes may also be used as a broadband source, if the laser line can be ignored in the measurement or appropriately filtered out.

The Toptica DL Pro 890nm tunable external cavity diode laser was tested. It can couple up to $15\,\mathrm{mW}$ of laser power into a SM800 fibre. When the laser line is removed from the spectrum by filtering, $660\,\mathrm{nW}$ of ASE power remains in the region of $885-935\,\mathrm{nm}$, yielding about $13\,\mathrm{nW/nm}$. After the cavity $8-12\times10^6$ photons/s were detected, depending on the exact cavity resonance wavelength. This is in the range of a rough theoretical estimation of 5×10^6 photons/s calculated using 4% cavity transmission on resonance, a cavity linewidth on the order of $10\,\mathrm{pm}$, fibre-to-cavity mode-matching of 70% and a photon detection quantum efficiency of 30%. With this low light level, shot-noise limited transmission measurements below 0.1% in $10\,\mathrm{ms}$ are already possible. Better cavity transmission and higher powered laser diodes may decrease this by another factor of 100. The spectrum of the ASE is shown in Fig. 3.7.1a. A modulation of the amplitude with a $0.2\,\mathrm{nm}$ period hints at a parasitic resonator of $2.2\,\mathrm{mm}$ length, most likely the end facets of the laser diode.

LED . A light emitting diode (LED) has the advantage of a broad emission wavelength profile, and simplified electronics for driving in comparison to a laser diode. The possibility of doing simple butt-coupling to a single mode fibre without sophisticated alignment further simplifies operation. The unpolarized nature of the emitted light simplifies polarization dependent cavity absorption measurements. However, due to lower or missing spatial coherence the light intensity that can be coupled to a single-mode fibre is significantly reduced in comparison to laser light or SLEDs.

A rough estimate for the power of a LED that can be butt-coupled into a single-mode fibre can be derived by treating the LED as a Lambertian source. The power launched into a single mode fibre (distributed over both polarization) only depends on the centre wavelength of the LED, λ, and its radiance, L [76]

$$P = \lambda^2 L\,. \tag{3.7.2}$$

Radiance is the power emitted per unit area of a light source to a unit solid angle and quantifies the spatial coherence of light, or number photons per spatial mode[77, 78]. It can not be increased with passive optical elements, because increasing *order* by putting more photons into a single optical mode would decrease entropy[77]. Common LEDs can emit around $100\,\frac{\mathrm{mW}}{\mathrm{mm^2 sr}}$ and therefore allow to couple a few hundred of nW into a single mode fibre (at $900\,\mathrm{nm}$) yielding about $3\,\mathrm{nW/nm}$. This may be enough to do broadband spectroscopy.

[15] Exalos EXS0840-050–05-0804130

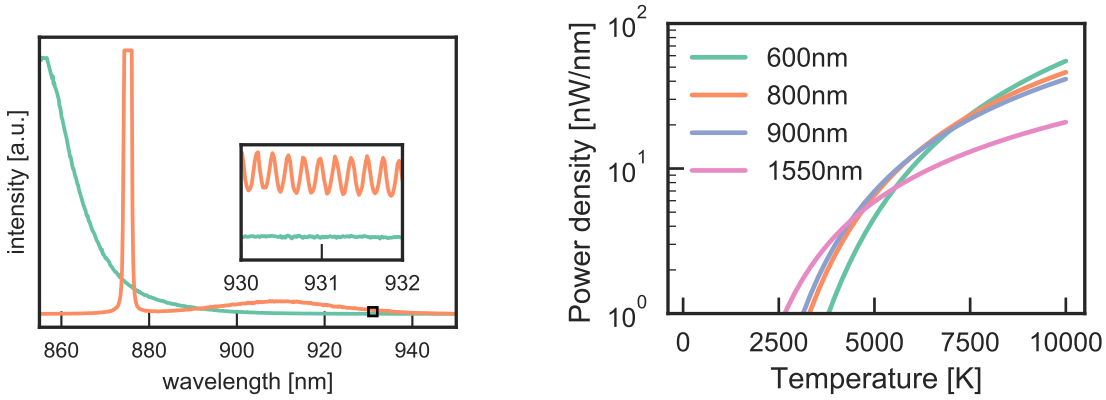

(a) **(b)**

Figure 3.7.1.: (a) Single mode fibre coupled spectrum of laser ASE (orange line , including laser line at $875\,\mathrm{nm}$ that is saturating the spectrometer) and a SLED (green line). The inset shows a zoom of the area marked by the black rectangle. (b) Power spectral density at different wavelengths that can be injected into a single mode fibre (both polarizations) as a function of thermal source temperature.

Thermal light sources. Emission into a single spatial mode from a thermal light source is governed by Bose-Einstein statistics and only depends on the temperature of the light source. The spectral power density at wavelength λ of a source at temperature T for both polarizations is given by [78]

$$P_\lambda = \frac{2hc^2}{\lambda^3\left(e^{hc/(\lambda k_B T)} - 1\right)}\,. \tag{3.7.3}$$

The coupling efficiency strongly increases with source temperature. As can seen in Fig. 3.7.1b, about $10\,\mathrm{nW/nm}$ could be coupled into a single mode fibre using a $6000\,\mathrm{K}$ source, e.g. a metal-halide lamp.

Optical feedback laser. The laser diode seeded by reflections from the fibre-cavity, introduced in Section 3.3, may also be used as a broadband light source for absorption spectroscopy. The transmission is broadband as the laser follows the resonance wavelength of the cavity. The advantage are the order of magnitude higher transmission levels achievable, beyond mW , as compared to μWlevels using the other light sources. This opens up the possibility for order of magnitude faster measurements using conventional photodiodes. However, modified feedback from the sample inside cavity may disturb the laser, and a non-trivial relation between transmitted power and laser power may be given.

External cavity laser. This is not a broadband light source but should be included here for completeness. An external cavity diode laser (ECDL) is a diode-based laser where usually an (optical) grating and the back side of the laser diode form a long (~ few cm) *external cavity*. This stabilizes the laser frequency and narrows the linewidth (free running 50kHz - 2MHz) well below the cavity linewidth which is usually in the pm range. This laser is usually used

for measuring the finesse of the cavity (for finesses > 1000) and for basic and quick scanning cavity absorption microscopy at a single frequency. However, the used *Toptica DLpro* laser has a motor for adjustment of the external cavity length and together with a laser diode with a broad gain medium allows for tuning the laser between $872\,\mathrm{nm}$ to $938\,\mathrm{nm}$ for automatized measurements. Repeated measurements at different wavelengths allow to take absorption spectra in this range.

3.7.4. Integrating detector (CMOS array)

CMOS sensors found in common digital cameras have the advantage of years of improvements for large markets and manufacturing in large quantities, making them cheap compared to scientific equipment. Basically, they are integrating photodetectors with millions of analogue-digital converters and electronics included. The quantum efficiency of these consumer-grade detectors can reach up to 80%.

Here, we use the near-infrared (NIR) optimized CMOS camera *UI-3241LE-NIR-GL* from IDS GmbH (chip by e2v, 10bit ADC, 1,31 1280×1024 pixel, 5.3µm pixel size). The camera offers a quantum efficiency of $30\,\%$ at $900\,\mathrm{nm}$. If only a small area of the chip is read out, frame-rates of up to $1500\mathrm{kHz}$ can be reached.

The detector can also resolve the shape of the transmitted cavity mode. By reading out different areas of the detector, the modes to measure can be filtered, e.g. the fundamental mode by only selecting the inner part of the light beam. This is handy in white-light illumination where several modes at different wavelengths can be resonant with the cavity simultaneously and may contribute to the transmission signal.

Calibrating detector for absolute number of photons. To get information on the sensitivity and limitations of the readout we first calibrate the detector's readout from arbitrary digital counts to photons. The readout of any photon counting pixel-detector can be easily calibrated using a fundamental property of photon statistics. For a process following Poissonian statistics, such as classical photon counting, the mean photon number ($\bar{N}_\nu$) is equivalent to the variance (or standard deviation squared, σ_ν^2)

$$\sigma_\nu^2 = \bar{N}_\nu \tag{3.7.4}$$

Assuming that the detector translates photons to digital counts by an approximately linear gain factor, g, this relation translates to the mean counts, $\bar{N}_c = \bar{N}_\nu \times g$, and the standard deviation, $\bar{\sigma}_c = \bar{\sigma}_\nu \times g$, of these counts. With this at hand we can extract the gain factor by just looking at statistics of the digital picture

$$g = \frac{\bar{\sigma}_c^2}{\bar{N}_c} \tag{3.7.5}$$

This is best done with sufficient bright and homogeneous illumination, that dark counts and readout noise are negligible, as they were ignored in the derivation above. Calculating g for different illumination levels can extract readout noise, while from measurements at different exposure times the dark count rate can be extracted. Note that the calibration also works on single structured images by looking at statistics in diffraction limited spots[79, 80].

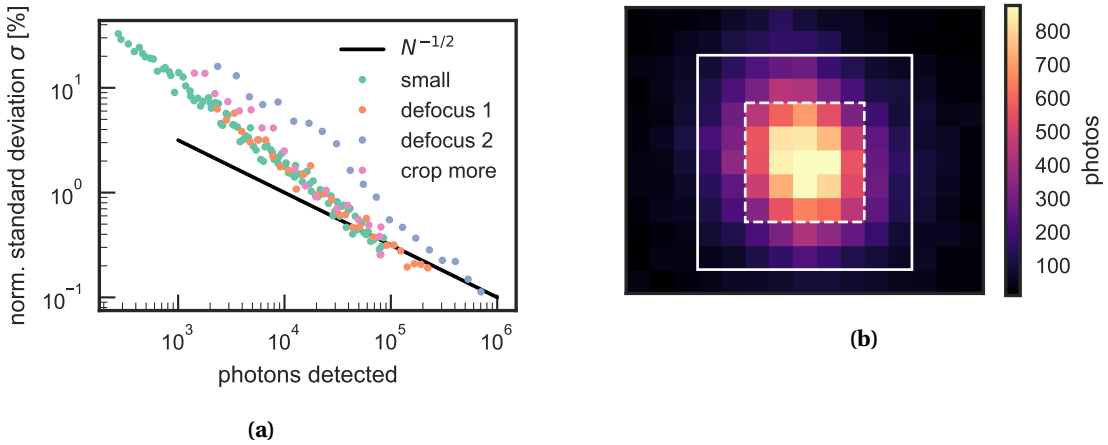

(a) (b)

Figure 3.7.2.: (a) Standard deviation normalized to detected photons σ/N for different measurements and integration times. The colours specify measurement runs with different settings. The black line is the shot noise $\sigma_{sn} = N^{-1/2}$. (b) Cavity mode imaged on CMOS detector.

For the detector at hand this yields to $g = 25 \pm 2$ and readout noise $\sigma_r = 3$ and dark counts of $300/s$.

Shot noise limited measurement. Here, we show experimentally that cavity transmission measurements are only limited by the number of photons detected - shot noise - if the light source and cavity length is sufficiently stable. Shot noise, σ_{sn}, is proportional to the number of photons detected, N,

$$\sigma_{sn} = \sqrt{N}\,. \tag{3.7.6}$$

When normalizing the noise to the signal, a shot noise limited measurement should follow

$$\frac{\sigma_{sn}}{N} = \frac{\sqrt{N}}{N} = N^{-1/2}\,. \tag{3.7.7}$$

The noise was determined experimentally by repeated transmission measurements of broadband laser ASE, in this case 20, and calculating the standard deviation. This was done for different exposure times, yielding different numbers of photons detected. Fig. 3.7.2a shows that for low number of photons detected (short detector exposure times), the noise is above the theoretical shot noise level. There, due to the low illumination of the pixels of the detector, the overall noise is dominated by readout noise (determined to be $\sigma_r = 6$ photons per pixel). Due to the short integration times thermal noise is negligible. When more photons are detected, shot noise dominates, and the noise approaches and adheres to the theoretical limit. Note that the theoretical line and the data has no free parameters. The expected kink and adherence to the shot noise limit therefore confirms the calibration of the detector.

Also this means, that no effects of cavity length fluctuations or parasitic interferometers disturb the transmission measurement, at least down to the an uncertainty of 0.1% and to the used measurement time there of $200\,\mathrm{ms}$.

High dynamic range. Even if no spatial information is needed, the array detector used can have an advantage. Each pixel can be thought of a detector on its own. If multiple pixels of the detectors are illuminated and the photons counts are summed, the dynamic range can be increased.

In Fig. 3.7.2b the image of the cavity transmission on the detector is shown. Although multiple modes could be resonant through the broadband illumination of the cavity, the mode profile seems to be clearly resemble the Gaussian fundamental mode and higher order modes seem to be suppressed. The total number of photons detected is the sum of the counts in the area given by the solid line.

The different measurements shown in Fig. 3.7.2a were performed under different focussing of the the beam onto the detector. Denoted by 'focussed' is a tightly focused beam only illuminating a few pixels. This limits the achievable maximum detectable number of photons, as the detector saturates at the so-called 'full well capacity' of about 10000 photon induced electrons. The measurement 'defocus 1' uses a broader beam on the detectors and therefore more photons can be detected and the noise can be reduced. Further defocussing ('defocus 2') allows detecting even more photons and consequently lower the shot noise limit. However, we see that the shot noise limit is reached only at higher photon numbers. This is because reading out more pixels and summing them also increases readout noise, which dominates in short exposure times. This can be validated by selecting a smaller area ('crop more') of the beam, where the intensity is high. This is illustrated as the dashed rectangle in Fig. 3.7.2b. As expected, due to lower readout noise, the shot noise limit is reached at lower photon numbers, but by throwing away photons, the lowest noise level is not achievable anymore. If an abundance of light is available this selection of the most illuminated pixels would be where the best signal can be achieved.

Adding the signals of each pixel in post-processing allows to work around saturation and finite analogue-to-digital conversion depth. Conceptually, the saturation increases linearly with the number of pixels illuminated, n, while the uncorrelated noise of each pixel only increases with $\sqrt{n}$.

Integration time. In Fig. 3.7.3, the same measurements are shown as a function of exposure time. The best transmission determination down to 0.1% can be reached in $200\,\mathrm{ms}$ exposure with the strongly defocussed beam. However, already at $20\,\mathrm{ms}$ a level of 0.3% can be reached with a tightly focused beam. As shown above, the noise is only set by number of photons detected and this is reflected in the detection time. Here, optimized cavity transmission, a stronger broadband light source or removing beamsplitters from excitation and detection can significantly enhance sensitivity.

3.7.5. Discussion

In Table 3.7.1, different broadband light-sources and their power launched into the cavities' single mode fibre together with the emission FWHM bandwidth are summarized. It was shown that not only expensive sources like supercontinuum lasers can be used to couple sufficient light into the cavity. Also SLEDs or even common laser diodes are an option. Potentially LEDs and thermal light sources may be used as inexpensive broadband sources.

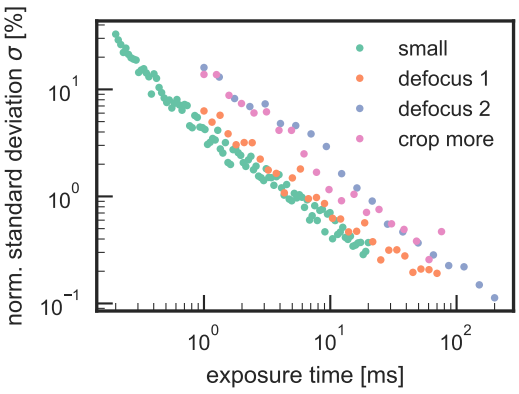

Figure 3.7.3.: Same measurement as in Fig. 3.7.2a, but as a function of exposure time.

Light source	P_λ[nW/nm]	-3 dBbandwidth [nm]
Supercontinuum, Fianium SC400, 2W	1500	≈ 1600
SLED, 3 mW fibre coupled, 50 nm broad	50	50
Laser ASE, 20 mW Laser	13	≈ 50
LED, 100 mW/sr/mm^2	3 (theoretical)	≈ 50
thermal, 6000 K	12 (theoretical, at 900 nm)	≈ 1000
Optical feedback laser	$\gg 10^6$	≈ 20

Table 3.7.1.: Comparison of measured spectral power density in single mode fibre and bandwidth of light sources for cavity based broadband spectroscopy

It was shown that the measurements of cavity transmission using the weak laser ASE is only limited by shot noise, at least down to 0.1%. A inexpensive industrial-grade CMOS camera can be used to achieve shot noise limited detection in less than 1 ms, and this time is only set by the power of illumination. The use of pixel detectors offers a large dynamic range, making it possible to still receive a cavity transmission image if the losses of the specimen inside the cavity exceed the cavity transmission by far.

Using 'pixelated polarizers', where thousands of wire-grid polarizes under different angles are patterned on a film, polarization resolved measurements could be gathered with a single CMOS detector.

Obviously, using more sensitive, less noisy detectors with higher dynamic range (16 bit '*sCMOS*' or 'CCD'), better light collection (factor 3 higher quantum efficiency) and detection speed and sensitivity same noise level could be improved straightforward.

4. Sensitivity and performance

This chapter explores the sensitivity limits and speed of the scanning cavity microscope in acquiring images, spectra and hyper-spectral images both in absorption and Raman scattering. The limitations of the system and their origin are investigated.

Chapter 2 provided a theoretical foundation for cavity-based enhancement of Raman and absorption spectroscopy. However, the real world sensitivity of a spectroscopic/microscopic apparatus must be qualified by the sensitivity of the final measurements, to account for known and unknown sources of error[3]. For example tuning a laser in frequency to take spectra can modify interferences that are not seen if the measurement is only performed at a single frequency. The same holds for spatially resolving features: at high sensitivity levels, parasitic interferometers or laser speckles may change with position. Also, as shown by Benedikter et al[62], for scanning cavity extinction microscopy, slight changes in mirror surface properties can change the properties of the cavity at different points of the sample, resulting in a strong spatial scattering background.

4.1. Extinction Microscopy/Spectroscopy

Here the sensitivity of extinction measurements using the method to measure the cavity transmission of a narrow laser (as introduced in Section 2.3.3) is investigated. First, noise of a single measurement and improvement by averaging repeated measurements is analysed. Then, the noise of full spectra and spatial varying background noise in scans will be measured. Finally, the results of the amplitude measurement method will be compared the measurements using an integrating detector and differences are discussed.

The total background noise limiting the minimum detectable extinction can be decomposed as follows

$$\sigma_{bg} = \sqrt{\sigma_A^2 + \sigma_{sp}^2 + \sigma_\lambda^2}\,, \tag{4.1.1}$$

into three uncorrelated sources of noise. The single point and single wavelength measurement error, σ_A, the noise due to spatial inhomogeneities when recording scanning images, σ_{sp}, and spectral variations when combining measurements at different wavelengths, σ_λ.

4.1.1. Single measurement

Here, the detection limit of a single measurement at a single point on the planar mirror is investigated. The measurement scheme uses the amplitude of the transmission resonance sampled using a narrow linewidth external cavity diode laser (*Toptica DL pro*) detected on an avalanche photodiode (*Thorlabs APD410A*, 10 MHz bandwidth). The error is determined by the standard deviation of repeated measurements.

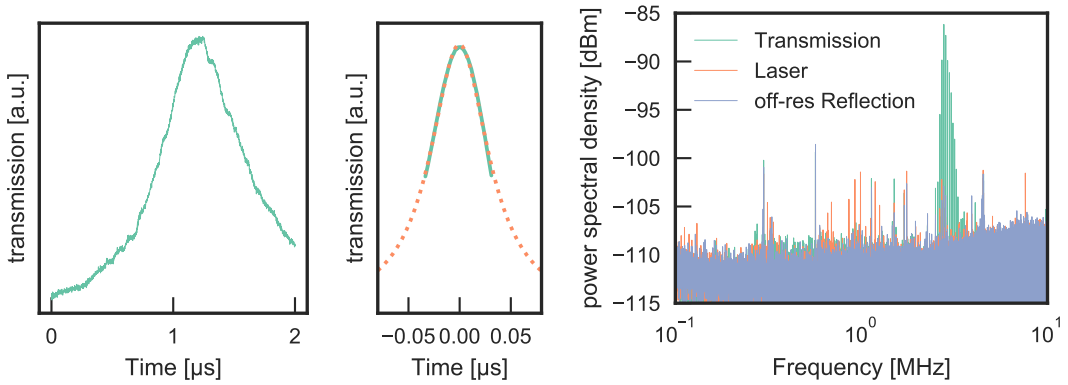

(a) **(b)** **(c)**

Figure 4.1.1.: (a) Narrow laser transmission under cavity length sweep. Clear modulations can be seen. (b) Same as (a) but with 20 times faster sweep speed. Dotted lines are Lorentzian fit to the data. (c) Fourier transform of transmission measurement, off-resonant reflection of the cavity and directly measuring the laser power.

The best transmission uncertainty achieved is 0.3%. At a finesse of 4×10^4, this translates via the cavity extinction gain, $A_c/A \approx \frac{2}{\pi}\mathcal{F}$ (see to Eq. (2.3.7)) to a single-shot minimum detectable extinction in the cavity of $\sigma_A = 0.1\,\mathrm{ppm}$.

It turns out that this noise depends on the sweeping speed over the resonance. For fast measurements, where the peak is traversed in less than $0.1\,\mu\mathrm{s}$ the transmission noise is 2%. This reduces to $0.3\,\%$ and saturates at this level for slower scanning speed, when the the peak is traversed in more than $1\,\mu\mathrm{s}$. This hints at high frequency noise at around $1 - 10\,\mathrm{MHz}$. In Fig. 4.1.1a, the traversing of the transmission peak in $2\,\mu\mathrm{s}$ is shown. Clearly, ripples in transmission can be seen on an otherwise smooth peak. The fluctuations are stronger at the peak, meaning they scale with the transmission signal. They can not originate from cavity length fluctuations due several reasons: First, their high frequency is unlikely to be a mechanical resonance. Second, length fluctuations would not translate to transmission amplitude fluctuations on the peak of the transmission, as the slope is zero there. Finally, at faster sweep rates, perfectly smooth Lorentzian peaks can be measured, that only vary in their absolute height, seeFig. 4.1.1b. Therefore, the noise has to originate from intensity fluctuations or detector noise. In Fig. 4.1.1c, the FFT of a transmission measurement is shown, where a clear peak at $3\,\mathrm{MHz}$ shows up. This peak is not present in measurements when the laser output power is directly measured, or in the reflection from the off-resonant cavity. This rules out intensity fluctuations or detector noise. Therefore, only tiny phase fluctuations, leading to amplitude fluctuations in a long parasitic resonator behind the cavity might be the source. This can be the front and end facet of the planar mirror ($3\,\mathrm{mm}$ thickness). The frequency peak constitutes of multiple sharp lines, probably at switching noise from a power supply. Further investigations are needed, but it seems that these problems can be overcome by low-pass filtering the laser current.

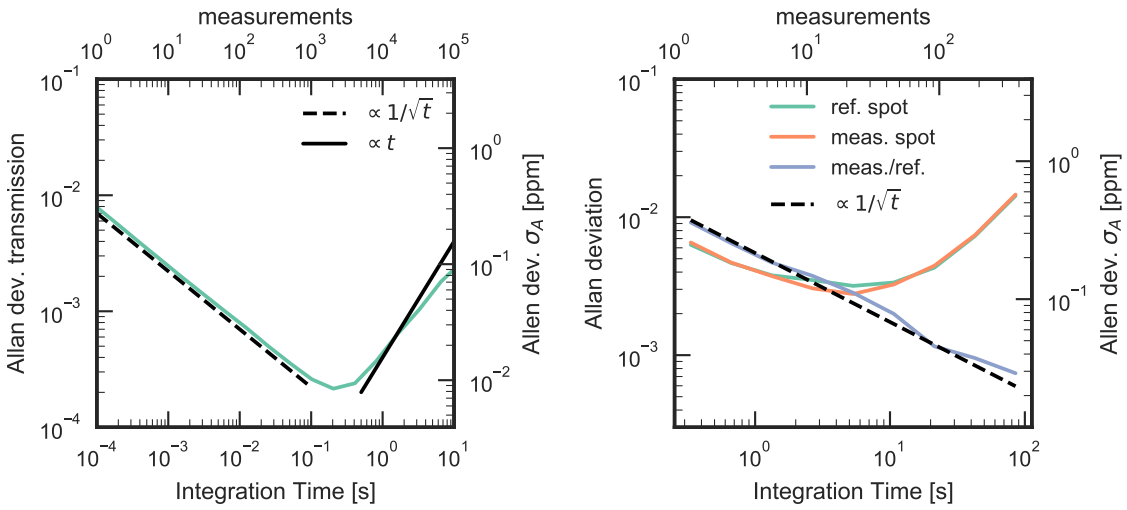

Figure 4.1.2.: (a) Allan deviation of cavity transmission peak amplitude measured at a single point with a rate of $10\,\mathrm{KHz}$. (b) Allan deviation of a 'reference spot' where the cavity is empty and a 'measurement spot' . Measured at a rate of 900 points per second on a scan area of 16×16 points and 3 frames per second. The normalized measurement decreases with square-root of number of measurement time over the whole integration time.

4.1.2. Averaging

Here, the increase in sensitivity by averaging multiple measurements at a single point is investigated.

Allan deviation. The Allan deviation indicates how accurate a quantity can be measured by averaging repeated measurements. Furthermore, it provides a way to discern different types of signal variations[81, 82, 83, 84].

The Allan deviation can be understood conceptually as follows: A repeated measurement is divided into bins of equal time length τ (or equally measurement repetitions). Then the averages of each cluster are compared, similar to calculating the standard deviation between the clusters. This is repeated for different cluster lengths. The Allen deviation of the shortest cluster length (length of a single measurement) coincides with the standard deviation of all measurements. The Allan deviation of the longest cluster length is obtained by just dividing the measurement in two parts and calculating the standard deviation of their respective averages.

Fig. 4.1.2a shows the Allen deviation for repeated measurements of cavity transmission with a rate of $10\,\mathrm{kHz}$ at a single point. The measurement uncertainty first decreases with time (or repetitions), proportional to $t^{-1/2}$, what is expected for uncorrelated white noise. For longer times it rises linear with time t^1, a signature of a steady drift, with additional minor parts of a random walk, $\propto t^{1/2}$[82]. This is attributed to laser intensity drifts, as a common short term stability is on the order of 0.01%.

The lowest achievable uncertainty is 2×10^{-4} at a measurement time of $0.2\,\mathrm{s}$, corresponding to 2000 measurements. Higher precision could therefore be achieved with faster measure-

ments, alleviating slow laser intensity drifts or if the single measurement noise is decreased (e.g. as suggested in the previous section).

Rapid referencing. As we have seen, the accuracy of a measurement increases with repeated measurements until drifts of the laser power kick in. This could be corrected with stabilizing the laser output, however, intensity fluctuations originating behind the laser source would not be reduced, for example due to polarization changes in the fibre or changes of fibre coupling (from temperature fluctuations).

As introduced in Section 2.3.2, the cavity-based extinction measurement relies on a comparison of transmission through the empty cavity and with the sample inside the cavity.

If measurements at the sample and next to it can be alternated at sufficient speed, both should see the same fluctuations in laser intensity. This allows to compensate intensity drifts by what one could call *rapid referencing*.

To test this compensation a small area scan ($16\,\text{points} \times 16\,\text{points}$, $5\,\mu\text{m} \times 5\,\mu\text{m}$) was repeated 1000 times with roughly 900 points per second (3 frames per second). In Fig. 4.1.2b, the Allan deviation of two locations in this scan is evaluated. While the Allan deviation of the two individual spots increases after 10s due to intensity fluctuations, normalizing them to each other decreases further and is insensitive to this common fluctuation. A total $70\,\text{s}$ long measurement of a whole scan yields an Allan deviation of 9×10^{-4}. Even at this long measurements no drifts appear and averaging may decrease noise even further for longer integration times.

4.1.3. Spatial fluctuations

When measuring absorption images, a spatial variations in the cavity transmission signal can be observed, leading to a noise we call σ_{sp} for spacial noise. The source may be attributed to mirror inhomogeneities or interferences in the detection path and their magnitude will be measured and their source discussed here.

Spatial background measurement. To characterize the spatial background noise that limits sensitivity when acquiring microscopy images, a mirror without a sample on it can be scanned. From the transmission measurements, the spatially varying parasitic scattering inside the cavity is extracted. To even exclude effects of potential dirt on the mirror surface, a mirror substrate without a capping layer is used. There, the cavity mode has zero intensity on the planar mirror surface. All spatial variations in transmission signal can then be attributed to mirror inhomogeneities or interferences in the detection path.

In Fig. 4.1.3a, scans over such a pristine mirror are shown. The scans are repeated with the same parameters and slightly shifted wavelengths to test reproducibility. Furthermore, the scan was performed at various cavity lengths, at adjacent longitudinal mode orders. It can be seen that the background scattering pattern is reproducible when using the same parameters and only slightly changes with wavelength. However, when going to different longitudinal mode orders, the pattern and overall strength of the background changes significantly. In Fig. 4.1.3b, it can be seen that for "good" mode orders the background noise (standard deviation of the background) is more than a factor 2 smaller than for "bad" mode orders. The best result

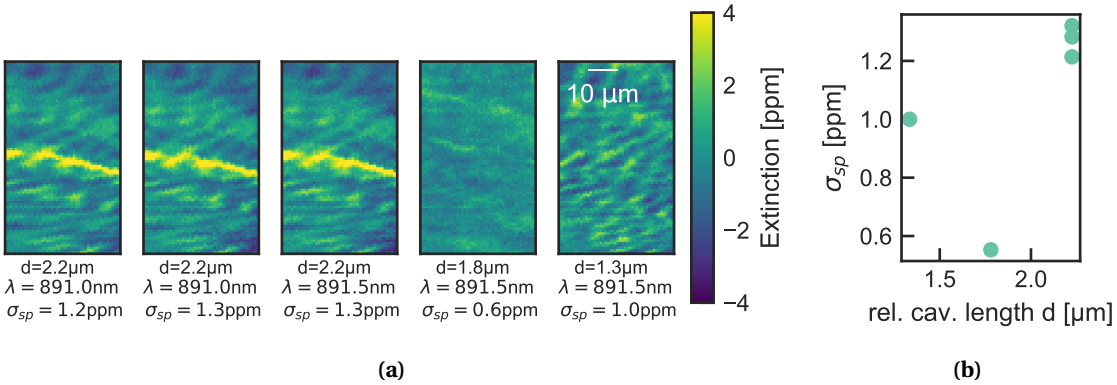

(a) **(b)**

Figure 4.1.3.: (a) Scans of background scattering of an empty mirror at the same position but different cavity lengths. The cavity length used ('d') and spatial standard deviation (σ_{sp}) are plotted. The first three panels measured at the same cavity length show the reproducibility of the background pattern. The third one has the wavelength shifted by $0.5\,\mathrm{nm}$. The absorption is extracted by normalizing to the mean transmission of the scan, which also yields negative values. (b) Extracted scattering background as a function of cavity length.

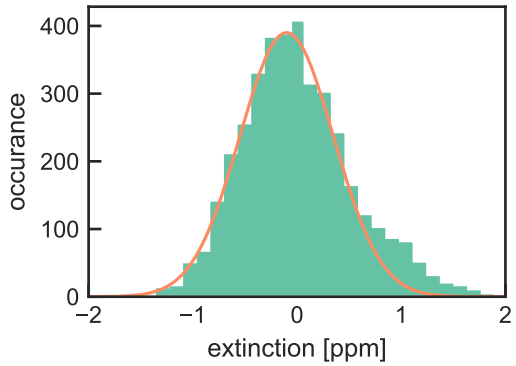

Figure 4.1.4.: Histogram of the $d = 1.8\,\mu\mathrm{m}$ measurements in Fig. 4.1.3a. The line is a Gaussian with $\sigma = 0.45\,\mathrm{ppm}$.

is $\sigma_{\mathrm{sp}} = 0.6\,\mathrm{ppm}$ and slightly better results can be obtained by combing all measurements, by taking the maximum transmission at each pixel ($0.5\,\mathrm{ppm}$).

Averaging multiple scans at length $d = 2.2\,\mu\mathrm{m}$ does not reduce the noise, which corroborates that the noise is dominated by spatial fluctuations σ_{sp} and not single point measurement uncertainty σ_A . The histogram of the lowest background extinction at $d = 1.8\,\mu\mathrm{m}$ shown in Fig. 4.1.4 reveals a Gaussian distribution with a tail to higher extinction. At these low noise levels, some parts may be attributed to σ_A which has the same order of magnitude as the overall noise, as determined previously.

Mode-mixing. The higher extinction at certain points is explained in the following. Different cavity fibre mirrors show a dramatic different background, ranging from $5\,\mathrm{ppm}$ to $0.6\,\mathrm{ppm}$. In general, fibres that exhibit higher scattering loss (manifested in a Finesse that is lower than expected from the mirror coating) also exhibit stronger background variations and meas-

urements at longer cavity lengths tend to show elevated background patterns. Furthermore, different mirror substrates show different levels of scattering. No quantitative numbers are available yet, but planar mirrors with lower roughness on short scales show better performance. This is based on qualitative information from the coating manufacturer Laseroptik GmbH which measured height profiles of mirrors with the same specified overall RMS roughness but featuring fluctuations on different length scales.

The dependence on cavity fibre, mode order and planar mirror roughness leads to the interpretation that cavity mode-mixing together with planar mirror inhomogeneities may be the driving force behind the observed background. The effect of cavity mode-mixing in imperfect fibre-cavity mirrors was is discussed by Benedikter et al.[62]:

When the cavity mirror profile deviates from a perfect sphere, which is commonly the case for longer cavity lengths and imperfect profiles, the eigenmodes of the cavity are no perfect Hermite-Gaussian modes any more. This can lead to significant coupling between usually orthogonal modes, e.g. the fundamental mode (on which the measurement is performed) and larger higher order modes, when they become resonant. This admixture of higher order modes then in turn can lead to a steep decrease of finesse. Since the exact resonance length or frequency of the modes can change with small surface variations on different positions of the planar mirror, this can lead to the spatially varying scattering background. In general, roughness below the diffraction limit leads to coupling of these higher order modes.

Background suppression via spectral information. When using the additional information of spectrally resolved scans, parts of the spatial background noise may be compensated. This is possible under the assumption that scattering (and especially the scattering background) does not depend strongly on the wavelength, and that in contrast to this, the absorption of the objects to analyse *does* vary with wavelength.

In Fig. 4.1.5a, again a pristine planar mirror substrate is raster scanned. A rather strongly scattering and therefore also bad performing cavity fibre was used, showing a strong background noise of around $\sigma_{sp} = 3\,\mathrm{ppm}$. The wavelength is varied between measurements over $36\,\mathrm{nm}$. The overall background noise is between $2-4\,\mathrm{ppm}$ for all measurements. A slightly varying but mostly similar background can be seen on all measurements. In Fig. 4.1.5b the average of all scans (taken for each point) is subtracted. We see that the high frequency ripples are strongly suppressed. This means that most of it is strongly wavelength independent. The pattern prevails in the edges of the measurement but is also decreased there. Without the small-scale pattern , now larger scale patterns moving through the measurement can be observed.

In Fig. 4.1.5c, the spatial noise of the scans is shown for each wavelength. The mean-subtracted measurements show a background noise decrease of up to a factor of two. For comparison, the scan at a single wavelength was subtracted. It still decreases the overall pattern but not as efficiently as the mean.

It is not clear if the change of the pattern between wavelength can be attributed to an unintentional change of polarisation. Further measurements with better polarization information are needed here, as well as measurements in a wider wavelength range.

The case that background is mostly independent of wavelength hints at mode-mixing with far off-resonant higher order modes or weak mixing with very high loss and thus broad modes. More investigation is needed here.

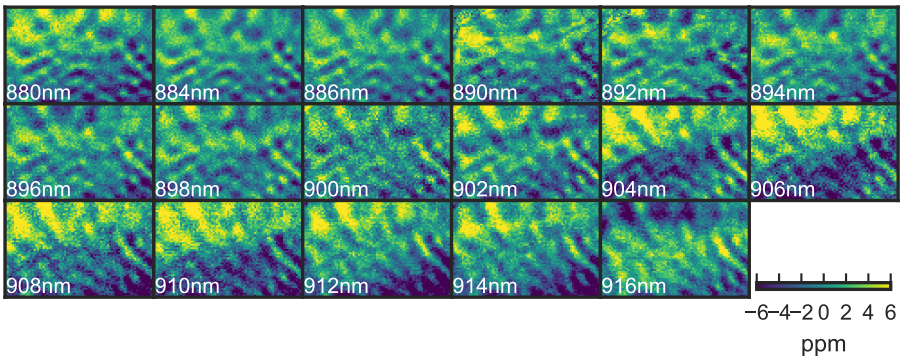

(a)

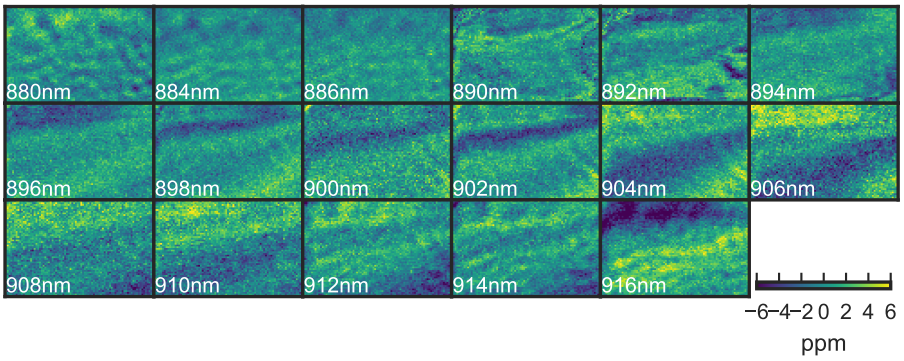

(b)

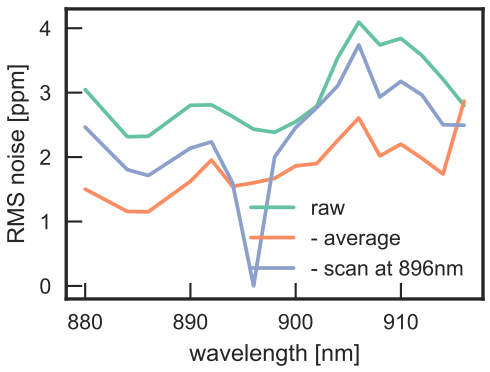

(c)

Figure 4.1.5.: (a) Transmission background scan at different wavelengths. (b) Compensated measurement by subtracting the mean value of all measurements for each pixel. (c) RMS noise of raw measurements (green), measurements compensated by mean subtraction (orange) and by subtracting a singe scan at $896\,\mathrm{nm}$.

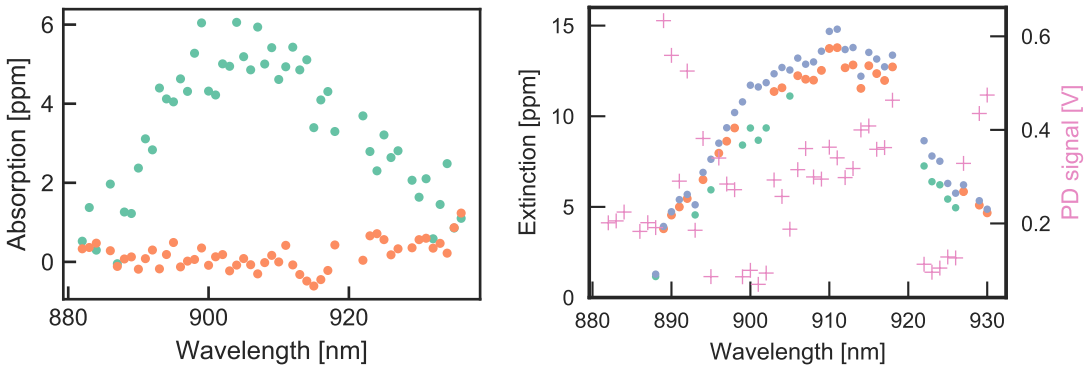

(a) (b)

Figure 4.1.6.: (a) Spectrum of a weakly absorbing carbon nanotube (green dots) and a background measurement at a clear spot (orange dots). (b) Extinction spectrum at a point. The green dots are measured at wavelengths where the laser has low power levels, the orange ones at higher levels. The blue dots have the background signal subtracted. The crosses are the raw photo diode signal in volt (right scale).

4.1.4. Spectral fluctuations

Next, the noise and its sources when acquiring a spectrum will be discussed. To collect a spectrum, the diode laser's wavelength is tuned by turning the grating using its built-in motor. For each wavelength a small 2D scan in recorded.

In Fig. 4.1.6a, a spectrum of a weakly absorbing carbon nanotube is shown (more details on the sample in Section 5.1). To remove spatial (σ_{sp}) and single-point measurement noise (σ_A) measurements are averaged over multiple points (100 points for transparent reference area and 20 points for absorbing spot). A peaked spectrum can be seen with maximum absorption of approximately $5\,\mathrm{ppm}$.

One way to quantify the spectral background noise, is to extract a spectrum at a transparent spot. This transparent spectrum is also shown in Fig. 4.1.6a and yields a standard deviation across the spectrum of $\sigma_\lambda = 0.4\,\mathrm{ppm}$.

Spectra furthermore critically depend on the transparent background used for normalizing the transmission and therefore converting cavity transmission to sample absorption (as introduced in Section 2.3.3). By comparing spectra extracted using normalization with different transparent spots and subtracting them from each other, the difference is found to have in all cases a deviation of $\sigma_\lambda < 1\,\mathrm{ppm}$. The residual structure present in these difference spectra suggests that the sample used is too dense and a completely transparent spot for normalization does not exist in the scanned area. The difference for the two best candidates for normalization, the two spatially and spectrally most unstructured spots,showed a difference of $\sigma_\lambda = 0.5\,\mathrm{ppm}$. For practical purposes, sparsely populated samples can also be normalized to the full scan without strong deviation.

Another source of spectral noise is that the laser strongly varies in intensity across different wavelengths. On some wavelengths it even does not run on a single mode and these

points are filtered out manually. In Fig. 4.1.6b, the spectrum of the another absorbing spot is shown together with absolute laser power at the measurement wavelength. Extinction extracted at wavelengths where the laser has low power levels differs strongly from points where the laser has high power levels. This hints towards a constant offset of the transmission photodiode signal that skews the extraction. Indeed, by properly subtracting a background photodiode voltage ($24\,\mathrm{mV}$), the spectrum is cleaned from most of the discontinuities and becomes significantly smoother. Measuring with higher voltage levels on the detector and reducing background by AC coupling the photodiode could further reduce errors due to laser intensity variations.

In summary, these tests showed reproducible spectra, independent of normalization spots and laser power, that can be acquired with sub-ppm spectral background.

4.1.5. Imaging speed

With the FPGA-based fast data-acquisition (introduced in Section 3.6) the scanning cavity microscope was operated in a completely new 'real time'-like mode: more than a full frame (25x35 pixel) per second can be captured and e.g. transversally moving the mirror allows to look at the sample as with a conventional wide-field microscope. This is shown by a measurement recorded with one image per second in Fig. 4.1.7. Note that, as has been shown above, the extinction sensitivity of such a single scan can be lower than $1\,\mathrm{ppm}$. Furthermore, ten times faster scans with up to 10000 points/s have been performed.

At a single point, even faster measurements can be performed. As shown in Section 3.4.7, the cavity length can be modulated up to MHz rate while still reliably resolving transmission resonances. With this, and the used FPGA data acquisition and handling, microsecond resolution time resolved measurements at full sensitivity are possible. This is an advantage over other extinction measurement techniques (especially the wide field approach presented in Section 4.1.6) that reach similar levels only by considerable averaging time.

4.1.6. Other approaches to sensitive extinction microscopy

Here, the sensitivity, speed and resolution of cavity enhanced detection is compared to other sensitive methods of absorption or extinction microscopy. Techniques to microscopically detect single molecules or single nanoparticles in absorption can be classified in three categories:

1. *Direct techniques* measure the transmission of an object by comparing the incoming and transmitted intensity.
2. *Modulation techniques* periodically vary intensity, position, frequency or polarization of light and use lock-in detection to separate signal form background.
3. *Indirect techniques* detect secondary effects of absorption like temperature changes and vibrations.

These methods greatly vary in sensitivity, speed and general applicability[49]. In Table 4.1.1, some the most sensitive methods, to the best of my knowledge, are summarized and will be discussed in more detail in what follows.

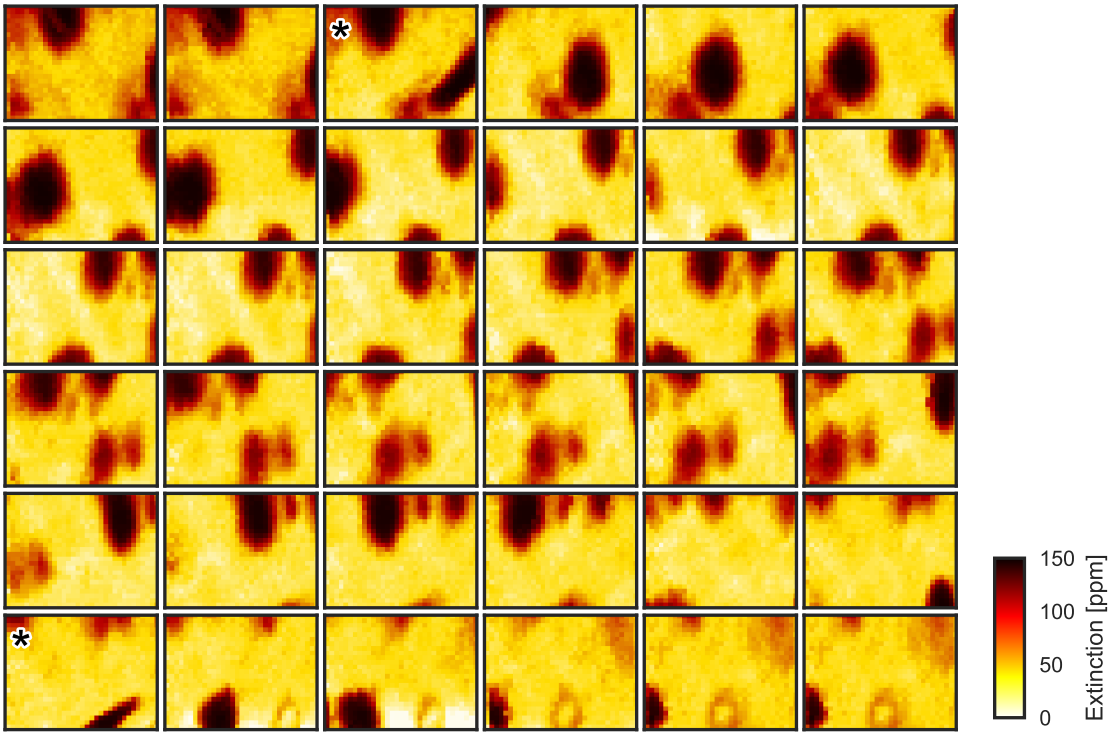

Figure 4.1.7.: Various frames of a real-time recorded sequence of extinction scans while moving the macroscopic mirror (in horizontal direction). Showing approximately every tenth frame of a video recorded at one frame per second. The scan speed was 900 points per second and spans $20\,\mu\text{m} \times 15\,\mu\text{m}$. At the images marked with "$*$", moving the mirror while line-by-line recording a frame leads to skewed images.

Technique	microscopy resolution	spectroscopy	single point noise σ_A	spatial noise σ_{sp}	speed [points/s] ([frames/s])
scanning cavity (this work)	$1.2\,\mu\text{m}$	yes (up to 150 nm wide)	0.01 ppm $0.04\,\text{nm}^2$	0.3 ppm $1.2\,\text{nm}^2$	5000 (10)
direct confocal[47]	diffr. limit/$\sqrt{2}$	not yet (possible)	0.7 ppm $0.05\,\text{nm}^2$	3 ppm $0.2\,\text{nm}^2$	35
direct wide-field [85]	diffr. limit	not yet (possible?)	0.5 ppm $1\,\text{nm}^2$	$4\,\text{nm}^2$	100 (2×10^{-4})
photothermal[86]	-	yes	$0.05\,\text{nm}^2$		10
spatial modulation[86]	dispersed	yes	$4.3\,\text{nm}^2$		10
polarization-based + modul.[87]	$1.5\,\mu\text{m}$	yes	10 ppm		

Table 4.1.1.: Comparison of different methods of ultra-sensitive absorption measurements. Frames per second means how many full pictures can be recorded at the sensitivity limited by spatial noise.

Microscopic, (so far) single-wavelength techniques. Using a 'simple' *direct* confocal approach, balanced detection with low-noise amplifiers, a stable laser source and averaging, Kukura et al. reached shot noise limited detection of $0.7\,\mathrm{ppm}$ at a single point[47, 88]. The spatial background was reduced to $3\,\mathrm{ppm}$ ($0.2\,\mathrm{nm}^2$) by embedding the sample (a fluorescence dye) in PMMA and using index matching gel. The detection of single fluorescence dye molecules with $4\,\mathrm{ppm}$ absorption was claimed. However, for this the absorption signal had to be differentiated from the background when the molecule are turned 'on' and 'off' in absorption, i.e. exploiting molecules with "blinking" behaviour.

Using a *direct* conventional wide field imaging approach, Payne et al. reached impressive $1\,\mathrm{nm}^2$ sensitivity limit on a single point[89, 90, 85]. This level was reached by averaging 256.000 images taken with a scientific CMOS array detector illuminated just below saturation. Rapid referencing between measurements, where the sample was shifted by a few µm reduced laser speckles and light source fluctuation in time. Using index matching gel, the spatial noise was reduced to $4\,\mathrm{nm}^2$ and optimized image post-processing reduced this further to $0.6\,\mathrm{nm}^2$ when assuming well-separated, point-like samples. A $100 \times 100\mu\mathrm{m}^2$ scan took 11 minutes integration time. Faster measurement speeds are promised with even more sensitive and faster cameras. This technique can differentiate between scattering and absorption when also the dark-field image is measured.

Photothermal heterodyne imaging is among the most sensitive methods to image single molecules. Here, an analyte is embedded in a host medium. The heat from absorption of this analyte is measured through heat-induced local change in refractive index of the host medium. This way sensitivities down to $0.05\,\mathrm{nm}^2$ have been shown[45]. However, the high light intensities and embedding into a host medium narrow the applicability to stable samples and specialized environments. Furthermore, lock-in technology, and usage of two lasers complicate the setup. The technique does not determine absolute values for the absorption cross section and is not easily extended to multiple wavelengths.

Spectroscopic and microscopic techniques. Broadband *spatial modulation* spectroscopy [86] using a supercontinuum laser source was used to demonstrate spectroscopy of gold nanoparticles and carbon nanotubes in the range 420–$1100\,\mathrm{nm}$ down to a sensitivity of $4.3\,\mathrm{nm}^2$. This technique is applicable to all kinds of nanomaterials but needs dispersed point-like particles separated by far more than the diffraction limit. However, the measurement rate is rather low, because the spatial modulation is mechanically limited to $750\,\mathrm{Hz}$ and therefore led to long dwell times of $100\,\mathrm{ms}$ per measurement point.

4.1.7. Discussion

It was shown that cavity based extinction measurements can reach sub-ppm extinction sensitivity levels for spatial, spectral and temporal measurements.

In contrast to prior techniques, cavity enhancement offers higher speed as well as extinction sensitivity without averaging. However, as the cavity mode is larger, the detectable absorption cross section is on the same order as other techniques at the moment. Note however, that in general in contrast to some of the alternative techniques presented, not all tricks are played at all. The detection and light sources are very basic and sensitivity as well as speed might be

improved by orders of magnitude with straightforward optimizations.

Detection of single molecules or nanoparticles is so far limited by spatial background of about $0.5\,\mathrm{ppm}$. This inhomogeneity could be improved with exploring better mirror coatings and smoother mirror substrates for the planar mirror. However, it was shown that for the same planar mirror, the strength on the noise depends also on fibre mirror and the profile used there. Better spherical shaped fibre mirror profiles, reducing scattering between higher order modes and the fundamental mode (mode-mixing), therefore can improve the extent to which these inhomogeneities play a role.

Image post processing, using spectral information or assuming point-like samples, could to increase effective sensitivity like the one order of magnitude increase achieved by Payne et al. for wide-field imaging[85].

Using monochromatic lasers, the sensitivity is so far only limited by phase fluctuations and drifts of the light source power. Light source fluctuations are effectively cancelled out by rapid referencing of the transmission to a transparent spot or power stabilisation of the light source. Here, balanced detection schemes might allow the cavity transmission to be measured to a few parts per million[88], leading potentially to single point sensitivity limits in the parts-per-trillion range, while still providing fast measurements.

As the spatial resolution is still well above the diffraction limit, there exists some room for improvement. Straightforward, but also more difficult to operate are smaller radii of curvature mirror profiles, see Appendix A.3.1. A $5\,\mu\mathrm{m}$ radius of curvature would lead to a $0.5\,\mu\mathrm{m}$ mode e^{-2} radius at $\lambda = 780\,\mathrm{nm}$ at cavity length $d = \lambda$. However, this would presumably also increase scattering and limit the cavity length to below approximately $2.5\,\mu\mathrm{m}$. The simultaneous measurement and combination of higher order modes as explored by Mader et al.[25], could improve the resolution by a factor 2.7 (and can ultimately lead to a resolution $\sqrt{2}$ below the diffraction limit), but again with the drawback of increased noise.

Spectral noise was shown to mainly originate from power fluctuations or multi-mode operation of the laser. Better separation from the background could be achieved by AC-coupling of the photo diode.

4.2. Raman Microscopy/Spectroscopy

As introduced in Section 2.4.3, Raman scattering can be enhanced in a cavity by the Purcell effect only (which we will call “single resonant”) or additionally by power build-up of the excitation light (which we call “double resonant”). Both effects as well as the efficiency of collecting the Raman scattered light will be quantified in this chapter.

4.2.1. Single resonance measurement

To measure the Purcell factor and demonstrate imaging and collection of Raman spectra, carbon nanotubes were used as a sample. Details about the properties and spectra of carbon nanotubes is postponed to Chapter 5. The results of this chapter can be also found in our publication on “Cavity-enhanced Raman microscopy of individual carbon nanotubes”[91].

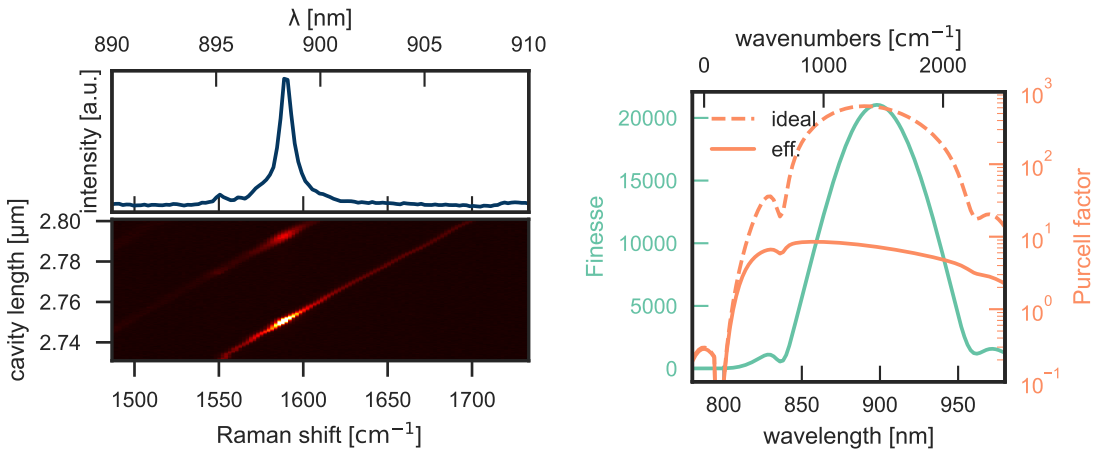

Figure 4.2.1.: (a) Upper panel: Part of a carbon nanotube Raman spectrum. Lower panel: collection of this spectrum by stepping through the cavity length. (b) Finesse, expected ideal Purcell factor and effective Purcell factor for a Raman feature with $Q_r = 1500$, cavity length $d = 2.75\,\mu\text{m}$, mode volume $V_m = 13\lambda^3$ and excitation laser at $786\,\text{nm}$.

Collection of a spectrum. To record a broadband Raman spectrum, we stepwise change the cavity length to sweep the cavity resonances across the desired spectral range where Raman features are expected. The signal is collected on a spectrometer for each cavity length. An example is shown in Fig. 4.2.1a. By summing these spectra, the full spectrum can be reconstructed. The spectral feature shown has a Lorentzian lineshape and a FWHM width of $0.7\,\text{nm}$.

Accessible Raman spectrum. The accessible cavity enhanced Raman spectrum is approximately 300–$2,000\,\text{cm}^{-1}$ for single resonant cavity enhanced Raman spectroscopy and given by the wavelength of the used excitation laser and the bandwidth of the optical coating, as can be seen in Fig. 4.2.1b. The upper limit can be lifted when a laser that is further apart from the stopband is used. The lower limit is set by the steepness of the onset of stopband of the coating. The effective Purcell factor will suffer in the region where the effective quality factor is dominated by a low cavity quality factor, $Q_c \lesssim Q_r$, which is the case in the low finesse region of the cavity. The expected effective and ideal Purcell enhancement including effects of imperfect placement of the sample relative to the field antinodes is shown in Fig. 4.2.1b.

Determination of Purcell factor

The determination of the Purcell factor (PF) was one of the most time consuming parts of this work. The PF relates the increased spontaneous emission rate inside a cavity to the free space spontaneous emission rate of a system. Usually, when looking at the Purcell effect of two-level systems, the rates can be measured using pulsed excitation and determination of lifetimes. The advantage of this is that no absolute intensity measurement has to be performed, only the determination of a time constant. However, the Raman process does not involve a stable excited state from which the lifetime can be measured. Therefore, only the comparison of

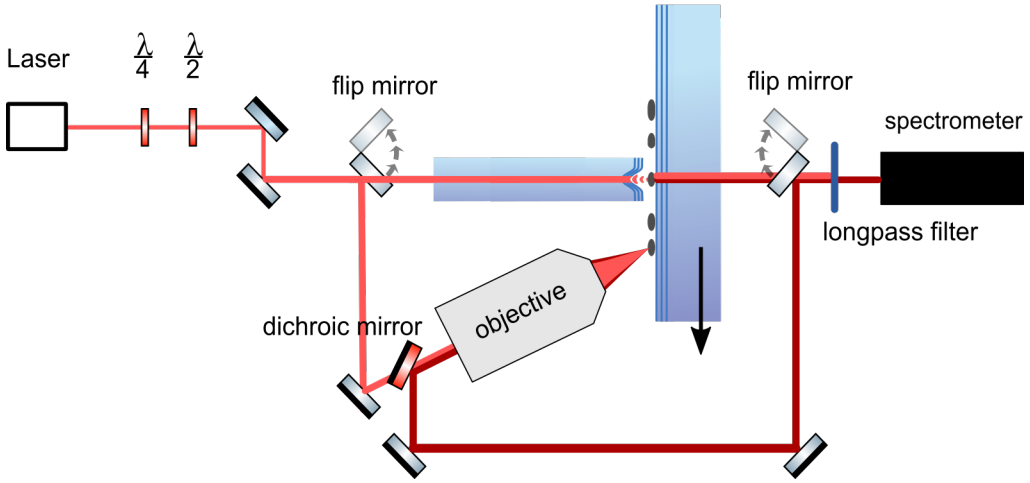

Figure 4.2.2.: Sketch of the setup for determining the Purcell factor. The planar mirror hosting the sample can be moved by a long distance to bring one and the same carbon nanotube (depicted by black cylinders) either into the cavity mode or in the focus of a NA=0.7 objective. In the cavity case the Raman scattered light (dark red) is coupled out through the planar mirror. When measuring with the objective, the Raman scattered light is separated using a dichroic mirror.

the absolute intensity of emission inside and outside the cavity can be used to measure the Purcell factor. This requires careful determination and comparison of many effects affecting the signal strength.

However, at least a *relative* measurement of the Purcell effect is easier possible and can be used to verify the findings: the Purcell effect inside the cavity should scale strongly dependent on the mode volume of the cavity, which can be tuned by simply changing the cavity length. Here, to first order only relative changes in the excitation power between different cavity lengths and slight mode diameter changes have to be accounted for.

To determine the Purcell factor, a objective-based measurement and multiple cavity-based Raman measurements on one and the same carbon nanotube were compared. This comparison was repeated for several tubes. To this end, the planar mirror hosting the sample was mounted on a long travel range positioning stage (Attocube ECS3030, 20mm travel) in order to bring the same position on the sample into the cavity or in into the focus of the large working distance objective, as sketched in Fig. 4.2.2. The relative position was calibrated using a pattern imprinted on the mirror.

Effects that affect the signal strength and that needed to be determined were polarisation, excitation power (considering standing wave effect inside cavity, or the sample sitting on the mirror in free space) , mode size of excitation, light collection (transmission through cavity mirror, objective collection and sample on mirror), the small Purcell effect of sample sitting on mirror in the free space case, losses in detection path and the linewidth of Raman feature compared to the cavity linewidth.

The Purcell factor is given by the ratio of the cavity (Γ_c) and free space emission rates (Γ_f) normalized to excitation power

$$F_{p,\text{eff}} = \frac{\Gamma_c}{\Gamma_f} = \frac{c_c/\eta_c P_c/w_c}{c_f \eta_f P_f w_f} \tag{4.2.1}$$

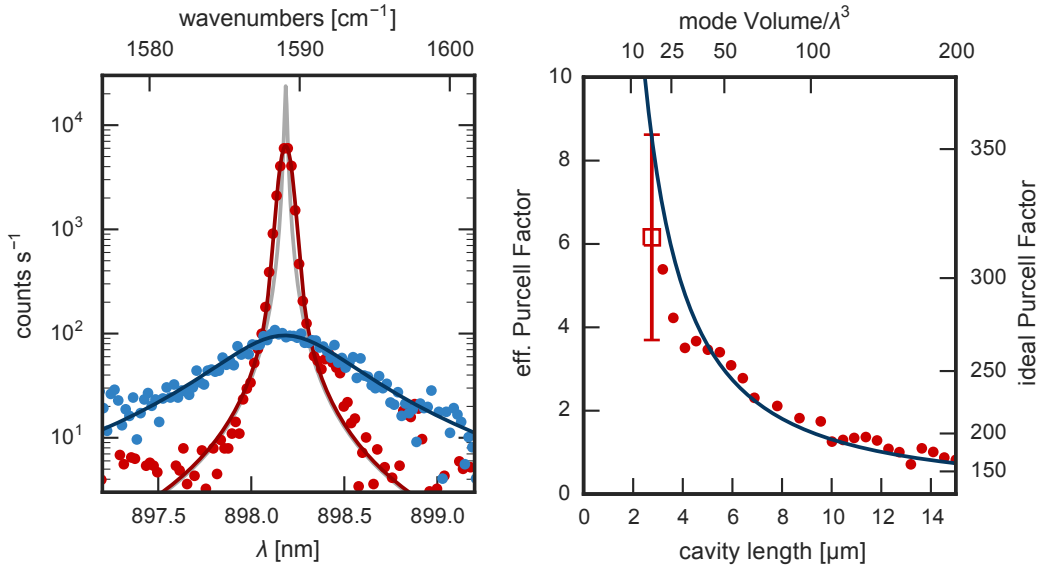

Figure 4.2.3.: (a) Spectra of the same nanotube acquired via objective (blue data points with Lorentzian fit) and the stabilized cavity at a cavity length $d = 2.75$µm (red data points with Voigt fit) normalized to the same intensity at the nanotube. The grey line shows the intrinsic cavity resonance. (b) Measured effective Purcell factor as a function of cavity length (red dots and red square). The red square is evaluated from the measurement shown in (a). The blue line is the theoretical predicted effective and ideal Purcell factor.

Estimation of error. The emission rates relate to the detected count rates (c_c, c_f) via the collection efficiency, $\eta_{c,f}$, excitation power, $P_{c,f}$, and mode radius, $w_{c,f}$, of the excitation. The total uncertainty is calculated by standard propagation of uncorrelated uncertainty. The relative error therefore becomes

$$\frac{\Delta F_{p,\mathrm{eff}}}{F_{p,\mathrm{eff}}} = \sqrt{\left(\frac{\Delta\eta_c}{\eta_c}\right)^2 + \left(\frac{\Delta P_c}{P_c}\right)^2 + \left(\frac{\Delta\rho_c}{\rho_c}\right)^2 + \left(\frac{\Delta\eta_f}{\eta_f}\right)^2 + \left(\frac{\Delta P_f}{P_f}\right)^2 + \left(\frac{\Delta w_f}{w_f}\right)^2} \tag{4.2.2}$$

The error in the collection efficiency is estimated to be $\Delta\eta_c/\eta_c \approx 5\%$ in the cavity and $\Delta\eta_f/\eta_f \approx 10\%$ in free space. The excitation power in the cavity is the most imprecise quantity $\Delta P_c/P_c \approx 30\%$ due to unknown residual cavity effects even in the transparent region of the coating. We assume conservative $\Delta P_f/P_f \approx 10\%$ for free space. The mode sizes can determined quite reliable from Raman scans and agrees with theoretical calculations from the radius of curvature. The error is assumed to be less than 10% for both free space and in the cavity. The total relative uncertainty therefore is $\Delta F_p/F_p = 36$.

Purcell factor

In Fig. 4.2.3a the cavity enhanced signal and the free space collected signal of the G^+phonon mode of one and the same nanotube is shown, normalized to equal excitation intensity at the nanotube. The location where the measurements were performed is shown in Fig. 4.2.4a. From comparison of the total count rates the effective Purcell factor was determined to be $F_{p,\mathrm{eff}} = 6.2\pm2.5$. The ideal Purcell factor can be obtained from the ratio of the peak spectral densities of the measurements. The peak spectral density of the intrinsic cavity line is extracted by matching its integral with the integrated count rate measured with the spectrometer. This yields an ideal Purcell Factor of $F_p = 320 \pm 120$.

These values are in good agreement to the calculated values $F_{p,\mathrm{eff}} = 8.5$ and $F_p = 354$ which were deduced from the cavity mode volume $V = 13\lambda^3$, the cavity quality factor $Q_c = 6.1 \times 10^4$ and the quality factor of the Raman G^+ band $Q_r = 1.5 \times 10^3$. The Raman Q-factor was obtained from a fit to the confocally collected Raman line.

In Fig. 4.2.3b, the Purcell factor measured for different cavity lengths is shown. The expected inverse scaling with the mode volume can be seen when compared to theoretical calculation.

Collection

An advantage of cavity assisted Raman scattering is that the emission is not only enhanced by the Purcell effect, but the light is furthermore collected very efficiently as it completely resides in the single cavity mode. The fraction of the light that can be collected at one side of the cavity is given by the transmission through the out-coupling mirror divided by all loss channels

$$\eta_c = \frac{T_2}{T_1 + T_2 + L_1 + L_2 + 2A} \tag{4.2.3}$$

As the transmission of the planar mirror behind which the signal is collected is higher (labelled "2", $T_2 > 300\,\mathrm{ppm}$) than the fibre mirror and mirror losses ($T_1 \approx 50\,\mathrm{ppm}$, $L_{1,2} < 20\,\mathrm{ppm}$) the collection efficiencies can exceed $\eta_c = 60\%$. This depends however on the strength of the extinction at the sample (given by A) , e.g. the nanotube itself.

Locked scan

In Fig. 4.2.4a a scan is shown where the cavity length is stabilized at the resonance with a particular Raman band. In this way, scans with a net speed improvement when locating carbon nanotubes via their known Raman signature. Single nanotubes showing a count rate of $15\,\mathrm{kCounts/s}$ can be identified.

Spatial resolution

The spatial resolution of the scan shown Fig. 4.2.4a is evaluated by Gaussian fits to the point spread function (PSF) evaluated at point-like objects. The resolution is found to be be $1.5\,\mu\mathrm{m}$, considerably smaller than the PSF of an extinction scan at the same cavity length. This can be explained from the fact that the PSF for Raman imaging is a product of the excitation and collection PSFs. The product of two Gaussians with radii $w_{0,e}$ and $w_{0,r}$ and yields again a Gaussian with a composite radius given by

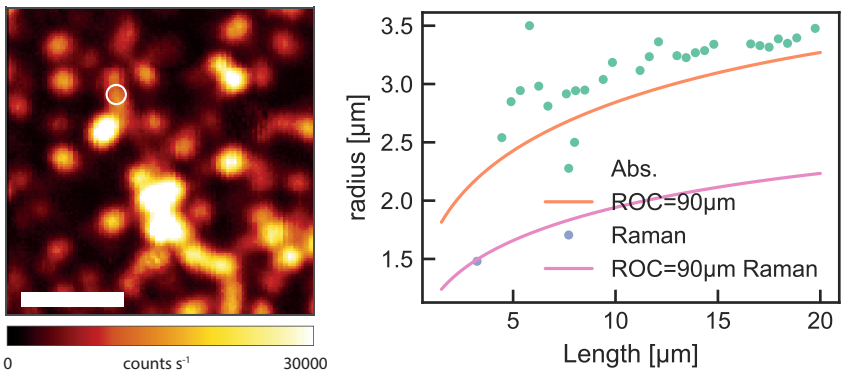

(a) **(b)**

Figure 4.2.4.: (a) Locked scan at Raman shifts where the carbon nanotube G^+ band is expected with $14\,\mathrm{mW}$ excitation. The scale bar is $10\,\mu\mathrm{m}$. (b) Cavity mode radii measured from scans (points) and calculated from mirror profile (lines) for absorption ($\lambda = 786\,\mathrm{nm}$) and Raman scattering ($\lambda_{ex} = 786\,\mathrm{nm}$, $\lambda_r = 898\,\mathrm{nm}$) .

$$w_{0,c} = \sqrt{\left(w_{0,e}^{-2} + w_{0,r}^{-2}\right)^{-1}}\,. \tag{4.2.4}$$

Assuming a residual low-finesse cavity at the excitation and calculating the corresponding theoretical mode waist radius of $w_{0,e} = 2.1\,\mu\mathrm{m}$ (using cavity length $d = 3.3\,\mu\mathrm{m}$, radius of curvature $R = 90\,\mu\mathrm{m}$, excitation wavelength $\lambda = 785\,\mathrm{nm}$) according to Appendix A.3.1) together with the mode radius at the Raman collection wavelength of $w_{0,r} = 2.2\,\mu\mathrm{m}$ (using $\lambda = 898\,\mathrm{nm}$) yields a theoretical combined mode waist of $1.5\,\mu\mathrm{m}$ matching the experimental observed value. Mode radii calculated and measured form absorption and Raman scans are shown in Fig. 4.2.4b.

Note that the resolution enhancement is inherent to the collection with the cavity mode. It is similar to the resolution increase observed in confocal imaging, where resolution improves by a factor of $\sqrt{2}$ (if excitation and collection wavelength are the same). However, in confocal imaging an aperture has to be introduced which clips some of the Raman scattered signal.

4.2.2. Double-resonant measurements

Double-resonant Raman measurement increases the excitation power by means of the cavity. Here we evaluate how much power at the sample was achieved using the optimized coating (Section 3.2) in combination with the optical-feedback laser (Section 3.3).

Excitation enhancement. To measure the peak power in the cavity, the known transmission of the planar mirror, T_2, is used in conjunction with a measurement of the transmitted power through the cavity, P_t. The power at the sample inside the cavity is given by

$$P_e = \frac{4}{T_2}\alpha_{ex} P_t\,, \tag{4.2.5}$$

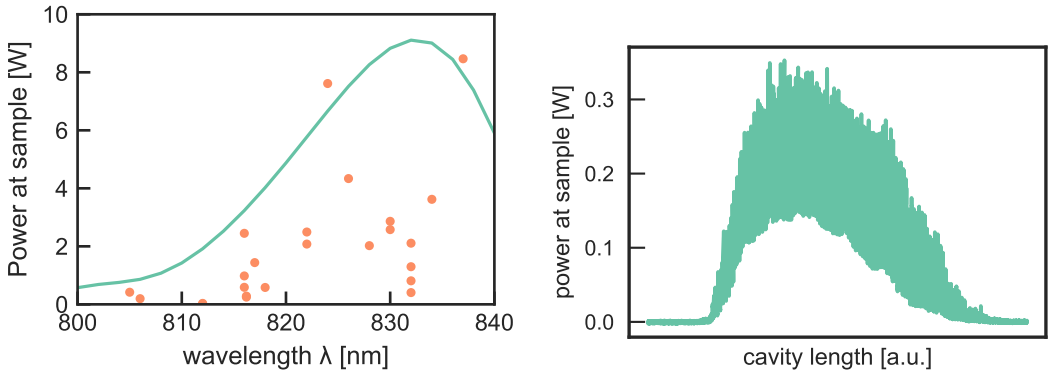

(a) (b)

Figure 4.2.5.: (a) Power at the sample. Solid line is theoretical power at the sample from coating simulation and with an incident assumed to be $3\,\mathrm{mW}$ and fibre mode to cavity mode matching 60%. Datapoints are power at the sample extracted from cavity transmission measurement. (b) Power at sample for a cavity length sweep (corresponding to a wavelength sweep between $\approx 810 - 820\,\mathrm{nm}$). The area appearing solid are fast oscillations of power with the cavity length.

as derived in Appendix A.1.7. Here, α_{ex} is a correction factor accounting for the non-optimal sample position away from the field maximum on the planar mirror. For the used mirror $\alpha_{ex} > 80\%$ in $800 - 840\,\mathrm{nm}$, as can be seen from mirror coating simulations in Fig. 3.2.7.

The transmitted power was measured on a photodiode calibrated according to a pre-calibrated optical power-meter. The power at the sample extracted this way using the optical feedback laser is shown in Fig. 4.2.5a for many measurements. The power strongly varies with the particular cavity-mirror used, angle optimization, the longitudinal mode order, laser to fibre coupling and polarization optimization of the optical-feedback laser. In general, many fibres exhibited strongly reduced cavity transmission and power inside the cavity, which coincided with a reduced finesse and unexpected coating performance. The exact source is unknown but this seems to be attributed to problems in the coating process or contamination and is discussed in Appendix C.1.2. The spectral width where this strong enhancement could be achieved also varied with the aforementioned parameters. In the better performing fibres FWHM of more than $5\,\mathrm{nm}$ was reached. However, the power showed fast modulation with cavity length changes of up to 50%, as can be seen in Fig. 4.2.5b.

The input power was measured and was in the order of $3\,\mathrm{mW}$. In conclusion, a strong enhancement of the in-coupled light of more than 1000 could be achieved with a maximum power of $8\,\mathrm{W}$ at the sample.

Signal strength

For double-resonant measurements, improved fibre mirrors with the tailored coating and smaller radii of curvature (10µm-30µm) were used. Due to smaller mode volume effective Purcell factors of up to 40 are expected. In combination with higher excitation powers, far stronger Raman signals compared to the old single-resonant case are expected. However, only preliminary results are available here. First measurements on carbon nanotube samples showed more than $100\,\mathrm{kCounts/s}$ for single carbon nanotube at the G^+phonon mode, with

$0.2 \pm 0.1\,\mathrm{W}$ excitation power at $816\,\mathrm{nm}$ inside the cavity. This is an order of magnitude more signal than was observed for single nanotubes in the single-resonant measurements, but less than expected. However, it has to be noted that more detailed measurements could not be performed as the used nanotube sample consisted of sorted $(5,4)$ chirality which turned out to be known to be very unstable even under µW illumination. Furthermore, it is suspected that the Raman signal originates from tubes with far off resonant electronic transition from the excitation laser, while the single-resonant case was most likely dominated by tubes resonant with a electronic transition resonant with the cavity.

In contrast to the previous Raman measurements, at $1544\,\mathrm{cm}^{-1}$ a $< 10\,\mathrm{cm}^{-1}$narrow feature showed up in all measurements. This is attributed to Raman scattering of O_2 in air and highlights the stronger sensitivity due to higher excitation power. This will be discussed in more detail in Section 5.3.

4.2.3. Discussion

It was shown and quantified that the cavity can enhance Raman scattering, and that for Raman features broader than the cavity linewidth this scales with the effective Purcell factor and therefore inversely with the mode volume. An effective Purcell of up to 6.2 at the shortest accessible cavity length was determined. Together with high collection a net speed gain at the same signal strength was shown when compared to a confocal measurement with $\mathrm{NA} = 0.7$ objective.

First measurements with double resonant enhancement showed a promising up to ten fold increase in signal from suspected single carbon nanotubes. However due to issues with the sample and reduced performance of the mirror coatings, a more detailed study has to be done.

5. Measurements on Materials

In this chapter we show the application of the presented fibre-based microscope both for absorption and Raman spectroscopy and microscopy of different nanoscale samples. Each material is briefly introduced and some spectral and spatial features are explained. These are exemplary measurements, in the sense that a proper extraction of novel information on theses systems would need more systematic measurements, data analysis and knowledge by solid state physicists. However, with measurements at these samples, the technology was developed and its applicability demonstrated. Furthermore, with each sample system, different methods of transferring or growing the sample on the mirror substrate are explored.

5.1. Carbon nanotubes

5.1.1. Introduction to single-walled carbon nanotubes

Single-walled carbon nanotubes, herein just called carbon nanotubes (CNTs), are basically atomically thin tubes created by conceptually rolling up a graphene sheet, as illustrated in Fig. 5.1.1a. Their outstanding properties have lead to numerous applications and experiments in electronics[92], photonics[93], nanomechanics[94], and quantum optics[95, 96] .

As a nanoscale solid system, CNTs have a high degree of flexibility. Not only tubes of different length can be formed, but the carbon sheet can be 'rolled up' to form tubes with diameters from $0.3\,\mathrm{nm}$ to above $10\,\mathrm{nm}$ and the angle of the rollup defines many different *chiralities*, yielding tubes with metallic to semiconducting properties and especially allowing to change optical properties such as the absorption wavelength in an almost continuous way.

Recently the flexibility to tailor optical properties got a new boost, by doping carbon nanotubes to form quantum dots where excitons are confined in three dimensions[97, 98, 99]. This leads to single photon emission slightly shifted from original emission wavelengths. More details of electronic and vibronic properties of carbon nanotubes are explained when the associated absorption and Raman scattering properties are discussed.

5.1.2. Sample preparation and transfer

Several different nanotube samples were used and were transferred onto the sample planar mirror using two different methods.

CNT5. For this sample, highly pristine carbon nanotubes were synthesized in the group of Alexander Högele at the LMU. They were transferred onto the mirror using a custom technique developed in the group.

Nanotubes were synthesized on a SiO_2 substrate by chemical vapour deposition (CVD)[91, 97]. Iron- ruthenium particles spin-coated on SiO_2 were used to catalyse the growth of CNTs

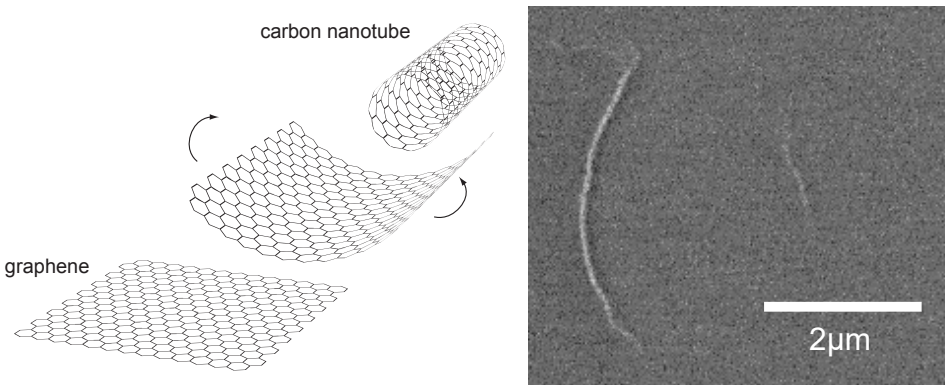

Figure 5.1.1.: (a) Illustration of the rolling up a graphene sheet to form a carbon nanotube. (b) Scanning electron microscopy of two individual carbon nanotubes.

with methane as carbon feedstock. Before the CVD growth the substrate with catalyst particles was treated by oxygen plasma to yield longer CNTs. Subsequently the substrate was transferred into a standard CVD furnace, heated in an argon– hydrogen (95%/5%) atmosphere to 850°C and kept in a flow of 1slm methane and 0.75slm hydrogen for 10min before the cool-down in an argon–hydrogen atmosphere.

The CNTs could not be grown directly on the planar cavity mirror because the temperatures involved in this process damage the optical dielectric mirror coating by delamination, which starts to deteriorate mirror performance above approximately $500\,^{\circ}\mathrm{C}$. For transfer to the cavity mirror, the SiO_2 chip hosting the nanotubes was pressed onto a mirror using a tiny custom-made vice and placed it into an ultrasonic bath of deionized water for 120 minutes.

Scanning electron microscopy was used to confirm isolated CNTs on the cavity mirror as can be seen in Fig. 5.1.1b. The mirror hosting the sample has a central reflection wavelength of $780\,\mathrm{nm}$.

CNT11. Nanotubes were synthesized and transferred the same way as CNT5 but with a higher concentrations of catalyst particles. This yielded a denser population of shorter tubes. The mirror used had a central reflection wavelength of $890\,\mathrm{nm}$.

CNT28-(9,1). Here, chirality sorted nanotubes of $(9,1)$-chirality were used. The nanotubes were filled with water and solved in Sodium deoxycholate (DOC). To transfer them on the sample with minimal solvent contamination, this source solution was first diluted 5000:1 in deionized water. From this, $0.25\,\mu\mathrm{L}$ was drop-cast onto the mirror. It spread to a drop about $1\times 1\mathrm{mm}^2$ and evaporated in a few seconds. Nanotubes are shorter than $1\mu\mathrm{m}$ due to the sorting process.

CNT28-(8,3). Here, chirality sorted nanotubes of $(8,3)$-chirality were used and prepared in the same manner as the previous sample.

5.1.3. Absorption

As a quasi one dimensional systems, Carbon nanotubes feature absorption resonances due to peaks in their electronic density of states, so-called van-Hove singularities. The location of these resonances depends mainly on the tube diameter and to a lesser extent on the chirality (or roll-up angle) of the nanotube[60].

Carbon nanotubes show strong polarization dependence in their optical properties due to the high aspect ratio of their dimensions, with absorption, Raman scattering and fluorescence strongly enhanced for light polarized parallel to the nanotube axis.

Imaging

In Fig. 5.1.2a an absorption scan of sample CNT5 is shown. To see carbon nanotubes independent of their orientation and therefore polarization properties, two scans with orthogonal linear polarization were combined by taking the maximum absorption at each point. Elongated structures of up to $100\,\mu\mathrm{m}$ length can be seen with predominant absorption cross sections around $400\,\mathrm{nm}^2$.

The extinction cross sections are commonly normalized by length to account for the elongated morphology. When assuming tubes longer than the mode radius of the cavity, w_0, the cross section per length is calculated via[1]

$$\sigma_l = \sqrt{\frac{2}{\pi}}\frac{1}{w_0}\sigma_{\mathrm{ext}}\,. \tag{5.1.1}$$

Using the experimentally determined mode waist $w_0 = 3.1\,\mu\mathrm{m}$ the scan scaled in this units is shown in Fig. 5.1.2b. Predominantly tubes with cross section of around $100\,\mathrm{nm}^2/\mu\mathrm{m}$ can be seen. However, also tubes with 50 and $200\,\mathrm{nm}^2/\mu\mathrm{m}$ are present. Absorption strength does not seem to depend on orientation of the tubes, which was the case when only using a single polarization scan. The strongest absorption may also be due to multiple bundled nanotubes. The absorption coefficient has an order of magnitude compatible with on or off-resonant carbon nanotubes. A more detailed discussion and comparison to literature values is provided later.

In contrast to this sample CNT11, shown in Fig. 4.2.4a, exhibits shorter tubes, due to the changes in the synthesis. Most of them are shorter than the point spread function of the cavity mode and their elongated structure can not be resolved.

Polarization contrast

Polarization resolved absorption measurements are performed to test for the strong polarization dependence absorption of carbon nanotubes. To this end, two absorption scans are recorded with linear polarized light rotated by 90°. The two polarization eigenmodes of the cavity are used and polarization before the cavity is adjusted to completely feed into one of the modes and consecutive into the perpendicular polarized mode. In Fig. 5.1.3a the polarization

[1] by normalizing to the integral of the intensity of the Gaussian mode, $I(x) = I_0 e^{-2x^2/w_0^2}$, along the axis of the nanotube, x, yielding $\int_{-\infty}^{+\infty} I(x) = I_0\sqrt{\frac{\pi}{2}}w_0$.

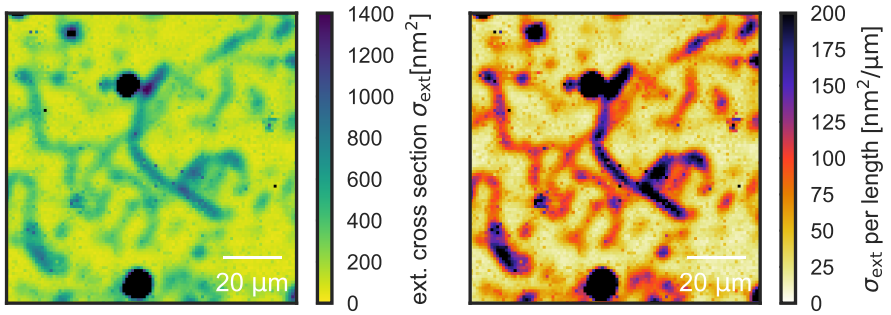

(a) **(b)**

Figure 5.1.2.: (a) Absorption scan of extended carbon nanotubes at 790 nm (sample CNT5). (b) Same scan normalized to extinction per nanotube length. The colourful scale is chosen to better differentiate tubes with different absorption levels.

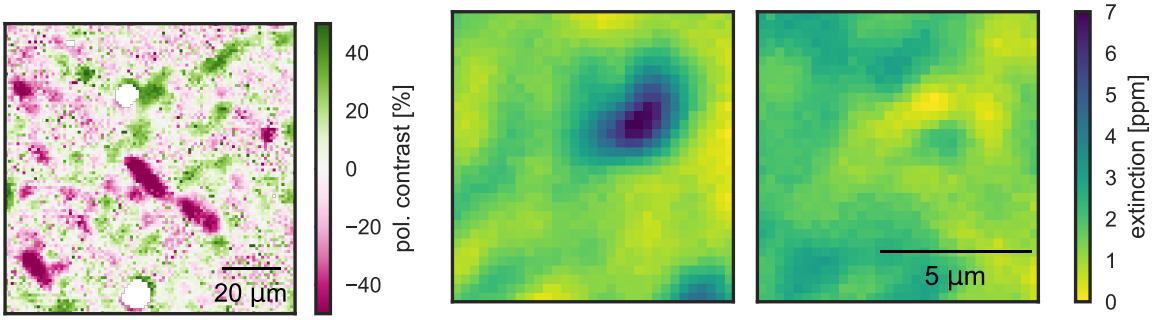

(a) **(b)**

Figure 5.1.3.: (a) Polarization contrast by subtracting two images with 90° polarization rotation. Approximately at the same scan area. (b) Measurement with orthogonal polarizations on sample CNT28-(9,1).

contrast between two scans is shown, for the same position as Fig. 5.1.2a. The contrast is given by

$$C_p = \frac{A_{0°} - A_{90°}}{A_{0°} + A_{90°}}, \tag{5.1.2}$$

where $A_{0°}$ and $A_{90°}$ is the measured absorption at the respective polarizations. High contrast, $|C_p| > 30\%$, can be seen at elongated objects rotated by $\pm 45°$ from the horizontal. The parallelism of these features and their angle leads to two conclusions: We see indeed elongated carbon nanotubes with strong absorption of light polarized parallel to their long axis and reduced absorption of perpendicular polarized light. Second, the axis rotated by $\pm 45°$ from the horizontal seem to be the polarization eigenaxis of the cavity, where the light was polarized, as features aligned with these axis show the strongest contrast.

To analyse arbitrary polarizations, a cavity mirror with reduced polarization splitting would be needed, or the cavity fibre would have to be rotated.

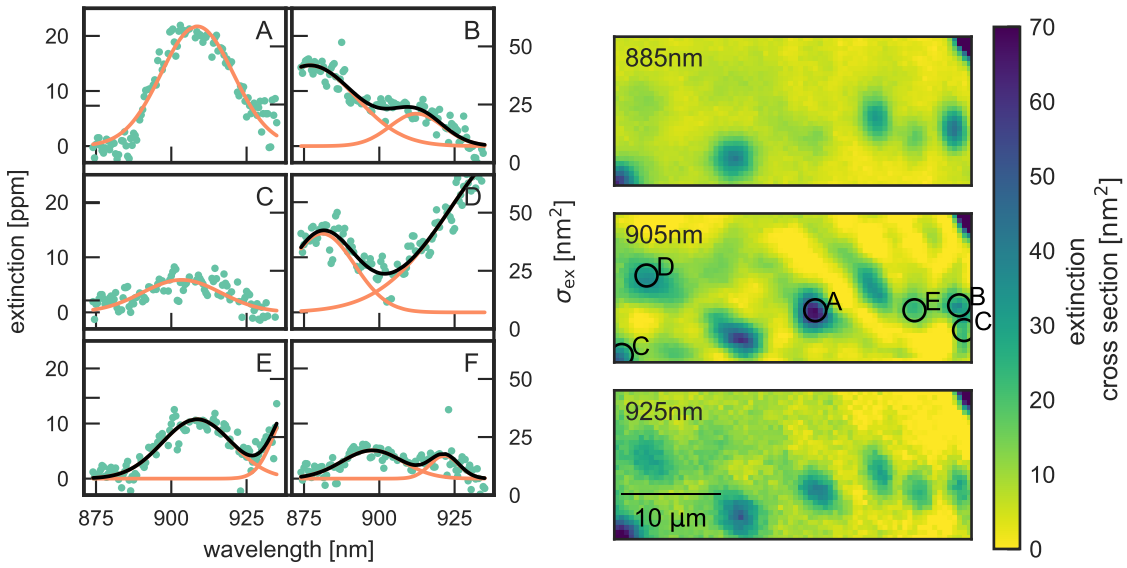

(a) (b)

Figure 5.1.4.: (a) Carbon nanotube extinction spectra extracted from the points labelled in (b). The lines are Gaussian fits, while the black line is the sum of two Gaussians. (b) Different wavelength images of a hyper-spectral extinction scan. The extinction of the various features changes differently with wavelength.

Spectral analysis

In Fig. 5.1.4a spectra of suspected carbon nanotubes are shown (sample CNT28-(8,3)). They are collected from the most significant spots in the extinction scan shown in Fig. 5.1.4b. Clearly, extinction peaked at different wavelengths can be seen. Gaussians peaks are fitted and their respective centre wavelengths and linewidth are shown in Fig. 5.1.5a. Excluding the higher wavelengths ($> 930\,\mathrm{nm}$) the FWHM linewidth is $25 \pm 6\,\mathrm{nm}$. To compare it to literature values, several previous studies of absorption and photoluminescence of carbon nanotubes are collected in Table 5.1.1. Most sources report linewidths of around $20\,\mathrm{nm}$ while some also report far broader lines. It has to be noted, however, that only a few measurements on individual nanotube extinction exist and that the properties of nanotubes in general depend strongly on the environment due to their high surface area and synthesis due to defect creation. We can see that our value for the linewidth agrees with the shown literature value.

The central wavelength of our tubes is $901 \pm 14\,\mathrm{nm}$. This wide spread is also present in fluorescence measurements on single tubes, where a span of $20\,\mathrm{nm}$ in centre wavelength and a factor of two in linewidth is reported, even for the same species[100]. The sample should be enriched (8,3) nanotubes which should show absorption at $950\,\mathrm{nm}$. And indeed we see from the fits some peaks at these wavelength, which is outside of our measurement wavelength range. However, more tubes are found at around $900\,\mathrm{nm}$, where (9,1) tubes are expected. Most probably we see a residual content of (9,1) tubes present in the sample. This is also supported by a measurement of a (8,3) tube sample, which shows much denser absorption at $900\,\mathrm{nm}$.

The peak extinction values are also spread in literature as well as in our measurements. Blancon et al.[103] compared one and the same nanotube suspended over a trench and on the

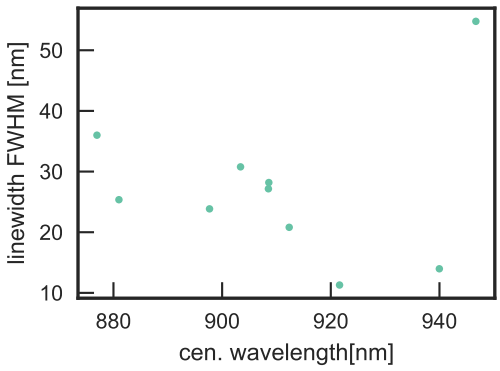

(a)

Figure 5.1.5.: Centre wavelengths and linewidths extracted from the spectra shown in Fig. 5.1.4a.

tubes	centre [nm]	linewidth FWHM [nm]	sample type	technique	peak abs. cross section [$\mathrm{nm}^2/\mu\mathrm{m}$]	peak abs. cross section [10^{-4}/C]
(9,1)? (8,3)?	901 ± 14 950	25 ± 6 60	single	cavity (this work)	>20-60	1.8-5.3
(8,3) (6,5) CoMoCat	952 986	60 70	single	spatial mod.[86]	40 80	3.5 7
(9,1)	895		single	PL@4K[101]	-	-
(6,4) (9,1) (8,3) (6,5)	81 ± 16 915 ± 16 955 ± 16 975 ± 16	21 (16-41)	single	PL[100]	-	-
(8,3) (6,5)		21 22	bulk	suspension orient. averaged[102]	200 299	17 25
(14,13) S_{33} (14,13) S_{33} CVD	642 663	16 78	single susp. single on Si	spatial mod.[103]	800 400	35 17

Table 5.1.1.: Examples of state of the art extinction (and two photoluminiscence (PL)) measurements on carbon nanotubes. The last row compares tubes on substrate to free-standing tubes.

sides where it touches a silicon substrates. At the substrate the tube exhibits shifted absorptions peaks that are broadened and have reduced peak absorption along with reduced polarization dependence.

The wide variety of absorption linewidths, cross sections, and peak positions found in this measurement as well as in the literature highlights the interest and importance of measuring extinction spectra on individual carbon nanotubes. To the best of my knowledge, absorption of individual nanotubes has so far only been measured using spatial modulation techniques.

Several improvements to the measurement process and sample could improve the gathered information. Better polarization stability of the incoupled light during a wavelength sweep or recording both polarizations simultaneously would improve the reliance of the spectral data independent of polarization effects. A more dilute sample would help to see if multiple absorption peaks originate from a single tube or from multiple different tubes sitting in close proximity. Combination with Raman spectroscopy, which is a straightforward possible with the cavity as we will see in the next chapter, could determine the radius and chirality of the tubes.

5.1.4. Raman spectroscopy

In the following, measurements of Raman spectra and images of carbon nanotubes will be presented. It will be shown that the spectra can be used to gain information on the nanotubes, often with a net signal gain using the cavity enhancement. A detailed explanation and derivation of the phonons involved in the process is not the scope of this work and the reader is referred to the excellent review by Dresselhaus et al. on Raman spectroscopy on carbon nanotubes[60].

Spectral features

In Fig. 5.1.6a a cavity based measurement of carbon nanotube spectra from individual nanotubes from sample CNT11 is shown. Several spectral features can be seen, varying in strength for different nanotubes.

For most spectra the D-band around $1300\,\mathrm{cm}^{-1}$, commonly associated with defects, is weak, which indicates high quality and pristine nanotubes as expected from the CVD growth process [60]. Only one tube shows a strong D feature and simultaneously a broadened $G^{\pm}$ band.

The $G^{\pm}$ band at $1590\,\mathrm{cm}^{-1}$ are phonons where adjacent carbon atoms move into opposite directions, as sketched in Fig. 5.1.6b[104]. Unlike in Graphite, where the individual G^{+} and G^{-} mode are degenerate, the symmetry breaking when rolling up the graphene sheet to form a nanotube, leads to a lifted degeneracy. The G^{-}band with atomic displacement along the circumferential direction is therefore lowered in frequency, as the curvature of the tube weakens the restoring forces in this direction.

The spectral distance between the G^{+} and G^{-} modes, $\Delta_{G^{\pm}}$, yields a simple yet accurate expression for the diameter of the carbon nanotube[60]

$$d_t = 6.8\,\mathrm{nm}\left(\Delta_{G^{\pm}}/\mathrm{cm}^{-1}\right)^{-1/2}. \tag{5.1.3}$$

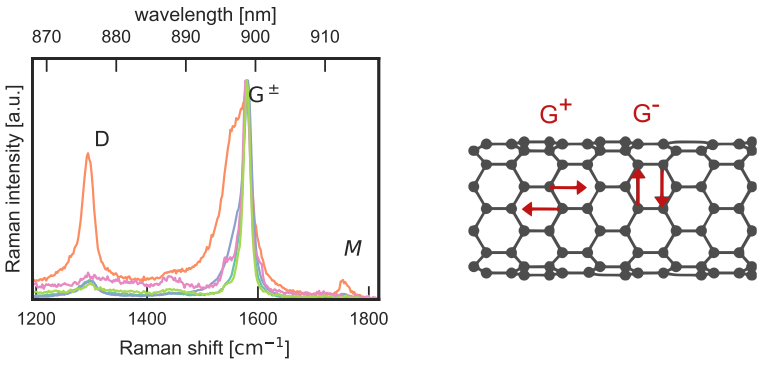

(a) **(b)**

Figure 5.1.6.: (a) Spectra of several carbon nanotubes normalized to their maximum intensity. Marked are the names of some Raman lines. (b) Sketch of a carbon nanotube with atomic motion in the G^+ and G^- vibrational modes.

This is valid for semiconducting tubes, while $d_t = 8.9\,\mathrm{nm}\left(\Delta_{G^\pm}/\mathrm{cm}^{-1}\right)^{-1/2}$ has to be used for metallic tubes.

The radial-breathing mode, where atoms move in the radial direction of the nanotube, shifts even stronger with the radius and would be even better suited to determine the tube diameter. However, due to its low Raman shift ($< 400\,\mathrm{cm}^{-1}$), it was not yet accessible in cavity enhanced measurements.

Hyper-spectral Raman imaging

When a Raman spectrum is collected at each point of a scan, hyper-spectral images can be collected. This is shown in Fig. 5.1.7a and Fig. 5.1.7b where the $G^\pm$ and G' band at $1590\,\mathrm{cm}^{-1}$ and $2650\,\mathrm{cm}^{-1}$, respectively, are visualized by integrating spectral bands of $20\,\mathrm{cm}^{-1}$ width. Clearly, elongated carbon nanotubes can be seen. Their location agrees well between the measurements and with the extinction scan shown in Fig. 5.1.7c.

This demonstrates that the the cavity can collect hyper-spectral information. However, this method to collect spectra and images is slower than confocal scans as many measurements at different cavity lengths need to be combined. Therefore we show in the following two methods for imaging where the cavity can actually improve measurement times.

To quickly acquire spatial Raman maps of carbon nanotubes, the cavity can be set resonant with a feature that is present in all tubes at the same Raman shift. This is for example the G^+ band at $1590\,\mathrm{cm}^{-1}$. It is rather strong and due to the large Raman shift low background is present. An image of such a scan for sample CNT11 is shown in Fig. 5.1.8. Individual nanotubes can be identified, yield a signal of typically $2\times10^4\,\mathrm{counts/s}$ and are stable at the used excitation power of $14\,\mathrm{mW}$. Also in the Raman scans it can be seen that the tubes of this sample are shorter than the tubes of sample CNT5.

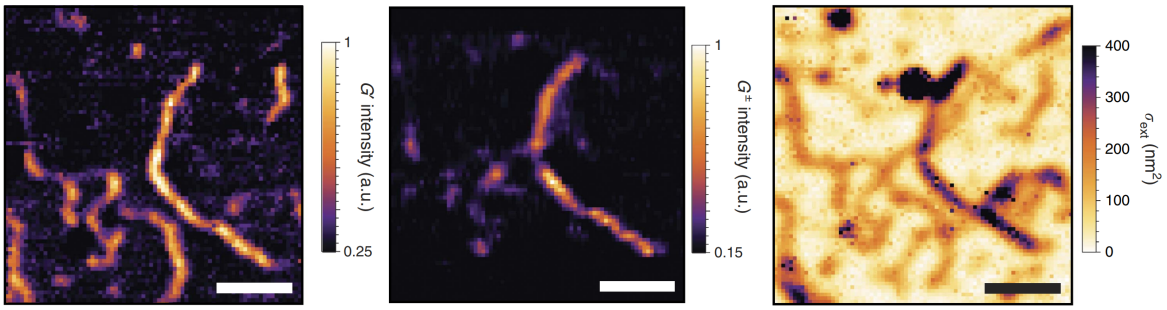

Figure 5.1.7.: Cavity enhanced Raman scan of sample CNT5 with (a) G' feature at $2650\,\mathrm{cm}^{-1}$ and (b) G^+ at $1590\,\mathrm{cm}^{-1}$. (c) Absorption scan at $790\,\mathrm{nm}$ for comparison. Scale bars are $20\,\mu\mathrm{m}$.

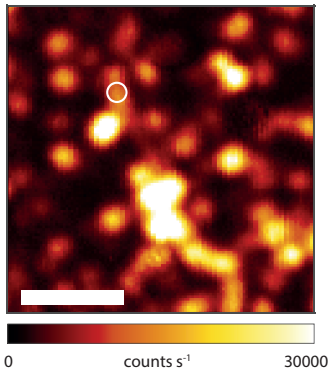

Figure 5.1.8.: Raman scan by stabilizing the cavity length to be resonant to the centre of the G^+ feature. Scale bar is $10\mu\mathrm{m}$.

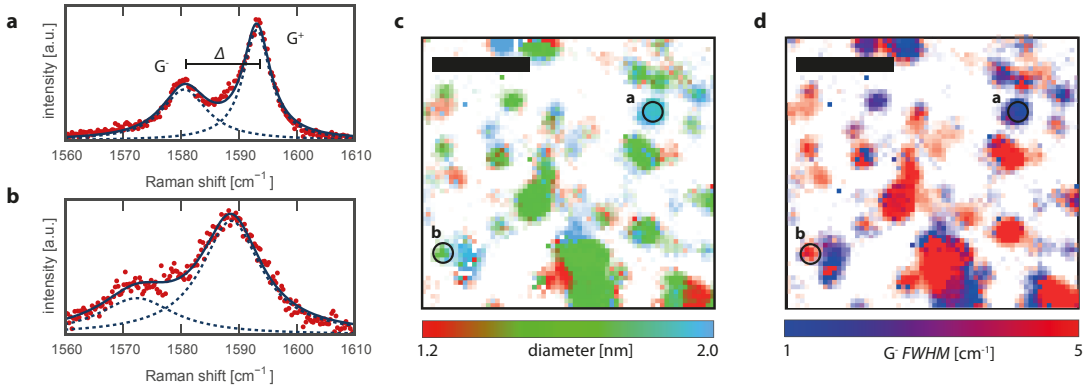

Figure 5.1.9.: (a) and (b) show tow exemplary measured spectra of a semiconducting and metallic nanotube (red dots). The difference between the $G^+$and G^- features is labelled Δ. The solid line is a sum of two Lorentzians fitted to the data and the dashed lines are the underlying individual Lorentzians of the $G^+$and G^- lines, respectively. (c) Extracted nanotube diameter (d) FWHM (full width at half maximum) linewidth of G^-line. Scale bars are $10\,\mu$m.

Broadband enhancement through modulated scan and species discrimination

As introduced in Section 2.4.2, by modulating the cavity resonance in a narrow spectral region, an effective time-averaged broadband enhancement can be achieved, and lineshapes or multiple lines in a spectrum can be measured. This way, hyperspectral images can be recorded. Here, this is used to spatially resolve properties of different carbon nanotubes by looking at linewidths and separations between lines. In Fig. 5.1.9 exemplary spectra at two different points, are shown. It can be seem that the $G^+$and G^- peaks differ strongly in their separation and linewidth. Fitting a sum of two Lorentzians to the spectra and doing this for each measurements, information on different nanotubes can be extracted. With the help of Eq. (5.1.3), the diameter of tubes is calculated from the splitting. In Fig. 5.1.9d, the width of the G^- resonances is evaluated . Here, clearly two different classes can be observed. Narrow linewidths of around $1\,\mathrm{cm}^{-1}$ hint at semiconducting nanotubes while broadened lines with $5\,\mathrm{cm}^{-1}$ hint at metallic nanotubes[60, 104]. For most of the nanotubes we obtain a clear indication of their diameter and electronic structure. This technique is particularly robust, since the cavity needs to be stabilized to a mirror separation within a few nanometres only.

5.2. 2D Materials

5.2.1. Introduction to 2D materials and transition metal dichalcogenides

Apart from Graphene[105], an atomically thin carbon film and the most prominent 2D material, in recent years a plethora of new single or few atom thin systems were isolated. A rather large class are transition metal dichalcogenides (TMDs), that allow exfoliation into two-dimensional layers of single unit cell thickness due to their layered structure with strong in-plane and weak out-of-plane bonds. They exhibit remarkable optical, spin, magnetic and (super) conductive properties for photo detectors, transistors, LEDs and solar cells[106, 107].

A recent advance, giving rise to a new class of materials is using multiple different monolayers and attaching them, even in desired angles, on top of each other[106]. Due to the forces holding

these layers together these materials are called *van der Waals solids*.

This chapter will look at the absorption properties of heterobilayers (HBLs) composed of the two TMDs $MoSe_2$ and WSe_2[108]. In this way we can get a taste of what cavity enhanced absorption microscopy and spectroscopy can reveal for 2D materials.

5.2.2. Sample preparation and transfer

Chemical vapour deposition (CVD) was used to grow $MoSe_2$ monolayers on a SiO_2 substrate and subsequently a WSe_2 monolayer was grown on top in a similar way[108]. Using this method the HBL self-assembles into triangular shaped flakes roughly $100\,\mu m$ in size. This sample was transferred to the cavity mirror by spin-coating PMMA (poly(methyl methacrylate)) onto it and lifting this supported film with the help of potassium hydroxide. In Fig. 5.2.1a the triangular shaped HBLs on the planar cavity mirror are shown.

5.2.3. Sample-locating using microscope

Using an optical microscope (common 30€ USB microscope) placed behind the planar cavity mirror, a wide-field image of a sample can be acquired while it is mounted inside the cavity setup. This can be used to locate the position on the sample if the sample is visible itself in some wavelength region. If not visible, at least markers on the mirror, or some dirt can be used as a position reference. As the HBL sample is absorbing in the visible spectrum, the exact location of the cavity on the HBL sample can be seen in Fig. 5.2.1a. In Fig. 5.2.1b even more details of the sample can be seen in-place by overlaying a microscope image taken beforehand in an conventional microscope.

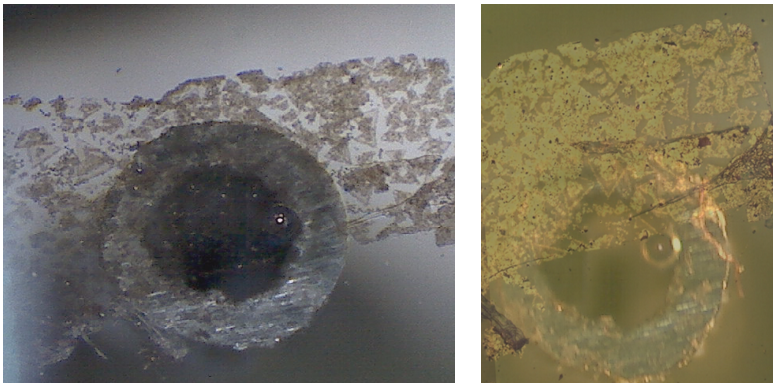

(a) **(b)**

Figure 5.2.1.: (a) Image from the back-side of the planar cavity mirror. The HBL sample can be seen as brownish triangles. The circular structure is the needle where the cavity fibre is glued to and can be seen inside on the right side. The cavity is in operation and the glowing core of the fibre can be seen. The outer diameter of the needle is 800µm (b) Again an image taken from behind the fibre but with an microscope image overlayed. The image was taken on a common optical microscope beforehand and combined using an image manipulation software.

5.2.4. Imaging sub structure

In Fig. 5.2.2, a scan of a distinctive feature of a HBL flake is shown both imaged using cavity enhanced absorption and in a conventional microscope. We see part of a triangular flake which seems to have a rupture going through it. The edges show strong extinction that can not be resolved in this measurement. This may be attributed to strong scattering. In the inner parts of the flake, the extinction is on the order of $800\,\mathrm{ppm}$ when measured at a wavelength of $930\,\mathrm{nm}$.

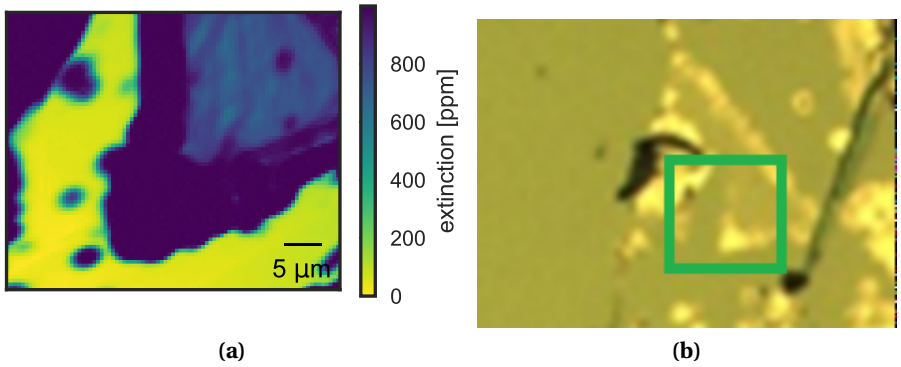

Figure 5.2.2.: (a) Extinction image of a part of a HBL flake at $930\,\mathrm{nm}$. (b) Conventional microscope image of this flake with the part scanned in (a) marked by the green rectangle.

In Fig. 5.2.3, a detail of the centre of the flake is shown for two different polarizations. In both images a sub-structure can be seen, deviating about $\pm 30\,\mathrm{ppm}$ from the mean. The length scales are in the µm region and is therefore only visible using high spatial resolution and high sensitivity extinction imaging. Elongated parts crossing through the centre of the flake show up, depending on polarization. It is so far unclear if this is due to variations in scattering or in absorption. The features are parallel to each other and may hint towards the crystal orientation or to ripples in the material from the transfer process. This structure is not present in the empty parts of the mirror and therefore attributed to the flake and not to some background.

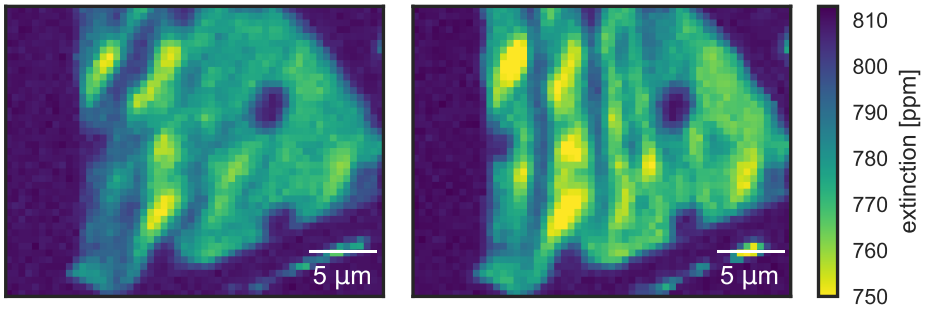

Figure 5.2.3.: Centre of HBL flake imaged with two different polarizations at $890\,\mathrm{nm}$.

5.2.5. Spectral analysis

Fig. 5.2.4a shows absorption spectra measured at the central part of the flake for two different polarizations, rotated by 90°. At $888\,\mathrm{nm}$ the polarization of the laser or the axis of the cavity birefringence flips in an uncontrolled way. This is not intended, and the peak and dip observed is an artefact of the measurement and not attributed to the material. However, this reveals a strong polarization dependence of absorption. We see that the absorption increases for one polarization while it decreases for the other. Also at other parts of the spectrum the absorption differs by up to a factor of three. Usually, no polarization dependent absorption should be expected from the used 2D materials. The observed dependence may originate from strain induced by the transfer process or interaction with the substrate.

Next, we try to explain the origin of the absorption. Due to the reduced dimensionality, two-dimensional TMDs have stronger Coulomb binding energies between holes and electrons than conventional semiconductors. This way, Coulomb-bound electron-hole pairs called excitons form, with a reduced energy compared to the ad-hoc expected band gap energy of the semiconductor[107]. Signatures of these strong ("intralayer") excitons can be seen in photoluminiscence (PL) spectra in Fig. 5.2.4b at wavelength $\approx 800\,\mathrm{nm}$ ($\approx 1.55\,\mathrm{eV}$) for $MoSe_2$ and $\approx 750\,\mathrm{nm}$($\approx 1.65\,\mathrm{eV}$) for WSe_2[109, 110]. This is well below the wavelengths where the absorption measurement was performed. One possibility of the observed absorption might be from from strongly off-resonant "tails" of these excitons. However, a better explanation might be weaker bound "interlayer" excitons. When combining two TMD layers, weak "interlayer" excitons can form by spatially separated electrons and holes residing in the different layers. This is sketched in the band structure diagram in Fig. 5.2.4c. They are mainly observed in PL at low temperatures and have their emission peak at around $890\,\mathrm{nm}$ at $20\,\mathrm{K}$ and $910\,\mathrm{nm}$ at room temperature.

Absorption is also visible at shorter wavelengths (higher energies) than PL. This can be explained by fast phonon-assisted non-radiative relaxation, only making the lowest energy state in the conduction excitonic band visible in PL, see Fig. 5.2.4c. In contrast to this, in absorption also transitions to higher excited states can be seen. This is an example for the relevance of sensitive absorption measurements, as they can reveal complementary information to emission measurements.

Certainly, measurements with more control over polarization, at lower temperatures and spanning a broader wavelength range would be of interest.

5.3. Gas sensing

Micro-cavity enhanced Raman spectroscopy of gases was first performed by Petrak et al.[17] in 2014. Here, atmospheric gases where detected using a fibre-fibre micro-cavity. To make the weak Raman signal detectable, the signal was enhanced double resonantly in excitation and collection. At both wavelengths a finesse of around 10000 was used. This work was extended to allow isotopic differentiation of CO_2 and a finesse of 30000[18]. In a subsequent work the cavity mode volume was further reduced by shrinking the mirror distance to $2\,\mu\mathrm{m}$, the radius of curvature to $50\,\mu\mathrm{m}$. There, the detection of about 2×10^5 CO_2 molecules at atmospheric pressure with 1000 photons/s is claimed[111].

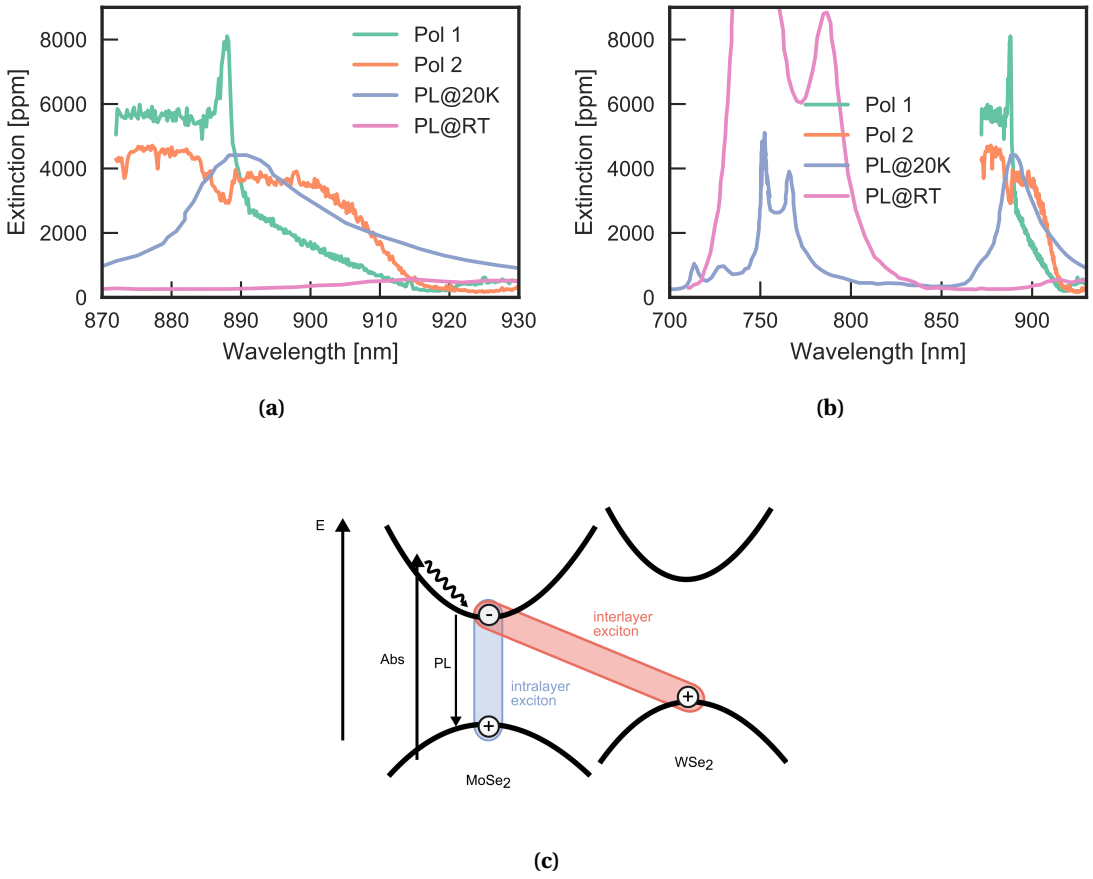

Figure 5.2.4.: (a) Absorption spectra of the inside of a flake for two different polarizations ("Pol 1/2"). Furthermore, photoluminescence spectra at room temperature ("PL@RT") and at 20 Kelvin ("PL@20K") of interlayer excitons taken from[109] are shown (in arbitrary units). (b) Zoomed out view of (a) where the intralayer excitons at lower wavelength (higher energy) can be seen in PL. (c) Band structure of $MoSe_2$ and WSe_2 where electrons (-) and holes (+) can form "intralayer" (blue) or "interlayer" (red) excitons. The wiggly line denotes non-radiative relaxation, potentially explaining the shorter wavelengths observed in absorption ("Abs") and PL.

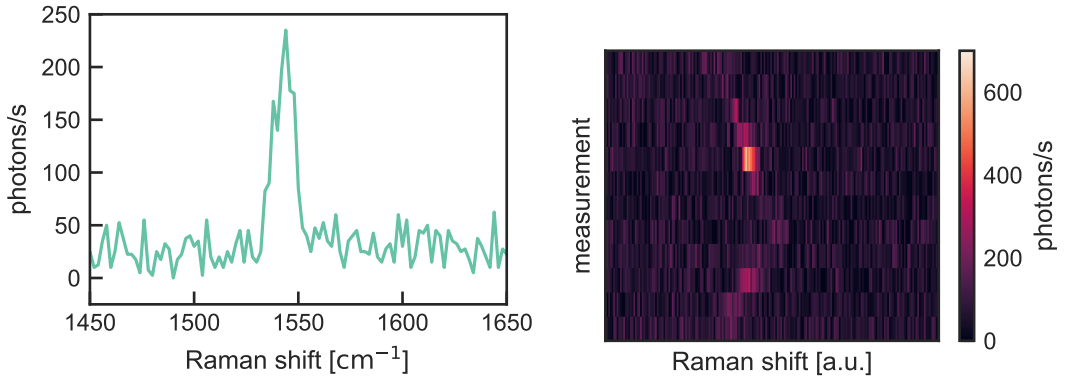

(a) **(b)**

Figure 5.3.1.: (a) Suspected Raman signature of O_2. (b) Sweeping of cavity resonance over the Raman feature.

Here, it is shown that this detection can be further simplified using the tailored coating. With this coating it is possible to measure at the shortest cavity length after touching of the two mirrors while spanning hundreds of cm^{-1}. The measurement volume is even more reduced by smaller radii of curvature mirrors and shorter cavity length.

As can be seen in Fig. 5.3.1a, at $1544\,\mathrm{cm}^{-1}$ a peak is observed. As this peak is present in all measurement it is attributed to the vibration mode of O_2 which is expected at $1556\,\mathrm{cm}^{-1}$ according to literature[112]. The slight shift of the line lies inside the calibration uncertainty of the spectrometer. The linewidth is limited by the spectrometer detection, smaller than $10\,\mathrm{cm}^{-1}$. The highest signal detected was 3.3×10^3 photons/s and the peak power in the cavity about $1\,\mathrm{W}$ at $823\,\mathrm{nm}$.

In a coarse approximation we can calculate the photons extracted per molecule. Assuming a physical cavity length between the mirror surfaces of $1\mu\mathrm{m}$ (of which $0.4\mu\mathrm{m}$ are the mirror profile depth) and the radius of curvature of the fibre mirror of $25\,\mu\mathrm{m}$,the part of the cavity mode volume residing outside of the optical coating is about $1\,\mu\mathrm{m}^3$. With 21% Oxygen in air and $22.4\,\mathrm{l/mol}$ at atmospheric pressure, $5\times10^6 O_2$ molecules are expected to contribute to the Raman signal.

With even higher excitation powers, cavity enhanced gas sensing of other trace molecules by their Raman signature may become feasible. With the tailored coating and an the optical feedback laser presented this might be integrated in a tiny easy to operate sensor.

6. Conclusion and outlook

Spectrally resolved scanning cavity microscopy for absorption and Raman scattering has been demonstrated in this work for the first time. To achieve high sensitivity and measurement speed, several technologies and methods have been introduced, ranging from digital electronics for fast data acquisition, a stable mechanical cavity setup and tunable lasers to custom made optical coatings.

Measurements on low dimensional solid state materials were shown to reveal information on phononic, electronic and structural properties.

As microscopy is an enabling technology for other fields of research, the current possibilities and further improvements as a general tool will be explored here.

6.1. Real-time extinction microscopy

Cavity enhanced extinction microscopy and spectroscopy with state-of-the-art sensitivity, low spectral and spatial background and fast measurement speeds was shown.

Using a stable ($< 200\,\mathrm{pm}$), high first-resonance frequency mechanical setup and integrated electronics, extinction at a single point was recorded at a rate of up to $1\,\mathrm{MHz}$ at the sub-ppm noise level. By means of mere averaging a noise limit of $0.01\,\mathrm{ppm}$ was achieved in $0.1\mathrm{s}$ integration time.

Real-time microscopic imaging across $80 \times 60\,\mu\mathrm{m}$ with a spatial resolution of $1\mu\mathrm{m}$ was shown. Spatially resolved measurements showed clear absorption signals of single carbon nanotubes on the few ppm level. The imaging of spatial substructure in 2D materials provides a hint that measurements on "strongly" (here around $0.1\% = 1000\,\mathrm{ppm}$) absorbing samples can still provide new insight by looking variations that are orders of magnitude smaller.

Spectra of carbon nanotubes were collected with $< 1\,\mathrm{ppm}$ detection threshold. Furthermore, absolute values of the absorption cross section could be extracted, in agreement with literature values.

Potential as a microscopy tool for research

The sensitivity and robustness of cavity enhanced extinction measurements shown in this work make it a candidate for a general applicable powerful microscopy tool. By looking at tiny, previously inaccessible optical absorption signatures researchers might get new insight into properties of nanoscale matter. The different samples and various methods of transfer onto the planar mirror demonstrate the general applicability of the microscope.

To reach different fields of research, however, a few more steps are needed to advance the technique from the first proof of principle measurements shown here to a usable tool. Increased measurement speed by more than four orders of magnitude was shown in this work.

This already improves usability, as the presented real-time scanning simplifies orientation and locating parts of a samples.

One area where the techniques is currently limited is the wavelength region of absorption spectra that can be accessed with cavity enhancement. This is set by the width of the high reflectivity coating stop-band. Designing an optimized coating that provides a moderate finesse over a broad wavelength region could improve the accessible wavelength region of a singe cavity beyond $150\,\mathrm{nm}$.

As many absorptive features are broadened or washed out at room temperature, a simple to operate cavity-based cryogenic absorption microscope could gain much deeper insight into nano-materials. First steps to a cryostat compatible setup were taken here by miniaturization of the setup and a design accounting for reduced piezo ranges at low temperatures.

Using broadband light sources and integrating detectors it was shown that absorption down to the few parts-per-billion level could potentially be measured with just pico-watts of intensity at the sample. This enables absorption measurements where other methods would destroy the sample, which could be especially relevant for applications in the life sciences.

Improvement in sensitivity

The reported sensitivity levels were achieved without thorough optimization. In contrast to other sensitive absorption measurement techniques, a lot of tricks can still be played. Using better light sources, careful measurement procedure optimization and post-processing provides a lot of room for improvements.

Using sophisticated detectors and electronics, like balanced photodetectors, low-noise pre-amplifiers and appropriate filtering, transmission was measured down to 10^{-6} in free space direct absorption measurements[47]. Directly transferring these techniques to measurements of the transmission of a cavity with finesse 100.000 [1] might enable to measure absorption (at a single point) in the parts-per-trillion magnitude.

Spatial resolved measurements, however, would require fairly clean samples and noise would be limited by intrinsic variations of background scattering and absorption present in the imperfect mirror surface. However, filtering this noise by its broadband spectral behaviour, post-processing images of sparsely separated nanoparticles and fibres and mirrors with reduced scattering could reduce the spatial background to few parts per billion.

Time resolved measurements

A key property of cavity enhanced absorption measurements, in contrast to other techniques, is that the fundamental gain in sensitivity is not based on averaging or lock-in detection. Therefore, another vast dimension that could be explored are sensitive time-resolved absorption measurements. As the cavity power build-up happens on nanosecond timescales, using fast photodetectors might allow absorption measurements with rates of several MHz. In combination with microscopy, fast time-dependent absorption processes in single nanoscale systems could be observed.

[1] Finesse of 170.000 was already demonstrated in our group[35]

6.2. Cavity enhanced Raman scattering

It was shown that by means of the Purcell effect, Raman scattering from carbon nanotubes inside the cavity can be enhanced. For the first time, this has been presented for single solid state systems in a controlled way. By directly comparing Raman emission strength of one and the same individual carbon nanotube inside the cavity to a free-space confocal measurement, the Purcell factor was determined. Furthermore, the expected scaling inversely with the mode volume of the cavity was shown. At the shortest cavity length an effective Purcell factor of 6 was determined and an ideal Purcell factor of 320. The efficiency of collecting the Raman scattered light was up to 60% , on par with the best oil-immersion objectives.

Hyperspectral cavity enhanced Raman imaging was shown to reveal information on the diameter and electronic properties of individual carbon nanotubes.

To further boost signals, Raman spectroscopy was extended to a scheme where the excitation laser and Raman scattering are simultaneously resonant with different longitudinal modes of the cavity. To this end, a tailored dielectric mirror coating was developed and characterized. It provides a wide continuously accessible region of the Raman spectrum ($900\,\mathrm{cm}^{-1}$to $1800\,\mathrm{cm}^{-1}$) by simply adjusting the cavity length. Thereby, it was discovered that the strong curvature of the micro-sized mirror affects light penetration into the high-reflective coating by variations of the effective thickness of the Bragg reflector layers.

With smaller mode volumes, effective Purcell factors of up to 40 are expected. However, the Purcell factor of smaller cavities and the double resonant Raman enhancement could not yet be determined due to problems with the general stability of the new carbon nanotube sample. However, first measurements are promising and show count rates exceeding the single resonant case by at least one order of magnitude.

Potential as a microscopy tool for research

In contrast to extinction spectroscopy, the gain of sensitivity and speed is lower for cavity enhanced Raman scattering than for extinction measurements. This is due to the fact that the effective Purcell factor is limited by the broad Raman features of solid state systems and therefore only scales with the inverse mode volume. This reduces the potential of a stand-alone Raman microscope based on cavity enhancement. However, as has been shown, Raman spectra can be recorded in addition to cavity enhanced extinction measurements, using the same setup and on the same position of the sample. This can help to reveal complementary information on the sample.

Furthermore, acquiring Raman spectra can be simplified in contrast to conventional Raman microscopes as no objective and in particular no spectrometer is required. The spectral information could be gained from the the cavity length directly.

Raman fluid sensor

With strong double resonance enhancement, a new pervasive signal was seen and attributed to Raman scattering at oxygen in air. The sampled volume is calculated to be only on the order of a pico-litre. This points out an application beyond microscopy: A miniature sensor that detects or analyses gases or liquids by their Raman scattering signature. Such a device might

be sensitive, inexpensive and broadband through the tailored mirror coating in combination with the presented optical feedback laser.

6.3. A quantum optics platform

The high mechanical stability of the cavity is another a key result of this work. It provides a three order magnitude better passive cavity length stability than the previous scanning cavity setup. A stable resonance frequency is crucial for coupling the cavity to solid state quantum emitters with linewidths narrower than the cavity line. This can be found for example in rare-earth ions, colour centres in diamond or semiconductor quantum dots at liquid helium temperatures. The stability together with transversal scanning can provide a way to first locate suitable quantum emitters and then strongly couple to them for fundamental research, quantum computation or quantum communication.

This way the presented cavity setup could be a general applicable platform for cavity quantum optical experiments and devices.

Appendix

This appendix is meant to be a hands-on-guide for following students and researchers working with fibre cavities. All calculations, simulations, data analysis and code used to create the graphics found in this appendix are available as source code. This should speed-up data analysis for following students and to improve reproducibility, understanding and minimize repeated work.

The data analysis and simulation is all performed using the python programming language and provided as an interactive computing Jupyter notebook[113, 114, 115], a structured document providing python code cells, plots (generated with the matplotlib[116] toolkit) explanatory text and sections, as can be seen in Fig. .0.1. The sections of the notebook are named accordingly to the sections used here and each figure used is annotated with an identifier to find the corresponding source inside the notebook file. Furthermore, the whole text of this appendix and all the contained formulas are available as a LaTeX and LyX files.

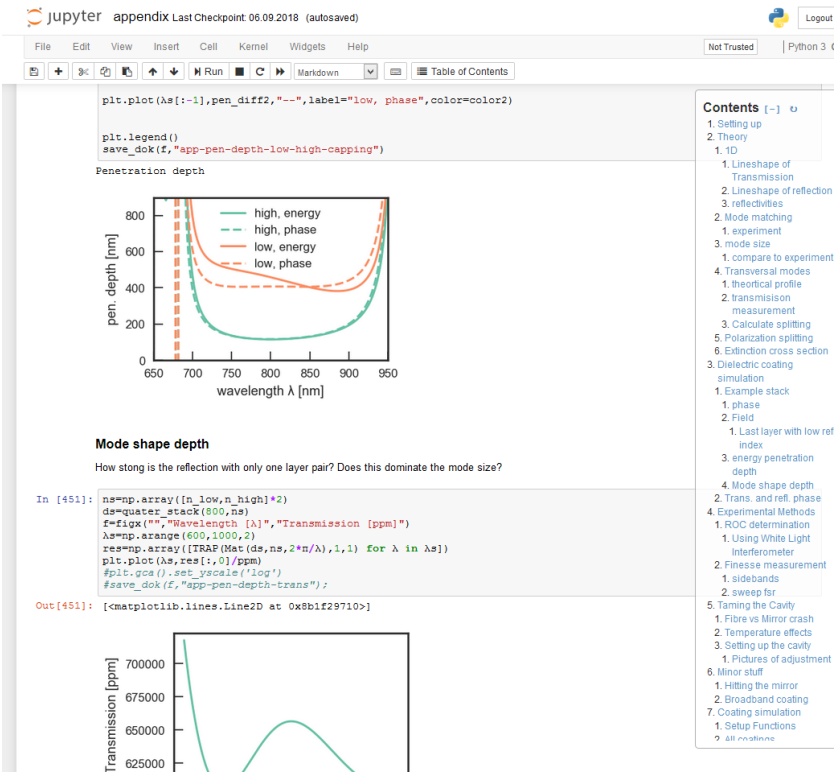

Figure .0.1.: Screenshot of the python Jupyter notebook of the calculations, simulations, data analysis and plotting used for creating this appendix.

A. Theoretical derivations

A.1. Cavity 1D modelling: transmission, reflection, out-coupling and power build-up

In this chapter, we derive key properties of the cavity, such as its transmission, reflection and field enhancement from the fundamental interference of light reflected at its mirrors. We model the cavity mirrors by simple "lumped" transversally infinite sized elements, which act on an incoming plane electromagnetic wave with reflection, absorption and transmission including possible phase shifts. These macroscopic properties of the mirror stacks can be measured or calculated from detailed thin film calculations as in Appendix C.1.1.

This derivation should be complete to include

- transmission, reflection, intra-cavity power, and out-coupling of light originating from inside the cavity
- on an off resonance and in between
- for high and low finesse cavities
- for cavities with asymmetric mirrors
- effects from additional loss channels by objects inside the cavity

This is done in detail here because often the derivations in the literature[33, 32] only focus on edge cases like highly reflective mirrors or symmetric cavities. However, these important special cases will be derived as well to get insight through easily understandable expressions.

The calculations are valid for the 'continuous wave' regime where the timescales of illumination are significant longer than the round-trip time between the cavity mirrors and allow a quasi-stationary interference to build up.

A.1.1. General effect of multi-reflection interference

We will start here with a general treatment of cavity resonances and later on analyse different cavity phenomena like transmission and reflection and there discuss the detailed dependence on wavelength and cavity length.

The key property of a cavity - e.g. in contrast to an interferometer - is that the final field is composed of *infinite* attenuated copies of an initial wave by reflection at its mirrors. This is sketched in Fig. A.1.1a. The most fundamental cavity properties can be simply derived and understood by calculating the field generated by the interferences. These lead to general resonances that later also manifest in resonances for transmission, reflection, power build-up in the cavity and more.

The spatial part of a continuous monochromatic plain wave with amplitude u_0 and wave vector $k = \frac{2\pi}{\lambda}$ travelling along the cavity axis z can be expressed as

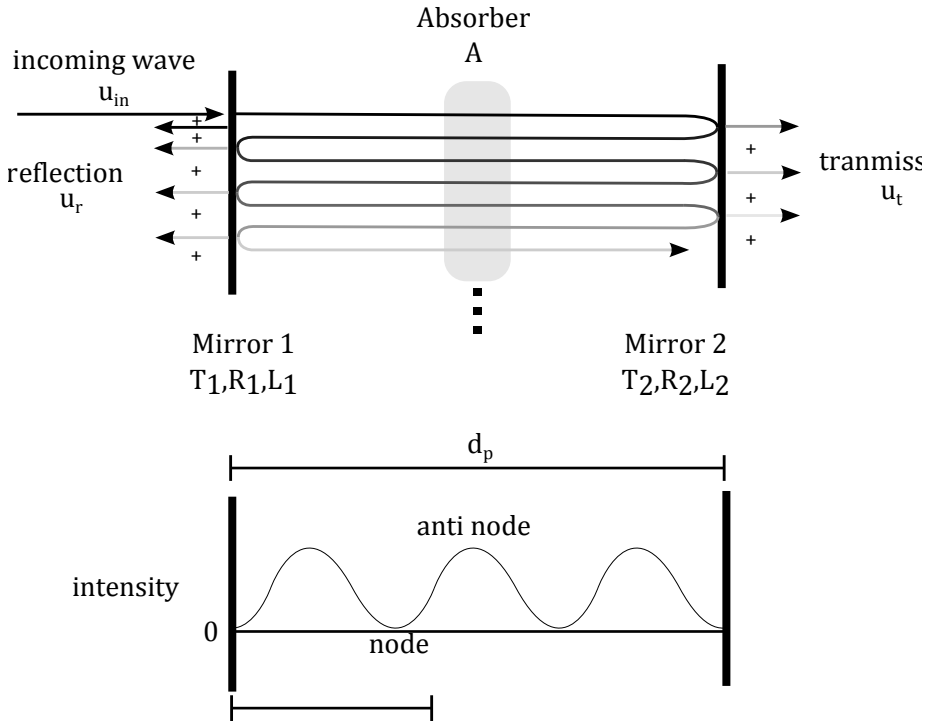

Figure A.1.1.: (a) Schematic of an incoming travelling wave between the mirrors of a cavity. For a continuous wave, the total field in reflection, transmission and inside the cavity are superpositions of the multiple reflected beams forming in (b) a standing wave pattern in the resonator.

$$u\left(z\right)=u_{0}e^{ikz}\,. \tag{A.1.1}$$

The two mirrors forming the resonator are represented by complex valued coefficients for reflection, $r_{1,2}$, absorption, $l_{1,2}$, and transmission, $t_{1,2}$ that may in general depend on the frequency of the wave. The coefficients for the field have their real-valued equivalents for the reflected, $R_i=|r_i|^2$, lost $L_i=|l_i|^2$, and transmitted, $T_i=|t_i|^2$, intensity. Conservation of energy demands $R_i+T_i+L_i=1$ for each mirror. Losses include scattering and absorption at the mirrors.

After each full round-trip between the two mirrors, a wave u_0 impinging onto a cavity mirror, is replicated with a (attenuated) copy of itself,

$$u_1=u_0 a\,e^{i\varphi}\,. \tag{A.1.2}$$

The introduced real-valued transmission (a) and phase (φ) factors are defined by

$$a\,e^{i\varphi}\equiv t_A^2 r_1 r_2 e^{i(2d_p(2\pi/\lambda n))}=|t_A|^2\,|r_1|\,|r_2|\,e^{i(2d_p(2\pi/\lambda n)+\arg r_1+\arg r_2+2\arg t_A)} \tag{A.1.3}$$

and include all the effects during the round trip: Finite reflection and phase shifts at the mirrors ($|r_i|\,,\arg r_i$). Furthermore a phase picked up by free propagation forth and back between the mirrors, separated by distance d_p, filled by a medium with refractive index n ($2d_p(2\pi/\lambda n)$). Also

included is finite transmission and a phase shift by an arbitrary object placed between the cavity mirror ($|t_A|$,$\arg t_A$). The coefficient is squared because it passes by the object twice each round-trip.

Since we apply a continuous wave, all these partial waves exist simultaneously and one has to sum over them to get the final superpositioned field

$$u = u_0 \sum_{n=0}^{\infty} \left(ae^{i\varphi}\right)^n = u_0 \frac{1}{1-ae^{i\varphi}} \,. \tag{A.1.4}$$

Here, the formula for the geometric series was used to rewrite the summation, which converges for $a < 1$.

The intensity of the total field, normalized to the initial field, is (from the absolute square of the field strength)

$$\begin{aligned} I_f &= \left|\frac{u}{u_0}\right|^2 = \left|1-ae^{i\varphi}\right|^{-2} \\ &= \frac{1}{1+a^2-2\cos(\varphi)} \\ &= \frac{1}{(1-a)^2+4a\sin^2(\varphi/2)} \,. \end{aligned} \tag{A.1.5}$$

We see that the infinite reflections can enhance or suppress the initial field, depending on the phase φ collected per cavity round-trip. The maximum of the intensity is observed when the *resonance condition* is met

$$\varphi = q \times 2\pi \qquad \text{with q} = 0, 1, 2, \ldots \tag{A.1.6}$$

meaning the phase collected per full cavity roundtrip is a multiple of 2π and the field therefore reproduces itself. There, the normalized maximum intensity is

$$I_{\text{max}} = \frac{1}{(1-a)^2} \,. \tag{A.1.7}$$

The minimum intensity is found at $\varphi = (q+1/2) \times 2\pi$ and given by

$$I_{\text{min}} = \frac{1}{(1+a)^2} \,. \tag{A.1.8}$$

A.1.2. Resonance and Finesse

We ca can rewrite the line shape using $I_{\text{max}}$to read

$$I_f = I_{\text{max}} \frac{1}{1+\frac{4a}{(1-a)^2}\sin^2(\varphi/2)} \,. \tag{A.1.9}$$

which has a full width at half maximum (FWHM) of

$$\delta\varphi = 4\arcsin\left(\frac{1-a}{2\sqrt{a}}\right). \tag{A.1.10}$$

For perfectly reflective mirrors, we would get infinitely sharp resonances, $\delta\varphi \to 0$, and only certain discrete wavelengths lead to constructive interference, reproducing themselves. These wavelengths are called to be *resonant* with the cavity. The field distribution fulfilling these properties for a certain cavity are called the eigen-modes, or short '*modes*' of a cavity.

We introduce a common figure to describe cavities, the *finesse*, as the distance between two resonance maxima divided by the FWHM linewidth

$$\boxed{\mathcal{F} \equiv \frac{2\pi}{\delta\varphi}} \tag{A.1.11}$$

The higher the finesse, the narrower the cavity resonances. The finesse is fully defined by the cavity's losses

$$\mathcal{F} = \frac{\pi}{2\arcsin\left(\frac{1-a}{2\sqrt{a}}\right)} \tag{A.1.12}$$

and in the next section we will see that this formula simplifies significantly when assuming low losses. The can be understood to quantify how many round-trips a photon takes in the cavity on average.

A.1.3. Approximations for low losses

The formulas up to now were exact for any level of reflectivity or absorption in the resonator. In the experiments we commonly employ highly reflective mirrors and low losses, meaning $a \approx 1$, to boost the signals at resonance, Eq. (A.1.7). We call this the regime of high finesse resonators.

In this case, I_f is small except in a narrow region around the resonances $\varphi_0 = q\pi$ and we can linearise $\sin$ and $\arcsin$ in the expressions of the lineshape (Appendix A.1.2) and linewidth (Eq. (A.1.10)) . With this, the peak approaches a Lorentzian line shape

$$I_f \approx I_{\max}\frac{1}{1 + {}^4/_{\delta\varphi^2}\,(\varphi_0 - \tilde{\varphi})^2}. \tag{A.1.13}$$

with FWHM

$$\delta\varphi \approx \frac{1-a}{\sqrt{a}} \tag{A.1.14}$$

and amplitude $I_{\max}$. $\tilde{\varphi}$ is the the phase detuning from the resonance. This can also be written in terms of the finesse

$$I_f \approx I_{\max}\frac{1}{1 + \left(\frac{\mathcal{F}}{\pi}\right)^2(\varphi_0 - \tilde{\varphi})^2} \tag{A.1.15}$$

Furthermore, the finesse simplifies to

$$\mathcal{F} \approx \frac{\pi\sqrt{a}}{1-a}\,. \tag{A.1.16}$$

As a side note, for symmetric cavity with $R \equiv R_1 = R_2$ with no absorption ($L_i = 0$, $A = 0$), this simplifies to often used formula for the finesse

$$\mathcal{F} = \frac{\pi\sqrt{R}}{1-R}\,. \tag{A.1.17}$$

Also for asymmetric cavities a simplified expression can be found when all the individual loss channels are small. To this end we introduce the power loss when passing the object in the cavity A via $|t_A| = \sqrt{1-A}$. We rewrite the round-trip transmission factor, a, in terms of mirror transmission, mirror absorption and the absorption by the object inside the cavity and do some approximations

$$\begin{aligned} a &= \left|r_1 r_2 t_A^2\right| = \sqrt{R_1 R_2}\,(1-A) \\ &= \sqrt{(1-T_1-L_1)}\sqrt{(1-T_2-L_2)}\,(1-A) \\ &\approx \left(1-\frac{1}{2}\,(T_1+L_1)\right)\left(1-\frac{1}{2}\,(T_2+L_2)\right)(1-A) \\ &\approx 1-\frac{1}{2}\,(T_1+T_2+L_1+L_2)-A = 1-\frac{1}{2}L_\Sigma\,. \end{aligned} \tag{A.1.18}$$

In the third line we Taylor expanded the square roots around 1 and in the last line omitted second and higher higher order terms in L_i, T_i, A. This formula is a good approximation if the losses are below a few percent. This leads to the simple relation that the finesse is inversely proportional to the sum of all the loss channels of the cavity, $L_\Sigma = T_1 + T_2 + L_1 + L_2 + 2A$,

$$\boxed{\mathcal{F} \approx \frac{2\pi}{L_\Sigma} = \frac{2\pi}{T_1+T_2+L_1+L_2+2A}\,.} \tag{A.1.19}$$

A.1.4. Transmission

Now let's calculate a measurable quantity of the cavity, namely the transmitted power through the cavity. Without loss of generality we conveniently denote here the mirror, from which light is coupled in with index 1 and the mirror behind which the transmission is measured with 2. The transmitted field ,u_t, normalized to the incoming field, u_{in}, can be found by multiplying the coefficients for transmission through mirror 1, intra-cavity transmission, free propagation through the cavity length and transmission through mirror 2. Furthermore, this has do be done for all number of round-trips, yielding

$$\frac{u_t}{u_{\text{in}}} = t_1 t_A e^{i(2\pi/\lambda n)} t_2 \sum_{n=0}^{\infty} \left(a e^{i\varphi}\right)^n\,. \tag{A.1.20}$$

The fraction of the intensity transmitted then evaluates to

$$T_{\text{c}} = \left|\frac{u_t}{u_{\text{in}}}\right|^2 = T_1 T_2 \sqrt{1-A}\, I_f = T_1 T_2 \sqrt{1-A}\,\frac{I_{\text{max}}}{1+\left({}^2/_{\delta\varphi}\right)^2 (\varphi_0-\tilde{\varphi})^2}\,. \tag{A.1.21}$$

We see that the transmission as a function of cavity length or wavelength (entering into φ) derives from $I_f(\varphi)$ and therefore usually takes a Lorentzian lineshape with transmission only around the cavity resonances.

The maximum transmission at resonance ($\tilde{\varphi} = \varphi_0$) is

$$T_{\mathrm{c,res}} = \frac{T_1 T_2 \sqrt{1-A}}{\left(1 - \sqrt{(1-T_1-L_1)(1-T_2-L_2)}\,(1-A)\right)^2} \tag{A.1.22}$$

and even can become unity in the case for symmetric cavities, $T_1 = T_2$, and in the absence of losses. This can be explained by constructive interference in forward direction and destructive interference in reflection.

For high finesse (low losses, low transmission) cavities, through expansion of the denominator in first order of losses and transmission (cf. Eq. (A.1.18)), the transmission on resonance can be approximated by

$$\boxed{T_{\mathrm{c,res,lowloss}} \approx \frac{4T_1T_2}{(T_1+T_2+L_1+L_2+2A)^2} = T_1T_2\frac{\mathcal{F}^2}{\pi^2}} \tag{A.1.23}$$

If we keep the cavity mirror parameters fixed and just vary the additional absorption inside the cavity, A, we see that in this case the transmission is approximately proportional to the square of the finesse

$$T_{\mathrm{c,res}}(A) \approx \mathcal{F}^2(A)/\pi T_1 T_2\sqrt{1-A} \approx \mathcal{F}^2/\pi T_1 T_2 \propto \mathcal{F}^2(A)\ . \tag{A.1.24}$$

For very highly transmissive mirrors the cavity transmission approaches to the product of the individual mirror transmission as would be expected without any interference effects

$$T_{\mathrm{c,res,highT}} = T_1 T_2\,. \tag{A.1.25}$$

A.1.5. Reflection

The reflection from the cavity can be calculated in a similar way as the transmission. We have to sum the light entering the cavity through mirror 1, getting reflected at the mirror 2 and leaving the cavity again through mirror 1 plus the infinite copies by full cavity round-trips. Furthermore we have to add the light directly reflected at mirror 1. Note that the light impinges from the outside of the cavity mirror, not from the inside, where the reflection phase factor and amplitude factor need not to be necessarily the same as from the inside. Therefore, we name the reflection and transmission coefficients for light coming from this site differently, $r_{1,\mathrm{out}}$ and $t_{1,\mathrm{out}}$. The reflected field (u_r) normalized to the incoming field (u_{in}) can be written as

$$\frac{u_r}{u_{\mathrm{in}}} = r_{1,\mathrm{out}} + t_{1,\mathrm{out}} t_1 r_1^{-1} a e^{-i\varphi} \sum_{n=0}^{\infty} \left(a e^{i\varphi}\right)^n\ , \tag{A.1.26}$$

where we used that $r_1^{-1} a e^{-i\varphi}$ is the full cavity round-trip except for the reflection at mirror 1. For a simpler evaluation we factor out some parts and separate the amplitudes and the phases

$$\begin{aligned}\frac{u_r}{u_{\text{in}}} &= r_{1,\text{out}}\frac{1}{1-ae^{i\varphi}}\left(\left(1-ae^{i\varphi}\right)+\frac{t_{1,\text{out}}t_1}{r_{1,\text{out}}r_1}ae^{i\varphi}\right)\\ &= r_{1,\text{out}}\frac{1}{1-ae^{i\varphi}}\left(\left(1-ae^{i\varphi}\right)+\left|\frac{t_{1,\text{out}}t_1}{r_{1,\text{out}}r_1}\right|^2 ae^{i(\varphi+(\arg t_1\arg t_{1,\text{out}}-\arg r_1-\arg r_{1,\text{out}}))}\right)\\ &\approx r_{1,\text{out}}\frac{1}{1-ae^{i\varphi}}\left(\left(1-ae^{i\varphi}\right)-\left|\frac{t_{1,\text{out}}t_1}{r_{1,\text{out}}r_1}\right|^2 ae^{i\varphi}\right).\end{aligned} \tag{A.1.27}$$

In the last step we used that although the phase of transmitted light and the reflected light may be arbitrary, the sum of these phases always is very close to π if losses are not too strong. This yields a factor of -1. Furthermore, we assume from now on that the amplitude of reflection and transmission from the left and the right are approximately the same, which is also a good approximation for low loss mirror coatings.

We get the fraction of the intensity reflected by taking the absolute square of the field

$$\begin{aligned}R_{\text{c}} = \left|\frac{u_r}{u_{\text{in}}}\right|^2 &= R_1 I_f\left|1-\left(1+\frac{T_1}{T_2}\right)ae^{i\varphi}\right|^2\\ &= I_f\left[R_1 - R_2\left|t_A\right|^2\left(T_1+T_2\right)^2 - 2\sqrt{R_1R_2}\left|t_A\right|\left(T_1+R_1\right)\cos\varphi\right].\end{aligned} \tag{A.1.28}$$

To get more insight we rearrange it to yield

$$R_{\text{c}} = 1 - I_f\left(1-R_1+R_2\left(1-A\right)^2\left(R_1-\left(1-L_1\right)^2\right)-2\sqrt{R_1R_2}\left(1-A\right)L_1\cos\varphi\right). \tag{A.1.29}$$

From this we see that the reflection is close to unity and only decreases close to resonance, where I_f is largest. Around resonance, $\cos\varphi \approx 1$ the reflection approaches the same lineshape as in transmission but with reversed sign, approximating a Lorentzian shaped dip for low losses. A typical reflection profile is shown in Fig. A.1.2a.

At resonance the reflection is minimal an takes the value

$$R_{\text{c,min}} = 1 - I_{\max}\left(1-R_1+R_2\left(1-A\right)^2\left(R_1-\left(1-L_1\right)^2\right)-2\sqrt{R_1R_2}\left(1-A\right)L_1\right) \tag{A.1.30}$$

With negligible losses in mirror 1 this simplifies to

$$R_{\text{c,min}} \approx \frac{1-R_1-R_2\left(1-A\right)^2+R_1R_2\left(1-A\right)^2}{\left(1-\sqrt{R_1R_2}\right)^2}. \tag{A.1.31}$$

This is a valid approximation if the mirror losses are about an order of magnitude lower than the mirror transmission.

For no losses inside the cavity and symmetric mirrors, the reflection on resonance is zero and all light gets transmitted. But also for other combinations of losses and pairs of mirror

reflectivity the reflection can go to zero as can be seen in Fig. A.1.2b. The *impedance matching condition* where reflection disappears is met when transmission of the in-coupling mirror (T_1) is equal to all other losses of the cavity ($L_1 + L_2 + T_2 + 2A$)[52].

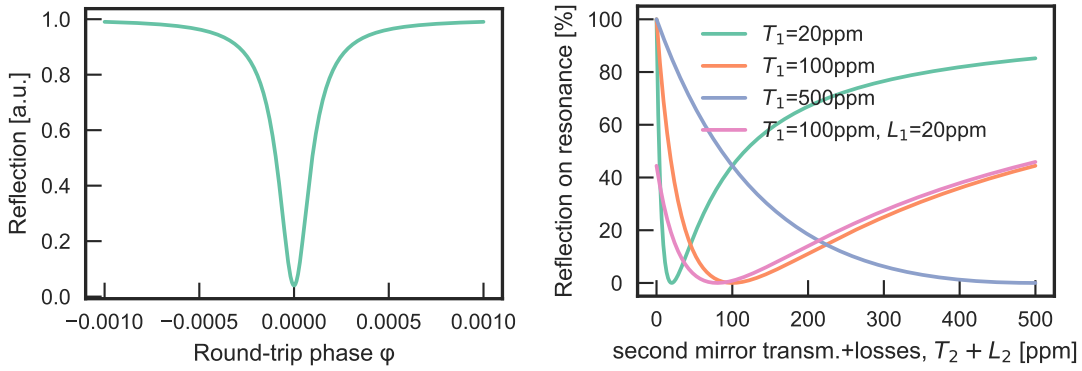

(a) **(b)**

Figure A.1.2.: (a) Cavity reflection as function of phase for $T_{1,2} = 100\,\text{ppm}$, $L_{1,2} = 10\,\text{ppm}$, $A = 20\,\text{ppm}$. (b) Reflection on resonance for different combinations of mirror transmissions and losses.

Effects of non-mode-matched light. If light is coupled into a fibre-based cavity via the fibre side, not all light is reflected at the mirror. Some part of the light is not mode-matched to the cavity mode and gets reflected due to bad mode matching[21, 52, 53]. This is discussed in detail by Gallego et al.[52] who show that this changes impedance matching and adds a dispersive shape to the reflection lineshape.

A.1.6. Out-coupling efficiency

When a photon is created inside the cavity mode and its wavelength is resonant with the cavity, the probability to leave the cavity through mirror i is given by the transmission of this mirror divided by all cavity loss channels

$$\eta_c = \frac{T_i}{T_1 + T_2 + L_1 + L_2 + 2A}\,. \tag{A.1.32}$$

A.1.7. Intra-cavity power enhancement

Here we calculate the power inside the cavity. The field at a certain point inside the cavity is given by the interference of a left and right running wave $u_{\rightarrow,\leftarrow}(\Delta_z)$. Here, Δ_z is a phase specifying the relative position inside the cavity. When coupling in the field u_{in} through mirror 1, the field inside the cavity becomes

$$\begin{aligned} u_{\mathrm{e}}\left(\Delta_z\right) &= u_{\rightarrow}\left(\Delta_z\right) + u_{\leftarrow}\left(\Delta_z\right) \\ &= u_{\mathrm{in}} t_1 \left(e^{i\Delta} + r_2 e^{i(\varphi - \Delta_z + \pi)}\right) \sum_{n=0}^{\infty} \left(a e^{i\varphi}\right)^n . \end{aligned} \tag{A.1.33}$$

Therefore, the power enhancement relative to the incoming power is

$$\begin{aligned} C_{\mathrm{e}}\left(\Delta_z\right) &= \left|\frac{u_e\left(\Delta_z\right)}{u_{\mathrm{in}}}\right|^2 \\ &= T_1 \left(1 + R_2 + \sqrt{R_2}\left(e^{i(\varphi - 2\Delta + \pi)} + e^{i(\varphi - 2\Delta + \pi)}\right)\right) I_f \\ &= T_1 \left(1 + R_2 + \sqrt{R_2}\left(4\sin^2\left(\varphi/2 - \Delta_z\right) - 2\right)\right) I_f \\ &\approx 4 T_1 \sin^2\left(\varphi/2 - \Delta_z\right) I_f . \end{aligned} \tag{A.1.34}$$

The last line is an approximation for high reflectivity cavities with $R_2 \approx 1$. We see that the power inside the cavity has a $\sin^2$ standing wave pattern.

For a high finesse cavity, the maximum intensity at resonance, $\varphi = 2\pi q$, and in an anti-node of the field, is given by

$$\boxed{C_{e,\max} = 4 T_1 I_{\max} \approx 4 T_1 \frac{\mathcal{F}^2}{\pi^2}} \tag{A.1.35}$$

For symmetric cavities with negligible mirror losses this simplifies to

$$C_{e,\max} \approx 4 \frac{\mathcal{F}}{\pi} . \tag{A.1.36}$$

Using Eq. (A.1.23), the power at an anti-node in the cavity relates to the transmitted power through mirror 2 as

$$\frac{C_{e,\max}}{T_c} = \frac{4}{T_2} . \tag{A.1.37}$$

With this the power inside the cavity can be measured from the transmitted power.

A.2. Resonance condition, Linewidths, ...

In this section we investigate when the cavity is resonant and how these resonances depend on cavity length and wavelength. Furthermore, the cavity's key numbers finesse and quality factor and their dependence on cavity length are explored.

Resonance condition. As stated before, resonances appear when constructive interference forms inside the cavity. The phase of an electromagnetic wave accumulated per cavity round-trip is (cf. Eq. (A.1.3))

$$\varphi = 2d_p \frac{2\pi}{\lambda} n + \varphi_{\mathrm{rtg}}(\lambda, \dots) \,. \tag{A.2.1}$$

where d_p is the physical distance of the mirror surfaces, n the refractive index of the material between the mirrors and $\varphi_{\mathrm{rtg}} = \varphi_{r,1}(\lambda) + \varphi_{r,2}(\lambda) - 2\zeta(d_p, R) + \varphi_t$ collects phases shifts at reflection, by the Gouy phase (depending on cavity length and mirror radius of curvature R, see Appendix A.3.1) and optionally by objects between the mirrors.

The light field reproduces itself after each round-trip when this phase is integer multiples of 2π

$$\varphi = q \times 2\pi \qquad q = 1, 2, 3, \dots \,, \tag{A.2.2}$$

We absorb these phases and the refractive index into an effective cavity length d

$$d = d_p n + \varphi_{\mathrm{rtg}}(\lambda, \dots) \frac{1}{2} \frac{\lambda}{2\pi} \,, \tag{A.2.3}$$

and get the simplified formula for the phase per round-trip

$$\varphi = 2d \frac{2\pi}{\lambda} \,. \tag{A.2.4}$$

This phase changes with the wavelength (frequency) of the light or when modifying the cavity length. The cavity is resonant with light of wavelength λ at lengths d when

$$d = q \frac{\lambda}{2} \qquad q = 1, 2, 3, \dots \,. \tag{A.2.5}$$

The quantity q is called the longitudinal mode order

$$q = \frac{d}{\lambda/2} \,. \tag{A.2.6}$$

It counts how many standing wave periods $(\lambda/2)$ can be found inside the cavity.

Resonance frequencies. Using the dispersion relation, $\omega = 2\pi\nu = ck$, to connect the wave-vector, k, the frequency ν and the angular frequency of light ω, along with the wavelength, $\lambda = \frac{2\pi}{k}$, relates the wavelength and the frequency

$$\nu = c/\lambda \,. \tag{A.2.7}$$

Therefore, the resonance frequencies are

$$\nu_q = q \frac{c}{2d} \tag{A.2.8}$$

and appear equally spaced in frequency space separated by the so-called *free spectral range* ()

$$\Delta\nu = \frac{c}{2d} \,. \tag{A.2.9}$$

Note that the free spectral range is inversely proportional to the cavity length. Therefore, in the micro-cavities used – in contrast to macroscopic cavities – the resonance frequencies are

quite far apart in frequency space.

Finesse. The finesse of the cavity is a physical quantity set only by the losses in the cavity (reflectivities of the mirrors and additional loss channels). It relates to the FWHM linewidth given in phase (as defined in Eq. (A.1.11)) as

$$\mathcal{F} = \frac{2\pi}{\delta\varphi}\,. \tag{A.2.10}$$

Next this will be related to other quantities describing a cavity such as spectral linewidth, photon lifetime, Q-factor and linewidth under cavity length change.

Q-Factor and lifetime. The quality factor (Q-factor) of a damped oscillation is a dimensionless quantity defined as the Frequency of an oscillation, ν, divided by the FWHM linewidth (or dissipation rate), $\delta\nu$,

$$Q = \frac{\nu}{\delta\nu}\,. \tag{A.2.11}$$

It quantifies how often a system oscillates until it is damped. Like the finesse, this quantity scales with the reflectivity of the mirror, but also depends on the cavity length

$$Q = q\mathcal{F} = \frac{d}{\lambda/2}\mathcal{F}\,. \tag{A.2.12}$$

Unlike the finesse, the Q-factor increases linear with cavity length and both numbers are equal for the theoretical minimum cavity length of $\lambda/2$. The Q-factor is a measure of the temporal storage of photons inside the resonator. The lifetime of a photon inside the cavity is given by

$$\tau = \frac{Q}{2\pi\nu}\,. \tag{A.2.13}$$

Although the finesse of the micro-cavities used is commonly very high, the quality factor might be significantly smaller than for macroscopic long cavities, and therefore the spectral linewidths (in frequency or wavelength) can be broader.

Resonance wavelengths and spectral linewidths. From the resonance condition, Eq. (A.2.5), the wavelengths where fundamental cavity modes are resonant is given by

$$\lambda_q = \frac{2}{q}d \tag{A.2.14}$$

Therefore, adjacent resonant wavelengths of mode orders q and $q+1$ are separated by

$$\Delta\lambda_{q,q+1} = 2d\left(\frac{1}{q} - \frac{1}{q+1}\right) = \frac{2d}{q\,(q+1)} = \frac{\lambda_q}{q+1}\,. \tag{A.2.15}$$

When changing the cavity length by ∂d, the resonance wavelength of order q shifts by

$$\partial\lambda_q = \frac{2}{q}\partial d\,. \tag{A.2.16}$$

Therefore, the longer the cavity, the weaker a length change translates to a spectral resonance shift and a longer resonator is hence more frequency-stable.

Using Eq. (A.2.4), we see that the spectral linewidth of a cavity resonance depends also on the cavity length (or mode order q)

$$\delta\lambda = \frac{\lambda^2}{2d}\frac{1}{\mathcal{F}} = \frac{\lambda}{q\mathcal{F}} \tag{A.2.17}$$

and the lines get narrower for longer cavities.

Resonances cavity lengths and linewidth under length change. When looking at a single wavelength, λ, and sweeping the cavity length, resonances appear at lengths equally spaced by

$$\Delta d = \frac{\lambda}{2}\,, \tag{A.2.18}$$

Which we can could call this the "free length range" but commonly also refer to it as the free spectral range (FSR), although slightly incorrect.

The length where the resonance can be found shifts with a wavelength by

$$\partial d_q = \frac{q}{2}\partial\lambda \tag{A.2.19}$$

and it therefore depends stronger on the wavelength for longer cavities. This can be understood easily when remembering that for longer cavity length more wavelengths fit inside the resonator and that if one changes the wavelength slightly, the new resonance length shifts by contribution of each wavelength that fits in.

The width of the resonances as a function of length change is

$$\delta d = \frac{\lambda/2}{2\pi}\delta\varphi = \frac{\lambda/2}{\mathcal{F}} \tag{A.2.20}$$

and also does not depend on the cavity length.

The finesse can therefore also be expressed simply as the ratio of the "free length range" and the FWHM linewidth under length change

$$\mathcal{F} = \frac{2\pi}{\delta\varphi} = \frac{\lambda/2}{\delta d}\,. \tag{A.2.21}$$

Comparison of spectral and length-change linewidth. As we have seen, the linewidth under length does not depend on the cavity length while the spectral linewidth does. The two are related by

$$\delta\lambda = \frac{2}{q}\delta d \tag{A.2.22}$$

and the spectral linewidth can be much smaller for longer cavities.

Overview. In Table A.2.1 an overview of the most important quantities of the cavity expressed or depending on accumulated phase, cavity length, wavelength and frequency is written. Here, linewidth means the needed change of a quantity (e.g. cavity length or wavelength) to move

	accumulated phase	cavity length	wavelength	frequency
resonance position (from length and wavelength)	$\varphi_q = q \times 2\pi$	$d_q = \frac{q}{2}\lambda$	$\lambda_q = \frac{2}{q}d$	$\nu_q = q\frac{c}{2d}$
shift under length change	$\frac{\partial\varphi}{\partial d} = \frac{2\pi}{\lambda}$	1	$\frac{\partial\lambda}{\partial d} = \frac{2}{q}$	$\frac{\partial\nu}{\partial d} = -q\frac{c}{2d^2} = -\frac{c}{\lambda d}$
free phase/length/spectral range (FSR)	2π	$\Delta d = \frac{\lambda}{2}$	$\Delta\lambda_{q,q+1} = \frac{2d}{q(q+1)} = \frac{\lambda_q}{q+1}$	$\Delta\nu = \frac{c}{2d}$
finesse, $\mathcal{F}$	$\frac{2\pi}{\delta\varphi}$	$\frac{\lambda/2}{\delta d}$	$\frac{1}{2d}\frac{\lambda^2}{\delta\lambda}$	$\frac{1}{q}\frac{\nu_q}{\delta\nu_q}$
FWHM linewidth	$\delta\varphi = \frac{2\pi}{\mathcal{F}}$	$\delta d = \frac{\lambda/2}{\mathcal{F}}$	$\delta\lambda = \frac{1}{\mathcal{F}}\frac{\lambda^2/2}{d} = \frac{1}{\mathcal{F}}\frac{\lambda}{q}$	$\delta\nu_q = \frac{\nu}{Q} = \frac{\nu}{q\mathcal{F}}$
Quality factor, Q	$\frac{2\pi}{\delta\varphi}\,q$	$\frac{d}{\delta d}$	$q\mathcal{F} = \frac{d}{\lambda/2}\mathcal{F} = \frac{\lambda}{\delta\lambda}$	$\frac{\nu_q}{\delta\nu_q}$
Lifetime τ				$\frac{Q}{2\pi\nu_q}$

Table A.2.1.: Cavity key figures expressed in terms of accumulated phase, cavity length, wavelength and frequency. The free spectral/length range is the spacing between adjacent modes in the respective quantity.

from half peak intensity to the other side of the peak (FWHM). For example, 'cavity length' linewidth means length changed associated between the sides of the transmission resonance.

A.3. Cavity 3D modelling: resonators with curved mirrors

Plane waves are only an idealised method to understand the basic resonances of the resonators. They are only valid for laterally infinitely extended beams impinging on perfectly flat infinitely extended mirrors. The resonator geometries used in this work include at least one curved mirror to confine the cavity mode laterally and make it stable against angle tilts of the mirrors. Therefore, one has to model them with finite extended beams in a 3D treatment. However, the above formulas still hold true except that the added dimension give rise to phase shifts (leading to effectively modified cavity lengths) and new degrees of freedom and therefore *higher order transversal modes* appear[33, 117]. Here, just the formulas for plano-concave cavities relevant for this work are listed. For more detail on working with the new set of cavity eigen-modes associated with this geometry please refer to other sources for detailed derivations[33, 118, 32, 31, 117].

A.3.1. Gaussian beams

The cavity geometry confines eigen-modes in the two additional transversal dimensions. For sufficiently small beam extension, the cavity mirrors is treated to be spherical in first order. Gaussian beams are a solutions of the Helmholtz equation in paraxial approximation. They have spherical wavefronts and therefore can match the curvature of spherical mirrors and are the eigen-modes of the cavity.

Mode radius

Gaussian beams are inherently diverging beams due to their finite transversal extent and diffraction.

For a plano-concave cavity as used in this work, the minimal mode waist radius (defined by $1/e^2$ of intensity) is located at the plane mirror and is given by [32, 30]

$$w_0 = \sqrt{\lambda/\pi \cdot \sqrt{d\,(R-d)}}\,. \tag{A.3.1}$$

Here, R is the radius of curvature of the concave mirror. At the concave mirror, the mode radius is given by

$$w_{\mathrm{m}} = w_0 \sqrt{1 + \left(\frac{\lambda d}{\pi w_0^2}\right)^2}\,. \tag{A.3.2}$$

As can be seen in Fig. A.3.1b, the beam radii decrease with the radius of curvature and cavity length. At cavity lengths approaching R the mode size on the curved mirror diverges and the resonator gets unstable. The spot size at the planar mirrors, where the sample of the scanning cavity setup is located, limits the resolution for microscopy. The diffraction limited spot radius, given by $\lambda/(\pi \mathrm{NA})$, using a conventional $\mathrm{NA} = 1$ objective is also shown, for comparison with the resolution of other (conventional non-superresolution) microscopy methods.

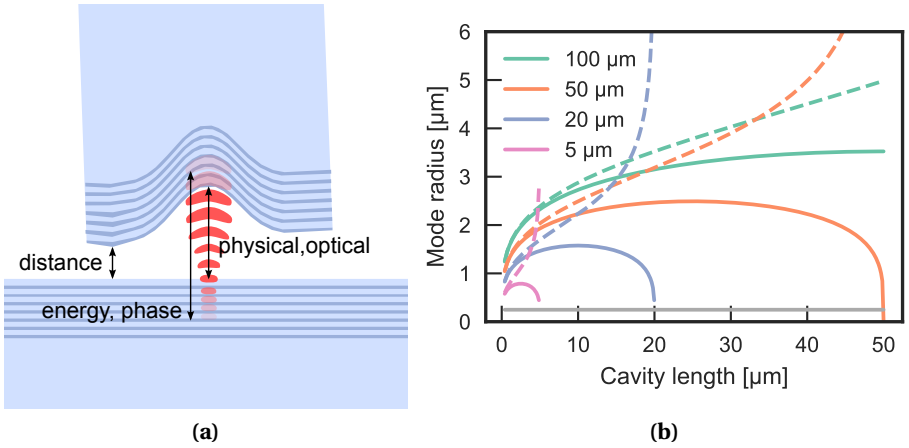

Figure A.3.1.: (a) schematic side view of a Gaussian resonator mode in a plano-concave cavity. The mode waist is located at the plane mirror, the cavity geometry constrains the mode shape. (b) Mode sizes on plane mirror w_0(solid lines) and curved mirror (usually fibre mirror) w_m(dashed lines) for different radii of curvature as a function of cavity length. Wavelength $\lambda = 780\mathrm{nm}$. The grey line is the diffraction limited spot radius for $\mathrm{NA} = 1$.

Coupling efficiency

The fraction of light coupled in and out of the cavity depends on the mode matching of the resonator mode to the external propagating modes. The high coupling efficiency is an important feature of Fabry-Pérot based cavities in contrast to many other micro-cavities.

Fibre to cavity. The light coupled into the cavity or out of it through the fibre is limited by imperfect matching of the profile of the eigen-mode of the cavity on the mirror and the profile of the guided eigen-mode of the fibre. The efficiency of coupling depends on the intensity

and phase profile of these modes, which are both well approximated by fundamental Gaussian modes. When neglecting the phase mismatch and just assuming two perfectly centred Gaussian modes with different sizes the energy coupling efficiency is given by [**Hunger2010**]

$$\epsilon_{size} \approx 4 \left(\frac{w_\mathrm{f} w_\mathrm{m}}{w_\mathrm{f}^2 + w_\mathrm{m}^2} \right)^2 . \tag{A.3.3}$$

Here, w_f is the radius of the fibre mode, basically given by the wavelength and the specifications of the fibre and the mode radius of the cavity mode w_m determined by the radius curvature of the mirror and the cavity length. If the wavefront curvature, and the curvature of the end facet of the fibre acting as an effective lens is included, the coupling efficiency is given by [**Hunger2010**]

$$\epsilon = \frac{4}{\left(\frac{w_\mathrm{f}^2 + w_\mathrm{m}^2}{w_\mathrm{m} w_\mathrm{f}} \right)^2 + \left(\frac{\pi n_\mathrm{f} w_\mathrm{f} w_\mathrm{m}}{\lambda R} \right)^2} . \tag{A.3.4}$$

Here, n_f it the refractive index of the fibre. As can be seen in Fig. A.3.2a, the mode matching for short cavity lengths is dominated by the size mismatch. However, for longer cavity lengths and small radii of curvature the phase mismatch clearly dominates and limits the overall mode matching.

In Fig. A.3.2, a measurement of cavity transmission is shown where clearly reduced mode matching for shorter cavity lengths can be seen.

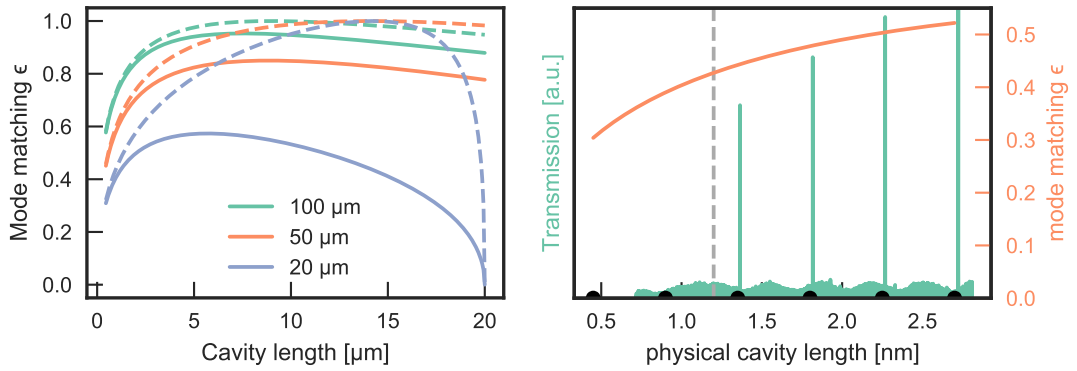

(a) **(b)**

Figure A.3.2.: (a) Mode matching of cavity mode on a curved fibre mirror to the mode guided in the fibre with radius $w_\mathrm{f} = 3\mu\mathrm{m}$, wavelength $\lambda = 0.9\mu\mathrm{m}$, and various radii of curvature for different cavity lengths. The dashed line is the simplified formula without phase-matching and lensing effects. The solid lines include these effects. (b) Measured transmission at very short cavity lengths (green) overlayed with the expected mode matching scaled appropriately(orange line). The vertical dashed line marks the point where the fibre starts to touch the planar mirror

Through plane-mirror. The mode size at the plane mirror is related to the divergence of the out-coupled beam by the formula for Gaussian beams

$$w_0 = \frac{\lambda}{\pi \mathrm{NA}} \tag{A.3.5}$$

For $\lambda = 800\,\mathrm{nm}$the numerical aperture (NA) of the beam can be up to about 0.25 for the smallest mode waists used cavities in this work ($w_0 \approx 1\,\mu\mathrm{m}$ for $d_p = 1\,\mu\mathrm{m}$ and $R = 20\,\mu\mathrm{m}$). Since the mode at the planar mirror exhibits a flat phase front it can be collected efficiently with a common aspheric lens that offers diffraction limited performance. Afterwards the light can efficiently be injected into single- or multi-mode fibres.

Gouy Phase shift

Gaussian beams feature an additional phase shift in the vicinity of their beam waist compared to planar waves. This phase shift is called the Gouy-Phase (*somehow* a frequently misspelled name) and depends on the focussing of the beam[119]. For our plano-concave cavities the summed up phase shift per half round trip is

$$2\zeta\left(d,R\right) = 2\arctan\left(\sqrt{\frac{d}{R-d}}\right) \tag{A.3.6}$$

(or $\arccos\sqrt{1-\frac{d}{R}}$) and depends on cavity geometry and length. This can be easily derived using the Gouy phase of a Gaussian beam ($\zeta\left(z\right) = \arctan\left(z/z_R\right)$), its curvature ($R\left(z\right) = z\left(1+\left(z_R/z\right)^2\right)$ and integrating from the waist (at the planar mirror, $z=0$) to the second mirror ($z=d$). Here z_R is the Rayleigh range of the beam.

This phase is positive and has to be added when determining the resonance condition of the cavity, cf. Eq. (A.2.1). In Fig. A.3.3a it is plotted for various cavity radii of curvature.

A.3.2. Higher order transverse modes

Apart from the fundamental Gaussian mode, resonators also support higher order modes, called Hermite-Gaussian modes[1]. They share the same wavefront as Gaussian beams, but with different transversal intensity profiles and Gouy-phase-factors.

They are characterized by the number of nodes in profile along the two transversal directions, depicted as n, m. The total number of nodes $n+m$ is called the transversal mode order. For example. $(0,0)$ specifies the fundamental Gaussian mode and $(2,0)$ or $(1,1)$ are both second order modes. The mode profiles are shown in Fig. A.3.3b. The accumulated Gouy-phase per cavity pass for higher order modes scales with the mode order

$$\zeta_{n,m}\left(d\right) = \left(n+m+1\right)\zeta\left(d\right) \tag{A.3.7}$$

Therefore, the cavity resonance condition for these higher order modes is

$$\varphi = 2kd - 2\left(n+m+1\right)\zeta\left(d\right) \equiv q\times 2\pi \tag{A.3.8}$$

The cavity lengths where modes can be found are

[1] Due to small braking of the rotational symmetry of the mirror, commonly no spherical symmetric Laguerre-Gaussian are commonly observed

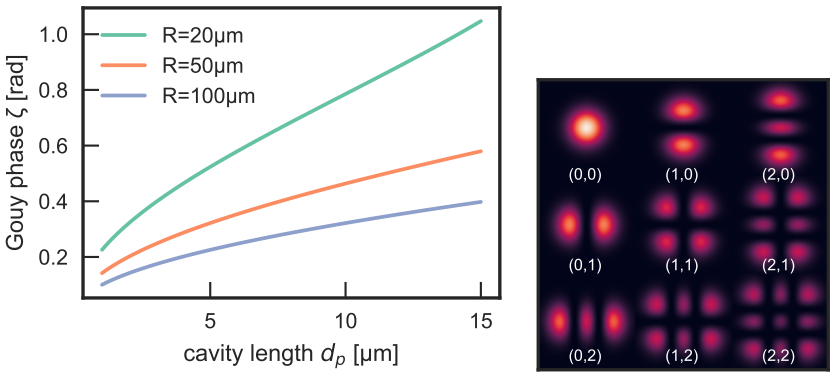

(a) **(b)**

Figure A.3.3.: (a) Gouy phase for different radii of curvature, R, for a plan-concave cavity. (b) Transverse mode profiles of fundamental and higher order modes with their respective mode order. Normalized to integrated intensity.

$$\begin{aligned} d &= \frac{\lambda}{2}\left(q + 2\left(n+m+1\right)\frac{\zeta\left(d\right)}{2\pi}\right) \\ &\approx \frac{\lambda}{2}\left(q + 2\left(n+m+1\right)\frac{\zeta\left(q\lambda/2\right)}{2\pi}\right) . \end{aligned} \tag{A.3.9}$$

In the second line, the dependence of the Gouy-phase on the cavity length is eliminated by an approximation with the length expressed through the longitudinal mode order. This is done to simplify the transcendental equation to a normal one.

The distance between adjacent higher order modes (or between the first higher order modes and the fundamental mode) is therefore approximately equidistant for each longitudinal mode order q,

$$\Delta d_{\mathrm{ho}} \approx \frac{\lambda}{2\pi}\zeta\left(d\right) = \frac{\lambda}{2\pi}\arctan\left(\frac{1}{\sqrt{R/\left(q\lambda/2\right)-1}}\right) , \tag{A.3.10}$$

and can be used to determine the cavity length (see Appendix B.2) or the radius of curvature R of the cavity mirror if the mode order is known. In Fig. A.3.4b, the mode spacing for different radii of curvature and longitudinal mode orders is plotted.

When measuring transmission of a fixed wavelength laser and sweeping the cavity length higher order modes appear at the side to longer cavity lengths, as can be seen in the measurement in Fig. A.3.4a.

In a spectral measurements using a broadband light source higher-order modes appear at the side of shorter wavelengths (higher frequencies) with respect to their corresponding fundamental mode.

When coupling a Gaussian into the cavity, either from the fibre or using free space optics from the planar mirror, not only fundamental but also higher order modes in the cavity can get populated. Since Hermite-Gaussian modes and the fundamental mode are orthogonal (and even form a complete basis set to express and mode in the cavity) they ideally should not get

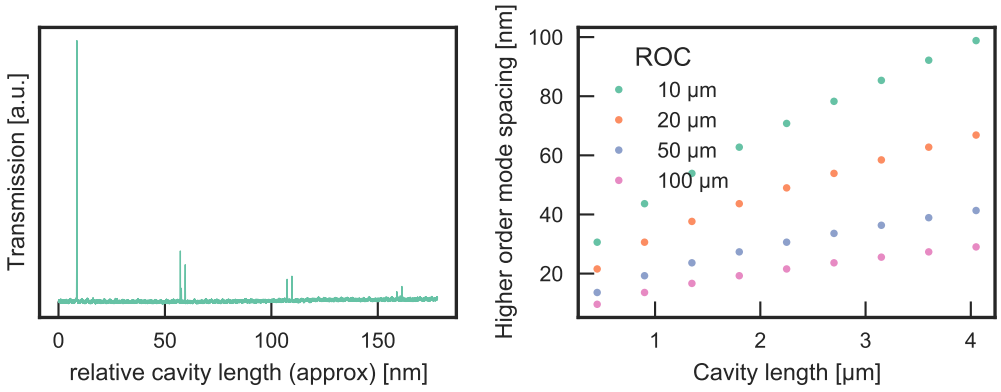

Figure A.3.4.: (a) Fundamental and higher order cavity modes recorded by sweeping cavity length and measuring transmission of a fixed-frequency laser. The higher order modes are weaker in intensity and appear in sets of two. Due to non perfectly spherical mirrors the two orthogonal (n, m) and (m, n) show slightly different resonant cavity lengths. (b) Cavity length resonance spacing, Δd_{ho}, of the first higher order mode (0,1 or 1,0) to the fundamental mode for the first ten cavity resonances, different radii of curvature (ROC) and $\lambda = 900\,\mathrm{nm}$.

excited. However, imperfect mode matching due to displacements between the mirror centre and the fibre centre, angle deviations or non-spherical mirror geometries lead to coupling between the external Gaussian mode and higher order modes.

Implications and use

Higher order modes can be useful to gather information about the cavity or to perform advanced measurements. However the can also be a source of parasitic signals deteriorating measurements.

Resolution increase or decrease Since the higher order modes have different and larger spatial profiles than the simple fundamental Gaussian mode, they can decrease the resolution when they are recorded together with the fundamental mode when taking scanning cavity microscopy pictures. However, the admixture of higher order modes can also be useful if the transmission of each mode is measured independently. When the resulting measurements are combined appropriately to reduce the effective mode size the microscopy resolution can be increased[25].

Finesse decrease due to mode mixing When the cavity mirror profile deviates from a perfect sphere, which is commonly the case for longer cavity lengths and imperfect profiles, the eigen-modes of the cavity are no perfect Hermite-Gaussian modes any more. This can lead to significant coupling between usually orthogonal modes, e.g. the fundamental mode and larger higher order modes[62], when they become resonant at the same time. This admixture of higher order modes then in turn can lead to a steep decrease of finesse. Since the exact resonance length or frequency of the modes can change with small surface variations on

different positions of the planar mirror, this can add a large spatially varying “scattering” background to extinction microscopy image.

Information on cavity geometry The ratio of light coupled into higher order modes and the fundamental mode yield information about the angular alignment of the mirrors and the mirror geometry. The splitting of the resonance of the $(0,1)$ and $(0,1)$ give information about the amount of asymmetry of the radii of curvature in two orthogonal cavity axis. See Appendix B.3 for radius of curvature, Appendix B.2 for length measurement and Appendix B.4.6 for angular alignment.

Filtering

Higher order modes can be filtered spatially by placing obstacles in the free-space out-coupled beam, e.g. a small pinhole to cut of higher order modes and prefer the fundamental mode.

They can also be filtered in frequency either by elements in the excitation or detection path of the cavity or by choosing appropriate cavity lengths.

Furthermore they often have different polarizations than the fundamental mode and can be attenuated using polarization optics.

A.3.3. Stability length range

For a plano-concave cavity with an ideal spherical mirror, fundamental cavity modes are only stable up to cavity lengths equal to the radius of curvature $0 \leq d \leq R$. However, for imperfect cavities mirror profiles as used in this work, that more or less resemble a Gaussian profile due to the manufacturing method, the stability of the cavity deteriorates already for shorter lengths[62]. The reason is that roughness of the mirrors introduces mode mixing between the fundamental mode and higher order transverse modes, substantially increasing the losses. This limits the accessible cavity length as a rule of thumb already at half the radius of curvature, $d \leq R/2$, for common Gaussian mirror profiles[62].

A.3.4. Mode volume

The mode volume of a cavity mode quantifies how strong the field of a photon (mode) is concentrated inside a cavity. This ‘spacial confinement’ of the photons enters in cavity quantum electrodynamics (QED) coupling rates like enhanced or suppressed emission in the Purcell effect It is defined as the inverse of the energy density at a certain point inside the cavity, $\vec{r}_0$, where an object that should be coupled to cavity field is placed, normalized to the total energy

$$V_m \equiv \frac{\int \mathrm{d}^3 r \epsilon(\vec{r}) \left|\vec{E}(\vec{r})\right|^2}{\epsilon(\vec{r}_0) \left|\vec{E}(\vec{r}_0)\right|^2} \tag{A.3.11}$$

Usually the point $\vec{r}_0$ is chosen at an anti-node, where the electric field is the maximal

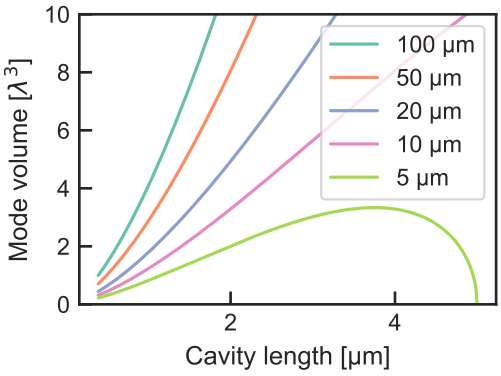

Figure A.3.5.: Mode volume in units of λ^3 for different radii of curvature and $\lambda = 780\,\mathrm{nm}$.

$$V_m = \frac{\int \mathrm{d}^3 r \epsilon(\vec{r}) \left|\vec{E}(\vec{r})\right|^2}{\max\left\{\epsilon(\vec{r}) \left|\vec{E}(\vec{r})\right|^2\right\}}. \tag{A.3.12}$$

Note that only in this definition, the mode volume (for a certain wavelength) is a property of the cavity geometry alone. In general it depends on the chosen position of interaction. For the used plan-concave cavities the mode volume for a certain wavelength depends on the radius of curvature, R, and the cavity length, d,

$$V_m = \frac{\pi}{4} \cdot w_0^2 d = \frac{\lambda}{4} d^2 \sqrt{\frac{R}{d} - 1}. \tag{A.3.13}$$

This is plotted for short cavity lengths and various radii of curvature in Fig. A.3.5.

A.3.5. Polarization splitting

If the cavity mirror does not have perfect circular symmetry, different polarizations in the cavity see effective different cavity lengths[36]. To first order, such a mirror can be modelled with two radii of curvature along two orthogonal axis, R_x, R_y. The phase shift difference per reflection between orthogonal linear polarizations along these axis is then given by

$$\Delta\varphi_{\mathrm{pol}} = \frac{1}{k} \frac{R_x - R_y}{R_x R_y} \tag{A.3.14}$$

and leads to a splitting of the two resonances.

With a fixed laser frequency and under cavity length sweeps (cf. Eq. (A.2.20)) this translates into a splitting of cavity lengths where the resonances appear,

$$\Delta d_{\mathrm{pol}} = \frac{\lambda}{2\pi} \Delta\varphi_{\mathrm{pol}}\,. \tag{A.3.15}$$

As for the linewidth under length change, it is independent of cavity length, unless the different mode size on the mirror does not change the effective radii of curvatures. If the splitting is larger than the linewidth it can be easily resolved , as shown in Fig. A.3.6.

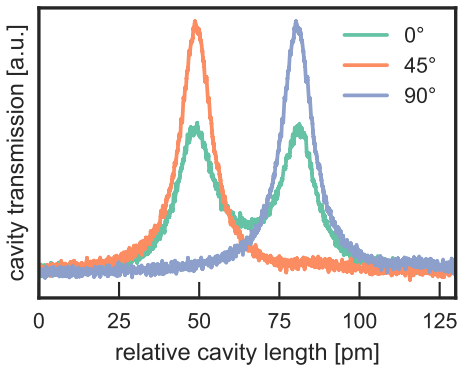

Figure A.3.6.: Polarization splitting of the fundamental cavity mode measured via transmission of a narrow laser while sweeping cavity length. By changing the angle of linear polarization in front of the fibre the power can be distributed to the different modes.

When the angle of the fibre relative to the mirror is modified, the effective radius of curvature changes, as the profiles are not perfectly spherical. This way, the splitting of the modes can be tuned (in a limited way). Measurements where the angle on one axis is changed continuously are shown in Fig. A.3.7a. In the last measurement (5, green), the polarization splitting can not be resolved any more.

In Fig. A.3.7b, cavity transmission was measured with equal power in both polarization modes. Depending of the polarization resolved detection, the two modes can interfere constructively or destructively.

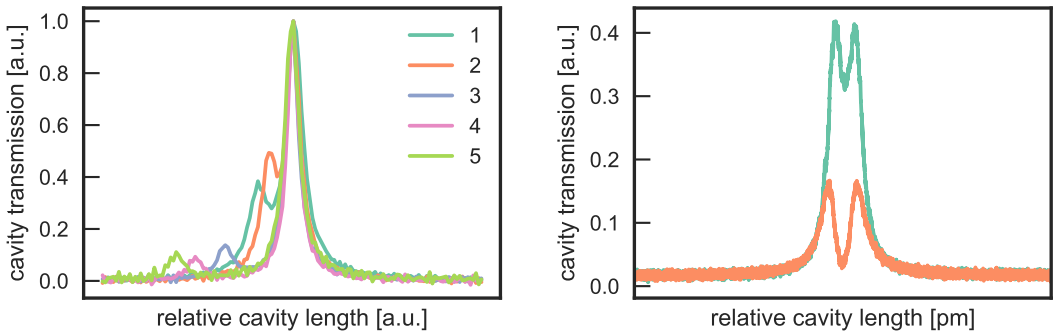

(a) **(b)**

Figure A.3.7.: (a) Polarization splitting recorded for different angular alignments of the fibre (numbered measurements). (b) Cavity transmission measurement with equal amount of power in both modes, but different polarization dependent detection, rotated by 90°.

A.4. Extinction cross section

Usually molecules or other nanoscale objects are much smaller than the diffraction limit of light. The absorption therefore only happens locally at a single point inside the much larger, in this case Gaussian beam. In optics, the extinction cross section (also known as attenuation

cross section) provides a measure of absorptivity and scattering of an object that is independent of the size of the illuminating beam.

The total power extinct by the particle P_{ex} divided by the intensity at the particle (I_0) has units of area and is called the extinction cross section [120, Ch 3][121, Ch 9]

$$\sigma_{\mathrm{ex}} = \frac{P_{ex}}{I_0}\,. \tag{A.4.1}$$

The cross section can be imagined as the virtual area the particle covers so that if it would be illuminated with a large homogeneous beam in geometrical optics, it would 'cast a shadow' of this size[122, 120]. However, for tiny particles smaller than the wavelength this has nothing to do with a real geometric cross section.

Extinction is the sum of absorption and scattering with their respective cross sections

$$\sigma_{\mathrm{ex}} = \sigma_{\mathrm{abs}} + \sigma_{\mathrm{scat}}\,. \tag{A.4.2}$$

However, in our experiments we can not differentiate between them because we do not measure the scattered light individually.

To derive the extinction cross section from measurements with a Gaussian beam one has to consider the profile of the beam. The radial intensity (=power per area) pattern is given by [33, chapter 3]

$$I\left(r\right) = I_0 \mathrm{e}^{-2\left(\frac{r}{w_0}\right)^2}\,, \tag{A.4.3}$$

where I_0 is the intensity in the centre of the beam and $w_0$the e^{-2} intensity beam radius. The total power of the Gaussian beam can be calculated by integrating over the infinite size of the beam in cylindrical coordinates

$$P = \int_0^{2\pi} d\varphi \int_0^{\infty} r\, I\left(r\right)\, dr = 2\pi \int_0^{\infty} r\, I\left(r\right)\, dr = I_0 \frac{\pi w_0^2}{2}\,. \tag{A.4.4}$$

The areaπw_0^2 is sometimes called the effective area of a Gaussian beam. If an object is much smaller than the beam ($\ll w_0$) and located in the centre of the cavity mode its absorption cross section according to Eq. (A.4.1) is given by

$$\sigma_{\mathrm{ex}} = \frac{B \times P}{I_0} = B\frac{\pi w_0^2}{2}\,, \tag{A.4.5}$$

where B is the absorption of the power on a single pass of the light by the object. This is calculated from e.g. the transmission of the cavity as in Section 2.3.2.

We commonly determine the transversal cavity beam profile by systematically measuring the extinction by a sub-wavelength object at different positions in the cavity mode.

A.5. Definitions of cavity length

In this section is dedicated to an important parameter of a cavity: it's length. It will explore why it is important to know the length, what determines the length and what the cavity length actually is. Several methods to measure the cavity length in an experiment are explained in

Appendix B.2. However, the 'length of the cavity' may not be a single number and also has ambiguous definitions. For example, the optical path cavity length a light-wave experiences does not necessarily coincide with the physical distance between the surfaces of the two cavity mirrors, both of what could be defined as the cavity's length. Furthermore, 'the cavity length' may even significantly vary depending on the wavelength of the light. The penetration depth into the optical coating can be rather large and span from several nm in metallic coatings to a few µm in sophisticated multi-layer Bragg reflectors. Especially at the edges of the stop band of a Bragg reflector the cavity length is strongly in increased by penetration. For commonly used macroscopic cavities these effects can be usually neglected, as their long mirror separation dominates over these tiny effect, and there is only one definition of cavity length. However, for microscopic cavities on the order of a fewµmlong, the exact definitions of 'cavity length' and penetration into the mirror plays a role.

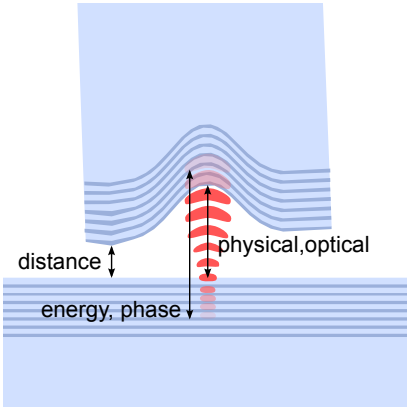

Figure A.5.1.: Illustration of different definitions of 'cavity length'. View of a cavity between a concave fibre-mirror and a plane macroscopic mirror. The alternating refractive indices of the Bragg mirrors are illustrated with brighter and darker blue shades. Different concepts of cavity lengths are illustrated as arrows. 'distance' is the distance between the fibre and the mirror, defined from the point where both mirrors would first touch. This point is affected by the slight residual tilt of the mirrors with respect to each other and surface imperfections. 'physical' and 'optical' are defined by the distance between of the mirror surfaces in the centre where the cavity mode can be found. The standing wave pattern of the field (red lobes) penetrates into the stack yielding the phase and energy effective cavity lengths depicted by 'phase' and 'energy'.

A.5.1. Physical/Optical cavity length

The physical cavity length can be defined as the distance between the two cavity mirror. Since one of the mirrors is concave and the mirrors may not be parallel to each other, the minimum achievable may be significantly longer (several µm) than the length when both mirrors start touching.

To get the optical cavity length the physical cavity length has to be multiplied by the refractive index of the material filling the cavity.

The first layer of the dielectric coating with high refractive index defines where the node of the electric field is (at least for wavelengths with high reflectivities). This constrains the shape of the eigen-mode of the cavity and therefore is relevant for calculating the geometry of the cavity mode, e.g. mode size on the plane mirror and mode-matching to the guided fibre mode.

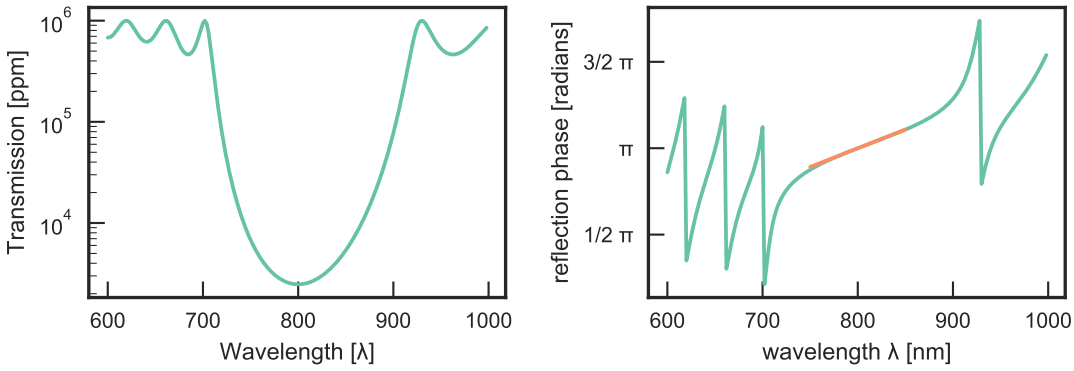

(a) **(b)**

Figure A.5.2.: (a) Transmission spectrum of a $\lambda/4$ Bragg mirror with 11 layer pairs. Around the design wavelength of the stack, $\lambda_0 = 800\,\mathrm{nm}$, the coating is highly reflective. (b) Simulation of the phase at the surface of the Bragg mirror for different wavelengths. At the design wavelength the reflection phase is π and can be well approximated with a linear slope. At the edges of the stop band the phase changes significantly due to the transmissivity of the stack.

A.5.2. Distance between fibre and macroscopic mirror

The distance between the fibre and the mirror is defined with respect to the point where the two mirrors start touching. Due to manufacturing imperfections the fibre end facet is not plain in general. Furthermore, both mirrors may have a slight angle with respect to each other. Therefore, even after the two mirrors start to touch each other, the physical/optical cavity length can be reduced further: When more force is applied the angle of the fibre changes slightly until more points touch the mirror. From experimental experience the physical cavity length can be reduced further 300nm to 1µm depending on the particular geometry. However, the macroscopic mirror may be damaged locally at the touching points. This is especially the case if it is capped with a softer material than glass, e.g. PMMA. See Fig. B.4.2 for an example of a damaged mirror.

A.5.3. Effective cavity length: Phase penetration depth

The mirrors used to build high finesse cavities are distributed Bragg reflectors that work by constructively interfering reflections from multiple interfaces of stacked dielectric layers with varying refractive indices, see Fig. A.5.1 for a schematic. A common realization is the so called $\lambda/4$ stack, yielding the highest reflectivity at the centre design wavelength λ_0, see Fig. A.5.2a. Here, alternating high and low reflective layers (n_l,n_h) with thicknesses chosen to obtain an optical path length of $\lambda_0/4$ in each layer are used. Depending if the top layer is of high or low refractive index these distributed reflections add up to a field with a node or anti-node of the electric field on the mirror surface, respectively. However, this is only true for the centre wavelength. When varying the wavelength, the reflected phase on the surface changes, as can be seen in the simulation of the reflected phase in Fig. A.5.2b effectively shifting the node (or-anti-node) in position relative to the surface.

In a small region around a wave vector, k_0, the change of phase as a function of wavelength

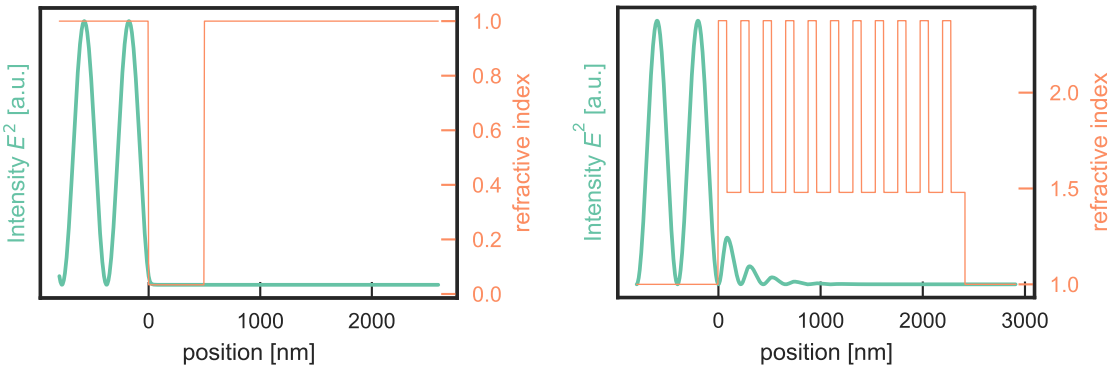

(a) **(b)**

Figure A.5.3.: (a) Simulated intensity (green) of a plane wave with $\lambda = 800\,\mathrm{nm}$ impinging from the left side onto a silver mirror with refractive index $n = 0.033687 - 5.4208i$. The mirror starts at position 0. In front of the mirror a standing wave can be observed. The field has almost an anti-node at the position of the mirror, only slightly penetrating into the mirror stack. The refractive index profile is plotted on the second y-axis, where in front and after the mirror air with refractive index 1 is used.. (b) A 11 layer pair $\lambda/4$ Bragg high reflectivity coating with centre wavelength $800\,\mathrm{nm}$. The field penetrates strongly into the first layers and inside the coating standing waves can be observed.

can be approximated as linear. Therefore, the mirror's phase response can be equivalently modelled as a immediately reflecting mirror sitting some distance behind the actual Bragg mirror surface[123, 124]. We define the effective phase penetration depth at a wave vector k_0 with the derivative of the phase

$$L_{\mathrm{ph}}(k_0) = \frac{1}{2\bar{n}} \frac{d}{dk} \phi(k_0) \ , \tag{A.5.1}$$

where $\bar{n}$ is the average refractive index of the coating ($\bar{n} = (n_{\mathrm{l}} + n_{\mathrm{h}})/2$ for $\lambda/4$stacks). With this, the phase at a point k in the vicinity around k_0 can be approximated by

$$\tilde{\phi}(k) \approx \phi(k_0) + 2\bar{n} L_{\mathrm{ph}}(k_0)(k - k_0) \ , \tag{A.5.2}$$

where $\phi(k_0)$ is the reflection phase at k_0. It therefore models the Bragg mirror with a linear phase response as a common fixed phase reflector sitting L_{ph}behind the mirror surface. In Fig. A.5.5a this phase penetration depth is shown.

Why is this relevant? When using spectral broadband length measurements, see Appendix B.2, the length determined is not the optical length but the separation includes this additional length.

For $\lambda/4$ reflectors at the design wavelength this phase can be calculated using an analytical formula[124].

A.5.4. Effective cavity length: Energy penetration depth

Another important aspect when especially dealing with the Purcell effect is the distribution of energy inside the cavity. The Purcell factor, Eq. (2.4.13), scales with the mode volume of the

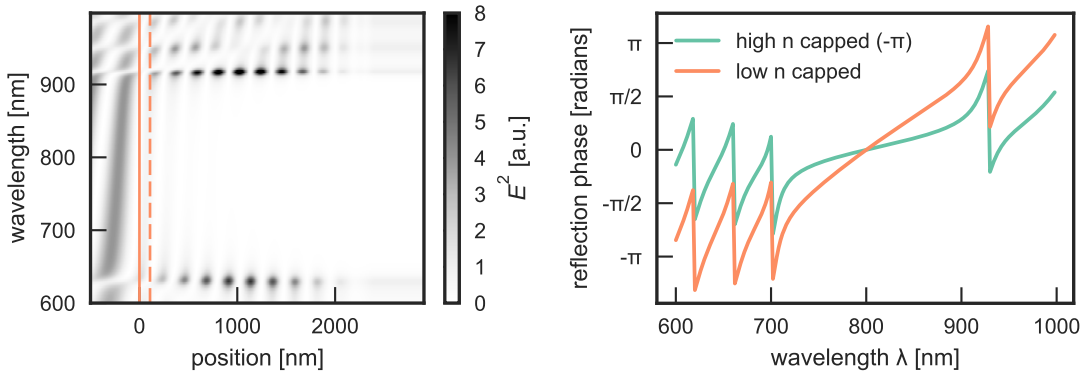

(a) **(b)**

Figure A.5.4.: (a) False-colour plot of the field distribution for different wavelengths impinging onto the stack. The top of the mirror is marked by the solid orange line. The dashed line marks the penetration depth at the design wavelengths. At the sides of the stop band the field penetrates into the stack and even shows pronounced resonances there. (b) Reflection phase as a function of wavelength for a stack with high ('high n capped') and low refractive index ('high n capped') last layer, respectively. The high capped is plotted with a shift by $-\pi$, it has a phase factor of π on reflection in the centre, leading to an node at the surface.

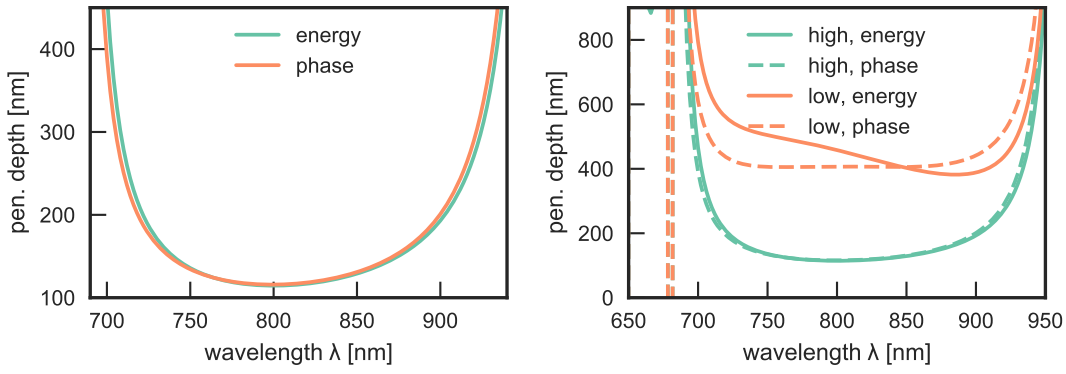

(a) **(b)**

Figure A.5.5.: (a) Comparison of energy and phase penetration depths. (b) Penetration depths for coatings where the top layer has 'high' or 'low' refractive index.

cavity, Eq. (A.3.11). This in turn depends on the size of the volume where the energy inside the cavity is distributed. When the field penetrates into the mirrors, the effective mode volume is increased.

An effective energy penetration depth into a mirror can de defined using the amount of energy that is stored inside the mirrors, W_{pen}[123]. The energy penetration depth, L_e, is then the length by which the cavity would have to be longer to accommodate that energy. Taking the energy stored inside the mirror stack, normalizing it to the energy inside a period of the standing wave in front of the stack, W_{front}, and multiplying with the period of the standing wave, $\lambda/2n$, yields a quantity with unit of length

$$L_e \equiv \frac{W_{\text{pen}}}{W_{\text{front}}} \frac{\lambda}{2n} . \tag{A.5.3}$$

To numerically evaluate this quantity, one has to remember that the energy density is proportionally to the refractive index and the electric field squared

$$w = \frac{1}{2}\epsilon_0 \epsilon_r(\omega)|E|^2 \propto n^2|E|^2 \tag{A.5.4}$$

The phase and energy penetration depth agree quite well for sufficiently high reflective coatings [123]. This can be seen in the simulation in Fig. A.5.5a, where the field inside the stack was integrated numerically. Note that for the example stack with a low refractive index top layer, both penetration depths disagree by up to 20% inside the stop band, as can be seen in Fig. A.5.5b.

Note, that the energy penetration depth as defined above is not necessary the physical length scale in which significant energy is present in the stack. The energy and phase penetration depths can be significantly longer than the stack itself. This is the case especially for complex coatings stacks where for certain wavelengths resonances inside the stack can form. There, the energy density inside the stack is higher than on the outside it may therefore lead to long energy penetration depths. In the same way these resonances lead to strong variations of the phase, also leading to long phase penetration depths. An example for such a case can be seen in Fig. 3.2.6a.

A.6. Scaling effects on cavity stability

Off-the-shelve nano-positioning components, not optimized for the particular task, exhibit large length fluctuations - just due to their size (especially if multiple positioners need to be combined serially). One obvious reason is that the large dimensions lead to large displacements, if the mirrors forming the cavity are connected by long 'arms'. On top of that, larger structures lead to lower resonance frequencies. This can be seen with a small Gedankenexperiment. If L is the characteristic length scale of a system (imagine just a block), the mass will scale approximately with $m \propto L^3$, while the spring constant $k = -dF/dx$, or stiffness, in a certain direction will scale as the cross section divided by the length $k \propto L^2/L \propto L$. Using the basic formula for the resonance frequency ν of 'a mass on a spring'[125] yields the proportionality

Quantity	scaling with system size	
axial beam resonance freq	L^{-1}	better when smaller
transversal beam resonance freq	L^{-1}	better when smaller
in-coupling of acoustics	L	better when smaller
inertial displacement of components	L^2	better when smaller
thermal expansion	L	better when smaller
displacement by external force	L^{-1}	worse when smaller
displacement at excitation energy	$L^{-1/2}$	worse when smaller

Table A.6.1.: Overview of scaling of several effects with the system size L

$$\nu = \frac{1}{2\pi}\sqrt{\frac{k}{m}} \propto L^{-1} \tag{A.6.1}$$

and we see that the resonance frequency increases with miniaturization. Another way to understand this effect is when looking at the deflection of a small beam, tube or string. The lowest eigenfrequency is related to the wavelength by the phase velocity, $v = \lambda\nu$. If we assume the phase velocity as independent of the scaling, this yields the same proportionality of the resonance frequency, $\nu \propto L^{-1}$ [125].

But apart from the resonance frequency, also other key parameters scale with the characteristic system length:

The in-coupled acoustic noise through air roughly scales as the area where sound can couple in (because sounds are pressure waves, $F \propto L^2$) over the strength, $\propto F/k \propto L^2/L = L$.

Also the movement due to inertia of individual parts induced by acceleration of the whole setup scales inversely to the strength-to-mass ratio $\Delta x = F/k = a \times m/k \propto L^2$ (analogue to the common formulas for deflection under own weight).

However, miniaturizing makes the system more susceptible to directly applied forces: the displacement by a given external force, F_{ext}, scales as $\Delta x = F_{\text{ext}}/k \propto L^{-1}$.

The energy of the a harmonic oscillator is related to its frequency ω and amplitude of the motion x_a by $E = \frac{1}{2}m\omega^2 x_a^2$. With this, the amplitude at constant excitation energy increases slowly with miniaturization

$$x_a \propto \frac{\sqrt{E}}{\sqrt{m}\nu} \propto \frac{1}{L^{3/2}L^{-1}} = L^{-1/2} \tag{A.6.2}$$

Another effect that changes the cavity length, but on a slower time scale are thermal drifts of the setup, also decreasing with the system size.

A.7. Scattering by surface roughness

The total integrated scatter (TIS) of a single surface relates the diffuse (scattering) reflection to the total reflection, given by scattering and specular (regular) reflection, and can be approximated by[126]

$$\text{TIS} = \frac{R_d}{R_s + R_d} \approx (4\pi\sigma_r/\lambda)^2 \tag{A.7.1}$$

Here, σ_r is the RMS surface roughness and $\lambda$the wavelength of the light.

For low roughness (low scattering) the losses due to scattering therefore are given approximately by

$$R_d \approx (4\pi\sigma_r/\lambda)^2 \, R_s \, . \tag{A.7.2}$$

A simple approximation treats a dielectric stack, which has approximately unity specular reflectance, as a single surface and therefore the losses are given by

$$R_d \approx (4\pi\sigma_r/\lambda)^2 \, . \tag{A.7.3}$$

However, when adding an extra layer on top, the additional scattering due to its roughness has to take into account the reflectance of this mirror. For example applying a capping layer of PMMA with $R_s \approx 0.04$ and $\sigma_r = 1\,\mathrm{nm}$ leads according to Eq. (A.7.2) to $R_d \approx 8\,\mathrm{ppm}$ and usually does not affect the finesse of the cavity too much. The altered transmission of the stack due to impedance changed by this additional layer may dominate here.

B. Experimental Methods

This chapter introduces methods to measure important quantities of fibre based cavities. Furthermore an applied guideline for working with these cavities is given.

B.1. Measuring cavity finesse

The finesse is one of the most central figures of an optical cavity. It is related to the cavity linewidth and hints at the quality of the mirrors used. Furthermore, it determinations the conversion factor to calculate absolute extinction values in cavity enhanced microscopy (see Section 2.3.2).

It's measurement is critical for any fibre based cavity setup and several methods for this have been used and developed in our group. They differ in complexity and precision. Here, their implementation is explained along with their advantages and limitations.

Be aware that the cavity finesse is not necessary a single number for a cavity. It may change for different mode orders, at different positions on the planar mirror and with dirt or samples inside the cavity.

In Table B.1.1 several methods to measure the cavity finesse are summarized and will now be discussed in detail.

B.1.1. Narrow Laser

For this measurement techniques a laser with a linewidth significantly lower than the cavity linewidth is used. By sweeping the cavity length linear over a resonance with the laser and recording cavity transmission, the intrinsic cavity line-shape and -width can be resolved. For this one has to be sure that the laser runs on a single frequency mode for which commonly an external cavity diode laser (ECDL) is used. If the laser runs on multiple modes the lineshape differs from a Lorentzian or multiple Lorentzians can be observed. Furthermore one has to make sure that the laser polarization is adjusted to show only a single polarization mode.

The lineshape is recorded temporally with a photo diode in transmission. To calibrate this temporal to get the finesse two methods can be used.

Method	Typical accuracy	Typical limit	Measures
Narrow laser with side-bands imprinted	1%	Q>200000, F>50000	Q
Narrow Laser sweep over FSR	10%	None	F
Transmission spectra	1%	F<1000	Q, d
Cavity ring-down	5%	F>1000	Q

Table B.1.1.: Comparison of different methods to measure cavity finesse

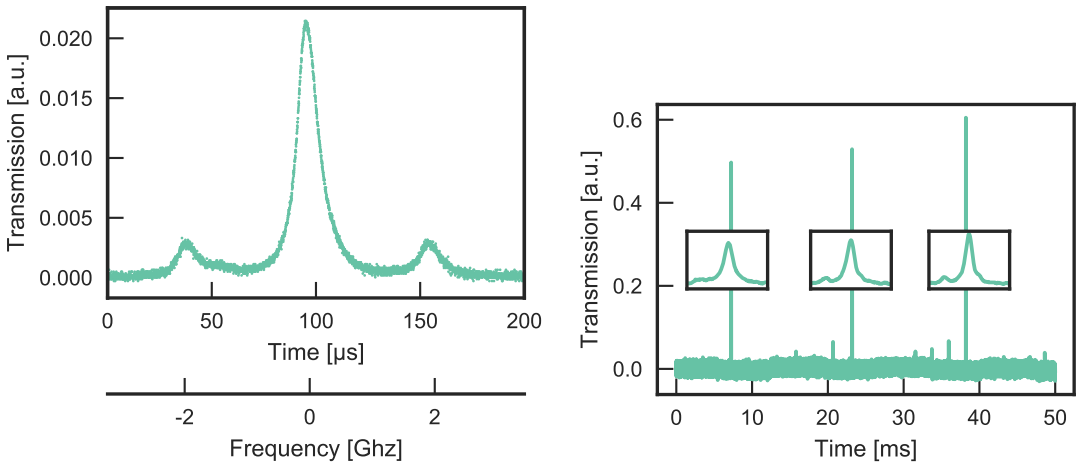

Figure B.1.1.: Measurement of cavity transmission of a narrow laser under linear length sweep to determine the cavity finesse. (a) Sweeping cavity length over laser line and imprinted side-bands, generated by 2 GHz phase modulation. The quality factor is about 8×10^5 and the finesse about 50000. (b) Sweeping over approximately three free spectral ranges with $10\,\mathrm{Hz}$. The insets show $5\,\mu\mathrm{s}$ wide zoom of the respective transmission peaks.

Imprinted side-bands

Using an electro-optic modulator (EOM), side-bands with a known frequency distance can be imprinted onto laser and be used as frequency markers. An electromagnetic wave with frequency ν, amplitude E_0 and a harmonic modulation of the phase with frequency ν_m can be written as

$$E_m(t) = E_0 e^{i(2\pi\nu t + m\cos(2\pi\nu_\mathrm{m} t))} \tag{B.1.1}$$

Under weak modulation amplitudes, $m \ll 1$, the exponential can be Taylor expanded to first order

$$\begin{aligned} E_m(t) &\approx E_0 \mathrm{e}^{2\pi i\nu t}\left[1 + \frac{im}{2}\left(e^{-i(2\pi\nu_\mathrm{m} t)} + e^{i(2\pi\nu_\mathrm{m} t)}\right)\right] \\ &= E_0\left(\mathrm{e}^{2\pi i\nu t} + \frac{im}{2}\mathrm{e}^{2\pi i(\nu-\nu_m)t} + \frac{im}{2}\mathrm{e}^{2\pi i(\nu+\nu_m)t}\right). \end{aligned} \tag{B.1.2}$$

Therefore, under weak modulation, two side-bands appear symmetrically around the laser frequency with the distance given by the modulation frequency,ν_m. For fast enough modulation and a high finesse cavity, these side-bands can be resolved in transmission when sweeping the cavity length. An example can be seen in Fig. B.1.1a for a $2\,\mathrm{GHz}$ phase modulated $780\,\mathrm{nm}$ external cavity diode laser using a fibre coupled EOM in front of the cavity fibre.

The linewidth in frequency space, $\delta\nu$, can be extracted by comparing to the known the distance of the peaks. With this the quality factor can be calculated and – when the cavity length is known – also the finesse using

$$Q = \frac{\delta\nu}{\nu} = \frac{d}{\lambda/2}\mathcal{F}\,. \tag{B.1.3}$$

For low finesse cavities the side-bands overlap with the carrier and the linewidth can be only extracted by computer assisted fitting. This imposes a limit for the lowest measurable finesse. For a common2 GHz modulation at $780\,\mathrm{nm}(\nu = c/\lambda = 385\,\mathrm{THz})$ this limits the measurable to about $Q \gtrsim 2 \times 10^5$. For a cavity finesse of 10000 that would mean that the finesse could only be measured starting from the 20th mode order.

The advantage of this method is the high precision of the measurement, only limited by acoustic noise changing the cavity length and laser amplitude noise and not by non-linearity of piezo movement.

However, usually a computer attached to a fast data acquisition device like an oscilloscope is needed to asses the transmission signal and a fitting method is used to locate the peaks. Therefore the acquisition is limited to a few Hertz if not implemented in an FPGA. Furthermore the method only measures the cavity Q directly and for the determination of the finesse the cavity length has to be known from another measurement. Furthermore, the needed microwave equipment (generator, amplifier, cabling), EOM and polarization optics easily sums up to costs above 20.000€.

Sweeping over FSR

A simpler and cheaper method to determine the FSR is to use the free spectral range under length change for calibration.

As derived in Appendix A.2, when changing cavity length finesse is also by the ratio of the free spectral range under length change, $\Delta d = \lambda/2$, and the linewidth under length change, δd,

$$\mathcal{F} = \frac{\Delta d}{\delta d} = \frac{\lambda/2}{\delta d}\,. \tag{B.1.4}$$

By sweeping the cavity length using a piezo element across more than a free spectral range multiple transmission peaks of the fundamental mode appear, as shown in Fig. B.1.1b. The ratio of this distance to the FWHM linewidth of a mode is the finesse. This requires is a finesse measurement with strongly reduced complexity and costs. It only needs sufficiently fast data acquisition electronics (like an oscilloscope) to resolve both narrow linewidth compared to the long free spectral range for high finesse cavities.

Precision is limited by mechanical fluctuations of the cavity length and the non-linearity of the piezo elements.

An advantage is that it directly measures the finesse and no cavity length calibration is needed.

B.1.2. Transmission spectra

By using a white light source and giving the cavity transmission signal onto a spectrometer, the finesse can be measured by comparing linewidth and distance of transmission resonances. At the same time, the cavity length can be extracted from these measurements.

Method	Light source	resolution (typical)	typical accessible range	points	Bandwidth
Distance of peaks in transmission spectrum	broad	200pm	10µm - stab. range	continuous	Hz
Shift of peaks in transmission spectrum	broad	200pm	$\lambda/2$-10µm	continuous	Hz
Injected laser in transmission spectrum	broad	<200pm		continuous	kHz
Resonances of fixed laser	fixed laser	fm	few pm around laser	$\lambda/2$+higher modes	MHz
Low finesse fringes (optionally with two lasers)	fixed laser(s)	nm	0µm - beyond stab. range	fully continuous	MHz(Hz)
Touching the mirror	fixed laser / broad	-	single point	one point	manual
Q-Factor	fixed laser	mode order	-10µm	$\lambda/2$	kHz
Higher order modes distance	fixed laser	10nm	-10µm	$\lambda/2$	kHz

Table B.2.1.: Overview of different methods to determine the cavity length.

However, the measurement is limited to low finesse cavities as the spectral resolution of common spectrometers will not allow to resolve and quantify narrow linewidths. Furthermore, the measurement is limited to longer cavities as multiple fundamental modes have to be inside the stop.band.

B.1.3. Cavity ring-down

As shown in Appendix A.2, the lifetime of the light inside the cavity is connected to the quality factor.

Using a pulsed laser, the cavity can be pumped with light and the exponential decay can be measured. The finesse is connected with the decay time

$$\mathcal{F} = \frac{c}{2d} 2\pi\tau \tag{B.1.5}$$

The timing resolution of the time-to-digital converter sets here a limit and only allows to measure cavities with high quality factor. This restricts to the measurement to either high finesse or long cavities.

B.2. Measuring cavity length

The cavity length is an important measure in cavity experiments. The absolute length is needed to calibrate experiments or to protect the mirrors from crashing into each other. The relative cavity length is needed to stabilize measurements and be resonant with lasers and certain transitions of materials inside the cavity, as well as in order to do spectroscopy.

The cavity length can only be measured when light is able to enter the cavity. When employing a measurement with a fixed frequency laser this is only possible when the cavity is

multiple wavelengths of the laser, except when working at wavelengths with low finesses ('Low finesse fringes').

In Table B.2.1 and overview of different methods to measure the cavity length is given. These methods will be detailed in the following.

Distance of peaks in transmission spectrum. When looking at white light transmission through the cavity, the length of the cavity can be inferred from the spectral distance of two neighbouring resonances,

$$d = \frac{\lambda_1 \lambda_2}{2\,|\lambda_1 - \lambda_2|} \approx \frac{\lambda^2}{2\Delta\lambda}\,. \tag{B.2.1}$$

When imaged on a sensitive spectrometer the white light can be used from a SLED, a supercontinuum source or even the amplified spontaneous emission (ASE) of a laser diode. The range where the length can be detected is limited towards shorter cavity lengths. There, the spacing between adjacent cavity lines might get larger than the bandwidth of the white light. Furthermore, the spacing might exceed the coating of the cavity, or even on the edges of the stop band of the coating the penetration depth changes and distorts the measurement.

The Bandwidth is limited by the limited amount of light when using a faint source and the readout of the spectrometer and can be typically be a few Hz-100Hz. Requires a digital computer program to get the length.

Shift of peaks in transmission spectrum. Even if only one peak in the transmission spectrum is visible, the length of the cavity can still be measured if the longitudinal mode order is known. The length is related to the mode order q and the wavelength λ where the transmission peak appears via

$$d = q\frac{\lambda}{2}\,. \tag{B.2.2}$$

The resolution is limited by the resolution of the spectrometer. With a homebuilt camera and a grating several hundred measurements per second where possible.

Resonances of fixed laser. Using a fixed laser, the cavity lengths where maxima of transmission appear indicate lengths where the cavity is resonant with the laser. If the laser wavelength is known, the absolute cavity length can be measured to a very high precision.

The distances between resonances can be used to calibrate piezo elements that change the cavity length.

The length of a cavity around resonance can be measured When using a high bandwidth photodiode.

Low finesse fringes (optionally with two lasers) Using a single frequency laser at a wavelength where the cavity has a low finesse yields broad lines or even sinusoidal transmission as a function of cavity length. This makes length measurement less accurate then working at high finesse but allows length detection across a much longer length. When using two lasers the length can even be detected absolutely if the signal is recorded

Touching the mirror. The point where the fibre touches the planar mirror can be detected by looking at the transmitted signal when changing cavity length, see e.g. Fig. B.4.4. This is common point of reference when the length should only be known roughly. Note that the length relative to the optical cavity length may change with angular alignment due to a non planar end-facet of the fibre.

Q-Factor. The Q-Factor and the finesse are related via the cavity length

$$Q = \frac{d}{\lambda/2}\mathcal{F} \tag{B.2.3}$$

If both cavity and Q-factor can be measured, the cavity length can be extracted. But even if only the Q-factor or even only the relative linewidth is measured, its change between consecutive mode orders can be used to extract the mode order and with it the length. With the mode order q relating quality factor and finesse by $Q = q\mathcal{F}$, the ratio of the Q factor of two consecutive mode orders is

$$\frac{Q_{q+1}}{Q_q} = \frac{q+1}{q}\,. \tag{B.2.4}$$

For short enough cavities, this allows to extract the mode order.

Higher order modes. As noted in Appendix A.3.2, the cavity length or the frequencies where higher order modes appear depend on the radius of curvature of the cavity mirror.

When recording cavity transmission of a monochromatic laser under cavity-length modulation the length of the cavity can be measured by measuring the spacing between higher order modes

$$d = R\left(\tan^{-2}\left(\frac{2\pi}{\lambda}\Delta d_{01}\right) + 1\right)^{-1}\,, \tag{B.2.5}$$

if the radius of curvature of the concave cavity mirror, R, is known.

B.3. Measuring mirror radius of curvature

Another important quantity of the cavity is the radius of curvature of the convex mirror on the fibre end facet. Together with the cavity length it determines, for example, the mode volume, the mode size and therefore the achievable resolution when used as a microscope and the mode matching. The radius of curvature is not completely fixed by the geometry of the fibre depression, but may also vary slightly with the angular alignment, if the depression is not perfectly spherical. Here, several methods to determine the radius of curvature are presented, both in-situ - when using the cavity fibre in the setup - or when looking at the fibre with a microscope.

White light interferometry.

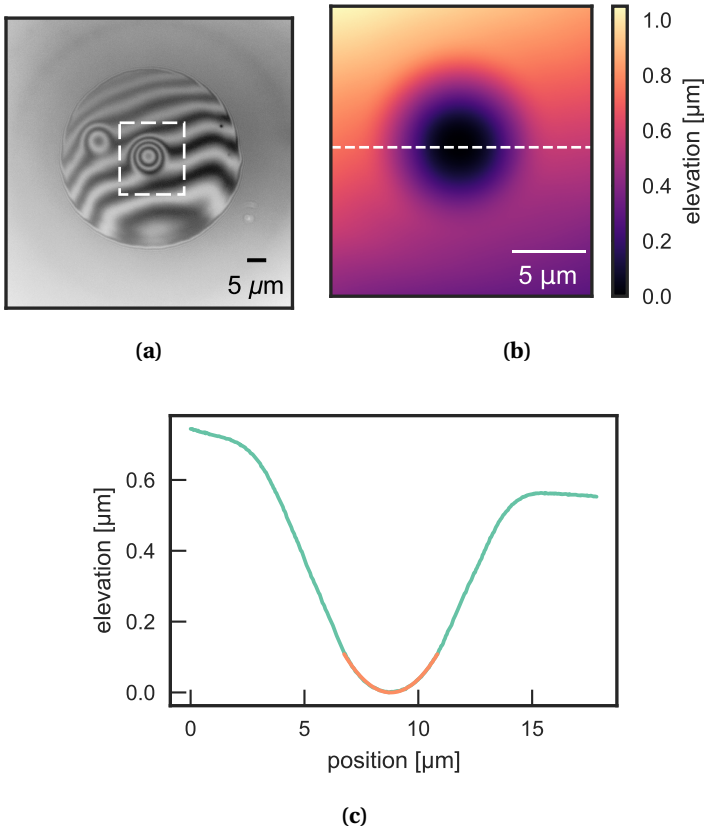

Figure B.3.1.: Radius of curvature measurement using the while light interferometer. (a) Raw white light image as recorded by the camera. The interference fringes can be clearly seen on the end facet of the fibre. The central depression inside the dashed rectangle is centred at the position of the (here invisible) fibre core. The outer parts of the fibre have been removed by laser machining and the remaining fibre can be seen in the background as grainy rings out of focus. (b) Phase unwrapped image of the central part marked by the dashed rectangle in (a). (c) Profile along the dashed line in (b). The orange line is a parabolic fit to the data with radius of curvature 19.3 µm in the centre.

Mode size. When a scanning cavity image of a point-like object is recorded, the mode waist of the cavity can be extracted. Repeating this measurement for different cavity lengths, the dependence of the mode waist on the cavity length can be used to coarsely extract the radius of curvature. A measurement of this type is shown in Fig. 4.2.4b.

Gouy phase of higher order modes. If the longitudinal mode order of the cavity is known the distance between higher order modes, d_{ho}, can be used to determine the radius of curvature of the mirror

$$R = q\frac{\lambda}{2}\left(\tan^{-2}\left(\frac{2\pi}{\lambda}d_{\mathrm{ho}}\right)+1\right)\,. \tag{B.3.1}$$

A measurement of higher order mode spacing and simulation how it scales with different radii of curvature is shown in Fig. A.3.4b.

B.4. Taming the cavity

This section is meant to be an applied introduction and guide for actual students and researchers working with a fibre based optical micro-cavity. The presented methods and best practices are derived from the collective experience learned in the years since the first fibre-based micro-cavity went operational in our group. Usually, this kind of knowledge is only passed along orally. Here, the idea is to describe the workflow with the cavity as detailed as possible to simplify the operation of the cavity, avoid some pitfalls but also unnecessary over-cautious behaviour and eventually safe a lot of time, nerves, and broken cavity fibres.

B.4.1. Glueing fibres into needles

In the stable cavity setup, the fibre is glued into a small tube for multiple reasons. First, once glued with care, the fibre is much more protected against breakage in the later usage. Most of the circumstances of loosing a cavity fibre are related to breaking the fibre end (see Appendix B.4.2). With the fibre glued into the protective metal shielding and only sub-millimetre protrusion, snapping the fibre is almost impossible. This also facilitates fibre cleaning, where a paper tissue is dragged over end facet of the fibre which usually can introduce strong lateral forces snapping the fibre (see. Appendix B.4.4).

The tube to be used is a stock syringe needle blunt (B.Braun Sterican 0.80x22mm (Blunt)) with a 0.8mm outer diameter. Also smaller needles were used (0.4mm outer diameter) but the large diameter improves stability and facilitates insertion.

The fibre with about 150µm diameter will be loose inside the needle. To decrease weight and therefore increase stability not the whole needle is filled with glue. The needle blunt needs to cut to the appropriate length. In order not to collapse the needle, what happens when using pliers, a fast rotary tool with a cutting wheel (Proxxon NO 28 809) is used, see Fig. B.4.1a.

Also multiple fibres can be glued into a single needle as is shown in Fig. B.4.1b.

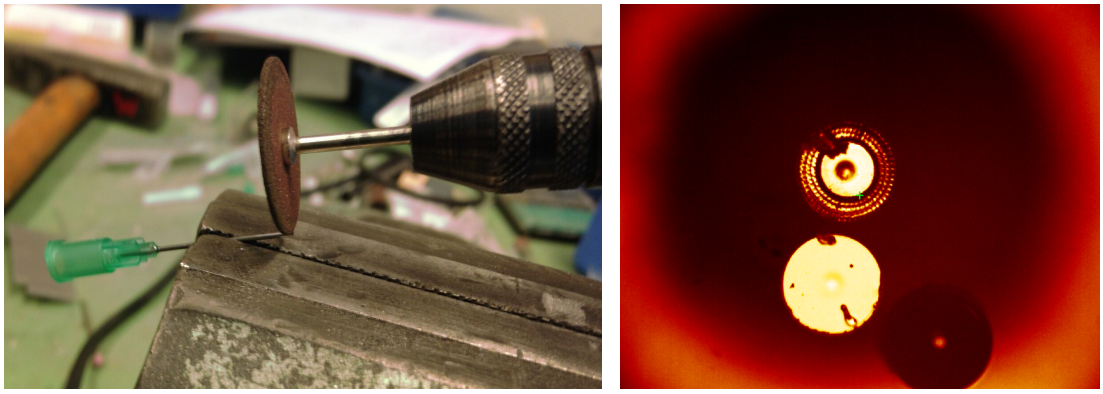

(a) (b)

Figure B.4.1.: (a) Preparation of the stock needle for glueing the fibre into it. (b) Microscopy picture (false colour) showing the front of the needle with three different fibres glued into it (top-most: sharpened cavity fibre, middle: cavity fibre with flat end facet, bottom: uncoated convex lensed fibre) . The blurred edge of the needle can be seen in the background.

B.4.2. Handling of fibres

It is common, when starting with fibre base cavities, that in the beginning several fibres get destroyed while experimenting until the researcher knows the common circumstances where this happens. The writer of this lines himself broke a lot of fibres, especially in the beginning, when a setup was changed fundamentally or in a rush and especially on Friday evenings (be careful!). However, with the correct handling, a cavity fibre can survive several years inside a heavily used setup. When following this guide, the hope is to accelerate this path paved with broken fibres and painful learning process and reduce the loss of cavity fibres with some simple precautions.

First, it is instructive to know how cavity fibres can be destroyed. The most common reasons to render a cavity fibre non-operational are

- snapping the fibre end under a shear load
- getting permanently sticking dirt on the fibre end-facet
- scraping the coating or scratching it

However, the cavity is also surprisingly robust in other circumstances. The fibre-end facet can hit the macroscopic mirror millions of times with speeds of $10^{\mathrm{mm}}/_{\mathrm{s}}$ ($10\,\mathrm{kHz} * 1\,\mu\mathrm{m}$) and push it back a few hundred nm without braking.

Also, so far no thermal damage due to excess optical power circulating in the cavity has be seen in our group even with few watts of power inside the ($36\,\mathrm{W}, 2^{\mathrm{GW}}/_{\mathrm{cm}^2}$[35]). This is presumably due to the ultra-low-loss coatings used. Furthermore, dirt picked up by the fibre, can be removed from the fibre in approximately 90% of cases.

Preventing cavity from getting dirty. Dirt on the fibre mirror leads to an unusable cavity if it is in the centre of the profile. In contrast, when the macroscopic mirror gets dirty this is not as critical since the cavity still works on other places.

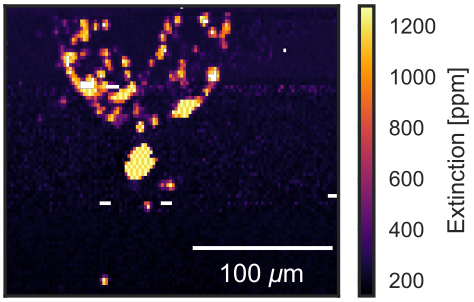

Figure B.4.2.: Radial imprint of the fibre-profile onto the plane mirror after crashing, roughly 125 µm in diameter. Measured through an extinction scan.

The orientation of the setup can have an influence on how easily dust or other particles contaminate the cavity fibre or macroscopic mirror. The best orientation found is with the cavity axis horizontally. With this, no dust in the air can settle on any of the mirrors. Furthermore, liquids used for cleaning the fibre mirror get washed away by gravity. When the plane mirror is placed above the fibre mirror, dirt or parts of the sample may drop onto the fibre mirror. A horizontally mounted cavity fibre can operate in a badly cleaned lab with dust bunnies in the corners for years at a finesses of 50000 without the need for cleaning.

Using a fibre with a deeper mirror profile prevents touching the mirror with the core and therefore no small dirt can be picked up in the central part.

Furthermore, when the mirror needs to be touched (e.g. for length determination or when setting up the cavity), choosing a clean spot prevents picking up dirt.

If the fibre gets dirty, cleaning inside the setup is commonly possible, see Appendix B.4.4.

Robustness of fibres

See Fig. B.4.2 for an example where fibre and planar mirror where repeatedly crashed into each other. The positioner was commanded 100µm to far into the mirror and the fibre pushed the whole mirror holder back. The position of the fibre was still triangular swept by a piezo for approx. 500nm at 100Hz for several seconds. A noise emerged from the piezo exciting acoustic vibrations in the whole setup. The planar mirror got damaged, but not the fibre mirror. The performance of the fibre was not reduced due to the critical part in the central depression of the fibre not touching the two and the harder glass surface compared to the softer PMMA layer on the planar mirror. Furthermore the central fibre part did not even get dirty. The softer PMMA layer on the plane mirror shows indentions of the fibre. However, the fibre high scattering losses only locally. This is an example of the robustness of the scanning cavity system, as long as snapping of the fibre is inhibited.

B.4.3. Diagnostics of cavity failure

When the fibre cavity is not working anymore as expected it is instructive to find the cause in a systematic ways. This determines if it would be sufficient to clean the fibre, (maybe even in it's present place inside the setup) or if a new fibre has to be used. When this can be done without having to remove the fibre, a lot of time can be saved.

Without experience it can be hard to judge if the fibre is broken, dirty or just some alignment of the setup got lost.

Looking at the transmission signal of a narrow-band laser should give information on the state of the cavity:

- If a broad linewidth transmission signal is observed, the coating of the cavity fibre was scraped off.
- No signal can be seen if fibre got dirty.
- no signal if alignment gone or cavity length too long
- Check to see if you see modulation with broad laser, check if cavity is short enough, turn up power and detector sensitivity
- Look at fibre mirror alone: if you see strong light transmission where high reflectivity should be, you are sure that the coating is gone.

B.4.4. Fibre cleaning

When dirt from the mirror is picked up on the fibre end facet, the cavity fibres can be easily cleaned most of the time. This worked in about nine out of ten cases. If the cavity fibre can be separated by at least 10mm from the mirror or if the mirror can be removed, the fibre end facet can be cleaned in place, keeping angle (and position) calibration of the setup. To do so a lint-free paper tissue (Kimtech Kimwipes[1]) soaked with isopropanol is pushed against the fibre end and is dragged over it. This can be either done by hand or with a small piece of tissue held with tweezers. A lot of pressure can be applied as long as the fibre end is protected against snapping under lateral forces (see. Appendix B.4.1). So far, even after hundreds of cleaning operations, sometimes using intense force to get persistent dirt off, the coating did never peel of. After cleaning the original finesse (of up to 50.000) was achieved. Due to the small mode size of the cavity on the fibre, the cleaning was only either completely successfully (yielding the intended original finesse) or no change in performance was observed.

B.4.5. Macroscopic mirror cleaning

A macroscopic mirror can also be easily cleaned and yield full finesse of more than 50.000. For this the mirror was washed with isopropanol and dragged over a lint free wipe.

B.4.6. Setting up the cavity

This is a guide to setup the cavity. Here, the critical part is that the cavity length is not known. Transmission signals from a laser at a wavelength where the cavity has high finesse only becomes visible for cavity lengths smaller than about $1/2$ of the radius of curvature of the mirror, and therefore commonly at about $5-20\,\mu m$. For a lot reasons however, this transmission signal can be missing (e.g. fibre dirty, dirty location on plane mirror, angle misalignment, no light in-coupled, detection path not well aligned) and one cannot check the cavity length and therefore might crash the fibre into the plane mirror and contaminate or destroy it. To always get a signal,

[1] Lens cleaning tissue can also be used but was not needed

Figure B.4.3.: A bare fibre and its reflection in the macroscopic planar mirror. The cavity length can be estimated by the distance between the end facet of the fibre and its reflection. In this picture is is about half of to the known diameter of the fibre($125\,\mu$m). Dividing this distance by two, because the distance to the mirror image is twice the distance to the mirror, the cavity length is about 30µm. Keep in mind that for a fibre with a sharpened tip the cavity length may even be shorter.

a laser at a wavelength where the cavity is transparent can be used. There, contaminations do not decrease the signal severely and no stable cavity is needed for transmission. Therefore, always transmission can be observed even for much longer cavity lengths $> 1\,\mathrm{mm}$.

This procedure should be followed when trying to get a signal from a new cavity.

1. Align fibre/needle roughly perpendicular to large mirror. Use the reflection of the fibre in the large mirror as a reference. The fibre and its mirror image have to form a straight line, see Fig. B.4.3. This has to be the case viewed from two angles.
2. Monitor length and safely reduce cavity length
   - Couple in a Laser with a wavelength where the cavity is almost transparent, e.g. has low finesse.
     - You can also simultaneously couple in a high finesse laser.
   - Place sensitive APD/PD directly after the second cavity mirror without any collimating optics. By just hitting the detector with the large light cone, large displacements of the fibre do not affect the alignment on the detector and therefore make subsequent angular alignment easier. If it is a variable gain detector: turn gain to highest sensitivity to see signal if alignment is imperfect or cavity length is not inside the stability criterion yet.
   - Modulate cavity length with piezo (slow e.g. 50 Hz, 1-2µm amplitude) and observe interferometer-like sinusoidal modulation of the cavity transmission on an oscilloscope. Trigger on the function generator to see a stable image.
   - Reduce cavity length and observe how the modulation of transmission shifts. The distance between nodes is half of the wavelength of the used laser.
   - Coarsely check the distance between the fibre and it's reflection in the plane mirror by looking from the side with bare eye or a camera, see Fig. B.4.3. Slow down when the space between the fibre and its reflection vanishes. Block light coupled into the fibre to better see the end of the fibre.

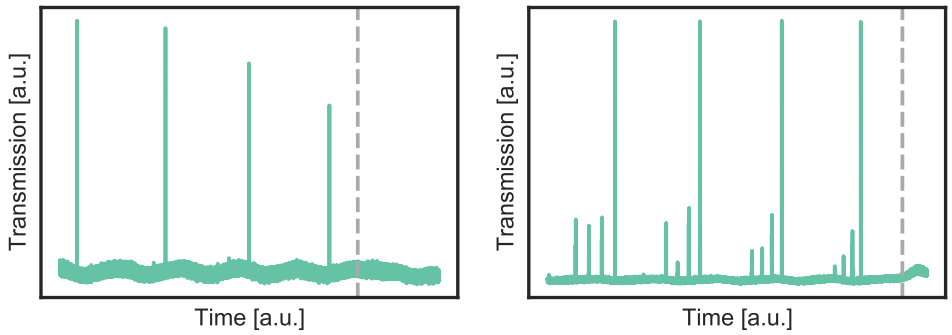

(a) **(b)**

Figure B.4.4.: Cavity transmission under linear cavity length sweep recorded on an oscilloscope. A narrow band Laser where the cavity has a high finesse produces characteristic sharp peaks in transmission. The low amplitude modulated background is due to a second laser where the cavity is almost transparent. The positive x-axis is towards shorter cavity lengths. The dashed lines mark the point where the two mirrors start to touch and the cavity length change is not linear with the piezo expansion (and therefore time) any more. (a) Here, only fundamental modes can be observed. The distance between these peaks is $\lambda/2 = 450\,\mathrm{nm}$. Their intensity decreases to shorter cavity length due to worsening mode-matching, see Appendix A.3.1, and hints at the near-by minimum cavity length. The dashed line marks the position where the mirrors touch (b) Here, the smaller sharp peaks are higher order modes, always on the side of longer cavity lengths. The touching of the mirrors can here again be seen by the absence of (higher order) high finesse modes. Furthermore the signal of the low finesse modulation changes.

- You should notice when entering the regime of a stable cavity (yet very low finesse) when the shape of the modulated signal changes from sinusoidal to a slightly more distorted shape. Here you should be careful and slow down approaching even more.
- Be sure to be transversally on a place where the mirror is clean to not pick up dirt or parts of the sample with the cavity fibre end facet.
- Stop when touching the mirror starts to 'stretch' the modulation .
- Retract 2 or 3 FSR to stop touching the mirror.

3. Couple in high finesse Laser
   - You should be able to see sharp cavity resonances on the oscilloscope, as can be seen in Fig. B.4.4.
   - If you see no sharp resonances look at cavity checklist, see Appendix B.4.8.
4. If no high finesse signal available yet, you have to adjust the cavity angle.
   a) Adjust the angle that the cavity looks with bare eye /camera approximately orthogonal to the mirror.
   b) Adjust the angle to maximize the modulation signal of the Laser at low finesse to
      i. see the highest modulation amplitude
      ii. or: sharpest resonance peaks
      iii. or better: sub-structure of different higher order modes inside a single free spectral range can be seen

5. Angle optimization
    - Adjust angle that the cavity length does not change when changing the angle. This is the point where the fibre is approximately orthogonal to the mirror.
    - Optimize the angle between the mirrors to maximize transmission of the fundamental mode. Assure that you are hitting the detector correctly not to spatially filter the fundamental mode.
6. Measure finesse
    - Use coarse finesse measurement by modulating over FSR, see Appendix B.1.1.
7. Angle fine-adjustment
    - Further refine the angle by maximizing the finesse in a live measurement
        - Make sure to do this in the centre of the stop-band where you expect the highest finesse, otherwise the maximum might be where the angle of the coating is tilted to yield an even stronger reflection of the coating stack.

B.4.7. Detector alignment

The detector behind the cavity can be aligned when coupling in a laser where the cavity is transparent. Alternatively, if there is already some small signal, one can modulate the cavity length narrow around a transmission resonance. Then, the cavity is transmissive for a significant part of time and the transmitted light may even be visible with bare eye.

B.4.8. High finesse cavity setup checklist

This checklist should be followed when no transmission signal at high finesse signal can be seen. It helped a lot of times not to disassemble the whole cavity or clean the fibre without a reason.

Check the following points of failure if the signal disappears:

1. Is the oscilloscope sampling fast enough not to miss the peaks?
2. Is light coupled in?
    a) Is the laser turned on / not blocked?
    b) Is it coupled in?
        i. Check power in second port of on fibre-beam splitter in front of cavity
        ii. Or: do I see light from the side with bare I / IR viewer / or on a camera?
    c) Is the Laser running single-mode? (slightly change current/motor)
3. Is the cavity length modulated (far enough)?
    a) Quick check: Is the modulation audible at higher frequencies (~ few kHz).
    b) Do I see modulation of transmission with a Laser coupled in at low finesse
    c) Try modulating with the longest piezo available
    d) Are amplifiers turned on / cables plugged.
4. Am I on an strongly absorbing part of the mirror?

a) Turn up detection sensitivity / laser power.

b) Move cavity transversally.

5. Is the cavity short enough?

   a) Can I approach to see when I hit the mirror (with Laser@low finesse)?

6. Problems in the detection path?

   a) Do I hit the detector?

   b) Is it blocked/filtered?

   c) Ramp up detector sensitivity if adjustable.

   d) Is polarization filtering in place and correct?

7. Is the cavity angle correct?

   a) Repeat angular alignment (see Appendix B.4.6) if there is the possibility that the angle changed.

8. Is the cavity fibre dirty?

   a) Follow Appendix B.4.4 to clean the fibre in-place.

9. Is the fibre broken?

   a) How does the cavity mode (with a low or high finesse Laser) look behind the cavity?

      i. Use Camera / paper / IR-detector card.

      ii. If it is pointing in a wrong direction the fibre is broken.

      iii. If it is ragged the fibre may be dirty but most certainly is broken.

   b) Look at the cavity fibre from behind the plane mirror with a microscope (see e,g, Fig. 5.2.1a).

B.4.9. Mirror markers

The planar mirrors commonly used in the scanning cavity microscope are 12.7mm (half-inch) in diameter. Placing markers on this rather large surface, compared to the single-picture scannable area of approximately $100\,\mu m$ by $100\,\mu m$and nano-scale sample sizes, can facilitate several tasks.

First, it allows to align the angle of the mirror reproducible and find the same position even after changing the mirror. This allows to compare samples on the mirror in different measurements and compare measurements with other methods, e.g. atomic force or electron microscopy. Even measurements before and after placing samples on the mirror can be compared to subtract background inhomogeneities (scattering, dispersion) of the mirror[27].

Furthermore, different samples can be placed on the same mirror in well-specified locations, reducing the need to exchange mirrors and saving mirror wastage.

Finally, length scales of the scan area can be calibrated using precisely spaced patterns and naked eye visible patterns can be used to identify mirrors.

For marking the mirror, the same CO_2-laser machining setup as for shooting of the concave depression into the fibre ends is used[27]. An monochromatic image of the pattern can be created in any graphics software. Then each dark pixel of this image is written on the mirror using a single shot. This way complex patterns, rectangles and labels can be written. For

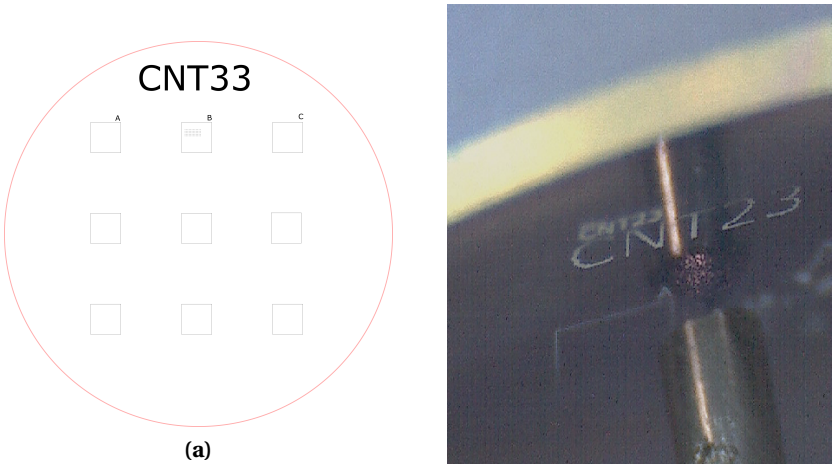

(a) (b)

Figure B.4.5.: (a) Markers and label for a half inch mirror (red border). Each black pixel is a laser machining shot. Rectangular areas are used for drop-casting different samples on a single mirror. Dots in square 'B' are shot with less power to be smaller and just visible inside the sensitive scanning cavity setup. (b) Photo of mirror with markers when assembled inside the experiment. The fibre tip inside the needle as well as some scattered light (red) can be seen.

being visible with the naked eye or a microscope, stronger shots are used, and enhancing the visibility even more with multiple rows of shots next to each other. When using drop-casting methods to place samples on the mirror, surface effects at these lines can even contain liquids in a area while drying. An example of a pattern and a marked mirror is shown in Fig. Fig. B.4.5.

High power laser shots lead to large indentations in the mirror surface ($> 10\,\mu$m diameter) where scattering is so high that basically no light enters the cavity. To generate small well-locatable structures visible inside the cavity, low power shots can be used. These just lead to local buckling of the dielectric mirror coating with ~µm diameter. Microscopic picture of such mirror markings are shown in Fig. B.4.6.

B.4.10. Cavity stability measurement

For quantifying the stability of the cavity, we commonly calculate the standard deviation of the length fluctuations of the cavity. The Fourier-transform of the cavity length is used to get further insight into the frequencies at which these fluctuations appear. The cavity length is measured using a photo-diode recording the transmission at the side of a cavity resonance. Because this is a common task, and a lot of care has to betaken to get the units and conventions using the particular Fourier transform right, this section covers in more detail the Fourier transform and unit conversion. For use with an oscilloscope, the derivation of plain voltage amplitudes from a power spectrum is derived. Furthermore, the conversion of the voltage to a length and the calculation of the standard deviation are derived.

Power density spectrum to voltage spectrum. The oscilloscope by *LeCroy* used has an internal Fast Fourier Transform(FFT) algorithm to display the frequency spectrum of a time trace. It outputs a power density spectrum in units $\mathrm{dBm}/\sqrt{\mathrm{Hz}}$. According to the definition of

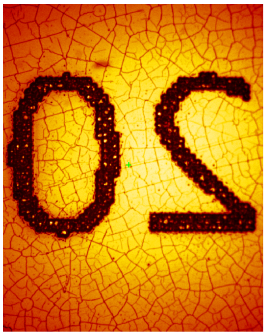

(a)

(b)

Figure B.4.6.: (a) "20" written on the mirror with 20µm pixel pitch. You can see cracks in the mirror formed by the powerful shots. (b) Grid for length calibration by four shots, 15µm apart.

the unitdBm we can convert it to a power using

$$P = 10^{-3} \times 10^{\frac{dBm}{10}} W \tag{B.4.1}$$

To get the voltage one has to know that the power is defined here from the voltage dumped into 50Ω, which is the impedance of the oscilloscope channel (check the proper configuration on the scope!). Using the relation between power, voltage, current and resistance, $P = U\,I$ and $P = U^2/R$ we arrive at a voltage from this

$$U = \sqrt{50\Omega \times P} \tag{B.4.2}$$

Notes on discrete Fourier transformations (DFT, FFT). The Fourier transform takes a function and transforms it into reciprocal space. For signals with discrete data points, the discrete Fourier transform (DFT) translates a signal consisting of N data points x_j to N complex coefficients $\hat{a}_k$

$$\hat{a}_k = \sum_{j=0}^{N-1} e^{-2\pi i j k/N} x_j,\ k = 1...\mathrm{N} \tag{B.4.3}$$

To yield the initial time signal from this frequency spectrum, the inverse transform includes the factor $1/N$ for normalization, $x_j = {}^1/_N \sum_{j=0}^{N-1} e^{2\pi i j k/N} \hat{a}_k,\ k = 1...\mathrm{N}$. Care must be taken because the convention whether to include the normalization constant in the forward, the inverse or distribute it to both transforms may vary between implementations and uses.

If the initial signal is real-valued, only $N/2$ complex coefficients are sufficient to define the signal. If the signal is recorded in time intervals spaced by τ_s, the k-th Fourier coefficient represents an harmonic oscillation of frequency

$$\nu_k = \frac{k}{\tau_s N} \tag{B.4.4}$$

The spacing between data points in frequency space is therefore

$$\Delta\nu = \frac{1}{\tau_s N} \tag{B.4.5}$$

and depends on the total number of points taken and the sampling rate. The maximum frequency is called the Nyquist frequency

$$\nu_{\mathrm{n}} = \frac{1}{\tau_s 2}\,, \tag{B.4.6}$$

and is half the sampling frequency. Signal components in the source signal that have higher frequency will not show up in the spectrum at their frequency, but at lower frequencies, an effect that is called *aliasing*. In this case faster sampling should be used to get a meaningful spectrum.

The zeroth coefficient is related to the average of the signal, $\bar{m} = \sum x_j/N$, or the 'DC'-part via

$$\hat{a}_0 = \sum_{j=0}^{N-1} e^0 x_j = N \times \bar{m} \tag{B.4.7}$$

Squaring the absolute value of the coefficients yields the power spectrum, $|\hat{a}_k|^2$.

To compare the strength of spectral components independent of sampling rates, the power spectral density is useful. It it the power divided by the frequency spacing

$$\mathrm{PSD}\,(k) = \frac{|\hat{a}_k|^2}{\Delta\nu}\,. \tag{B.4.8}$$

Standard derivation (or RMS) from spectrum. The standard deviation of a signal with N data-points x_j and average $\bar{m} = \sum x_j/N$ is defined as

$$\sigma = \sqrt{\frac{1}{N}\sum_{j=0}^{N-1} |x_j - \bar{x}|^2}\,. \tag{B.4.9}$$

For a signal centred around 0, $\bar{x} = 0$, this is the same as the root mean square (RMS) and these terms are often used interchangeable although not the same in a strict sense.

The standard deviation can also be directly derived from the Fourier transform of a signal. According to Parceval's theorem, the total power of the signal in time and frequency space is conserved,

$$\sum_{j=0}^{N-1} |x_j|^2 = \frac{1}{N}\sum_{k=0}^{N-1} |\hat{a}_k|^2\,. \tag{B.4.10}$$

Therefore, the RMS is given by the sum of the absolute square of all coefficients

$$\mathrm{RMS} = \sqrt{\frac{1}{N}\sum_{j=0}^{N-1} |x_j|^2} = \frac{1}{N}\sqrt{\sum_{k=0}^{N-1} |\hat{a}_k|^2} \tag{B.4.11}$$

Keeping in mind that the zeroth coefficient is the mean of the signal, the standard deviation is the sum of all coefficients except the zeroth

$$\sigma = \frac{1}{N-1}\sqrt{\sum_{k=1}^{N-1} |\hat{a}_k|^2} \tag{B.4.12}$$

For a real signal, it is sufficient to sum over the first half of the coefficients if a factor of two is included

$$\sigma = \frac{1}{N-1}\sqrt{2\sum_{k=1}^{N/2} |\hat{a}_k|^2}\,. \tag{B.4.13}$$

B.4.11. Parasitic resonators

Even only very small reflections can lead to large fluctuations if a parasitic resonator is present in the beam path. Following the derivation of the transmission through a resonator from Appendix A.1.4 we can derive the transmission on and off resonance. The maximum modulation amplitude between maximum and minimum transmission of a resonator with reflectivities $R_{1,2}$ evaluates to

$$\frac{T_{\max} - T_{\min}}{T_{\max}} = 1 - \left(\frac{1-\sqrt{R_1 R_2}}{1+\sqrt{R_1 R_2}}\right)^2 \approx 4\sqrt{R_1 R_2}\,. \tag{B.4.14}$$

The last term is an approximation for small reflectivities. As can be seen in Fig. B.4.7, even a reflection of 10^{-3} can lead to fluctuations of the transmission of 10% if one of the mirrors is highly reflective. If the fibre mirror used is terminated with a straight cleave, this may lead to reflections of about 4% and transmission amplitude fluctuations of already 30%. Using angle cleaved fibres can significantly reduce reflections down to about $1\,\mathrm{ppm}$ ($-60\,\mathrm{dB}$) but still yields fluctuations of up to 0.5%. The same level of reflection appears at common fibre beamsplitters and fibre fusion splices.

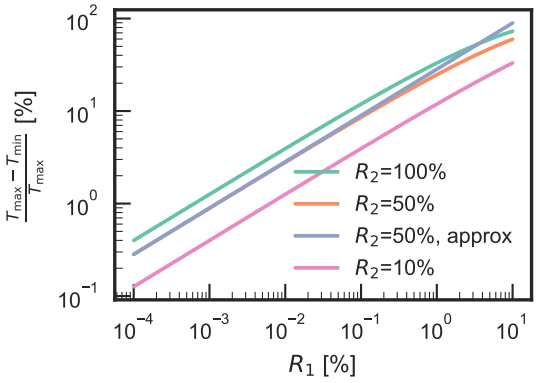

Figure B.4.7.: Modulation amplitude of a parasitic resonator (off-vs-on resonant transmission) for different mirror reflectivity pairs R_1, R_2 forming the resonator. The straight line is the approximation for with $4\sqrt{R_1 R_2}$ for very low finesse resonators.

According to Appendix A.2, when the resonator length drifts, modulations have periodicity $\Delta d = \lambda/2$, where λ is the wavelength of the laser. When the laser wavelength drifts, modulations have periodicity $\Delta\lambda_{\mathrm{par}} = \lambda^2/(2d_{\mathrm{par}})$ where d is the length of the parasitic resonator.

B.4.12. Guide to cavity stability

This section describes methods and pitfalls on the way to the maximum stable cavity length.

- First get rid of ground loops
  - Look at vibrations at 50Hz
  - Modulate with 51Hz vs 50Hz to see ground loops
  - Disconnect all piezos...
- Look at the cavity's passive stability (without an active feedback lock). This way you can discriminate better between influences on the setup's mechanics and more complicated electronic feedback resonances.
- Continuously monitor the passive stability.
- Modulate the cavity length to measure coarse cavity length changes by looking at the position of the resonance on an oscilloscope. Then hit or press with a screwdriver on different parts of the setup, to qualitatively see the influence on the cavity length of different parts.
- Check that all parts are fixed to each other properly with enough pressure.
- To see if photothermal effects play a role in stabilizing or destabilizing the cavity, see if locking to the other flank of the transmission peak or at a different set point changes the stability.

B.5. General Lab and data analysis tips

Here are some general tips for lab work and data analysis. They might be strongly biased but in my opinion simplified and sped up several tasks a lot.

Building measurement setups.

1. Always use hex cap screws (e.g. ISO 4762): Slit or cross screw heads tend break easily (cam-out), need pressing to be turned and the screwdriver easily slips from the screw. Especially together with ball end screwdrivers these allow to fasten screws even in badly accessible regions.
2. Use sensitive detectors for aligning stuff: If you have a very sensitive (single photon level) detector like a CCD or CMOS camera, fibre coupling can be achieved easier, especially with weak signals in the beginning.
3. Use fibre coupled components due to the simplicity of chaining and switching out different components. Fibre coupled beam-splitters help to determine power coupled into a fibre. Fibre to fibre butt-coupling with APC fibres and cheap (5€) couplers has a power transmission repeatability better than 2% when repeatable unplugging and reattaching.

4. Use switchable gain detectors for simplicity to quickly adapt to changing light levels.
5. When building electronics, look for components targeted for 'makers', as hobbyists that play around with electronics are often called. These components are less bare-bone than raw electronic components, lengthy documented (and a lot of tutorials exist) and cheap. Using these can save a lot of time. In this work stepper- and DC-motor controllers, *arduino* microcontroller boards, FPGAs, level shifters, relays, power supplies, ... have been used.
6. Interferences of parasitic cavities can be large, also when the reflectivity of one mirror is only low, but the other is high, see Appendix B.4.11. Especially cheap waveplates can cause a lot of fringes.

Data analysis and writing.

1. Save all data you see, both as a screenshot (to find it easier and to get an overview) and as measurement data together with all measurement procedure parameters
2. Python *jupyter* notebooks[2] are a great way to analyse and plot data.
3. Python's matplotlib produces excellent plots for publication, with less post-processing needed than in Mathematica
4. Use the graphical LyX LateX editor[3] for writing thesis and papers. Especially for formulas the instant graphical representation speeds up the process a lot, while keeping the advantages of LateX: You can still write normal LateX commands and use the whole power and look of LateX. When writing the thesis split your document in chapters.
5. Give your measurements short names with serial numbers e.q. ('ABS01','RAMAN12','SHOT02'). This way you can find them across your notes, data analysis and filesystem. Details on measurement parameters are better kept in the notebook instead of a filename.
6. The online tool WebPlotDigitizer [4] can be used to automatically extract data from graphs found in the literature. Here, only a screenshot of the plot is needed. This data often facilitates comparing and validating own measurements or to build models and simulations.

Avoiding ground loops.

1. Ground loops manifest them in sharp signals exactly at 50Hz in a Fourier transform. Also higher harmonics may show up.
2. Twist wires of cables, or better use coaxial cables or double shielded twisted pair network cables
3. Ground loops can also be guided on digital cables (trigger, ...). There, the ground can also be separated.
4. Be sure to use isolated Ethernet cables.
5. Attach equipment with a common ground to the same power strip.

[2] https://jupyter.org/
[3] https://www.lyx.org/
[4] https://automeris.io/WebPlotDigitizer/

6. Think about separating devices optically (e.g. using multiple photo diodes in parallel if several devices need the signal) or physical (attach multiple piezos in series if multiple devices need to change a length).

B.6. Photothermal effects on cavity length

High optical powers in fibre cavities can lead to *photothermal* effects that change the cavity length through absorption of optical power and thermal expansion. During this work two different effects were of importance.

B.6.1. Cavity internal effects (resonant)

As shown by Brachmann et al., absorption of optical power inside the cavity, when the cavity length is close to a resonance with a narrow linewidth laser, can strongly affect the cavity length on microsecond timescales and total length changes over several picometre[35, 52]. This effect plays a role when locking the cavity length and starts to play a row with intra-cavity powers of $\gtrsim 1\,\mathrm{W}$ (from e.g. lasers of $\gtrsim 1\,\mathrm{mW}$ in a high finesse cavity). Depending on the side of the resonance, the heating of the fibre Bragg mirrors can stabilize or destabilize the cavity length by negative or positive feedback.

A similar effect that the cavity length changes on resonances was also observed for much lower finesse but higher excitation powers. However, the timescale involved were orders of magnitude larger as well as the length change. A $100\,\mathrm{mW}$ laser (at 780nm) was used for Raman excitation in the transparent part of the spectrum. At this wavelength the finesse was well below 10 and the transmitted power (and therefore the intra-cavity power) was modulated by a factor of only 3. When the Laser was resonant, the cavity length reduced several 100nm with a much time constant on the order of 10s. This longer time constant makes sense if it is assumed that stronger heating, due to stronger absorption in this band and stronger laser power, penetrates further back into the fibre.

B.6.2. Effects in fibre (off-resonant)

A second effect was discovered during this work, present even when the cavity is not resonant.

The effect was observed when the power of a few mW laser (890nm) was changed while modulating the cavity length. The change of power lead to a drift of the position of the resonances on the order of $100\,\mathrm{nm}$ with an exponential time scale of a few seconds. The time constant of the exponential decaying cavity length change was observed to be on the order of seconds, see Fig. B.6.1 for a measurement. The effect is assumed to be due to thermal expansion of the cavity fibre end due to heating of light scattered or absorbed at the mirror. The heat induced length change always shortens the cavity. Due to its long time constant the effect also seems to involve a macroscopic part of the fibre.

In the following the source of this effect is explored.

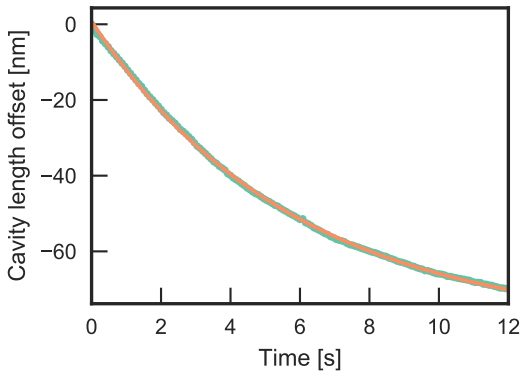

Figure B.6.1.: Cavity length change after suddenly switching on the laser with $\approx 2.0\,\mathrm{mW}$ power coupled into the cavity fibre. Green dots: measurement, orange line: exponential decay fit with time constant $t_0 = 5.8\,\mathrm{s}$

Calculation of thermal expansion from absorption

To get more insight into the source of the expansion we estimate the thermal expansion due to the power dissipated into the fibre. We approximate the fibre as a simple glass cylinder here. The length change of the fibre is proportional to the temperature change, ΔT, the length of the part of the fibre that is heated, l_h, and the coefficient of thermal expansion of glass, $\alpha = 5.4\text{×}10\text{–}7/K$,

$$\Delta d{=}\alpha\,\Delta T\,l_\mathrm{h} \tag{B.6.1}$$

The temperature change depends on the heat energy deposited, ΔQ, the specific heat of (fused silica) glass, $c = 1052\frac{J}{kg\,K}$ and the mass heated

$$\Delta T = \frac{\Delta Q}{c\,m}\,. \tag{B.6.2}$$

The mass in turn is given by the length heated, the density, $\rho = 2.201 g/cm^3$, and the cross section of the fibre, A, (with diameter 125µm), $m = \rho A l_h$. When inserting this into Eq. (B.6.1), we see that the length change gets independent of the length heated (which would be hard to measure or estimate anyway)

$$\Delta d = \frac{\alpha \Delta Q}{c\rho A}\,. \tag{B.6.3}$$

We assume that all power absorbed gets converted to heat, and that in a short time period after switching on the light, Δt, (and for low temperature increases) the process is adiabatic, meaning no heat gets dissipated from the fibre into the surrounding. Therefore we can set

$$\Delta Q \approx P_\mathrm{abs}\Delta t \tag{B.6.4}$$

The observed length change of about $10\,\mathrm{nm}$ in the first $1\,\mathrm{s}$ corresponds to a $0.5\,\mathrm{mW}$power dumped on average. This is far larger than the losses inside the cavity and suggests that the light before the fibre heats the fibre end. This is confirmed with a measurement where the cavity is kept off-resonant by just stopping the cavity modulation, instead of switching off the

laser. There, no light should enter the cavity. After switching on the modulation the cavity is already at the shortened length due to temperature changes, meaning that not the absorption inside the cavity is responsible.

It still is not known what causes the strong absorption at the fibre mirror. However, light scattered from the core into the cladding at the fibre mirror might get absorbed effectively in the fibre jacket

Using the parasitic effect

This parasitic effect hinders cavity length stability by adding slow drifts depending on the laser power. Furthermore, even two cavity fibres mechanically attached to each other will exbibit length differences depending on the power dissipated in each of them. However, the effect could also be used to tune the cavity length by up to a few hundred nanometre when simply altering the power of a few mw off-resonant laser. At cryogenic temperatures this effect might even be used to tune across several free spectral ranges.

C. Setup characteristics

C.1. Dielectric coatings

C.1.1. Dielectric coating simulation

Following [127], code for simulating optical coatings has been developed. This way reflection, absorption and transmission as well as the field distribution inside the coating stack could be simulated. The code was implemented in Mathematica and the python programming language. Mirror coating calculations from coating manufacturers could be reproduced.

C.1.2. Overview of coatings used

In Table C.1.1, the optical coatings of the cavity mirrors used in this work are listed.

In Fig. C.1.1a the transmission of three of the optical coatings used is shown, as calculated from simulations. From this the theoretically expected Finesse of some of the mirror combinations is shown in Fig. C.1.1b.

C.1.3. Deviation and scattering of fibre performance

The optimized mirror coating (Section 3.2) showed strong deviation from the expected finesse. This is shown in Fig. C.1.2a for nine different fibres. Only a few fibres achieved the low losses that were expected for the coating processes. Many fibres showed orders of magnitude larger losses than expected, see Fig. C.1.2b.

To find the source of this error more than 20 fibres were analysed systematically. To see if the low finesse correlates with some parameter, finesse measurements performed with each fibre were combined with properties of the production process, as is shown exemplary in Fig. C.1.3. However, no correlation were found with concave profile depth, radius of curvature, position during the manufacturing process ("holder", "position in holder", "z-position"), profile asymmetry, deviation from a perfect spherical mirror ("residual"), displacement between profile and fibre core, manufacturing date or fibre cleave angle.

Name	centre wavelength	centre transmission	last layer	type	Manufacturer
890-100	896	80 ± 30 ppm	low refractive	planar	Layertec
890-300	898	190 ± 30 ppm	low refractive	planar	Layertec
890-chirp	830+950 –> 878	35 ± 5 ppm	high refractive	fibres, planar	Laseroptik
890-atf	890	50 ± 5 ppm	high refractive	fibres, planar	Advanced thin films
780-atf	780		high refractive	fibres, planar	Advanced thin films

Table C.1.1.: Overview of fibre and planar mirror coatings used in this work. "last layer" specifies if the last layer is high or low refractive

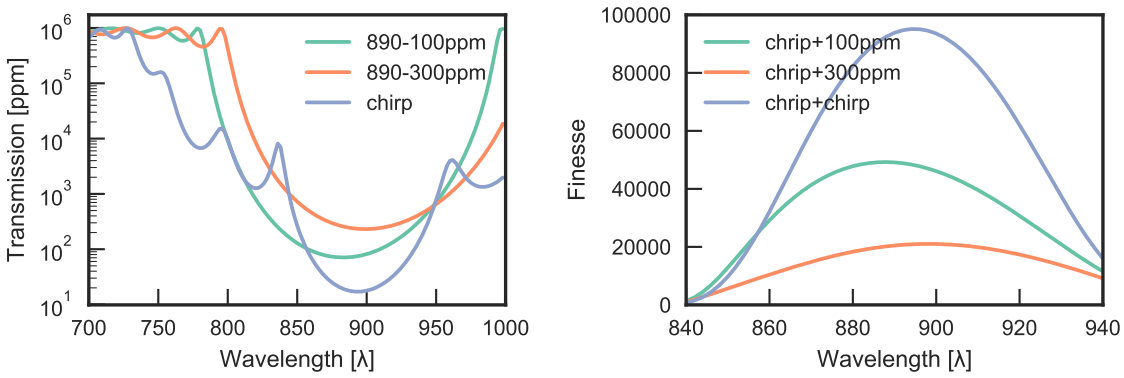

(a) **(b)**

Figure C.1.1.: (a) Theoretical expected transmission of the mirror coatings used. (b) Expected finesse of mirror combinations.

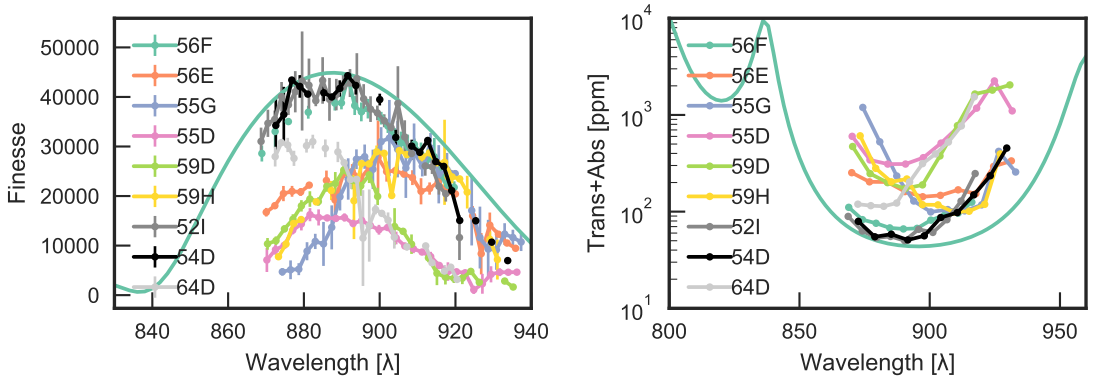

(a) **(b)**

Figure C.1.2.: (a) Wavelength resolved Finesse measurements of nine different cavity fibres (labelled with their identifier). The solid line is the expected finesse. (b) Losses of the fibre mirror extracted from the finesse measurements in (a) by assuming ideal performance of the planar mirror.

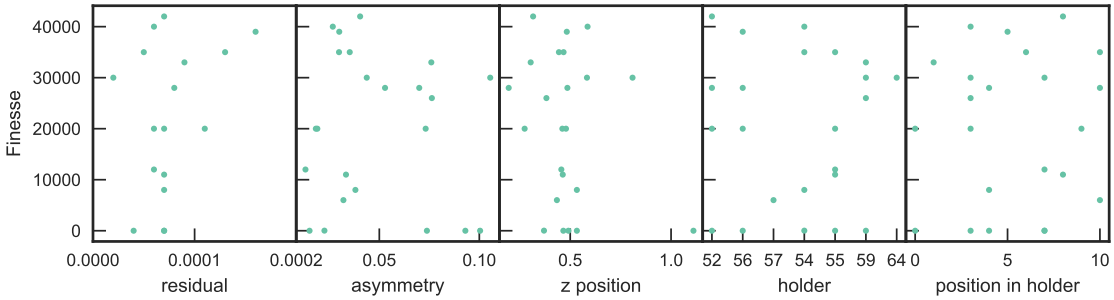

Figure C.1.3.: Maximum finesse of different fibres correlated with various manufacturing parameters.

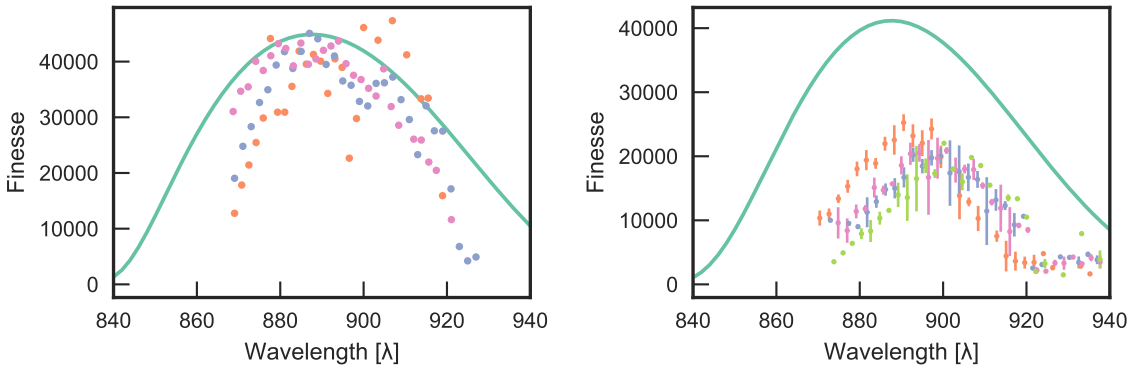

(a) **(b)**

Figure C.1.4.: Finesse as a function of wavelength with different angular alignments. Measurements for two different fibres. One with a central finesse as expected (a) and a second one with strong additional losses (b). The solid line is the expected finesse.

So far, the scattered performance remains a mystery and most likely may be attributed to random contamination.

Angle dependence

The angle between both cavity mirrors can also change the finesse of the cavity. In Fig. C.1.4, measurements of the cavity finesse under different angular alignments are shown. It can be seen that the angle affects the maximum achievable finesse, width and the centre of the high finesse region. While in the centre the finesse is affected by only a few percent, at the sides of the stop band, the alignment can change the finesse strongly.

C.2. Computer control and data acquisition

A key component in developing scanning cavity microscopy was a flexible real-time control of the cavity and data acquisition. Sequential programs that do a complete mirror scan at a time were not sufficient for the complexity of the measurements. The cavities, especially in its early incarnations needed real time feedback both from the computer as well as from the human operating it. Being able to get real-time information, and be able to change cavity or scan parameters again in real-time were especially important to improve and optimize scanning processes quickly.

For e.g. seeing live how noise levels of a measurement, be it transmission accuracy, cavity stability or coupling to a certain detector, change during the measurement helped a lot to speed up the development of the setup.

For the general principles of the computer control setup, the following principles were followed:

- Unify control of all experiments: All scanning cavity experiments (with their different positioners and measurements) in the lab should be controlled by a single code base.

- Abstract away display/input complexity: For other group members to quickly improve the setup the code had to be short and readable.
- Real time programming: being able to improve the program while it is running enables one to iterate much faster.
- Modular measurement modules: Enable different scanning measurements on top of the same core program.

C.2.1. Tools

During the first year of my thesis the scanning cavity setups was built using the proprietary LabView visual environment and programming language by National instruments as the central computer control. The advantages were the availability through the university, the ease of getting started, the broad knowledge base on the Internet and the availability of instrument drivers for almost all equipment in the lab.

However, the more the requirements to the experiment control software grew and the more complex it got, the more the limitations in LabView became apparent.

The first problem is that scaling programs in LabView is possible, but it takes a lot of work. Second, adapting the program for all the different setups (at that time three cavity setups and one confocal setup) and keeping the code base in sync proved to be complex due to the nature of a visual programming language. Furthermore, debugging errors became a 'nightmare', especially with hardware related issues.

Additionally, documenting and getting my fellow co-workers to understand the code provided more and more complex and time consuming.

As these problems increased more and more over time, a cut was made and the whole LabView based control system was replaced with a new software based on the Python programming language. The language was chosen as it has a very concise syntax and is widely adopted in the science *and* also in general use. This offers a plethora of tools and knowledge and no limits to scalability. Immediately, the advantages and hurdles became visible. Python offered faster programming and led to better documented code (a lot more self explanatory due to the concise syntax). Furthermore, better scalability and adaptability to the different setups was given due to the nature of a common text-based programming language.

However, it came with the downside of initial effort to do the right choices for tools (python installation, user-interface toolkits, plotting libraries, data formats) and the need to write instrument drivers for a few devices. However, most devices either provided drivers or were available as open-source code on the internet.

C.2.2. Implementation details

All control systems are based on simple state machines. This means a 'main loop' is constantly running and the program is in one state at a time. This state does some actions and decides the next state to enter. The main loop can be halted and started in the user interface at any time. If there is an error (in the code, in an instrument or in a special value) instead of crashing and halting the whole program, only the main loop stops with an error message shown in the

console. The loop can be manually restarted e.g. after the source of error has been removed or it (magically) disappeared.

Scanning cavity setup

The 'scan' program is used to

- raster scan an area on a sample
- manually move the cavity to a certain position
- or sequentially perform measurements on a list of predefined points

In its normal state it continuously sets the position, performs measurements and records the data.

The area on the sample is defined by by origin coordinates (x,y), width, height, and resolution (in µm per pixel). Scanning can be paused and the current position of the cavity fibre on the sample can be moved arbitrarily. The cavity length can be adjusted. Multiple measurement modes are available, e.g. using an oscilloscope, a spectrometer, or time-to-digital converters for lifetime measurements. These measurement modules are called from the main program. They are abstracted in its own modules which offer the methods to initialize the instrument, take a measurement and validate the measurement to determine if it has to be repeated. New modules or modifications of old modules can be easily developed.

Addressing of the positioners for cavity length and transversal coordinates on the sample is also abstracted in own modules for the program to be usable on different setups with different positioning hardware.

To understand the program it is best to have a look at the flow of states depicted in Fig. C.2.1. There, the flow of the main program and its calls to the positioner, measurement and lock modules is shown.

Fibre fabrication

The LabView-based fibre fabrication setup was replace with a python based version mainly because (as common for LabView projects - a result of being developed in a graphical language and its complexity) documentation was quite scarce and code hard to understand. Errors (mainly due to buggy hardware) appeared commonly but the not really be traced to its origin. When rewriting the software in python, feature parity with the original system could be achieved after a bit more then a week.

Real time- scanning cavity setup

For the demands of the new stable cavity setup (Section 3.4) , the scanning software had to be rewritten. This was done to increase measurements speed and be able to record thousands of points per second. To do so, the program controls the cavity position by issuing a single output as waveform to the piezo elements that control the cavity position and length. Synchronized to this output, a batch of data is collected for multiple points at once. The recorded data is also acquired in a single step and unwrapped in the program afterwards. This is in contrast to the old setup where positioning and data acquisition was executed at each point and the

delay due to commands being sent to the positioners and retrieved from the data acquisition devices as well as internal program logic limited the data acquisition rate to 10 to a few 100 points per second, depending on the particular measurement procedure.

Spectral data analysis

To analyse hyperspectral images, also custom graphical user interface programs were written in python. This was crucial to test reproducibility and data quality when extraction spectral information from scans. The amount of data made solutions based on Mathematica or jupyter notebooks to slow to be used.

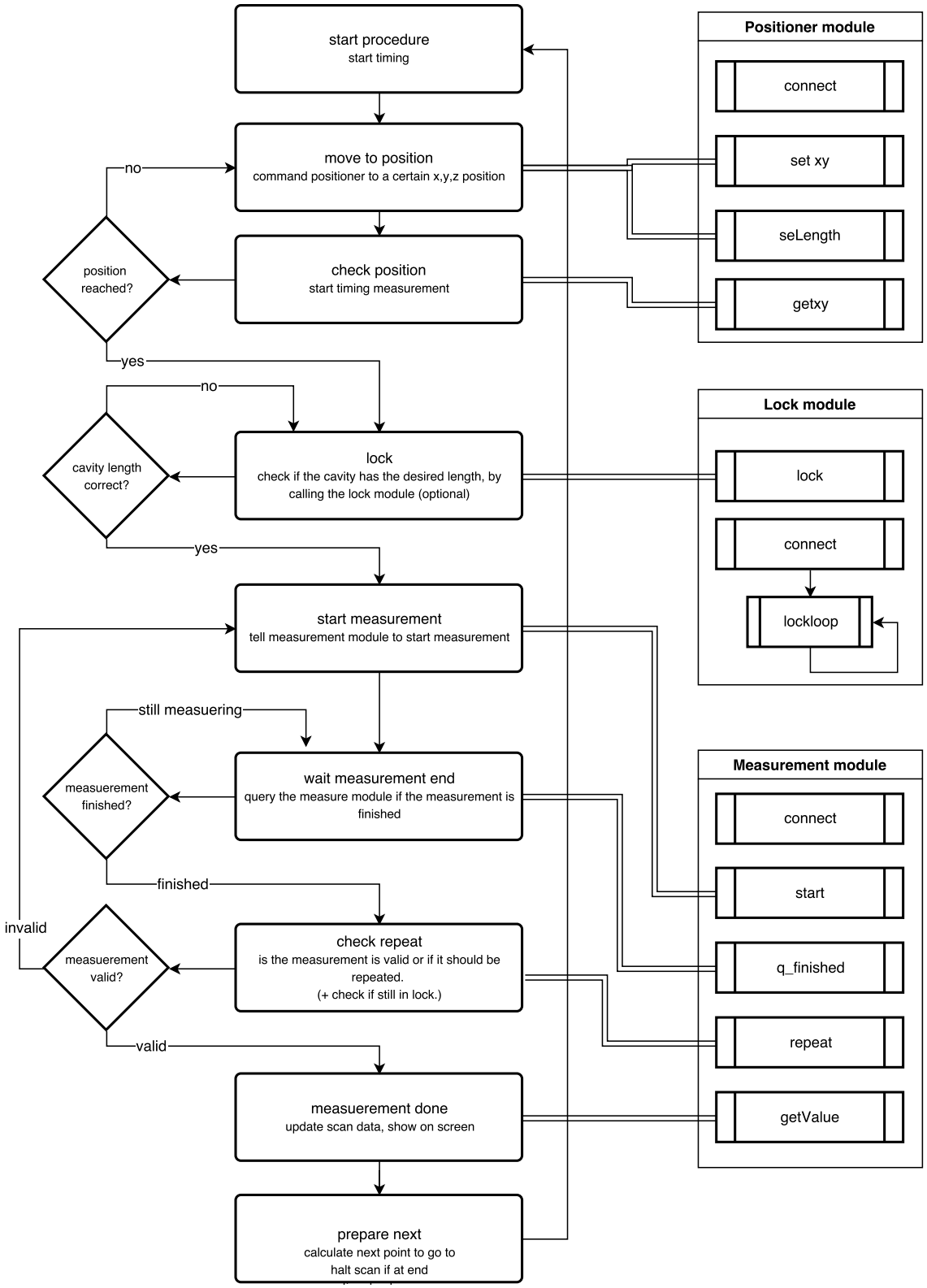

Figure C.2.1.: State flow of the main loop of the 'scan'-program and its relation to the measurement, lock and positioner modules. Rounded rectangles are the states of the main state machine. On the right side the sub modules with their methods are shown and the double lines indicate where they are called from the main state machine.

D. Abbreviations and Symbols

D.1. Abbreviations

APD	Avalanche photo diode
DBR	Distributed Bragg reflector
Eq.	Equation
FDTD	Finite-difference time-domain
FWHM	Full width at half maximum
HWHM	Half width at half maximum
FPGA	Field programmable gate array
DOS	density of states
MM	Multi-mode
PMMA	Polymethylmethacrylat
SEM	Scanning electron microscope
AFM	Atomic force microscope
STM	Scanning tunnelling microscope
FPGA	Field programmable gate array
SM	Single-mode
SNR	Singal-to-Noise Ratio
ppm	parts per million,10^{-6}
ppb	parts per billion, 10^{-9}
RMS	Root mean square. Here often synonymous with standard deviation.
WLI	white light interferometer
CMOS	CMOS array photodetectors
FSR	Free spectral range

CCD	charge coupled device array photodetector
SLED	Superluminiscent Light emitting diode
FPGA	Field Programmable Gate Array
FFT	Fast Fourier Transform
FEM	Finite Element Analysis
ASE	Amplified Spontaneous Emission
EOM	electro-optical modulator

D.2. Common symbols

d	Cavity length
d_p	Physical cavity length (physical separation between mirrors)
λ	Wavelength
q	Cavity mode order
A	Extinction by specimen between the cavity mirrors
$\mathcal{F}$	Cavity finesse
Q	Quality factor
Q_{eff}	effective Quality factor
η_c	Out-coupling efficiency
(n,m)	higher order Hermite-Gaussian mode
L,T,R	Cavity mirror losses, transmission, absorption
A	absorption at a sample inside the cavity
L_Σ	total losses of the cavity
NA	numerical aperture
φ	phase accumulated per cavity round trip
V_m	cavity mode Volume
F_p	Purcell factor
$F_{p,\text{eff}}$	effective Purcell factor
SNR	signal-to-noise ratio

Bibliography

[1] Joseph Fraunhofer. “Bestimmung des Brechungs-und des Farbenzerstreungs-Vermögens verschiedener Glasarten, in Bezug auf die Vervollkommnung achromatischer Fernröhre”. In: *Annalen der Physik* 56.7 (1817), pp. 264–313.

[2] Gustav Kirchhoff and Robert Bunsen. “Chemische analyse durch spectralbeobachtungen”. In: *Annalen der Physik* 186.6 (1860), pp. 161–189.

[3] *Cavity-Enhanced Spectroscopy and Sensing*. Springer Series in Optical Sciences. Berlin Heidelberg: Springer-Verlag, 2014.

[4] Chandrasekhara Venkata Raman. “A new radiation”. In: (1928).

[5] T.W. Hänsch. “Einstein Lecture – Passion for precision”. en. In: *Annalen der Physik* 15.9 (Sept. 2006), pp. 627–652.

[6] A. Perot and Charles Fabry. “On the application of interference phenomena to the solution of various problems of spectroscopy and metrology”. In: *The Astrophysical Journal* 9 (1899), p. 87.

[7] Jackson Derek Ainslie. “The spherical Fabry—Perot interferometer as an instrument of high resolving power for use with external or with internal atomic beams”. In: *Proceedings of the Royal Society of London. Series A. Mathematical and Physical Sciences* 263.1314 (Sept. 1961), pp. 289–308.

[8] P. Connes. “L’étalon de Fabry-Perot sphérique”. fr. In: *Journal de Physique et le Radium* 19.3 (Mar. 1958), pp. 262–269.

[9] Theodor W. Hänsch. “Edible lasers and other delights of the 1970s”. In: *Optics & Photonics News* (2005).

[10] Barbara A. Paldus and Alexander A. Kachanov. “An historical overview of cavity-enhanced methods”. In: *Canadian Journal of Physics* 83.10 (2005), pp. 975–999.

[11] Richard Kounai Chang and Anthony J. Campillo. *Optical Processes in Microcavities*. en. Google-Books-ID: 02tsScNcMlAC. World Scientific, 1996.

[12] F. De Martini et al. “Anomalous spontaneous emission time in a microscopic optical cavity”. In: *Physical review letters* 59.26 (1987), p. 2955.

[13] Kerry J. Vahala. “Optical microcavities”. In: *Nature* 424.6950 (2003), pp. 839–846.

[14] F. Cairo, F. De Martini and D. Murra. “QED-vacuum confinement of inelastic quantum scattering at optical frequencies: A new perspective in Raman spectroscopy”. In: *Physical Review Letters* 70.10 (Mar. 1993), pp. 1413–1416.

[15] A. Fainstein, B. Jusserand and V. Thierry-Mieg. “Raman efficiency in a planar microcavity”. In: *Physical Review B* 53.20 (1996), R13287.

[16] A. Fainstein, B. Jusserand and V. Thierry-Mieg. “Raman Scattering Enhancement by Optical Confinement in a Semiconductor Planar Microcavity”. In: *Physical Review Letters* 75.20 (Nov. 1995), pp. 3764–3767.

[17] Benjamin Petrak, Nicholas Djeu and Andreas Muller. “Purcell-enhanced Raman scattering from atmospheric gases in a high-finesse microcavity”. In: *Physical Review A* 89.2 (Feb. 2014), p. 023811.

[18] B. Petrak et al. “Isotopic gas analysis through Purcell cavity enhanced Raman scattering”. In: *Applied Physics Letters* 108.9 (Feb. 2016), p. 091107.

[19] Rachel Symes, Robert M. Sayer and Jonathan P. Reid. “Cavity enhanced droplet spectroscopy: Principles, perspectives and prospects”. In: *Physical Chemistry Chemical Physics* 6.3 (2004), pp. 474–487.

[20] Hisashi Sumikura et al. “Cavity-enhanced Raman scattering of single-walled carbon nanotubes”. In: *Applied Physics Letters* 102.23 (June 2013), p. 231110.

[21] D Hunger et al. “A fiber Fabry–Perot cavity with high finesse”. In: *New Journal of Physics* 12.6 (June 2010), p. 065038.

[22] Yves Colombe et al. “Strong atom–field coupling for Bose–Einstein condensates in an optical cavity on a chip”. en. In: *Nature* 450.7167 (Nov. 2007), pp. 272–276.

[23] Roland Albrecht et al. “Coupling of a Single Nitrogen-Vacancy Center in Diamond to a Fiber-Based Microcavity”. In: *Physical Review Letters* 110.24 (June 2013), p. 243602.

[24] Hanno Kaupp et al. “Scaling laws of the cavity enhancement for nitrogen-vacancy centers in diamond”. In: *Physical Review A* 88.5 (Nov. 2013), p. 053812.

[25] Matthias Mader et al. “A scanning cavity microscope”. In: *Nature Communications* 6 (June 2015), p. 7249.

[26] Hrishikesh Kelkar et al. “Sensing Nanoparticles with a Cantilever-Based Scannable Optical Cavity of Low Finesse and Sub- λ^3 Volume”. In: *Physical Review Applied* 4.5 (Nov. 2015).

[27] Matthias Mader. “A Scanning Cavity Microscope”. PhD thesis. 2018.

[28] Christian Gebhardt et al. “Polariton hyperspectral imaging of two-dimensional semiconductor crystals”. In: *arXiv preprint arXiv:1803.08690* (2018).

[29] Julia Benedikter et al. “Cavity-enhanced single-photon source based on the silicon-vacancy center in diamond”. In: *Physical Review Applied* 7.2 (2017), p. 024031.

[30] Hanno Kaupp et al. “Purcell-enhanced single-photon emission from nitrogen-vacancy centers coupled to a tunable microcavity”. In: *Physical Review Applied* 6.5 (2016), p. 054010.

[31] Hanno S. Kaupp. “Coupling nitrogen-vacancy centers in diamond to fiber-based Fabry-Pérot microcavities”. Text.PhDThesis. Ludwig-Maximilians-Universität München, Oct. 2017.

[32] Norman Hodgson and Horst Weber. *Optical Resonators: Fundamentals, Advanced Concepts, Applications*. Springer, June 2005.

[33] Bahaa EA Saleh, Malvin Carl Teich and Bahaa E. Saleh. *Fundamentals of photonics*. Vol. 22. Wiley New York, 1991.

[34] M. Trupke et al. "Microfabricated high-finesse optical cavity with open access and small volume". In: *Applied Physics Letters* 87.21 (Nov. 2005), p. 211106.

[35] Johannes FS Brachmann et al. "Photothermal effects in ultra-precisely stabilized tunable microcavities". In: *Optics express* 24.18 (2016), pp. 21205–21215.

[36] Manuel Uphoff et al. "Frequency splitting of polarization eigenmodes in microscopic Fabry–Perot cavities". In: *New Journal of Physics* 17.1 (2015), p. 013053.

[37] Benjamin T. Walker et al. "Driven-dissipative non-equilibrium Bose–Einstein condensation of less than ten photons". In: *Nature Physics* (2018), p. 1.

[38] C. Buerhop et al. "Glass surface treatment with excimer and CO2 lasers". In: *Applied surface science* 46.1-4 (1990), pp. 430–434.

[39] Ziyun Di et al. "Controlling the emission from semiconductor quantum dots using ultra-small tunable optical microcavities". en. In: *New Journal of Physics* 14.10 (2012), p. 103048.

[40] A. A. P. Trichet et al. "Open-access optical microcavities for lab-on-a-chip refractive index sensing". en. In: *Lab on a Chip* 14.21 (2014), pp. 4244–4249.

[41] Christina J. Hood, H. J. Kimble and Jun Ye. "Characterization of high-finesse mirrors: Loss, phase shifts, and mode structure in an optical cavity". In: *Physical Review A* 64.3 (Aug. 2001), p. 033804.

[42] Garrett D. Cole et al. "High-performance near- and mid-infrared crystalline coatings". In: *Optica* 3.6 (June 2016), pp. 647–656.

[43] Matthias Mader. *A Cavity Nanoscope*. 2012.

[44] Jaime Ortega Arroyo. "Non-fluorescent Single-Molecule Approaches to Optical Microscopy". In: *Investigation of Nanoscopic Dynamics and Potentials by Interferometric Scattering Microscopy*. Springer Theses. Springer, Cham, 2018, pp. 7–35.

[45] A. Gaiduk et al. "Room-temperature detection of a single molecule's absorption by photothermal contrast". In: *Science* 330.6002 (2010), pp. 353–356.

[46] Michel Orrit and J. Bernard. "Single pentacene molecules detected by fluorescence excitation in a p-terphenyl crystal". In: *Physical review letters* 65.21 (1990), p. 2716.

[47] Philipp Kukura et al. "Single-molecule sensitivity in optical absorption at room temperature". In: *The Journal of Physical Chemistry Letters* 1.23 (2010), pp. 3323–3327.

[48] P. Kukura et al. "Imaging a Single Quantum Dot When It Is Dark". In: *Nano Letters* 9.3 (Mar. 2009), pp. 926–929.

[49] Aurélien Crut et al. "Optical absorption and scattering spectroscopies of single nano-objects". en. In: *Chemical Society Reviews* 43.11 (May 2014), pp. 3921–3956.

[50] Thomas Juffmann et al. "Multi-pass microscopy". en. In: *Nature Communications* 7 (Sept. 2016), p. 12858.

[51] Thomas Juffmann et al. “Multi-pass transmission electron microscopy”. En. In: *Scientific Reports* 7.1 (May 2017), p. 1699.

[52] J. Gallego et al. “High-finesse fiber Fabry–Perot cavities: stabilization and mode matching analysis”. In: *Applied Physics B* 122.3 (Mar. 2016).

[53] A. Bick et al. “The role of mode match in fiber cavities”. In: *Review of Scientific Instruments* 87.1 (Jan. 2016), p. 013102.

[54] Y. R Shen. *The principles of nonlinear optics*. English. Hoboken, N.J.: Wiley-Interscience, 2003.

[55] “Quantum Description of Raman Scattering”. en. In: *Raman Spectroscopy in Graphene Related Systems*. John Wiley & Sons, Ltd, 2011, pp. 103–119.

[56] Walter Heitler. *The Quantum Theory Of Radiation*. 3rd. Dover Books On Physics. Dover Publications, 1984.

[57] S. V. Gaponenko. “Effects of photon density of states on Raman scattering in mesoscopic structures”. In: *Physical Review B* 65.14 (Mar. 2002), p. 140303.

[58] A. Meldrum, P. Bianucci and F. Marsiglio. “Modification of ensemble emission rates and luminescence spectra for inhomogeneously broadened distributions of quantum dots coupled to optical microcavities”. EN. In: *Optics Express* 18.10 (May 2010), pp. 10230–10246.

[59] G. Rempe et al. “Measurement of ultralow losses in an optical interferometer”. In: *Optics letters* 17.5 (1992), pp. 363–365.

[60] M. S. Dresselhaus et al. “Raman spectroscopy of carbon nanotubes”. In: *Physics Reports* 409.2 (2005), pp. 47–99.

[61] Aurélien A. P. Trichet et al. “Topographic control of open-access microcavities at the nanometer scale”. EN. In: *Optics Express* 23.13 (June 2015), pp. 17205–17216.

[62] Julia Benedikter et al. “Transverse-mode coupling and diffraction loss in tunable Fabry–Pérot microcavities”. In: *New Journal of Physics* 17.5 (2015), p. 053051.

[63] Carl E. Wieman and Leo Hollberg. “Using diode lasers for atomic physics”. In: *Review of Scientific Instruments* 62.1 (Jan. 1991), pp. 1–20.

[64] Daniele Romanini et al. “Measurement of trace gases by diode laser cavity ringdown spectroscopy”. In: *Environmental Sensing and Applications*. Vol. 3821. International Society for Optics and Photonics, 1999, pp. 94–105.

[65] John H. Moore et al. *Building scientific apparatus*. Cambridge University Press, 2009.

[66] J. Morville and D. Romanini. “Sensitive birefringence measurement in a high-finesse resonator using diode laser optical self-locking”. In: *Applied Physics B* 74.6 (2002), pp. 495–501.

[67] Y. K. Yong et al. “Invited Review Article: High-speed flexure-guided nanopositioning: Mechanical design and control issues”. In: *Review of Scientific Instruments* 83.12 (Dec. 2012), p. 121101.

[68] Jason D. Hackley et al. “High-stability cryogenic scanning tunneling microscope based on a closed-cycle cryostat”. In: *Review of Scientific Instruments* 85.10 (2014), p. 103704.

[69] Guillaume Martinet et al. *Low temperature properties of piezoelectric actuators used in SRF cavities cold tuning systems*. Tech. rep. 2006.

[70] R. P. Taylor et al. “Measurements of the material properties of a laminated piezoelectric stack at cryogenic temperatures”. In: *AIP Conference Proceedings*. Vol. 824. AIP, 2006, pp. 200–207.

[71] MatWeb, LLC. *Online Materials Information Resource - MatWeb*. 2018.

[72] JPE Precicion Engineering. *JPE - Precision Point: Free engineering knowledge*. 2018.

[73] Lukas Greuter et al. “A small mode volume tunable microcavity: Development and characterization”. In: *Applied Physics Letters* 105.12 (Sept. 2014), p. 121105.

[74] Daniel Najer et al. “A gated quantum dot far in the strong-coupling regime of cavity-QED at optical frequencies”. In: *arXiv:1812.08662 [quant-ph]* (Dec. 2018). arXiv: 1812.08662.

[75] K. Huang et al. “Microcontroller-based locking in optics experiments”. In: *Review of Scientific Instruments* 85.12 (Dec. 2014), p. 123112.

[76] W. van Etten. “Coupling of LED Light into a Single-Mode Fiber”. In: *Journal of Optical Communications* 9.3 (Jan. 1988).

[77] René Dändliker. “Concept of modes in optics and photonics”. In: *Sixth International Conference on Education and Training in Optics and Photonics*. Vol. 3831. International Society for Optics and Photonics, 2000, pp. 193–199.

[78] Lena Simone Fohrmann et al. “Single mode thermal emission”. In: *Optics express* 23.21 (2015), pp. 27672–27682.

[79] Kim I. Mortensen and Henrik Flyvbjerg. “Calibration-on-the-spot: How to calibrate an EMCCD camera from its images”. en. In: *Scientific Reports* 6 (July 2016), p. 28680.

[80] Rainer Heintzmann et al. “Calibrating photon counts from a single image”. In: *arXiv:1611.05654 [astro-ph, physics:physics]* (Nov. 2016). arXiv: 1611.05654.

[81] Xiaoji Niu et al. “Using Inertial Sensors in Smartphones for Curriculum Experiments of Inertial Navigation Technology”. In: *Education Sciences* 5 (Mar. 2015), pp. 26–46.

[82] *IEEE 952-1997 - IEEE Standard Specification Format Guide and Test Procedure for Single-Axis Interferometric Fiber Optic Gyros*.

[83] D. W. Allan. “Historicity, strengths, and weaknesses of Allan variances and their general applications”. en. In: *Gyroscopy and Navigation* 7.1 (Jan. 2016), pp. 1–17.

[84] d v land. *The use of the Allan deviation for the identification and measurement of noise and drift in measurement data*. 2014.

[85] Lukas M. Payne, Wolfgang Langbein and Paola Borri. “Wide-Field Imaging of Single-Nanoparticle Extinction with Sub-nm^2 Sensitivity”. In: *Physical Review Applied* 9.3 (Mar. 2018), p. 034006.

[86] M. P. McDonald et al. “Supercontinuum spatial modulation spectroscopy: Detection and noise limitations”. In: *Review of Scientific Instruments* 84.11 (Nov. 2013), p. 113104.

[87] Kaihui Liu et al. “Systematic determination of absolute absorption cross-section of individual carbon nanotubes”. In: *Proceedings of the National Academy of Sciences* 111.21 (2014), pp. 7564–7569.

[88] Michele Celebrano et al. “Single-molecule imaging by optical absorption”. In: *Nature Photonics* 5.2 (2011), p. 95.

[89] Lukas M. Payne, Wolfgang Langbein and Paola Borri. “Polarization-resolved extinction and scattering cross-sections of individual gold nanoparticles measured by wide-field microscopy on a large ensemble”. In: *Applied Physics Letters* 102.13 (Apr. 2013), p. 131107.

[90] Lukas Payne et al. “Optical micro-spectroscopy of single metallic nanoparticles: quantitative extinction and transient resonant four-wave mixing”. In: *Faraday Discussions* 184.0 (Dec. 2015), pp. 305–320.

[91] Thomas Hümmer et al. “Cavity-enhanced Raman microscopy of individual carbon nanotubes”. In: *Nature Communications* 7 (July 2016), p. 12155.

[92] Phaedon Avouris, Zhihong Chen and Vasili Perebeinos. “Carbon-based electronics”. In: *Nanoscience And Technology: A Collection of Reviews from Nature Journals*. World Scientific, 2010, pp. 174–184.

[93] Phaedon Avouris, Marcus Freitag and Vasili Perebeinos. “Carbon-nanotube photonics and optoelectronics”. en. In: *Nature Photonics* 2.6 (June 2008), pp. 341–350.

[94] J. Moser et al. “Nanotube mechanical resonators with quality factors of up to 5 million”. en. In: *Nature Nanotechnology* 9.12 (Dec. 2014), pp. 1007–1011.

[95] Adrien Jeantet et al. “Widely tunable single-photon source from a carbon nanotube in the Purcell regime”. In: *arXiv:1508.06297 [cond-mat, physics:physics]* (Aug. 2015). arXiv: 1508.06297.

[96] Alexander Högele et al. “Photon antibunching in the photoluminescence spectra of a single carbon nanotube”. In: *Physical review letters* 100.21 (2008), p. 217401.

[97] Matthias S. Hofmann et al. “Bright, long-lived and coherent excitons in carbon nanotube quantum dots”. en. In: *Nature Nanotechnology* 8.7 (July 2013), pp. 502–505.

[98] Xuedan Ma et al. “Room-temperature single-photon generation from solitary dopants of carbon nanotubes”. en. In: *Nature Nanotechnology* advance online publication (July 2015).

[99] Yuhei Miyauchi et al. “Brightening of excitons in carbon nanotubes on dimensionality modification”. en. In: *Nature Photonics* 7.9 (Sept. 2013), pp. 715–719.

[100] Achim Hartschuh et al. “Simultaneous fluorescence and Raman scattering from single carbon nanotubes”. In: *Science* 301.5638 (2003), pp. 1354–1356.

[101] Jonathan C. Noé et al. “Environmental Electrometry with Luminescent Carbon Nanotubes”. In: *Nano Letters* 18.7 (July 2018), pp. 4136–4140.

[102] Jason K. Streit et al. “Directly Measured Optical Absorption Cross Sections for Structure-Selected Single-Walled Carbon Nanotubes”. In: *Nano Letters* 14.3 (Mar. 2014), pp. 1530–1536.

[103] Jean-Christophe Blancon et al. “Direct measurement of the absolute absorption spectrum of individual semiconducting single-wall carbon nanotubes”. en. In: *Nature Communications* 4 (Sept. 2013), p. 2542.

[104] A Jorio et al. “Characterizing carbon nanotube samples with resonance Raman scattering”. In: *New Journal of Physics* 5 (Oct. 2003), pp. 139–139.

[105] K. S. Novoselov et al. “Electric Field Effect in Atomically Thin Carbon Films”. en. In: *Science* 306.5696 (Oct. 2004), pp. 666–669.

[106] Saptarshi Das et al. “Beyond Graphene: Progress in Novel Two-Dimensional Materials and van der Waals Solids”. In: *Annual Review of Materials Research* 45.1 (July 2015), pp. 1–27.

[107] Thomas Mueller and Ermin Malic. “Exciton physics and device application of two-dimensional transition metal dichalcogenide semiconductors”. En. In: *npj 2D Materials and Applications* 2.1 (Sept. 2018), p. 29.

[108] Michael Förg et al. “Cavity-control of bright and dark interlayer excitons in van der Waals heterostructures”. en. In: (Oct. 2017).

[109] Pasqual Rivera et al. “Observation of long-lived interlayer excitons in monolayer $MoSe_2$–WSe_2 heterostructures”. en. In: *Nature Communications* 6 (Feb. 2015), p. 6242.

[110] Chanyeol Choi et al. “Enhanced interlayer neutral excitons and trions in trilayer van der Waals heterostructures”. En. In: *npj 2D Materials and Applications* 2.1 (Sept. 2018), p. 30.

[111] Juan Gomez Velez and Andreas Muller. “Purcell-enhanced microcavity Raman scattering from pressurized gases”. In: *Applied Physics Letters* 112.4 (Jan. 2018), p. 041107.

[112] Wayne R. Fenner et al. “Raman cross section of some simple gases”. In: *JOSA* 63.1 (Jan. 1973), pp. 73–77.

[113] Helen Shen. “Interactive notebooks: Sharing the code”. In: *Nature News* 515.7525 (Nov. 2014), p. 151.

[114] Thomas Kluyver et al. “Jupyter Notebooks – a publishing format for reproducible computational workflows”. In: *Positioning and Power in Academic Publishing: Players, Agents and Agendas*. IOS Press, 2016, pp. 87–90.

[115] Fernando Pérez and Brian E. Granger. “IPython: a System for Interactive Scientific Computing”. In: *Computing in Science and Engineering* 9.3 (May 2007), pp. 21–29.

[116] John D. Hunter. “Matplotlib: A 2D graphics environment”. In: *Computing in science & engineering* 9.3 (2007), pp. 90–95.

[117] H. Kogelnik and Tingye Li. “Laser beams and resonators”. In: *Applied Optics* 5.10 (1966), pp. 1550–1567.

[118] Dietrich Marcuse. *Light transmission optics*. Van Nostrand Reinhold, 1982.

[119] Simin Feng and Herbert G. Winful. “Physical origin of the Gouy phase shift”. In: *Optics letters* 26.8 (2001), pp. 485–487.

[120] Craig F. Bohren and Donald R. Huffman. *Absorption and Scattering of Light by Small Particles*. Weinheim: Wiley-VCH, Mar. 1998.

[121] Lukas Novotny and Bert Hecht. *Principles of Nano-Optics*. Cambridge University Press, June 2006.

[122] *The Feynman Lectures on Physics Vol. I Ch. 32: Radiation Damping. Light Scattering.*

[123] Dubravko I. Babic and Scott W. Corzine. "Analytic expressions for the reflection delay, penetration depth, and absorptance of quarter-wave dielectric mirrors". In: *IEEE Journal of Quantum Electronics* 28.2 (1992), pp. 514–524.

[124] L. R. Brovelli and U. Keller. "Simple analytical expressions for the reflectivity and the penetration depth of a Bragg mirror between arbitrary media". In: *Optics communications* 116.4-6 (1995), pp. 343–350.

[125] Michel Wautelet. "Scaling laws in the macro-, micro-and nanoworlds". In: *European Journal of Physics* 22.6 (2001), p. 601.

[126] James E. Harvey et al. "Total integrated scatter from surfaces with arbitrary roughness, correlation widths, and incident angles". In: *Optical Engineering* 51.1 (2012), p. 013402.

[127] Sh A. Furman and A. V. Tikhonravov. *Basics of Optics of Multilayer Systems*. Atlantica Séguier Frontières, Jan. 1992.

[128] T. Hümmer et al. "Weak and strong coupling regimes in plasmonic QED". In: *Physical Review B* 87.11 (Mar. 2013), p. 115419.

[129] Bernardo Casabone et al. "Cavity-enhanced spectroscopy of a few-ion ensemble in Eu3+:Y2O3". en. In: *New Journal of Physics* 20.9 (Sept. 2018), p. 095006.

[130] Mark Jenkins et al. "Coupling single-molecule magnets to quantum circuits". In: *New Journal of Physics* 15.9 (2013), p. 095007.

Publications

- *Cavity-enhanced Raman microscopy of individual carbon nanotubes*
  T. Hümmer, J. Noe, M.S. Hoffmann, T. W. Hänsch, A. Högele and D. Hunger
  Nature Commununications 7, 12155 (2016). [91]
- *Weak and strong coupling regimes in plasmonic QED*
  T. Hümmer, F.J. García-Vidal, L. Martín-Moreno, D. Zueco
  Phys. Rev. B 87, 115419 (2013)[128]w
- *Transverse-mode coupling and diffraction loss in tunable Fabry–Pérot microcavities*
  J. Benedikter, T. Hümmer, M. Mader, B. Schlederer, J. Reichel, T.W. Hänsch, D. Hunger
  New J. Phys. 17, 053051 (2015)[62]
- *Purcell-Enhanced Single-Photon Emission from Nitrogen-Vacancy Centers Coupled to a Tunable Microcavity*
  H. Kaupp, T. Hümmer, M. Mader, B. Schlederer, J. Benedikter, P. Haeusser, H.-C. Chang, H. Fedder, T. W. Hänsch, and D. Hunger
  Physical Review Applied **6**, 054010 (2016) [30]

- *Cavity-Enhanced Single-Photon Source Based on the Silicon-Vacancy Center in Diamond*
  J. Benedikter, H. Kaupp, T. Hümmer, Y. Liang, A. Bommer, C. Becher, A. Krueger, J. M. Smith, T. W. Hänsch, D. Hunger
  Physical Review Applied **7**, 024031 (2017) [29]
- *Versuchsanleitung Fortgeschrittenenpraktikum: Versuch H2 Laserspektroskopie*
  T. Hümmer
  http://www2.mpq.mpg.de/∼haensch/pdf/Versuch_H2_Laserspektroskopie6.pdf (2015)
- *Cavity-enhanced spectroscopy of a few-ion ensemble in* $Eu^{3+} : Y2O3$
  B. Casabone, J. Benedikter, T. Hümmer, F. Oehl, K. de Oliveira Lima, T. W. Hänsch, A. Ferrier, P. Goldner, H. de Riedmatten, D. Hunger
  New J. Phys. 20, 095006 (2018)[129]
- *Coupling single-molecule magnets to quantum circuits*
  M. Jenkins, T. Hümmer, M.J. Martínez-Pérez, J. García-Ripoll, D. Zueco, F. Luis .
  New J. Phys. 15(9), 095007 (2013)[130]

Danke

Während dieser Doktorarbeit, die doch einen beträchtlichen Teil meines bisherigen Lebens eingenommen hat, habe ich viele neue Dinge gelernt, Orte bereist, Erfahrungen gesammelt und viele nette, interessante und höchst unterschiedliche Menschen kennen gelernt. Gleichzeitig ist eine Doktorarbeit, vielleicht auch aufgrund des persönlichen Ehrgeizes und der Schwierigkeit Neues zu finden und zu erfinden, nicht immer ein Zuckerschlecken. Dass mich aber trotz Herausforderungen und Rückschlägen am Rande des Unbekannten und des technisch Möglichen nicht der Mut verlassen hat, habe ich vielen Leuten zu verdanken.

Ich danke Herrn Professor Hänsch für die Aufnahme als Doktorand in seinen Lehrstuhl und die Schaffung einer guten Arbeitsatmosphäre mit vielen sympathischen Mitarbeitern. Das positive Menschenbild, der Forscherdrang, die Begeisterung für große und kleine Problemlösungen an diesem Lehrstuhl und in der Abteilung haben mir sehr gefallen. Die große Freiheit, das Vertrauen und die Möglichkeiten die Doktoranden hier haben sind fantastisch.

David Hunger danke ich für seine positive Art, seine Aufmunterungen und den ansteckenden Optimismus ("das geht in einem Nachmittag"). Die gute Laune, die Begeisterungsfähigkeit und die unterstützende Haltung spiegelten sich auch klar in der Besetzung und Stimmung in der Arbeitsgruppe wieder. Die vielen wertvollen Diskussionen, sein großes Wissen, und die Möglichkeit jederzeit zu reden, haben mir die Arbeit sehr erleichtert.

Ich danke allen meinen Kollegen, die mich auf dem Weg zu dieser Arbeit begleitet haben. Sei es mit interessanten Diskussionen, Aufmunterung und Rat oder auch der geteilten Begeisterung für die erstklassige Mensakost. Stets ermunternd waren auch die gemeinsamen Spaziergänge zum Mittagessen der gesamten Arbeitsgruppe. Die richtige Balance zwischen fachlichem Forschergeist aber auch Interesse für alle möglichen anderen Dinge (Züge, Sprachgeschichte, Weltverbesserung, Wandern, Thermomix) wurde in dieser Gruppe auf jeden Fall gut getroffen. Die gegenseitige Unterstützung in der Gruppe war mir auch stets eine große Freude. Ich finde es sehr schön das wir uns technisch und persönlich so gut ergänzen konnten.

Meinem ersten Laborgenossen, Hanno Kaupp, danke ich für die konstruktive, lustige Stimmung. Seine Gesellschaft und positive Art hat mir geholfen in schweren Zeiten nicht aufzugeben. Gerne denke ich an die zusammen gehörten Radiobeiträge auf Deutschlandfunk (z.B. über den kreisrunden Haarausfall). Matthias Mader danke ich für die vielen Tipps und Informationen über Fachgebiete die mir gefallen (Kochen, Schienenfahrzeugtechnik) und nicht gefallen (Analogelektronik, Bestellformalitäten, Normen) sowie der Hilfestellung bei vielen Aufgaben des täglichen Unibetriebs und viele kostbare Diskussionen. Julia Benedikter danke ich für die gute Zusammenarbeit, fachlichen Diskussion und stets ein offenes Ohr, aber vor allem auch für die sonstigen interessanten Gespräche, Erkenntnisse und das ertragen der koreanischen Radltour (42°C, 100% Luftfeuchtigkeit, 4 Tage).

Dank gebührt auch allen weiteren Arbeitsgruppenkollegen, die für viele lustige und interessante Stunden gesorgt haben, und die ich vermisse, insbesondere Michael Förg, Bernardo

Casabone, Larissa Kohler, Frederik Bopp, Johannes Brachmann, Andreas Weissl, Eric Bersin, Tolga Bagci, Max Pallmann, Franziska Beck, Christian Gebhardt, Pradyumna Paranjape, Benedikt Schlederer. Auch die unzähligen Freunde am Lehrstuhl Hänsch, in der Gruppe von Prof. Weinfurter und am MPQ waren sehr wertvoll. Jonathan Noé und Alexander Högele danke ich für die gute Zusammenarbeit und freue mich sehr auf zukünftige Unternehmungen. Auch das ganze Team der AG Högele sei gegrüßt.

Die Möglichkeiten auf Konferenzen verschiedene Winkel der (wissenschaftlichen) Welt zu entdecken haben die Zeit sehr bereichert. Ein Highlight jedes Jahres waren auch die Gruppentreffen auf Schloss Ringberg, die neben interessantem wissenschaftlichem Programm auch kulinarische Schmankerl, musikalische Darbietungen der Arbeitsgruppe(nleitung) und für Vortragsvorbereitung durchgearbeitet Nächte zu bieten hatten. Frau Hermann danke ich für die Organisation und dem Team von Schloss Ringberg für den tollen Tagungsort und den mir zugedachten Nachschlag beim Essen (im speziellen Frau Linsinger), der mich jedoch leider des öfteren wertvolle Sekunden beim Tegernseer-Hütten-Lehrstuhl-Berglauf gekostet hat.

Frau Gschwendtner danke ich für für die mir entgegengebracht Sympathie und Begeisterung wenn bei mir mal wieder eine Vertragsverlängerung anstand, sowie vielfältige intensive organisatorische Unterstützung.

David Zueco danke ich für die Unterstützung im Vorlauf zu meiner Doktorarbeit und die Möglichkeit ein Jahr in Spanien forschen zu können.

Meiner Familie verdanke ich meinen Forscherdrang und dass ich bin wer ich bin und dass ich dort bin wo ich bin. Meiner Schwester Sarah danke ich für Unterstützung, gute Gespräche und stets willkommen zu sein in ihrer tollen Familie. Meinen Eltern Danke ich für meine Erschaffung, geistige und seelische Inspiration, bedingungslose Liebe, Unterstützung und Geborgenheit insbesondere in schweren Zeiten. Meiner Frau Edie danke ich für ihre Liebe, Humor, Trost, Nachsicht und viel Unterstützung. Kuss. Der Welt danke ich für ihre interessante Komplexität und Vielfalt, ohne die man wohl gar keine Physiker bräuchte.